

TECHNISCHE UNIVERSITÄT MÜNCHEN  
Lehrstuhl für Carbon Composites

# **Forming of tailored thermoplastic composite blanks: material characterisation, simulation and validation**

**Alexane Margossian**

Vollständiger Abdruck der von der Fakultät für Maschinenwesen der Technischen Universität München zur Erlangung des akademischen Grades eines

**Doktor-Ingenieurs**

genehmigten Dissertation.

Vorsitzender: Prof. Dr.-Ing. Veit Senner

Prüfer der Dissertation: 1. Prof. Dr.-Ing. Klaus Drechsler  
2. Prof. Philippe Boisse, Ph.D.

Die Dissertation wurde am 19.09.2016 bei der Technischen Universität München eingereicht und durch die Fakultät für Maschinenwesen am 27.03.2017 angenommen.

Technische Universität München  
Fakultät für Maschinenwesen  
Lehrstuhl für Carbon Composites  
Boltzmannstraße 15  
D-85748 Garching bei München

Tel.: +49 (0) 89 / 289 – 15092

Fax.: +49 (0) 89 / 289 – 15097

Email: [info@lcc.mw.tum.de](mailto:info@lcc.mw.tum.de)

Web: [www.lcc.mw.tum.de](http://www.lcc.mw.tum.de)

*“Well done is better than well said”*  
*Benjamin Franklin (1706-1790)*



# ACKNOWLEDGEMENTS

I would like to thank Univ.-Prof. Dr.-Ing. Klaus Drechsler for giving me the opportunity to carry out this doctoral dissertation at the Chair of Carbon Composites of the Technical University of Munich (TUM-LCC). Working in such a leading-edge research environment was a fantastic experience! I am thankful to Prof. Dr. Philippe Boisse for supporting this work and for all the interesting discussions we had together. Also, I sincerely thank Prof. Dr. techn. Roland Hinterhölzl for the pleasant collaboration throughout the last three years.

I am particularly grateful to Prof. Assist. Dr. Sylvain Bel for being my mentor. Sylvain, thank you for your excellent guidance, for our fruitful discussions and for the time you took to answer my (countless) questions. Your support was definitely of great help in the completion of this work!

During my time at the TUM-LCC, I had the chance to work with skilled and passionate engineers. In particular, I would like to thank Theodosia, Philipp and Thorsten for their advice and most importantly, for the good laughs we had together. In addition, I am thankful to all my students for their help in my research. I really appreciated working with all of you.

I gratefully acknowledge the German Federal Ministry of Education and Research (BMBF) and diverse Austrian organisations (Federal Ministry for Transport, Innovation and Technology and Federal Ministry for Economy, Family and Youth) for funding this doctoral dissertation through the project MAIdesign and the COMET-program, respectively. Furthermore, I thank the Fraunhofer Institute for Chemical Technology (F-ICT) for the preparation of the tailored thermoplastic composite blanks and FACC Operations for supplying the thermoset pre-impregnated composite material.

I would like to thank Dr.-Ing. Steffen Beck (BMW) and Dipl.-Ing. Alexander Schug (F-ICT) for the valuable discussions. Also, I am thankful to Dr.Ir. Sebastiaan Haanappel (AniForm Engineering) and M.Sc. Dennis Brands (Thermoplastic Research Center) for their kind collaboration in the scope of our benchmark.

Last but not least, I would like to thank all my friends and express my deepest gratitude to my parents, Sylvie and Hratch, my sister, Anahide, my brother, Sevan, and my future wife, Florie, for their love, support and encouragement throughout this work.



# ABSTRACT

The increasing demand for composite components has driven the development of automated manufacturing processes. With their short manufacturing cycle time, thermoforming technologies appear to be good candidates for high volume production. Furthermore, they enable the manufacturing of complex parts which cannot be achieved with other automated techniques, e.g. Automated Fibre Placement machines. Nevertheless, while forming complex geometries, composite blanks undergo severe deformations which can lead to the occurrence of defects, such as out-of-plane wrinkles and fibre reorientations. To investigate such issues, Finite Element (FE) simulations have demonstrated to be more efficient than trial-by-error approaches.

The goal of this doctoral dissertation is to develop macroscopic FE thermoforming simulation models able to anticipate the occurrence of the aforementioned defects. Before being applied in an industrial context, models need to be validated. The reliability of their predictions is assessed by comparing computed outcomes to experimental measurements. In this work, validation is carried out with a generic double-curved component formed in a laboratory-scale thermoforming process.

To determine proper input parameters for the development of FE thermoforming simulation models, material behaviour is characterised under similar environmental conditions as forming occurs, e.g. temperature. The intrinsic behaviour of a unidirectional fibre-reinforced polyamide 6 tape and a polyimide separation film are investigated. Contact properties, such as tool/film, film/ply and interply-slip interactions, are also investigated. To assess whether the test methods considered for molten thermoplastic materials are also suitable for the characterisation of non-cured thermoset composite materials, a non-cured unidirectional thermoset pre-impregnated composite tape is tested under environmental forming conditions.

Thermoforming process simulation models are subsequently developed using a commercially available software. Input parameters are identified from experimental data using an inverse method. Validation, which is carried out with three different tailored blanks, demonstrates the ability of the simulation to properly predict preform geometries and external fibre orientations. Results also show the ability of the simulation to determine critical areas where out-of-plane wrinkles can potentially occur, although their exact shapes and amounts cannot be predicted.

Two case studies are conducted with the developed simulation approach. The first one highlights the importance to model separation films as composite plies, i.e. with shell elements and a dedicated material model, while the second shows that the transverse tensile properties of the composite tape only have limited influence on simulation results.





# KURZFASSUNG

Die steigende Nachfrage nach Bauteilen aus Faserverbundwerkstoffen hat zur Weiterentwicklung automatisierter Fertigungsprozesse geführt. Aufgrund der kurzen Zykluszeiten sind Technologien aus dem Bereich der Thermoumformung zur Produktion von Bauteilen mit großen Stückzahlen prädestiniert. Weiterhin ermöglichen sie die Herstellung komplexer Geometrien, die mit anderen automatisierten Fertigungsverfahren wie beispielsweise dem Automated Fibre Placement nicht realisierbar sind. Die bei komplexen Geometrien auftretenden starken Deformationen der Faserhalbzeuge können jedoch zu Defekten wie Faltenwurf in Dickenrichtung und Änderung der Faserorientierung führen. Mit Hilfe von Finite Elemente (FE) Methoden können diese Defekte effizienter untersucht werden als mit experimentellen Trial-and-Error Methoden.

Das Ziel dieser Dissertation ist es makroskopische FE Modelle zur Simulation von Thermoumformprozessen zu entwickeln, die die zuvor beschriebenen Defekte abbilden können. Vor der industriellen Anwendung müssen die Simulationsmodelle validiert werden, wofür numerische Ergebnisse und experimentelle Messwerte miteinander verglichen werden. Im Rahmen dieser Arbeit wird die Validierung anhand einer doppelt gekrümmten, generischen Struktur durchgeführt, die in einem Thermoumformprozess im Labormaßstab hergestellt wird.

Zur Bestimmung geeigneter Eingabeparameter für die Entwicklung der FE Modelle, wird das Materialverhalten bei Umgebungsbedingungen, die für den Thermoumformprozess repräsentativ sind, wie beispielsweise erhöhter Temperatur, charakterisiert. Das Verhalten eines unidirektionalen, faserverstärkten Polyamid-6 Tapes sowie einer polyimiden Trennfolie wird experimentell untersucht. Weiterhin werden die Eigenschaften der Interaktion Werkzeug/Trennfolie, Trennfolie/Tape und Tape/Tape ermittelt. Um die Eignung der Testmethoden, die zur Charakterisierung schmelzflüssiger thermoplastischer Tapes verwendet werden, für unausgehärtete Duroplast-Prepregs zu bewerten, wird ein entsprechendes unidirektionales Tape unter Umgebungsbedingungen, die dem Thermoumformprozess ähnlich sind, charakterisiert.

Die FE Modelle werden mittels einer kommerziell verfügbaren Software erstellt. Basierend auf den experimentellen Messwerten werden die Eingabeparameter anhand eines inversen Vorgehens identifiziert. Die Validierung wird mit drei unterschiedlichen Faserhalbzeugen durchgeführt. Hierbei kann die Eignung des Simulationsansatzes, die Preformgeometrien und Oberflächenfaserorientierung zu bestimmen, nachgewiesen werden. Die Ergebnisse zeigen weiterhin, dass mit der Simulation die kritischen Bereiche bestimmt werden können, in denen Faltenwurf in Dickenrichtung potentiell auftreten kann. Die Häufigkeit und Gestalt dieses Defekts können jedoch nicht näher spezifiziert werden.

Mit dem entwickelten Simulationsansatz werden zwei Fallstudien durchgeführt. Die erste zeigt die Relevanz der eigenständigen Modellierung der Trennfolie über Schalen-

elemente mit zugehörigem Materialmodell. Die zweite Fallstudie zeigt im Rahmen einer Sensitivitätsanalyse den geringen Einfluss der Eigenschaften quer zur Faserrichtung auf die Simulationsergebnisse.

# RESUME

Pour répondre à l'augmentation de la demande, la production de pièces composites devient de plus en plus automatisée. Grâce à leur mise en œuvre rapide, les procédés de thermoformage permettent la fabrication de grandes quantités de pièces en un minimum de temps. De plus, ces procédés sont capables de réaliser des pièces aux géométries complexes qui ne peuvent pas être fabriquées à l'aide d'autres méthodes automatisées, e.g. machines utilisées pour la dépose sur moule. Cependant, le procédé de mise en forme soumet les composites stratifiés à de sévères déformations qui peuvent entraîner des défauts tels que des plis ou des réorientations de fibres. Les simulations par éléments finis ont démontré leur efficacité pour étudier leur survenue.

Cette thèse a pour but de développer un outil de simulation du thermoformage à l'échelle macroscopique capable d'anticiper la survenue de ces défauts. Avant d'être appliqué en milieu industriel, cet outil doit être validé. Dans le cadre de cette étude, sa fiabilité est vérifiée en comparant les résultats numériques aux mesures effectuées sur une pièce générique à double courbure mise en forme par un procédé de thermoformage.

Afin de déterminer les paramètres d'entrée du modèle numérique, les comportements mécaniques d'un renfort unidirectionnel composé de fibres de carbone pré-imprégnées de résine thermoplastique (polyamide 6) et d'un film en polyimide sont déterminés dans les conditions environnementales de mise en forme, e.g. température. Les interactions entre moule/film, film/pli et pli/pli sont également testées. Afin de s'assurer que les méthodes utilisées pour tester les matériaux thermoplastiques au-dessus de leur point de fusion peuvent également être appliquées aux composites pré-imprégnés à matrice thermodurcissable, un composite thermodurcissable unidirectionnel composé de fibres de carbone est caractérisé dans les conditions de mise en forme.

Les simulations sont développées à l'aide d'un logiciel commercial. Les paramètres d'entrée du modèle numérique sont identifiés à l'aide des résultats expérimentaux (méthode inverse). La validation, qui est réalisée sur trois cas-tests différents, montre que l'outil numérique est capable de prédire la géométrie des pièces et l'orientation des fibres en surface. Les résultats montrent également la capacité de la simulation à prédire les régions dans lesquelles les plis se développent, bien que leurs tailles et formes ne puissent pas être précisément prédites.

Les modèles numériques développés dans le cadre de cette thèse sont enfin appliqués à deux études. La première justifie l'importance de modéliser les films polyimides de la même manière que les plis composites, i.e. avec des éléments coques et un modèle matériau adéquat. La deuxième montre que les propriétés de tension transverse du composite influent peu sur les résultats numériques.



# Contents

<b>Contents</b> .....	<b>xiii</b>
<b>Nomenclature</b> .....	<b>xvii</b>
<b>List of Abbreviations</b> .....	<b>xxv</b>
<b>List of Figures</b> .....	<b>xxix</b>
<b>List of Tables</b> .....	<b>xxxix</b>
<b>1 Introduction</b> .....	<b>1</b>
1.1 Industrial context .....	2
1.2 Motivation and goals .....	5
1.3 Outline .....	6
<b>2 Forming of thermoplastic composite blanks</b> .....	<b>9</b>
2.1 Main thermoforming technologies .....	9
2.1.1 Double diaphragm forming .....	9
2.1.2 Hot stamp forming .....	10
2.2 Deformation mechanisms occurring in thermoforming processes .....	12
2.2.1 Intra-ply shear .....	12
2.2.2 In-plane tension/compression .....	14
2.2.3 Out-of-plane bending .....	16
2.2.4 Single and multi-ply compaction .....	18
2.2.5 Tool/ply and ply/ply interactions .....	19
2.3 Typical defects induced by thermoforming processes .....	21
<b>3 Thermoforming simulation</b> .....	<b>25</b>
3.1 Mapping methods .....	25
3.2 Mechanical methods .....	27
3.2.1 Macroscopic Finite Element approaches .....	28
3.2.2 Mesoscopic Finite Element approaches .....	32
3.2.3 Semi-discrete Finite Element approach .....	32
3.2.4 Microscopic Finite Element approach .....	33
3.3 Selected approach .....	33
3.3.1 Motivation and goals .....	33

3.3.2	Software description .....	34
<b>4</b>	<b>Material characterisation .....</b>	<b>39</b>
4.1	Characterisation of a unidirectional thermoplastic composite material .....	39
4.1.1	Intra-ply shear .....	40
4.1.2	Out-of-plane bending .....	48
4.1.3	In-plane tension .....	59
4.1.4	Viscosity .....	64
4.2	Characterisation of a separation film .....	66
4.3	Characterisation of contact properties .....	68
4.3.1	Literature review .....	68
4.3.2	Development of a new friction test setup .....	69
4.3.3	Experimental results .....	74
4.4	Characterisation of a non-cured unidirectional thermoset composite material .....	82
4.4.1	Intra-ply shear .....	82
4.4.2	Out-of-plane bending .....	87
4.4.3	Transverse tension .....	90
4.4.4	Inter-ply slip .....	94
4.5	Discussion .....	95
4.5.1	Benefits and limits of presented test methods .....	95
4.5.2	Investigation of a non-cured unidirectional thermoset composite material .....	98
<b>5</b>	<b>Calibration of simulation models .....</b>	<b>101</b>
5.1	Calibration of composite material model .....	101
5.1.1	Longitudinal tension and density .....	101
5.1.2	Transverse tension and viscosity .....	102
5.1.3	Out-of-plane bending .....	108
5.1.4	Intra-ply shear .....	111
5.1.5	Sensitivity analysis .....	115
5.2	Calibration of separation film material model .....	115
5.3	Calibration of contact properties .....	117

5.4	Results and discussion .....	119
<b>6</b>	<b>Validation and applications .....</b>	<b>123</b>
6.1	Validation.....	123
6.1.1	Thermoforming process and demonstrators .....	123
6.1.2	Validation criteria and comparison methods .....	125
6.1.3	Experimental results .....	126
6.1.4	Simulation modelling .....	128
6.1.5	Results .....	129
6.2	Applications .....	137
6.2.1	Influence of separation films on thermoforming simulation results.....	137
6.2.2	Influence of composite transverse tensile properties on thermoforming simulation results.....	140
6.3	Conclusion .....	143
<b>7</b>	<b>Conclusions and recommendations.....</b>	<b>145</b>
7.1	Material characterisation.....	145
7.2	Thermoforming simulation .....	147
7.3	Validation and applications.....	148
	<b>References .....</b>	<b>151</b>
<b>A</b>	<b>Appendix.....</b>	<b>169</b>
a	Appendix to Chapter 1.1 .....	169
b	Appendix to Chapter 4.1.1.3 .....	170
c	Appendix to Chapter 4.1.4.2 .....	175
d	Appendix to Chapter 4.3.2 .....	177
e	Appendix to Chapter 4.3.3.2 .....	178
f	Appendix to Chapter 4.4.1 .....	181
g	Appendix to Chapter 4.4.2 .....	182
h	Appendix to Chapter 4.4.3 .....	183
i	Appendix to Chapter 5.1.4 .....	184
j	Appendix to Chapter 5.1.5 .....	186
k	Appendix to Chapter 5.4.....	189

l	Appendix to Chapter 6.1.4 .....	190
m	Appendix to Chapter 6.1.5.2 .....	191
<b>B</b>	<b>Publications .....</b>	<b>193</b>
<b>C</b>	<b>Supervised student theses .....</b>	<b>195</b>



# Nomenclature

Symbol	Unit	Description
<b>Greek letters</b>		
$\alpha_1$	°	Angle which defines the first fibre direction with respect to the reference direction
$\alpha_2$	°	Angle which defines the second fibre direction with respect to the reference direction
$\alpha_{\text{lock}}$	°	In-plane shear locking angle
$\dot{\gamma}$	1/s	Intra-ply shear strain rate
$\dot{\gamma}_{L,\text{max}}$	1/s	Maximum longitudinal shear strain rate
$\dot{\gamma}_{T,\text{max}}$	1/s	Maximum transverse shear strain rate
$\gamma$	-	Intra-ply shear strain
$\gamma_0$	-	Shear strain amplitude of $\gamma(t)$
$\gamma_L$	-	Longitudinal shear strain
$\gamma_{L,\text{max}}$	-	Maximum longitudinal shear strain
$\gamma_{\text{max}}$	%	Maximum shear strain (end of LVE region)
$\gamma(t)$	-	Time-dependent intra-ply shear deformation
$\gamma_T$	-	Transverse shear strain
$\gamma_{T,\text{max}}$	-	Maximum transverse shear strain
$\delta$	° or rad	Phase lag
$\Delta t$	ms	Time step
$\Delta X_L$	mm	Longitudinal displacement at the specimen tip
$\Delta X_T$	mm	Transverse displacement at the specimen tip
$\eta$	Pa.s	Viscosity
$\eta_{\text{PAM}}$	GPa.ms	PAM-FORM viscosity

<b>Symbol</b>	<b>Unit</b>	<b>Description</b>
$\eta_t$	Pa.s	Transverse viscosity
$\theta$	°	Fibre orientation
$\theta$	mrاد	Angle of twist
$\theta_0$	mrاد	Angle of twist amplitude of $\theta(t)$
$\theta(t)$	mrاد	Time-dependent angle of twist
$\kappa$	1/cm	Bending curvature
$\mu$	-	Friction coefficient
$\mu_{d,tool}$	-	Dynamic friction coefficient between film and tool
$\mu_{s,0/0}$	-	Static friction coefficient between two 0° molten thermoplastic plies
$\mu_{s,0/90}$	-	Static friction coefficient between 0° and 90° molten thermoplastic plies
$\mu_{s,90/90}$	-	Static friction coefficient between two 90° molten thermoplastic plies
$\mu_{tool}$	-	Friction coefficient between film and tool
$\nu$	-	Poisson's ratio
$\nu_{UD-CF/PA6}$	-	Composite Poisson's ratio ( $\nu_{12}$ )
$\nu_f$	-	Fibre Poisson's ratio
$\nu_{film}$	-	Separation film Poisson's ratio
$\nu_m$	-	Matrix Poisson's ratio
$\xi$	-	Internal damping
$\rho$	kg/mm <sup>3</sup>	Density
$\sigma_B$	MPa	Bending stress in the outer fibre at middle-span

<b>Symbol</b>	<b>Unit</b>	<b>Description</b>
$\sigma_{\text{fric}}$	MPa	Pressure applied on the carrier
$\sigma_{ij}$	MPa	Cauchy stress tensor
$\sigma_m$	MPa	Hydrostatic stress
$\sigma_t$	MPa	Transverse tensile stress
$\tau$	MPa	Transient intra-ply shear stress
$\tau_0$	MPa	Shear stress amplitude of $\tau(t)$
$\tau_{\text{fric}}$	MPa	Inter-ply shear stress ( $\tau_{13}$ )
$\tau(t)$	MPa	Time-dependent intra-ply shear stress
$\dot{\epsilon}_B$	1/s	Out-of-plane bending strain rate
$\dot{\epsilon}_{ij}$	1/s	Strain rate tensor
$\dot{\epsilon}_t$	1/s	Transverse tensile strain rate
$\epsilon_B$	-	Maximum strain in the outer fibre at mid-span
$\epsilon_t$	-	Transverse tensile strain
$\omega$	rad/s	Angular frequency

Symbol	Unit	Description
<b>Latin letters</b>		
a, b	-	Curve fitting coefficients
A	mm <sup>2</sup>	Nominal contact area
A <sub>0</sub>	mm <sup>2</sup>	Initial cross-section
B <sub>1</sub>	GPa	Longitudinal out-of-plane bending modulus
B <sub>2</sub>	GPa	Transverse out-of-plane bending modulus
c	m.s	Speed of sound
$\dot{d}$	mm/min	Crosshead speed
d	mm	Gap thickness
d	mm	Crosshead displacement
$\dot{D}$	mm/min	Speed
D	mm	Displacement
E	GPa	Tensile modulus (Young's modulus)
E <sub>1</sub>	GPa	Longitudinal tensile modulus
E <sub>2</sub>	GPa	Transverse tensile modulus
E <sub>B</sub>	MPa	Out-of-plane bending modulus
f	Hz	Frequency
F	N	Force
F <sub>ave</sub>	N	Average frictional force
F <sub>b1</sub>	-	Longitudinal bending factor
F <sub>b2</sub>	-	Transverse bending factor
F <sub>bm</sub>	-	Matrix bending factor
F <sub>fric</sub>	N	Inter-ply shear force or frictional force

<b>Symbol</b>	<b>Unit</b>	<b>Description</b>
$f_i$	N	Simulation value at iteration $i$
$F_N$	N	Normal force
$F_{s1}$	-	Longitudinal out-of-plane shear factor
$F_{s2}$	-	Transverse out-of-plane shear factor
$F_{sm}$	-	Matrix out-of-plane shear factor
$F_T$	N	Frictional force
$G$	MPa	Intra-ply shear modulus
$G_\infty$	MPa	Curve fitting coefficient corresponding to the equilibrium shear relaxation modulus
$G_{lock}$	MPa	Shear modulus after locking
$G_r$	MPa	Longitudinal shear relaxation modulus
$G^*$	MPa	Complex shear modulus
$G'$	MPa	Shear storage modulus
$G''$	MPa	Shear loss modulus
$G'_L$	MPa	Longitudinal shear storage modulus
$G'_T$	MPa	Transverse shear storage modulus
$G''_L$	MPa	Longitudinal shear loss modulus
$G''_T$	MPa	Transverse shear loss modulus
$H$	mm	Half transverse length of the specimen
$h_0$	mm	Initial thickness
$He$	1/m	Hersey number
$I, I_x, I_y$	mm <sup>4</sup>	Second moments of area
$I_{ij}$	-	Identity matrix in $ij$ -plane

<b>Symbol</b>	<b>Unit</b>	<b>Description</b>
k	-	Ratio of strains along and transverse loading direction
K	-	Scale factor
K	N/m	Specimen stiffness
l	mm	Element side length
L	mm	Length in fibre direction
L	mm	Half longitudinal length of the specimen
L <sub>0</sub>	mm	Initial specimen free length
L <sub>frame</sub>	mm	Side length of a picture frame test rig
M	gf	Bending moment per unit width
M <sub>0</sub>	mN.m	Torque amplitude of M(t)
M(t)	mN.m	Time-dependent torque
n	-	Number of cycle
N	N	Normal force
P	MPa	Pressure
S <sub>ij</sub>	MPa	Deviatoric stress in ij-plane
SS <sub>res</sub>	N <sup>2</sup>	Sum of squared errors
t	s	Time
T	°C	Temperature
T	mm	Thickness
T <sub>n</sub>	ms	Time after <i>n</i> cycles
U	m/s	Speed
V	mm/min	Speed

<b>Symbol</b>	<b>Unit</b>	<b>Description</b>
$V_f$	%	Fibre volume fraction
$V_{ol}$	$\text{mm}^3$	Volume of the specimen
$W$	mm	Length perpendicular to fibre direction
$x, y, z$	-	Cartesian coordinate system
$X_1, X_2$	-	Fibre orientations
$y_i$	N	Experimental value at iteration $i$

---

<b>Symbol</b>	<b>Unit</b>	<b>Description</b>
<b>Mathematical symbols</b>		
{P}	N	Force vector
{ $\ddot{u}$ }	m/s <sup>2</sup>	Acceleration vector
{u}	m	Nodal displacement vector
[K]	N/m	Stiffness matrix
[M]	kg	Mass matrix

---



# List of Abbreviations

---

<b>Abbreviation</b>	<b>Description</b>
1D, 2D, 3D	1-, 2-, 3-Dimensions
AFP	Automated fibre placement
ATL	Automated tape layer
BL	Boundary lubrication
BMC	Bulk moulding compound
CATIA	Computer aided for three-dimensional interactive application
CF	Carbon fibre
CFM	Composite fiber modeler
CFRP	Carbon fibre-reinforced polymer
CFRTP	Carbon fibre-reinforced thermoplastic
CNTAC	Contact model or contact card
CO <sub>2</sub>	Carbon dioxide
COP	Climate change conference
CPD	Composite design
DIC	Digital image correlation
DIN	German institute for standardization
DMA	Dynamic mechanical analysis
DSC	Differential scanning calorimeter
(E)HL	Elasto-hydrodynamic lubrication
EU	European union
FE	Finite element

---

<b>Abbreviation</b>	<b>Description</b>
FEA	Finite element analysis
FEM	Finite element methods
FRICT	Friction coefficient
FSVNL	Parameter for non-linear penalty stiffness
GB	Gigabyte
HS	Harness-satin
IATA	International air transport association
IFRM	Ideal fibre-reinforced Newtonian fluid model
ISHG	Flag for shell elements hourglass prevention
ISINT	Flag for shell integration rule
ISO	International organization for standardization
KINDA	Kinematic damping
LCC	Chair of Carbon composites
LVE	Linear visco-elastic
MAT	Material model or material card
ML	Mixed lubrication
MP	Megapixel
NCF	Non-crimp fabric
PA6	Polyamide 6
PA66	Polyamide 66
PEEK	Polyether ether ketone
PEI	Polyetherimide
PP	Polypropylene

---

<b>Abbreviation</b>	<b>Description</b>
PPS	Polyphenylene sulfide
Prepreg	Pre-impregnated reinforcement
RAM	Random-access memory
RELAY	Rapid efficient layup
RFLAG	Flag for Reinforcement architecture type
ROI	Region of interest
SEPSTR	Separation Stress
SMC	Sheet moulding compound
TUM	Technical University of Munich
UD	Unidirectional
UNFCCC	United nations framework convention on climate change
UPM	Universal testing machine
XDMP1	Stiffness proportional damping ratio

---



# List of Figures

Fig. 1-1: Preparation, consolidation and thermoforming of tailored blanks (process chain adapted from [11]) .....	3
Fig. 1-2: Thermoformed rib for aerospace application [29] .....	3
Fig. 1-3: FibreForge RELAY Station equipment and operating system [32].....	4
Fig. 2-1: Schematic of a double diaphragm forming process (adapted from [11] and [39]) .....	10
Fig. 2-2: Schematic of a hot stamp forming process (adapted from [11]).....	11
Fig. 2-3: Intra-ply shear curves of dry plain, 4-HS and 2:2 twill glass fabric reinforcements (adapted from [37], [44] and [58]) .....	13
Fig. 2-4: Intra-ply shear curves of a 5-HS carbon/PPS prepreg at different temperatures (left) and different test speeds at 300°C (right) [53] .....	13
Fig. 2-5: Different types of intra-ply shear occurring in a unidirectional reinforcement .....	14
Fig. 2-6: Typical biaxial tensile test results of a fabric reinforcement [44].....	15
Fig. 2-7: Front (top) and cross-sectional (bottom) views of a fabric at rest (left) and subjected to longitudinal tension (right) [58] .....	15
Fig. 2-8: Transverse tension of a unidirectional fibre-reinforced composite material (adapted from [58]) .....	16
Fig. 2-9: Longitudinal compression of a yarn (adapted from [58]) .....	16
Fig. 2-10: Typical bending hysteresis of a dry fabric reinforcement (adapted from [76]) .....	17
Fig. 2-11: Bending of a prepreg composite laminate (adapted from [64] and [66]).....	17
Fig. 2-12: Compaction of a single dry woven fabric layer [58].....	18
Fig. 2-13: Typical compaction curves of a plain woven fabric [44].....	18
Fig. 2-14: Relative rotational and translational motion between plies [58].....	19
Fig. 2-15: Typical evolution of a Stribeck curve [92] .....	20
Fig. 2-16: Influence of blank size on forming results (adapted from [27]) .....	21
Fig. 2-17: Photomicrograph of in-plane fibre waviness in a UD-CFRTP component [104] .....	22
Fig. 2-18: Matrix migration observed at bend angle section of a CF/PP laminate (adapted from [27]) .....	22

Fig. 3-1: Mapping of a composite blank onto a generic double-curved surface [34] .....	26
Fig. 3-2: Macroscopic, mesoscopic and microscopic representation of a balanced plain weave fabric (figures of the mesoscopic scale [112] and the microscopic scale [113]).....	27
Fig. 3-3: “Bi-phase” material model for fibre-reinforced materials (adapted from [155]) .....	35
Fig. 4-1: Schematic of state-of-the-art test methods for longitudinal intra-ply shear characterisation (adapted from [62] and [160]) .....	40
Fig. 4-2: Picture frame test setup enclosed within an environmental chamber and mounted in a universal testing machine [adapted from S.Bel].....	42
Fig. 4-3: Typical picture frame test results of a molten unidirectional fibre-reinforced thermoplastic composite material tested at 280°C [S. Bel] .....	43
Fig. 4-4: (Left) Specimens of rectangular cross-section (from left to right: 20 x 15, 25 x 12 and 30 x 10 mm <sup>2</sup> , where the first value gives the dimension in fibre direction); (Right) Specimen positioned between two disposable circular platens.....	43
Fig. 4-5: Typical thickness variations of upper (left) and lower (right) disposable platens.....	44
Fig. 4-6: Unidirectional fibre-reinforced PA6 thermoplastic composite specimen enclosed within an environmental chamber and mounted on a rheometer .....	45
Fig. 4-7: Average amplitude sweep test results of molten UD-CF/PA6 specimens .....	46
Fig. 4-8: Average frequency sweep test results of molten UD-CF/PA6 specimens .....	47
Fig. 4-9: Approximated shear relaxation modulus of a molten UD-CF/PA6 composite material .....	47
Fig. 4-10: Stress-strain response of a molten UD-CF/PA6 composite material subjected to longitudinal intra-ply shear deformations .....	48
Fig. 4-11: Fibre orientation and geometry of specimens used for longitudinal bending tests .....	51
Fig. 4-12: Specimens mounted in different test fixtures: (a) Single cantilever; (b) Double cantilever; (c) Three-point bending (20 mm) and (d) Three-point bending (50 mm) .....	53

Fig. 4-13: Unidirectional thermoplastic specimen mounted in a DMA three-point bending tool (20 mm) .....	56
Fig. 4-14: Average bending stress-strain results of UD-CF/PA6 specimens (investigations performed at 280°C for different test speeds) .....	57
Fig. 4-15: Strain rate dependency of the longitudinal out-of-plane bending modulus of a UD-CF/PA6 material (280°C).....	58
Fig. 4-16: Transverse out-of-plane bending: specimen deformations after 15 minutes at 280°C .....	59
Fig. 4-17: Thermoplastic specimen mounted in a universal testing machine and enclosed within an environmental chamber [adapted from S. Bel] .....	61
Fig. 4-18: Unidirectional thermoplastic specimen mounted in a DMA tensile clamp .....	62
Fig. 4-19: Average stress-strain transverse tensile test results of UD-CF/PA6 specimens (investigations performed at 280°C with a DMA system) .....	63
Fig. 4-20: Average composite viscosities calculated according to equation (4-8) for different loading rates.....	65
Fig. 4-21: Evolution of composite viscosity over the investigated range of loading rates .....	65
Fig. 4-22: Polyimide film mounted in a DMA tensile clamp .....	67
Fig. 4-23: Typical stress-strain tensile test response of a polyimide film (investigation performed at 280°C with a DMA system) .....	67
Fig. 4-24: Schematic of a pull-out (left) and pull-through (right) test setup .....	68
Fig. 4-25: Schematic of the “carrier test setup” introduced by DIN 14882 (adapted from [195]) .....	70
Fig. 4-26: Enhanced “carrier test setup” suitable for wet friction characterisation .....	70
Fig. 4-27: Isometric view of the base-plate body (adapted from [S6]).....	71
Fig. 4-28: Isometric view of the pull-push toggle clamp assembly (adapted from [S6]) .....	71
Fig. 4-29: Exploded view of the pulley assembly (adapted from [S6]).....	71
Fig. 4-30: Isometric view of the specimen-plate body (adapted from [S6]).....	72
Fig. 4-31: Isometric view of the carrier body (adapted from [S6]) .....	72
Fig. 4-32: Exploded view of the carrier body (adapted from [S6]) .....	73
Fig. 4-33: Tooling for specimen preparation (adapted from [S6]) .....	73

Fig. 4-34: Typical outcome of a treated separation film/tool surface friction test.....	75
Fig. 4-35: Typical outcome of a molten thermoplastic/molten thermoplastic friction test.....	78
Fig. 4-36: Evolution of peak shear stresses with respect to test speed in a 0°/0° configuration .....	79
Fig. 4-37: Evolution of peak shear stresses with respect to test speed.....	79
Fig. 4-38: Evolution of steady-state shear stresses with respect to test speed in a 0°/0° configuration .....	80
Fig. 4-39: Evolution of steady-state shear stresses with respect to test speed .....	80
Fig. 4-40: Non-cured unidirectional thermoset specimen clamped in a picture frame setup, mounted in a testing machine and enclosed within an environmental chamber .....	82
Fig. 4-41: Transverse ply tearing and tow bending within a sheared specimen (final state).....	83
Fig. 4-42: Typical evolution of a picture frame test of a non-cured unidirectional thermoset specimen .....	83
Fig. 4-43: Rotational rheometer used with a Peltier temperature control unit.....	84
Fig. 4-44: Microscopy from a non-cured unidirectional thermoset specimen [S7].....	84
Fig. 4-45: Unidirectional fibre-reinforced thermoset composite specimen enclosed within an environmental chamber and mounted in a rheometer for torsion tests .....	85
Fig. 4-46: Average amplitude sweep test results of non-cured unidirectional thermoset pre-impregnated composite specimens.....	85
Fig. 4-47: Average frequency sweep test results of non-cured unidirectional thermoset pre-impregnated composite specimens.....	86
Fig. 4-48: Approximated shear relaxation modulus of a non-cured composite material .....	86
Fig. 4-49: Stress-strain response of a non-cured unidirectional thermoset pre-impregnated tape subjected to longitudinal shear deformations .....	87
Fig. 4-50: Non-cured unidirectional thermoset specimen mounted in a DMA three-point bending tool (20 mm) .....	88
Fig. 4-51: Average bending stress-strain results of non-cured unidirectional thermoset specimens (investigations performed at 60°C for different test speeds) .....	88



Fig. 4-52: Strain rate dependency of the longitudinal out-of-plane bending modulus of a non-cured unidirectional thermoset composite material (60°C).....	89
Fig. 4-53: Non-cured unidirectional thermoset specimen whose tips are wrapped in aluminium tapes (left) and non-cured unidirectional thermoset specimen mounted in a DMA system (right) .....	90
Fig. 4-54: Typical stress-strain result of a non-cured unidirectional thermoset composite material tested at 60°C with a universal testing machine (example given for 25 mm/min) .....	91
Fig. 4-55: Typical stress-strain result of a non-cured unidirectional thermoset composite material tested at 60°C with a DMA system (example given for 0.1 N/min).....	92
Fig. 4-56: Evolution of transverse tensile modulus with respect to strain rate of a non-cured unidirectional thermoset composite material tested at 60°C .....	93
Fig. 4-57: Schematic of typical carrier rotation observed during inter-ply slip investigations .....	95
Fig. 4-58: Typical resin squeeze-out observed at the tip of a thermoplastic composite material specimen after testing [S10] .....	96
Fig. 4-59: Typical ply tearing observed in a 90° specimen-platen specimen (tearing on the left hand side of the plate are caused by specimen removal after testing) .....	97
Fig. 5-1: Experimental (left) and numerical (right) transverse tensile tests of a UD-CF/PA6 specimen .....	103
Fig. 5-2: Typical test speed evolution of a transverse tensile test performed at a constant loading rate with a DMA system .....	103
Fig. 5-3: Sensitivity analysis performed for the identification of the viscosity parameter.....	104
Fig. 5-4: Simulation of transverse tensile tests of molten UD-CF/PA6 specimens – Comparison between experimental and simulation results (constant loading rates).....	105
Fig. 5-5: Typical “equivalent” test speed of experiments performed at constant loading rates .....	106
Fig. 5-6: Simulation of transverse tensile tests of molten UD-CF/PA6 specimens – Comparison between experimental, simulation at a constant loading rate and simulation at a constant test speed results.....	106
Fig. 5-7: Correlation between simulation input $E_2$ and speed .....	107

Fig. 5-8:	Experimental (left) and numerical (right) longitudinal three-point bending tests of a UD-CF/PA6 specimen.....	108
Fig. 5-9:	Typical test speed evolution of a three-point bending test performed at a constant test speed with a DMA system .....	108
Fig. 5-10:	Comparison between experimental and numerical longitudinal out-of-plane bending behaviour .....	109
Fig. 5-11:	Correlation between simulation input $B_1$ and speed.....	110
Fig. 5-12:	Picture frame simulation model applied to the identification of $G$ and $B_2$ parameters.....	112
Fig. 5-13:	Experimental (left) and simulation (right) results after 20 mm displacement .....	113
Fig. 5-14:	Experimental (left) and simulation (right) results after 90 mm displacement.....	113
Fig. 5-15:	Side view - Simulation (top) and experimental (bottom) final shapes of a specimen tested with a picture frame test setup .....	114
Fig. 5-16:	Front view - Simulation (top) and experimental (bottom) final shapes of a specimen tested with a picture frame test setup .....	114
Fig. 5-17:	Typical outcome of a sensitivity analysis (investigated parameter: density) .....	115
Fig. 5-18:	Experimental (left) and numerical (right) tensile tests of a polyimide film .....	116
Fig. 5-19:	Comparison between experimental and numerical tensile test results of a polyimide film (280°C) .....	116
Fig. 5-20:	Simulation model applied to the identification of friction coefficients....	118
Fig. 5-21:	Comparison between experimental and simulation test results for interactions occurring between a tool surface and a treated kapton film (left) and two 0° molten UD-CF/PA6 plies (right).....	119
Fig. 5-22:	Material model of a molten UD-CF/PA6 tape (MAT 140).....	120
Fig. 5-23:	Material model of a polyimide film (MAT 101).....	121
Fig. 6-1:	Demonstrator (or “double-sinus wave” component) considered for validation .....	124
Fig. 6-2:	Double-sinus wave tooling mounted on a universal testing machine and enclosed in an environmental chamber (left) and schematic of the thermoforming process (right).....	124
Fig. 6-3:	Cut-outs of a treated polyimide film .....	125

Fig. 6-4:	Position of the five regions of interest (ROI) considered for validation.....	125
Fig. 6-5:	Thermoforming outcomes of $[0]_8$ tailored blanks.....	126
Fig. 6-6:	Thermoforming outcome of the $[0_2 90_2]_S$ tailored blank .....	127
Fig. 6-7:	Influence of separation films on surface finish.....	127
Fig. 6-8:	Setup for fibre orientation measurements .....	128
Fig. 6-9:	Macroscopic FE simulation model used for validation .....	128
Fig. 6-10:	Preform geometries after forming for the $[0]_8$ tailored blank (300 x 300 mm <sup>2</sup> ).....	130
Fig. 6-11:	Preform geometries after forming for the $[0]_8$ tailored blank (350 x 350 mm <sup>2</sup> ).....	132
Fig. 6-12:	Preform geometries after forming for the $[0_2 90_2]_S$ tailored blank .....	134
Fig. 6-13:	Deviations between computed and measured fibre orientations (3D visualisation) .....	136
Fig. 6-14:	“Classical” macroscopic FE simulation model in which separation films are not modelled “explicitly” (approach 2).....	137
Fig. 6-15:	Preform geometries after forming for the $[0]_8$ tailored blank (300 x 300 mm <sup>2</sup> ).....	138
Fig. 6-16:	Preform geometries after forming for $[0]_8$ tailored blank (350 x 350 mm <sup>2</sup> ).....	138
Fig. 6-17:	Preform geometries after forming for the $[0_2 90_2]_S$ tailored blank .....	138
Fig. 6-18:	Preform geometries after forming for the $[0]_8$ tailored blank (300 x 300 mm <sup>2</sup> ).....	141
Fig. 6-19:	Preform geometries after forming for the $[0]_8$ tailored blank (350 x 350 mm <sup>2</sup> ).....	141
Fig. 6-20:	Preform geometries after forming for the $[0_2 90_2]_S$ tailored blank .....	141
Fig. A-1:	Thermoforming unit belonging to the <i>Chair of Carbon Composites of the Technical University of Munich (TUM-LCC) [S3]</i> .....	169
Fig. A-2:	Typical cycle applied to the consolidation of tailored thermoplastic composite blanks.....	169
Fig. A-3:	Typical sinusoidal strain and stress signals during dynamic experiments .....	170

Fig. A-4:	Front view (left) and top view (right) of a rectangular unidirectional composite specimen subjected to shear in a parallel platens test setup mounted on a rotational rheometer.....	171
Fig. A-5:	Typical determination of storage/loss transverse and longitudinal shear moduli using the method introduced by Rogers .....	172
Fig. A-6:	Schematic of a transverse tensile test.....	176
Fig. A-7:	Cut-outs on the bottom side of the base-platen (left) and the specimen-platen (right) [S6].....	177
Fig. A-8:	Carrier body positioned on top of the specimen-platen using positioning rods [S6] .....	177
Fig. A-9:	Heat gun used to heat thermoplastic specimens above melting temperature (left) and specimen preparation tooling protected with kapton tape (right) [S8] .....	178
Fig. A-10:	(Left) Thermoplastic specimen clamped at room temperature; (Right) Heat applied with a heat gun [S8] .....	178
Fig. A-11:	(Left) Hood used to form a molten thermoplastic specimen; (Right) Forming of a molten thermoplastic specimen into carrier geometry [S8].....	179
Fig. A-12:	Top (left) and bottom (right) views of a carrier specimen [S8] .....	179
Fig. A-13:	Addition of screws on specimen attachment plates.....	180
Fig. A-14:	Addition of a metallic plate behind the carrier.....	180
Fig. A-15:	Prismatic bar specimen made out of non-cured unidirectional thermoset tapes .....	181
Fig. A-16:	Typical (left) and extreme (right) localised inter-ply shear deformations at the tips of the specimen .....	181
Fig. A-17:	Typical external fibre orientation of a non-cured unidirectional thermoset specimen (scale [-90°, +90°]).....	182
Fig. A-18:	Typical external fibre orientation of a non-cured unidirectional thermoset specimen (scale [-10°, +10°]).....	182
Fig. A-19:	Typical external fibre orientation of a non-cured unidirectional thermoset specimen (scale [-45°, +135°]).....	183
Fig. A-20:	Analyses performed to identify proper velocity scale factor .....	184
Fig. A-21:	Outcome of the sensitivity analysis (investigated parameter: $E_I$ ).....	186
Fig. A-22:	Outcome of the sensitivity analysis (investigated parameter: mesh size) .....	186

Fig. A-23: Outcome of the sensitivity analysis (investigated parameter: $E_1$ ).....	187
Fig. A-24: Outcome of the sensitivity analysis (investigated parameter: $\rho$ ) .....	187
Fig. A-25: Outcome of the sensitivity analysis (investigated parameter: mesh size).....	188
Fig. A-26: Superimposed (left) and disorganised (right) layup.....	190
Fig. A-27: Typical fibre orientations detected from a measurement taken on a marked surface .....	191
Fig. A-28: Histogram representing the distribution of fibre orientation of the measurement presented in Fig. A-27 .....	191



## List of Tables

Tab. 1-1: Main material properties of a UD-CF/PA6 tape from Celstran® [31] .....	4
Tab. 4-1: Overview of the main test methods for out-of-plane bending characterisation .....	49
Tab. 4-2: Average dimensions and standard deviations in millimetres of (a) the specimens used for preliminary investigations and (b) the specimens used for material characterisation .....	52
Tab. 4-3: Outcome of screening investigations for longitudinal bending characterisation .....	54
Tab. 4-4: Three-point bending (20 mm): specimen widths at punch location before and after testing for experiments performed at 230°C.....	55
Tab. 4-5: Standard deviations of the stresses presented in Fig. 4-14 .....	57
Tab. 4-6: Equivalence between test speeds and strain rates for specimens of ideal geometry.....	58
Tab. 4-7: Main properties of the polyimide film supplied by Airtech [192].....	66
Tab. 4-8: Test matrix for treated separation film/tool contact characterisation.....	74
Tab. 4-9: Friction coefficients between treated separation film and tool surface calculated according to equation (4-10) for experiments performed without wall. Numbers in brackets correspond to the friction coefficients calculated for experiments performed with the left wall.....	76
Tab. 4-10: Average friction coefficients between treated separation film and tool surface calculated for “fresh” friction test results (tests #1 in Tab. 4-9).....	76
Tab. 4-11: Test matrix for inter-ply contact characterisation .....	77
Tab. 4-12: Inter-ply static and kinetic friction coefficients calculated for 50 mm/min .....	81
Tab. 4-13: Standard deviations of the stresses presented in Fig. 4-51 .....	89
Tab. 4-14: Equivalence between test speeds and strain rates for specimens of ideal geometry.....	90
Tab. 4-15: Average strain rates for investigations conducted on a non-cured unidirectional thermoset composite material at constant loading rates (DMA system) and constant test speeds (universal testing machine) – Standard deviations are also plotted in Fig. 4-56 (see horizontal bars) .....	94

Tab. 5-1:	Results of the identification analysis performed to determine material model parameters (viscosity, transverse tensile moduli and “equivalent” test speeds) .....	107
Tab. 5-2:	Experimental and numerical longitudinal out-of-plane bending moduli after parameter identification .....	109
Tab. 5-3:	Results of the identification analysis performed to determine material model longitudinal out-of-plane bending parameters .....	110
Tab. 5-4:	Configurations investigated for the identification of simulation friction coefficients.....	117
Tab. 5-5:	Results of the identification analysis performed to determine simulation friction coefficients.....	119
Tab. 6-1:	Lengths and widths indicated by white arrows in Fig. 6-10 .....	130
Tab. 6-2:	Comparisons between computed and observed out-of-plane wrinkles for the $[0]_8$ tailored blank (300 x 300 mm <sup>2</sup> ) .....	131
Tab. 6-3:	Lengths and widths indicated by white arrows in Fig. 6-11 .....	132
Tab. 6-4:	Comparisons between computed and observed out-of-plane wrinkles for the $[0]_8$ tailored blank (350 x 350 mm <sup>2</sup> ) .....	133
Tab. 6-5:	Lengths and widths indicated by white arrows in Fig. 6-12 .....	134
Tab. 6-6:	Comparisons between computed and observed out-of-plane wrinkles for the $[0_2 90_2]_8$ tailored blank.....	135
Tab. 6-7:	Deviations in degree (°) between computed and measured fibre orientations .....	136
Tab. 6-8:	Lengths and widths indicated by white arrows in Fig. 6-15, Fig. 6-16 and Fig. 6-17. The first values correspond to simulation results for approach 1, the second to the experimental measurements and the third to simulation results for approach 2.....	139
Tab. 6-9:	Evaluation of both simulation approaches: cumulative errors between measured and computed fibre orientations.....	140
Tab. 6-10:	Lengths and widths indicated by white arrows in Fig. 6-18, Fig. 6-19 and Fig. 6-20. The first values correspond to simulation results for $E_2$ multiplied by 0.1, the second to simulation results for original $E_2$ and the third to simulation results for $E_2$ multiplied by 10 .....	142
Tab. 6-11:	Influence of transverse tensile properties on computed fibre orientations: cumulative error between measured and computed fibre orientations. The first values correspond to comparisons performed with $E_2$ multiplied by 0.1, the second to comparisons performed with	



original  $E_2$  and the third to comparisons performed with  $E_2$   
multiplied by 10 ..... 142

Tab. A-1: Matrix and fibre Poisson's ratios ..... 189



# 1 Introduction

To protect the environment and avoid severe climate modifications, members of the United Nations Framework Convention on Climate Change (UNFCCC) agreed at the twenty-first Climate Change Conference (COP 21) held in Paris, France, in December 2015 to reduce their greenhouse emissions at the earliest possible time [1]. In 2010, transportation represented 14% of global greenhouse gas emissions [2]. According to the United States Environmental Protection Agency, greenhouse gas emissions from this sector mainly concern Carbon Dioxide (CO<sub>2</sub>) produced by air, road, rail and marine vehicles [3]. In its report published in 2010, the International Transport Forum reported that global CO<sub>2</sub> emissions grew by 45% between 1990 and 2007 and “are expected to continue to grow by approximately 40% from 2007 to 2030” [4]. To regulate first and then reduce CO<sub>2</sub> emissions, governing bodies, e.g. European Union (EU), and international associations, e.g. International Air Transport Association (IATA), established middle-term and long-term targets [5, 6]. For example, EU legislation set for cars a mandatory 40% reduction of their CO<sub>2</sub> emissions by 2021 [5]. To meet these new regulations, the transportation industry is currently developing new types of vehicles, which have lower fuel consumptions. [7-9]

Because of their interesting specific mechanical performances, i.e. high mechanical properties for low densities, composite materials appear to be good candidates to enable important weight saving and thus, significant fuel consumption reduction. Originally reserved to high performance applications, e.g. military aircrafts, composite components are nowadays used in various sectors, e.g. civil aviation, automotive (BMW [10], Renault, etc.), marine, energy (e.g. wind turbines blades), sport (ski equipment, bicycles, etc.) etc. Composites, which comes from Latin *componere*, meaning “put together”, are materials composed of at least two different raw materials: the reinforcement, which carry most of structural loads, and the resin (also called matrix), which, on the one hand, holds the reinforcement together and, on the other hand, protects it from environmental conditions. Although different types of composite materials exist, only those composed of organic resins are considered in this work. [11-13]

Despite their large variety, polymer resins can be classified into two main groups: thermosets and thermoplastics. While thermosets solidify through an irreversible chemical reaction referred to as cross-linking or curing, thermoplastics solidify without chemical reaction. Thermoplastics have thus the particularity to be easily reusable. Due to the lack of chemical reaction, thermoplastics can be remoulded under the application of sufficient heat, i.e. when the polymer is in its softened/molten state. [11]

Organic composite materials can be reinforced with several different types of fibres, e.g. carbon, glass, aramid. These can be continuous (endless) or discontinuous (short or long) and aligned or randomly oriented. Their type as well as their arrangement affect the properties of composite materials and must thus be selected upon requirements. [11]

For structural applications, i.e. applications in which the product is dedicated to a load-bearing role, continuous and aligned fibrous reinforcements made out of carbon fibres are often favoured because of their advanced mechanical properties. In the scope of this doctoral dissertation, only continuous and aligned carbon fibre-reinforced polymer (CFRP) composites are thus further considered. [11]

## 1.1 Industrial context

Even if thermoset composite materials have always been clearly dominating the composite market, the release of new thermoplastic composite materials have opened new opportunities [14-17]. Thermoplastic composites have valuable benefits compared to their thermoset counterparts: they offer superior solvent resistance, increased toughness capabilities and much less restrictive storage conditions. They also have enhanced recycling abilities and better potential for high-rate manufacturing. Due to their high resin viscosities and high processing temperatures, continuous thermoplastic composite materials are, however, rather difficult to process. To avoid difficulties, e.g. bad impregnation, thermoplastic composite components are therefore often manufactured with pre-impregnated materials (also called prepregs). Prepregs<sup>1</sup> are already impregnated reinforcements. Their impregnation is performed beforehand by material suppliers using specific machines and techniques, e.g. powder impregnation. As high quality and high performance semi-finished products, prepregs are expensive materials with low void content and uniform fibre distribution. [11, 18]

Unidirectional pre-impregnated composites are often processed by means of automated technologies, such as Automated Fibre Placement (AFP) and Automated Tape Laying (ATL) devices [11, 13, 19, 20]. These machines can be fed either with thermoset or thermoplastic tapes which are directly laid onto a mould. The material is often locally softened by use of a laser or infrared heaters to ease the lay-up process. To prevent air entrapment between the plies, a compaction roller is used to compact the material. An exhausting review of the different existing methods is given by Lukaszewicz et al. [20]. The restriction of these automated equipment lies in their capability to lay tapes on complex geometries, i.e. highly curved components with short radii. Moon et al. correlated the occurrence of defects to the smallest steering radius encountered during the process [21]. [P2]

---

<sup>1</sup> Both thermoset and thermoplastic pre-impregnated composites exist. [11]

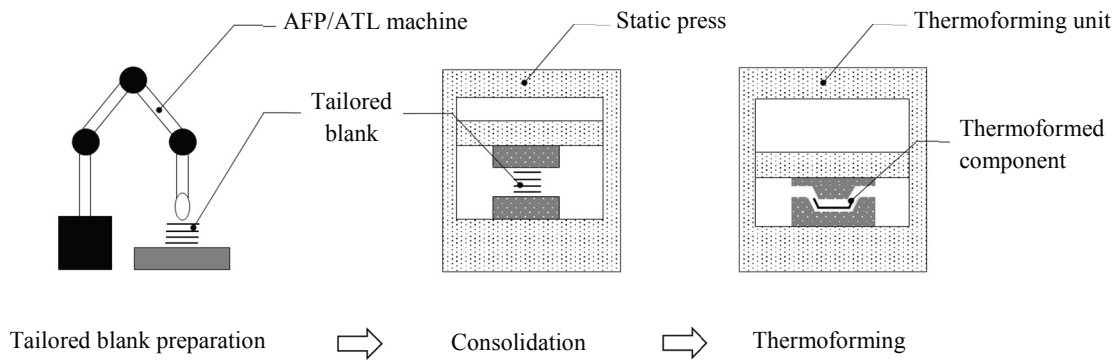


**Fig. 1-1: Preparation, consolidation and thermoforming of tailored blanks (process chain adapted from [11])**

Tailored blanks are first prepared by automated technologies using continuous thermoplastic prepreg tapes. They are subsequently consolidated under controlled temperature and pressure conditions. Preconsolidated tailored blanks are eventually thermoformed under specific temperature and pressure conditions.

To overcome common defects induced by AFP and ATL technologies, e.g. tow buckling and bridging, and to use the main advantage of these machines, i.e. high lay-up rates, an alternative process has arisen (see Fig. 1-1). Instead of laying tapes directly onto a mould, tapes are rather laid onto a flat plane and formed in a subsequent step. Such blanks are called tailored, or customised, since they are composed of several layers of unidirectional pre-impregnated tapes oriented in different directions [22]. The usage of tailored blanks for forming purposes already showed good potential for cross-plyed stacks of unidirectional pre-impregnated composites [23-25]. In the case of thermoplastics, tailored blanks are subsequently consolidated using a static or a double-belt press [11, 13]. Consolidated thermoplastic composite blanks are eventually processed by means of a thermoforming process [26-28]. The combination of temperature and pressure enables the material to deform and comply with mould geometry. An example of a thermoformed component for aerospace applications is presented in Fig. 1-2. [P2]

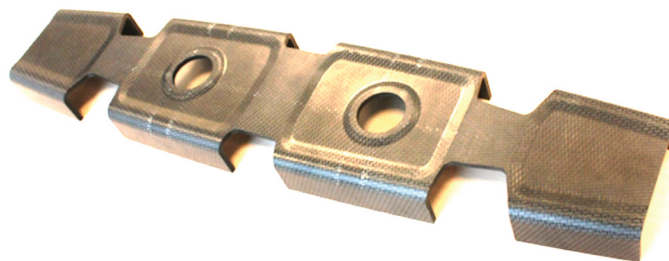


**Fig. 1-2: Thermoformed rib for aerospace application [29]**

In the scope of this doctoral dissertation, a continuous unidirectional carbon fibre-reinforced thermoplastic (CFRTP) prepreg tape composed of Polyamide 6 (PA6) supplied by Celanese Chemicals Europe GmbH is considered. As a semi-crystalline thermoplastic, this composite has the particularity to remain solid until it reaches its melting temperature. In its molten state, it becomes highly viscous and behaves like a viscoelastic liquid [30]. The main material properties are presented in Tab. 1-1. All of them, except for the melting temperature that was measured using a Differential Scanning Calorimetry system (DSC Q2000, TA Instruments), are taken from material datasheet [31]. [P2]

**Tab. 1-1: Main material properties of a UD-CF/PA6 tape from Celstran® [31]**

Material property	Value	Unit
Density	1.447	[g.cm <sup>-3</sup> ]
Theoretical tape thickness	0.13	[mm]
Theoretical fibre volume fraction	48	[%]
Glass transition temperature	57	[°C]
Melting temperature	219	[°C]

Unidirectional thermoplastic carbon fibre tapes are laid using a FiberForge RELAY 2000 station (see Fig. 1-3). This technology is an ATL process technology in which tapes are laid onto a two-axis motion table. During the process, ultrasonic spot-welds are generated to ensure the good stability of the lay-up. This technique enables the easy and rapid preparation of multi-ply tailored blanks. [P2], [22, 32]



**Fig. 1-3: FibreForge RELAY Station equipment and operating system [32]**

Tailored blanks prepared by the FibreForge RELAY Station are consolidated using a mechanical press (see Fig. A-1 and Fig. A-2 in Appendix a) and eventually thermoformed under temperature-controlled conditions.

## 1.2 Motivation and goals

Because of high manufacturing and raw material costs, e.g. carbon fibre, composite materials have been experiencing difficulties to broaden their use for industrial applications [12, 19, 33]. Compared to their thermoset counterparts, thermoplastic composites offer good potential for high-rate manufacturing and thus, significant cost saving opportunities. Besides, their inherent properties make them easily recyclable, which is a considerable benefit in a long term view.

By combining the advantages of several automated manufacturing techniques, i.e. AFP/ATL machines and a thermoforming unit, the process chain presented in Fig. 1-1 offers good potential for short manufacturing cycles, significant labour time reduction and increased reproducibility. The consideration of a thermoforming unit also enables the manufacturing of complex parts which could not be achieved with conventional techniques, i.e. direct lay-up on moulds. Besides, the implementation of tailored blanks participates to the reduction of material scrap and thus, enables important cost saving. [11, 22]

However, thermoforming is a complex process during which the material undergo severe deformations and from which defects, such as out-of-plane wrinkles (also called out-of-plane buckles), can occur [27, 34]. To avoid time and cost intensive trial-by-error approaches, simulations based on Finite Element (FE) methods have been developed to investigate and optimise forming processes [35-37]. These enable a better understanding by providing insights on the interactions existing between different stakeholders (composites, tooling etc.). Thermoforming simulations therefore aim to anticipate ahead of any trials the occurrence of defects, e.g. fibre reorientations and wrinkles (in-plane and out-of-plane), that could potentially occur during experimental thermoforming processes. For quality and performance purposes, the detection of such defects is particularly important since they alter the shapes and the mechanical properties of final components. [P2]

Based on the aforementioned motivations, the goals of this doctoral dissertation are:

- To develop, using a commercial software package, macroscopic FE thermoforming simulation models able to predict the potential occurrence of defects, such as out-of-plane wrinkles and fibre reorientations.
- To select an appropriate material model which accounts for the specific behaviour of thermoplastic materials under environmental forming conditions, i.e. when they are in their molten/softened state.
- To determine required simulation input by investigating the mechanical behaviour of thermoplastic composites under environmental forming conditions. The development of new test methods might be necessary to ensure proper material characterisation.

- To ensure that the test methods used and, if applicable, developed within this work can also be applied for the characterisation of thermoset prepregs under their environmental forming conditions. The aim is to assess whether these can be re-applied for future studies, e.g. development of forming simulations of thermoset tailored blanks.
- To consider a suitable approach for the modelling of separation films in FE thermoforming simulation. Such films are used in experimental forming processes to ease part removal.
- To validate the simulation approach by comparing virtual and experimental results. For this purpose, components with generic geometries will be experimentally thermoformed. The validation is to be achieved based on macroscopic observations, i.e. identification of defects such as out-of-plane wrinkles, scientific measurements of fibre orientations and final preform geometries.

Once validated, the simulation can be used to support industrial decision making regarding the design of new components and the development of new manufacturing techniques.

## 1.3 Outline

This doctoral dissertation is composed of seven chapters.

**Chapter 1** introduces the context of the work and presents the motivation and goals of this doctoral dissertation.

**Chapter 2** gives a description of two of the most common thermoforming technologies. This chapter also addresses the fundamental deformation mechanisms occurring during thermoforming processes, on the one hand, and the typical defects resulting from such deformations, on the other hand.

**Chapter 3** describes the advantages and limits of different approaches for the modelling of thermoforming processes. The approach considered within this thesis is presented at the end of this chapter along with a description of the selected software.

**Chapter 4** details material characterisation investigations. Both the unidirectional thermoplastic composite tape and the separation film considered for thermoforming experiments are characterised under similar environmental conditions as forming occurs. A non-cured unidirectional pre-impregnated thermoset composite tape is eventually tested under environmental forming conditions to assess whether the test methods considered for molten thermoplastic materials are also suitable for the characterisation of soft thermoset prepregs.

**Chapter 5** presents calibration analyses which aim to identify convenient simulation input via an inverse engineering approach. Because of particularities inherent to the constitutive model, experimental results presented in Chapter 4 cannot be directly used as simulation input.



**Chapter 6** focuses on the validation and application of the developed FE simulation model. The validation is based on macroscopic observations, comparisons between measured and computed preform geometries, on the one hand, and measured and computed fibre orientations, on the other hand. Once validated, two case studies are investigated. The first one assesses two approaches for the modelling of separation films in FE thermoforming simulations, while the second analyses, via a sensitivity study, the influence of the transverse tensile properties of the composite tape on simulation outcomes.

**Chapter 7** reviews the work presented in this doctoral dissertation, summarises major achievements and gives recommendations for future studies.



## **2 Forming of thermoplastic composite blanks**

Forming corresponds to the manufacturing step during which a flat blank (also called “sheet”) is shaped into the geometry of the final component [38]. Forming can be performed with dry or pre-impregnated (thermoset and thermoplastic) reinforcements. Forming of thermoplastic composite blanks occurs under the application of temperature, to soften polymer matrix, and pressure, to force preconsolidated tailored fibre-reinforced blanks to conform to mould geometry. As the application of elevated temperatures is essential, forming technologies used to process thermoplastic composite blanks are often referred to as “thermoforming processes”.

Various types of thermoforming technologies have been developed throughout the years [11, 28, 39]. In the following, focus is placed on two of the most common methods used to form thermoplastic composite blanks, i.e. diaphragm forming and hot stamp forming. Their operational usage as well as their relative merits are detailed. Other methods, such as bladder-moulding and roll forming, are not presented [39]. When thermoplastic composite blanks are formed, they are subjected to diverse types of deformations, which can lead to the appearance of defects. Deformation modes and typical resulting defects are eventually presented.

### **2.1 Main thermoforming technologies**

#### **2.1.1 Double diaphragm forming**

The double diaphragm forming process consists of placing a thermoplastic blank between two flexible silicon membranes (also called diaphragms) and, after having reached sufficient temperature, form the composite by creating vacuum between the lower membrane and the mould. While membranes are clamped to a surrounding rigid tooling frame, the thermoplastic composite blank, which is only held by air evacuation in-between both membranes, remains free-floating during the whole process. Although several variants of diaphragm forming exist, only the two main methods are described hereinafter. The major differences between these two concerns the method used to apply heat and to form the composite blank. [11]

In the first alternative (see Fig. 2-1), the membrane-composite stack is initially placed in an oven to heat the thermoplastic polymer matrix beyond its softening point. Once the desired temperature is reached, the membrane-composite stack is transferred onto a

rigid tooling. Forming happens when vacuum is created between the lower membrane and the rigid tooling and/or when pressure is applied on the upper membrane. Consolidation occurs when the blank enters into contact with the tooling, since the mould is usually unheated. [11]

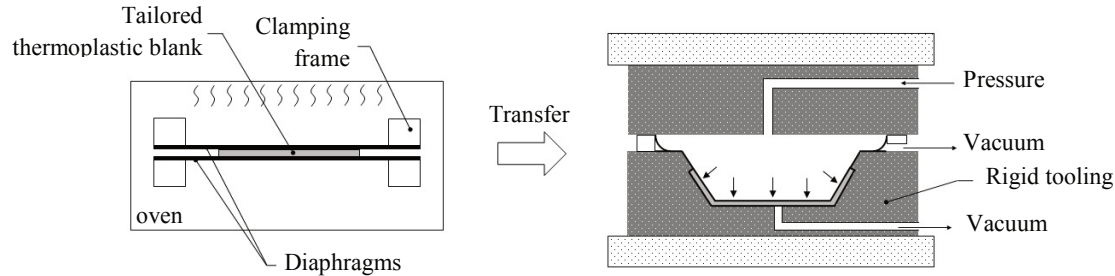


**Fig. 2-1: Schematic of a double diaphragm forming process (adapted from [11] and [39])**

The composite blank is firstly placed between two membranes and heated in an oven. The membrane-composite stack is subsequently placed onto a rigid tooling. Forming happens when vacuum is made and/or pressure is applied.

In the second diaphragm forming variant, the membrane-composite stack is placed within a dedicated tooling and enclosed in an autoclave. With this method, no transfer is required since the whole process, i.e. heating and forming, occurs inside an autoclave. In a first step, the temperature inside the autoclave is raised until the thermoplastic polymer matrix softens. In a similar manner as in the first variant, vacuum is created between the lower membrane and the rigid tooling. Pressure is also applied on the upper membrane. In this version of diaphragm forming, pressure is managed by an autoclave, which enables the application of much higher pressures, e.g. up to 7 bars. After forming, consolidation occurs by decreasing the temperature inside the autoclave. [11, 39]

Diaphragm forming techniques appear to be suitable methods to shape thermoplastic composite blanks to complex geometries. In particular, high quality components can be produced, i.e. low void content [40]. However, such technologies also demonstrated to be rather slow because of time consuming mounting/unmounting of membrane-composite stacks and long heating/cooling cycles. To reduce manufacturing time and thus, fully benefit from the fast manufacturing potential of thermoplastic composites, new approaches, such as stamp forming processes, have been developed. [38, 39]

## 2.1.2 Hot stamp forming

Hot stamp forming is a manufacturing process in which a softened thermoplastic blank is formed by means of a mechanical press [28, 40, 41]. The usage of a mechanical press, enables considerable time saving. This manufacturing process appears to be particularly interesting for high volume production since short cycle time can be achieved.

Hot stamp forming is a derived version of compression moulding forming used to form flow materials like BMC and SMC. In a similar manner as for all thermoforming processes, the blank is firstly heated beyond the softening point of its polymer matrix before being rapidly transferred (see Fig. 2-2). Forming eventually occurs under the application of pressure. Consolidation occurs when the blank enters into contact with the moulds, since these are usually cooled with fresh water. To ensure proper consolidation, pressure remains applied during the whole cooling down process. [11, 28, 39]

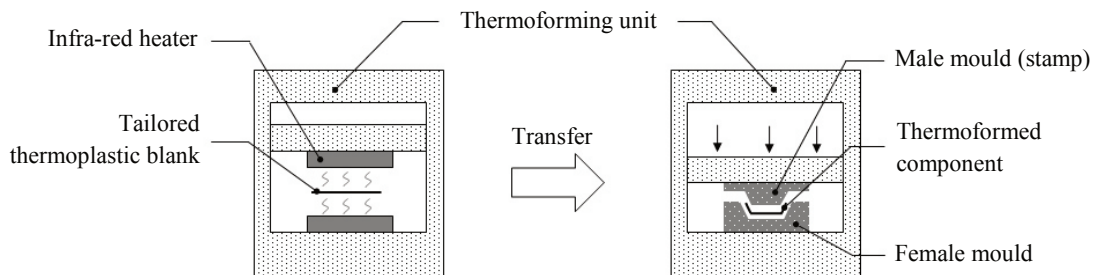


**Fig. 2-2: Schematic of a hot stamp forming process (adapted from [11])**

The thermoplastic blank is heated by means of infra-red heaters beyond the softening point of the polymer matrix and subsequently rapidly transferred to be thermoformed by means of a mechanical press.

To minimise transfer time, heating and forming often occur within the same processing unit. Called “thermoforming units”, such technologies are composed of heating and forming areas (see Fig. A-1 in Appendix a) [42]. Heating is often achieved by means of infra-red heaters. These are located near the mechanical press to minimise transfer time. The transfer from the heating area to the forming area is managed by a conveyor belt. Thermoforming units are fully automated technologies with high potential for industrial applications since they ease the handling of softened thermoplastic blanks, on the one hand, and enable considerable time saving, on the other hand.

Several different types of hot stamp forming processes exist, e.g. matched metal-die, rubber-block moulding and hydroforming. The matched metal-die technology is usually preferred in industrial applications because of its similitude to other compression moulding techniques, e.g. forming of metallic sheets. In this process, both moulds are made out of metallic materials. Due to uneven pressure distribution issues, especially for vertical regions of moulds, rubber-block moulding and hydroforming techniques have been developed. The rather soft aspect of the rubber block enables a better compliance of the stamp to the geometry of the mould and thus, a better pressure distribution. In the case of hydroforming, the inflation of a soft membrane under hydraulic pressure enables close contact between the thermoplastic blank and the female mould. Rubber-based materials in rubber-block moulding and hydroforming processes have, however, the main drawback not to be good thermal conductors. This prevents efficient cooling down and thus, does not enable as fast consolidation as matched-metal die processes. [11, 28, 39]

## 2.2 Deformation mechanisms occurring in thermoforming processes

Because of advanced mould geometries, i.e. double curvatures and short radii, composite blanks are subjected to severe deformations during forming. Despite their complexity, all deformations can be considered as a combination of several basic mechanisms. Depending on the length scale at which investigations are performed, different deformation mechanisms can be identified [43]. All deformations observed on a macroscopic scale, i.e. blank level, are caused by fibre/matrix reorganisations occurring on microscopic and mesoscopic scales, i.e. level of fibres and yarns, respectively. In the case of unidirectional tape, macroscopic and mesoscopic scale can, however, not be distinguished, since fibres are not gathered in yarns.

To apprehend the differences existing between textile and unidirectional reinforcements as well as between dry and pre-impregnated composites, a general overview of the deformation mechanisms occurring during forming processes is presented hereinafter. This comprises:

- Intra-ply shear,
- In-plane tension/compression,
- Out-of-plane bending,
- Single ply and multi-ply compaction,
- Interactions, e.g. inter-ply slip and tool-ply friction.

### 2.2.1 Intra-ply shear

As the main deformation mode governing the behaviour of dry textiles and NCFs, intra-ply shear has been considerably investigated in the field of textile composite forming [36, 44-57]. This mechanism corresponds to the plane deformation of composite reinforcements subjected to shear loads. For textiles, it consists of the rotations of yarns at their cross-over points [44].

Typical shear behaviour are presented in Fig. 2-3 for three dry woven fabrics. Although all curves depict similar non-linear trends, some show more resistance to deformation, e.g. dashed curve (plain weave) compared to plain grey curve (4-HS). This is to be imputed to the inner structure of the fabrics. Because of the friction existing between the yarns, reinforcements with more cross-over points, e.g. plain weave, are more difficult to shear than others, e.g. 4-HS [44].

As depicted in Fig. 2-3, the initiation of shear in textile composites is relatively easy. However, as shear angles grow, resistance to deformation increases. Because of yarn contacts and, eventually, yarn compactions, forces required to shear textile reinforcements rapidly increase, e.g. about 55 degrees of shear for the plain weave material.

The angle at which no further shear deformations can be undergone by the reinforcement is referred to as “locking angle”. Beyond this angle, deformations cannot occur in-plane anymore, which lead to the occurrence of out-of-plane wrinkles. The identification of a “locking angle” must, however, be handled carefully. Research studies indeed reported “locking angles” not to be intrinsic material properties but to be influenced by internal stresses such as yarn tensions [49, 50]. [44]

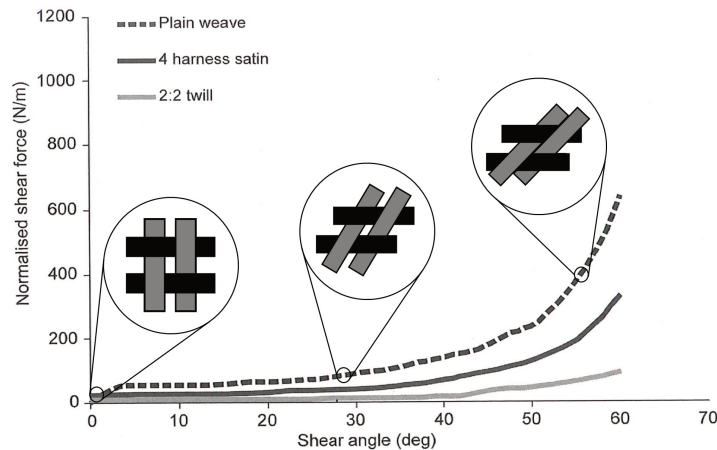


**Fig. 2-3: Intra-ply shear curves of dry plain, 4-HS and 2:2 twill glass fabric reinforcements (adapted from [37], [44] and [58])**

Illustrations of typical rearrangements occurring at the mesoscopic scale during intra-ply shear of a fabric reinforcement are depicted for three levels of shear.

Left: Initial state; Middle: Shearing, compaction and friction; Left: Compaction limit (locking angle).

Mechanisms controlling intra-ply shear of textile prepreg composites are similar to these governing dry reinforcements. The main difference lies, however, in the contact between the yarns. In the case of dry reinforcements, dry friction occurs, while in textile prepregs, lubricated friction takes place because of the presence of polymeric resin [44]. Textile prepregs therefore exhibit temperature- and strain rate-dependent behaviour [44, 53-57]. In particular, as temperature increases, shear forces decrease (see Fig. 2-4 left) and as deformation rate, i.e. test speed, increases, shear forces increase (see Fig. 2-4 right).

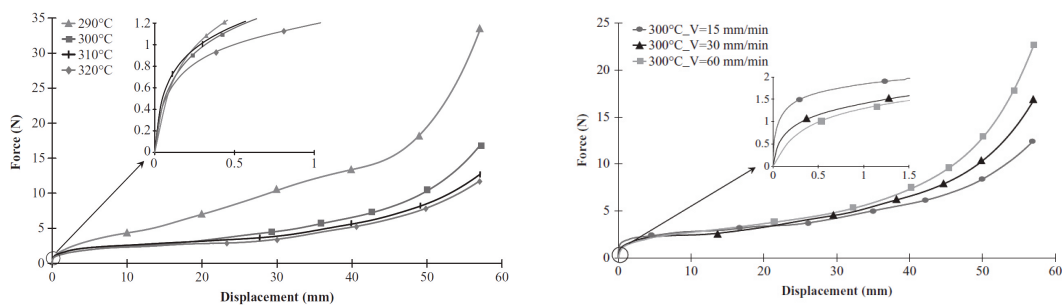


**Fig. 2-4: Intra-ply shear curves of a 5-HS carbon/PPS prepreg at different temperatures (left) and different test speeds at 300°C (right) [53]**

Because fibres of unidirectional composites are oriented in a single direction, the intra-ply shear mechanisms of such materials are solely different than those described for fabrics. In literature, two types of intra-ply shear are identified for unidirectional fibre-reinforced composites: longitudinal and transverse. While longitudinal intra-ply shear corresponds to the parallel sliding of fibres, transverse intra-ply shear corresponds to the relative displacement of fibres within a plane orthogonal to the orientation of the reinforcement (see Fig. 2-5) [34, 59-61]. During draping, longitudinal intra-ply shear plays a more important role than the transverse one [62].

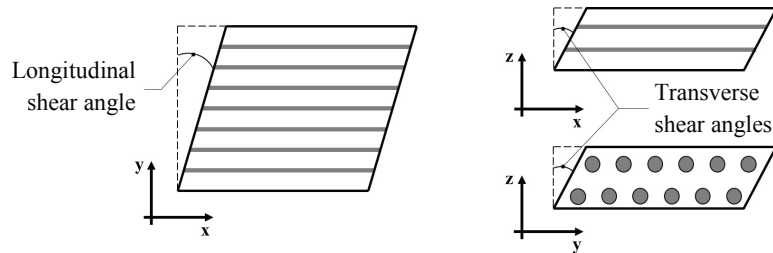


**Fig. 2-5: Different types of intra-ply shear occurring in a unidirectional reinforcement**

The reinforcement is oriented along the x-direction. The y- and z-directions are perpendicular to the x-direction.

Left: Longitudinal intra-ply shear; Right: Transverse intra-ply shear.

Longitudinal intra-ply shear deformations are governed by the viscous behaviour of the matrix and the fibre-matrix interface [63]. As such, these are sensitive to temperature and strain rate variations [62]. Because of considerable fibre-fibre contact interfaces, unidirectional reinforcements show more resistance to shear than their textile counterparts [63]. The lack of reinforcement in a second direction seems to enable unidirectional composites to accommodate intra-ply shear deformations without limit [60]. However, in practical situations, unidirectional composites cannot withstand large intra-ply shear deformations because of imperfections within the material, which initiate the development of transverse strains, i.e. strains perpendicular to fibre direction. The rapid occurrence of damages like ply tearing, i.e. failure due to excessive transverse tensile stresses, is eventually promoted by weak matrix and fibre-matrix interface behaviour [38, 62, 64, 65].

Transverse intra-ply shear, which is relatively similar in trends and magnitudes to longitudinal intra-ply shear [66], can be introduced relatively easily in unidirectional reinforcements [38]. Since this mechanism is mainly induced by out-of-plane deformations [38, 59, 67], it is further detailed in Chapter 2.2.3.

## 2.2.2 In-plane tension/compression

In-plane tension and compression consist of introducing tension and compression within a reinforcement, respectively. Deformations along the direction of the fibres is referred to as longitudinal, whereas they are transverse when they are perpendicular to fibre direction. Depending whether the material is a textile or a unidirectional rein-



forcement, longitudinal tension may involve two or one direction(s), respectively. Transverse tension is only experienced by unidirectional reinforcements, as they are composed of a single family of fibres.

Longitudinal tension depicts linear and non-rate dependent behaviour. As governed by the property of the fibres, deformations are characterised by high forces and low strain values. Longitudinal tension is much stiffer than other deformation mechanisms, such as intra-ply shear and out-of-plane bending. [36, 44, 68]

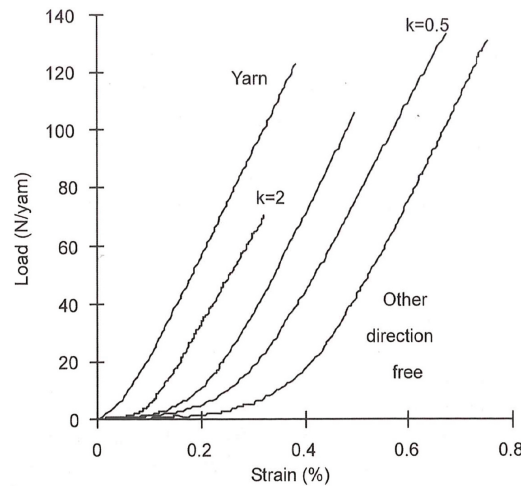


**Fig. 2-6: Typical biaxial tensile test results of a fabric reinforcement [44]**

As reference is presented the behaviour of a single yarn subjected to longitudinal tension. The factor  $k$  represents the ratio of strains along and transverse loading directions.

The behaviour of fabrics subjected to longitudinal tension differs slightly from this of unidirectional reinforcements. Because of fibre undulations (also called “crimps”), yarns show initial non-linear behaviour (see Fig. 2-6). This straightening effect (also called “de-crimping” of the yarns, see Fig. 2-7) is influenced by the strain states of the transverse yarns. The higher the transverse strain, the less “slack” at the beginning of the tensile response (see Fig. 2-6 and the influence of factor  $k$ ). Also, the larger the undulation, the more non-linear the behaviour. [44, 50, 68-70]

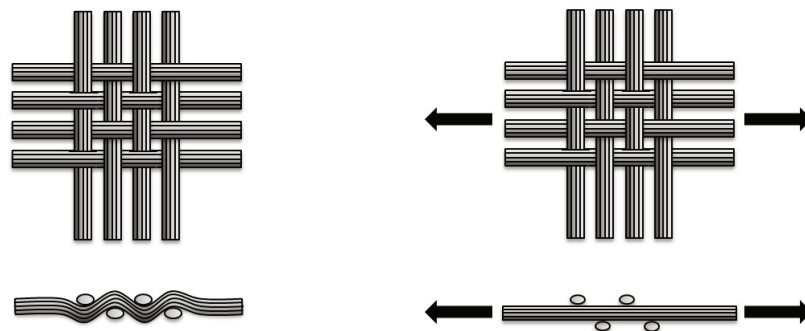


**Fig. 2-7: Front (top) and cross-sectional (bottom) views of a fabric at rest (left) and subjected to longitudinal tension (right) [58]**

Left: Initial state (with crimps); Right: After longitudinal tension (de-crimping).

Because fibres are continuous and can transfer stresses all over the blanks, the occurrence of longitudinal tension influences the mechanical response of composite reinforcements, e.g. intra-ply shear behaviour of fabrics [47, 49, 54].

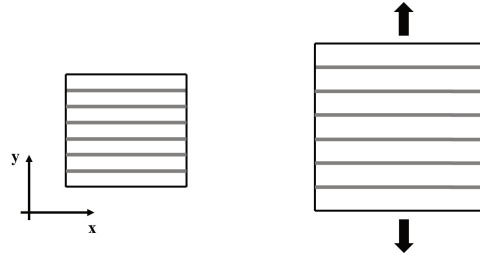


**Fig. 2-8: Transverse tension of a unidirectional fibre-reinforced composite material (adapted from [58])**

The reinforcement is oriented along the x-direction.  
Left: Initial state; Right: After deformation.

Transverse in-plane tension of unidirectional prepregs is depicted in Fig. 2-8. This deformation mechanism is governed by matrix and fibre-matrix interface behaviour. As such, it depicts important temperature and strain rate dependencies. This mechanism is significantly weaker than others, such as intra-ply shear [65].



**Fig. 2-9: Longitudinal compression of a yarn (adapted from [58])**

The reinforcement is oriented along the x-direction.  
Left: Initial state; Right: After deformation (yarn buckling).

Longitudinal compression of yarns occurs when longitudinal compressive forces are introduced into a reinforcement (see Fig. 2-9). Because of their slenderness, fibrous yarns buckle relatively easily under compressive loads. Transverse compression, which is the application of compressive forces within a plane orthogonal to the orientation of the reinforcement, plays an indirect role during forming since it influences other deformation mechanisms, such as intra-ply shear and biaxial tension of dry fabrics [71, 72].

### 2.2.3 Out-of-plane bending

As the main mechanism governing out-of-plane deformations, bending plays an important role in forming processes. In particular, it enables the material to comply with complex mould geometries. The out-of-plane bending behaviour of dry reinforcements is solely different than this of continuous materials, e.g. steel. Because dry reinforcements are composed of fibrous yarns, classical bending theories are not applicable, e.g. Euler-Bernoulli [73-75]. Bending rigidity can therefore not be derived from in-plane tensile properties [75]. In fact, bending of dry reinforcements must be considered as a

multi-scale phenomenon in which macroscopic bending is governed by reorganisations occurring at microscopic, i.e. fibre sliding and friction, and mesoscopic scales, i.e. inter-yarn friction [36, 74, 76]. Out-of-plane bending is often characterised by moment-curvature diagrams (see Fig. 2-10) [73, 76, 77]. Experimental investigations reported bending of dry reinforcements to be anisotropic, non-linear and non-elastic [44, 76]. Because of intra- and inter-yarn sliding and friction, bending rigidities are much weaker than in-plane tensile ones [36, 44].

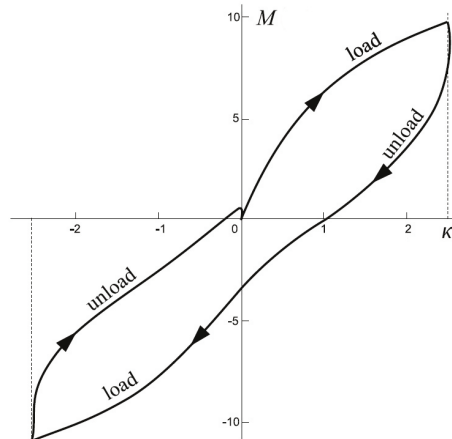


**Fig. 2-10:** Typical bending hysteresis of a dry fabric reinforcement (adapted from [76])  
Loading/unloading curves presented as the evolution of bending moments per unit width  $M$  over curvatures  $\kappa$ .

The bending behaviour of prepreg composites under environmental forming conditions has not been much investigated. According to Sachs, bending of molten thermoplastic composites is closely interrelated to intra-ply shear and inter-ply slip (see Fig. 2-11). Martin et al. and Dykes et al. even considered bending of prepreg composites to be exclusively controlled by intra-ply shear deformations [78-80]. [43, 64]

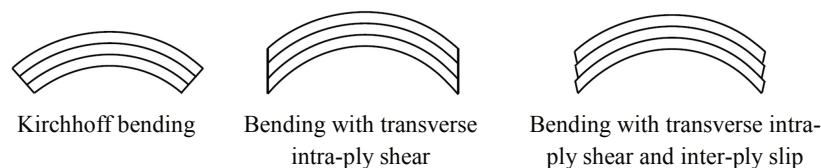


**Fig. 2-11:** Bending of a prepreg composite laminate (adapted from [64] and [66])

Investigations performed by Scherer and Friedrich [38, 67] and Haanappel [66] showed transverse intra-ply shear to play a significant role in large bending deformations of molten fibre-reinforced thermoplastics. Upon layup arrangement [67] and blank consolidation quality [66, 81, 82], inter-ply shear can also occur (see Fig. 2-11). Recent investigations performed on unidirectional and woven fabrics reinforced thermoplastic composites in their molten configurations show bending properties to be non-linear, temperature and rate dependent [P2, K3, 43, 66, 83].

## 2.2.4 Single and multi-ply compaction

Compaction corresponds to the transverse, i.e. through-thickness, compression of a single ply or a multi-ply layup (see Fig. 2-12). This mechanism plays a relatively minor role during forming but a major one after, since it aims to increase fibre volume fractions and eliminate voids of prepreg composite components [44]. Although compaction of single plies is considered non-linear elastic [84], compaction of multi-ply fabrics has been reported to behave non-linear non-elastic [85]. Results of compaction tests are usually presented as the evolution of fibre volume fraction (or thickness) with respect to compaction pressure [44] (see Fig. 2-13).



Fig. 2-12: Compaction of a single dry woven fabric layer [58]

The introduction of compaction pressure within a single dry fabric ply leads to a reorganisation of its internal structure, i.e. yarn crimp flattening [84, 86]. In the early compaction, the thickness of the ply rapidly decreases, which, in return, results in a rapid increase of the fibre volume fraction (see Fig. 2-13). When pressure reaches a certain level, no further compaction can take place. As a result, thickness and fibre volume fraction tend to asymptotic values. The compaction of multi-ply fabric reinforcements is mainly due to the nesting of the plies [84]. This mechanism, which is characterised by the intimate contact between adjacent layers, further influences the permeability of the laminate and the mechanical performance of the final component. Research analyses showed nesting to become more significant as the number of plies increases (see Fig. 2-13). [44, 84, 86, 87]

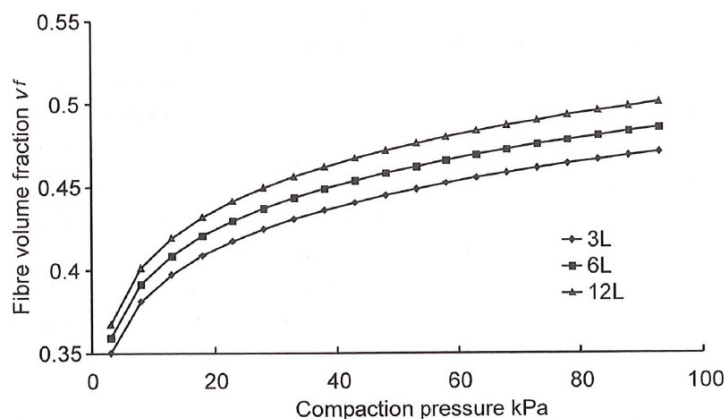


Fig. 2-13: Typical compaction curves of a plain woven fabric [44]

The evolution of fibre volume fraction with respect to compaction pressure is presented for stacks composed of three layers (3L), six layers (6L) and twelve layers (12L). Because of nesting, layups with more plies reach higher fibre volume fractions.

Because of the presence of polymeric resin, prepreg composites exhibit temperature and rate dependencies under compaction [44]. When pressure is introduced, deformations are initially dominated by viscous effects induced by resin flows. As compaction pressure is increased, deformations become, however, dominated by the stiffness of the elastic fibre bed. In a similar manner as for dry reinforcements, when no further compaction can occur, thickness and fibre volume fraction eventually reach asymptotic values. Despite the application of high pressures, which aim to reduce the content of voids in the final components, most of thermoplastic and thermoset prepreg composites show limited thickness reductions (< 20%). [44, 88]

## 2.2.5 Tool/ply and ply/ply interactions

Interactions are related to all types of contacts occurring in forming processes. Two types of interactions are usually distinguished: tool-ply, which corresponds to the interactions between a tool and a ply, and inter-ply, which corresponds to interactions between plies (see Fig. 2-14). Both types of interactions play an important role during forming since they govern the transfer of loads. [44]

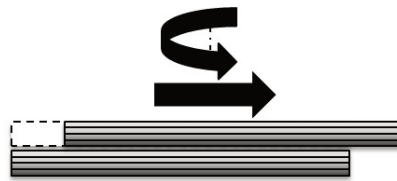


Fig. 2-14: Relative rotational and translational motion between plies [58]

Behaviour of interactions are driven by contact properties and thus, friction. Friction is characterised as the force resisting to the motion of two objects in contact. Two types of friction have to be distinguished: static and kinetic (also called “dynamic” and “steady-state”). While static friction is characterised by the force to overcome to initiate motion, kinetic friction corresponds to the resistive force acting during the motion of an object with respect to another. [37, 43, 89, 90]

Tool/ply and ply/ply interactions involving dry reinforcements and/or solid tool material, e.g. steel, are dependent on reinforcement arrangements, e.g. fibre orientation, but not on temperature and relative motion speed. A slight dependency with respect to normal load is, however, noticed. As pressure is applied, the surface of the dry textile flattens leading to a slight reduction of the friction coefficient. Despite this minor dependency, interactions of dry reinforcements are often described using Coulomb theory which assumes friction to be independent from relative motion speed. Coulomb friction coefficient  $\mu$  is considered to be directly proportional to the ratio between the frictional force  $F_T$  and the normal load  $N$ : [43, 44, 91]

$$\mu = \frac{F_T}{N} \quad (2-1)$$

Because of polymeric resin, interactions involving prepreg composites exhibit viscous behaviour. In the case of textile prepreg composites, several researchers reported interactions to be influenced by temperature, normal pressure and relative motion speed. Consequently, friction coefficients are usually presented as a function of the Hersey number  $He$ , which is related to temperature  $T$ , via viscosity  $\eta$ , relative contact speed  $U$  and normal pressure  $P$ . Such curves are referred to as Stribeck curves in literature (see Fig. 2-15). [37, 43, 44, 92-94]

$$He(T, v, P) = \frac{\eta(T)U}{P} \quad (2-2)$$

Stribeck curves are divided into three parts (see Fig. 2-15): boundary lubrication (BL), mixed lubrication (ML) and elasto-hydrodynamic lubrication ((E)HL). Whether friction behaves as BL, ML or (E)HL depends on the thickness of the inter-layer resin film. Tool/ply and ply/ply interactions involving textile prepreg composites usually occur within the elasto-hydrodynamic lubrication part. In most cases, full hydrodynamic lubrication is even considered because of the presence of resin-rich inter-layer films. [43, 92-94]

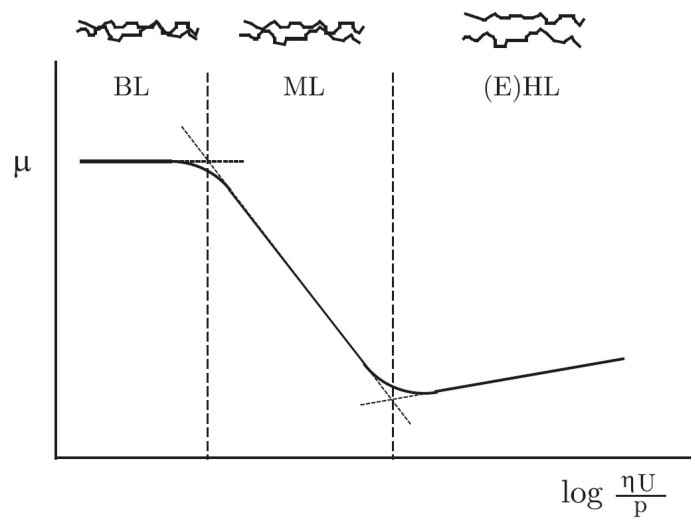


**Fig. 2-15:** Typical evolution of a Stribeck curve [92]

Evolution of friction coefficients  $\mu$  with respect to the logarithm of the Hersey number. Three parts are to be distinguished: boundary lubrication (BL), mixed lubrication (ML) and elasto-hydrodynamic lubrication ((E)HL).

The mechanisms governing tool/ply and ply/ply interactions of unidirectional prepreg composites appear to be more complex to investigate because of thinner resin film thicknesses [43]. Early experimental analyses reported such interactions to behave like textile prepreg composites and thus, show temperature, relative motion speed and normal pressure dependencies [82]. However, in a recent study, Sachs reported unidirectional thermoplastic composites to exhibit pressure independent contact properties at low sliding speeds when in contact with steel foils [43].

Although interactions involving textile and unidirectional prepreg composites are dominated by hydrodynamic friction [43], a certain amount of Coulomb friction can also occur. This is particularly the case when fibres enter into contact with solid material, e.g. steel tool [82, 90]. Besides, tool/ply and ply/ply interactions can also be influenced by the intra-ply shear of the layers. This phenomenon seems, however, to be layup dependent [67].

## 2.3 Typical defects induced by thermoforming processes

The occurrence of defects in thermoforming processes is due to a combination of several different aspects which can be related to either manufacturing processes, e.g. mould geometry, temperature and forming speed, or composite blanks, e.g. cut-out geometry and material type/stacking sequence.

Out-of-plane and in-plane wrinkles are the most common encountered defects (see Fig. 2-16 and Fig. 2-17) [37, 95-98]. These are particularly critical because they alter the mechanical performance of final components [37]. Besides, out-of-plane wrinkles, also referred to as out-of-plane buckles, affect the shape of the components [99]. The onset of out-of-plane wrinkles is complex and has been studied by several researchers. For a given material, experimental studies reported that, amongst other factors, stress conditions induced by manufacturing boundary conditions, forming speeds, original blank dimensions and strain gradients play a role in their development (see Fig. 2-16) [27, 41, 82, 99-102]. Boisse et al. also showed the appearance of out-of-plane wrinkles to be a global phenomenon depending on process conditions, e.g. blank-holder pressure, and all types of strains and rigidities of the composite material [97]. [P2]

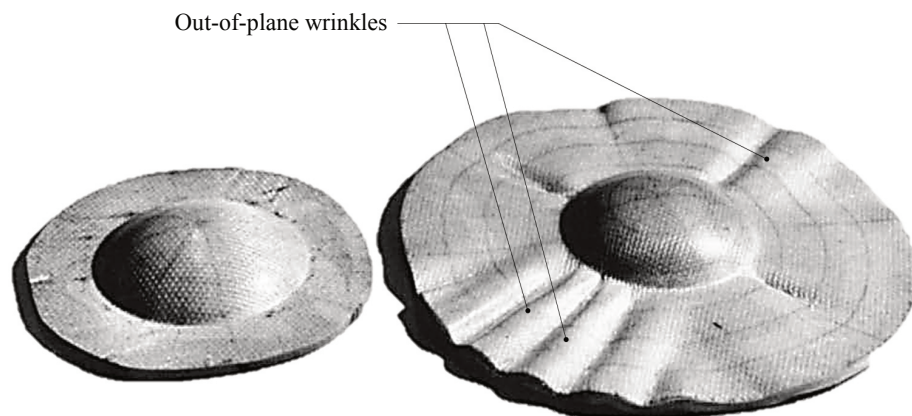


**Fig. 2-16: Influence of blank size on forming results (adapted from [27])**  
Forming of a glass-fibre fabric reinforced PEI composite laminate.  
Left: Original blank size (78 mm); Right: Larger blank size (120 mm).

Besides out-of-plane and in-plane wrinkles, thickness variations due to uneven pressure distribution can also occur. Hou and Friedrich reported thickness variations of +12% and -8% for the hot stamp forming of a hemisphere with a glass-fibre woven fabric reinforced thermoplastic (PEI) composite [41]. The localised high pressure at the apex of the hemisphere led fibres and molten resin to flow away. As a consequence, while the section at the apex is the thinnest, the accumulation of resin and fibres results in a thickness increase in adjacent areas. Thickness variations are, however, more important for unidirectional than textile thermoplastic composites because of the ease with which transverse flow can occur [27]. Besides altering the mechanical properties of the final component, thickness variations can also eventually induce part distortions, e.g. spring-in/spring-back effects [103].

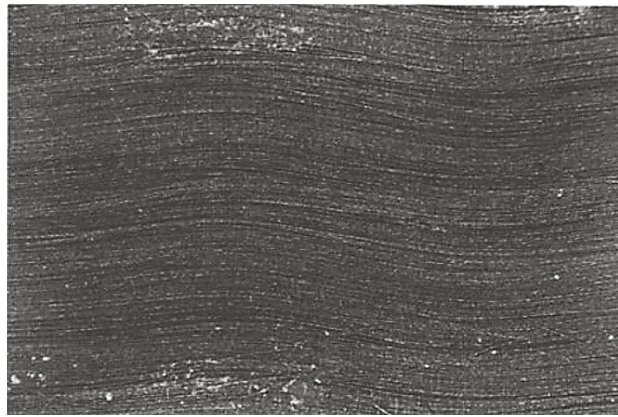


**Fig. 2-17:** Photomicrograph of in-plane fibre waviness in a UD-CFRTP component [104]

Because of low resin viscosity and high pressure, matrix migration can also be observed in bend specimens when resin is squeezed into the outer area (see Fig. 2-18). Friedrich et al. explains this phenomenon as a lack of time for the inter-ply slip deformation mechanism to occur [27].

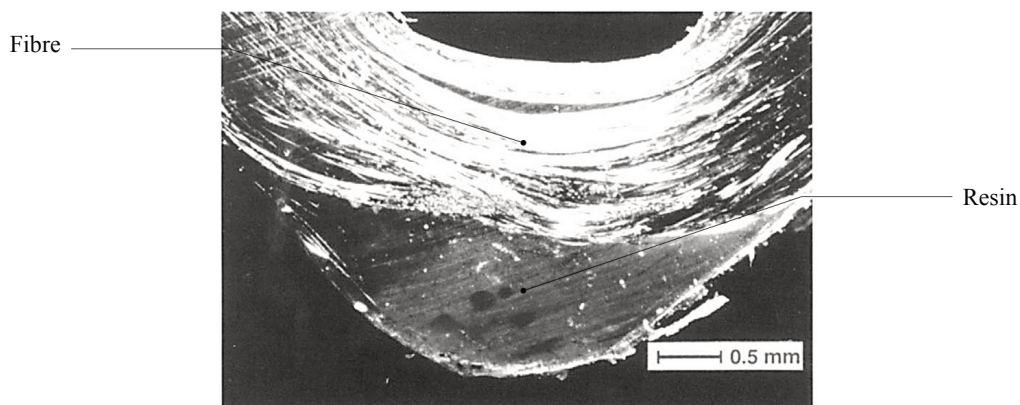


**Fig. 2-18:** Matrix migration observed at bend angle section of a CF/PP laminate (adapted from [27])



The manifold of parameters to take into account is a challenge in the manufacturing of defect-free components. To avoid time and cost expensive experimental test campaigns, simulation methods are often preferred to trial-by-error approaches. Chapter 3 presents several simulation approaches applied to the prediction of defects induced by thermoforming processes.



## 3 Thermoforming simulation

Thermoforming simulations consist on the numerical investigation of thermoforming processes, e.g. diaphragm forming and hot stamp forming. Such methods are used to assist the development of component design, i.e. geometry, and optimisation of process parameters, e.g. temperature. Their predictive capabilities offer cost and time effective solutions to identify the potential occurrence of defects, e.g. in-plane and out-of-plane wrinkles (see Chapter 2). Simulation results are thus used in the early stage of development, when no experimental trial have been performed, to support decision making, and initiate, if applicable, appropriate modifications.

Depending on the requested level of details and computational power available, different simulation approaches have been developed. These can be divided into mapping and mechanical methods. Both types of approaches are thoroughly described in their respective sections. Based on their advantages and disadvantages, on the one hand, and on the requirements of the project from which this doctoral dissertation is funded, on the other hand, the approach selected in the scope of this research study is eventually presented.

### 3.1 Mapping methods

Mapping methods consider the composite blank as a rectangular network of nodes, also referred to as “mesh” (see Fig. 3-1). The goal of mapping algorithms is to determine the coordinates of each node when the mesh is fitted onto the surface of a pre-forming tool in order to predict resulting fibre orientations. As long as surfaces can be mathematically discretised, no restriction on the geometry applies. Although several mapping methods exist, e.g. kinematic and energy models, all are based on the same assumptions that the initial mesh (i) is composed of perpendicular and inextensible fibres and (ii) can only undergo shear deformations [105]. Any other deformation mechanisms, e.g. friction or out-of-plane bending, are not taken into account. [S4, 34, 106]

Although many researchers published variants of the original kinematic model presented by Mack and Taylor [107], all algorithms are based on the same principle. These assume the mesh to be rectangular and act like a pin-jointed medium. In kinematic models, mapping starts from an initial point and two fibre directions. When the mesh is draped onto a surface, nodal coordinates are determined such that the distance between adjacent nodes does not vary (no fibre extension): nodes are thus determined by creating quadrilateral cells (see Fig. 3-1). [S4, 34, 106]

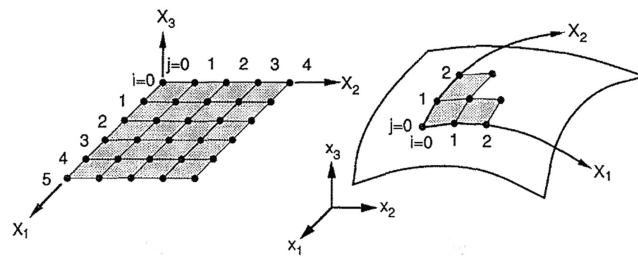


**Fig. 3-1: Mapping of a composite blank onto a generic double-curved surface [34]**

The reinforcement is oriented along the  $X_1$ - and  $X_2$ -directions.

Left: Initial state; Right: Partially mapped onto a surface, node (2, 2) is next to be mapped.

In 1991, Van der Weeën developed a mapping model based on elastic energy minimisation. Instead of determining nodal coordinates using geometrical approaches, like for kinematic models, mesh cells were mapped by considering the minimum energy required to extend fibres. In 2002, Long et al. published an enhanced energy method based on the minimisation of shear strain energy. The approach considers a conventional kinematic model within an iterative algorithm. Results showed good potential to predict changes in fibre orientations while accounting for material particularities, i.e. fibre architecture. [S4, 34, 105, 106, 108]

Final fibre orientations and shear angles, i.e. angles between fibre directions, are the main output of mapping models. Although defects cannot be predicted as such, their locations can be assumed by analysing the final shear angles distribution. For example, locations where shear angles are larger than a certain user-defined value, i.e. locking angle, can be interpreted as areas prone to the development of out-of-plane wrinkles. Another output of mapping models concerns the identification of optimum blank geometry, i.e. cut-out. This feature is particularly interesting since it enables the reduction of material scrap in forming processes. Last but not least, output of mapping models can be transferred into other types of simulation. Information regarding the final shear angles distribution can be particularly interesting for flow simulations, for example, since intra-ply shear angles alter preform permeability [108]. [109]

Several companies commercialise mapping software, e.g. Dassault Systèmes Simulia (CATIA CPD/CFM), ESI Group (PAM-Quikform) and MSC.Patran (Laminate Modeler). Each of them enables the selection of different mapping strategies, i.e. propagation methods, and algorithms. For example, MSC.Patran offers the possibility to use either a kinematic or a minimum energy method. [106, 109]

Mapping algorithms are easy-to-use and rapid simulation methods (within a few seconds). Although several methods were developed over the years, Van der Weeën showed energy ones to be the most efficient in terms of computational cost [105]. However, their initial assumption (all deformations are governed by pure intra-ply shear) restrains their application. Because mapping methods do not account for any material properties and process parameters, these are not suited for the modelling of multi-ply layups and pre-impregnated materials. In fact, the validity of mapping mod-

els seems to be limited to hand layup processes of dry balanced single-ply plain weave reinforcements over convex tooling. The accurate prediction of defects, e.g. in-plane and out-of-plane wrinkles, requires advanced simulation tools such as Finite Element methods. [35, 106, 109]

## 3.2 Mechanical methods

Finite Element Methods (FEM) are numerical approaches able to approximate solutions of partial differential equations issued from scientific applications. The main principle of FEM is to divide the domain of study into several subdomains, i.e. finite elements, find simple polynomial solutions for each subdomain and, eventually, assemble them to describe the behaviour of the global system. [110]

Since 1990s, several mechanical approaches based on FEM have been developed to simulate composite forming processes [106]. Unlike mapping methods, FEM enable complete mechanical analyses by taking process boundary conditions, e.g. temperature, and material behaviour, e.g. interactions, into account.

Finite Element Analyses (FEA) can be performed at different length scales: macroscopic, mesoscopic and microscopic (see Fig. 3-2). Macroscopic investigations consider composite layers as continuum media. As discrete approaches, mesoscopic and microscopic analyses consist of the modelling of yarns and fibres, respectively. The type of discretisation is selected based on the objectives of the study, in particular on a trade-off between level of detail and computational time [111].

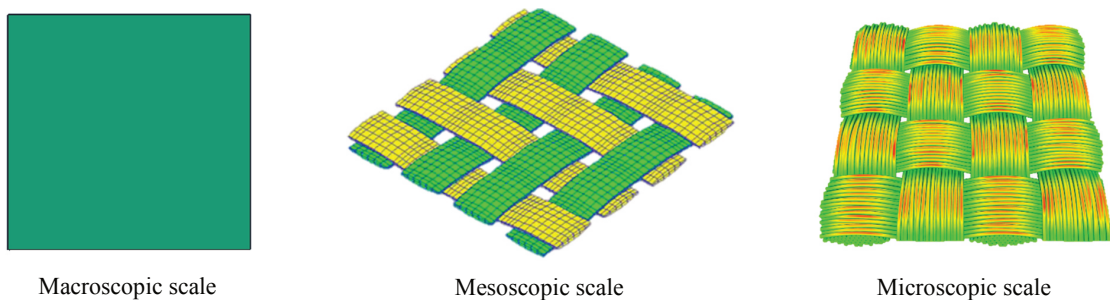


**Fig. 3-2: Macroscopic, mesoscopic and microscopic representation of a balanced plain weave fabric (figures of the mesoscopic scale [112] and the microscopic scale [113])**

At the macroscopic scale, the reinforcement is considered as a continuum: no detail about internal material structure is considered. At the mesoscopic scale, the yarn architecture of the reinforcement is taken into account, but fibres, which compose the yarns, are not modelled. At the microscopic scale, all details are considered.

In the following, an overview of different approaches based on FE-methods applied to the simulation of thermoforming processes is presented. Further details, especially in terms of constitutive equations, can be found in the literature [35, 36, 106, 111, 114].

### 3.2.1 Macroscopic Finite Element approaches

Rogers [61] was amongst the first to publish constitutive relations governing the behaviour of molten unidirectional thermoplastic composite materials during forming. His approach was derived from studies performed by Spencer in 1984 [115]. Rogers assumed the material to behave like an incompressible, linear viscous fluid reinforced with one or two family of inextensible, stiff and collimated fibres. These are assumed to lay in-plane and to be continuously distributed. This model, referred to as “Ideal Fibre-Reinforced Newtonian fluid Model” (IFRM), was implemented by Ó Brádaigh et al. in a 2D implicit FE program called FEFORM. Simulations were performed for a unidirectional fibre-reinforced composite under specific plane strain and stress conditions. To prevent element locking issues [116, 117], which occur when element edges are not aligned along fibre directions, a mixed penalty finite element system was considered [118]. [66, 119, 120]

Ó Brádaigh et al. assessed the validity of this numerical model by comparing simulation results to experimental data. Punch experiments were performed with circular eight layers blanks composed of unidirectional CF/PEEK prepreg composite plies (APC-2). To reproduce single diaphragm process conditions, experiments were carried out with a membrane on top of the composite stack. For validation purposes, a polar grid pattern was printed on the blanks prior to forming. Simulation results using velocity boundary conditions were in good agreement with experimental measurements, especially along fibre direction. This demonstrated the ability of the simulation tool to predict blank deformations. Discrepancies for displacements in transverse direction were assumed to be due, amongst other assumptions, to incorrect simulation input and/or to the fact that the diaphragm was not accounted for in the numerical analysis. Comparisons held between numerical stress distributions and the appearance of out-of-plane wrinkles showed encouraging results, since areas with high stress concentrations corresponded to some extent to the locations where instabilities were experimentally observed. In further investigations, the authors suggested, based on experimental evidence, to govern inter-ply shear by a lubricated friction law applied to frictional contact elements, i.e. elements placed in-between adjacent plies. The IFRM was also applied by McGuinness and Ó Brádaigh to analyse picture-frame test results of cross-plyed molten fibre-reinforced thermoplastic composite materials [60]. [119]

The model initially proposed by Rogers was further extended by Johnson [121], McGuinness and Ó Brádaigh [122], Spencer [123] and Harrison et al. [124] for fabric-reinforced blanks.

In 1995, Pickett et al. developed a 3D explicit FE approach able to simulate thermoforming processes [125]. This solution, which was developed as the composite variant of the metal stamping code PAM-STAMP, is nowadays commercialised by ESI Group as PAM-FORM [35]. In order to account for both intra- and inter-ply shear mechanisms, composites plies were modelled by shell elements. These were said to be

“bi-phase” as the material law included linear elastic and viscous models representing fibres and matrix, respectively. As a macroscopic approach, each layer of the composite stack was modelled by a layer of shell elements. Inter-ply mechanisms were managed by imposed sliding constraints with viscous-dependent penalty friction law. In the numerical model, all stakeholders were modelled (punch, die, plies) and all process parameters taken into account. Results for the punch forming of a single ply of CF/PEEK material (APC-2) showed numerical results to be consistent with experimental observations [125]. Later, de Luca et al. investigated the forming behaviour of stacks composed of 20 layers of unidirectional CF/PEEK (APC-2), on the one hand, and eight layers of CF/PEI (CETEX) woven fabric, on the other hand, over a double-dome preforming tool [126]. The authors investigated the influence of forming speed, stacking sequence, clamping system and blank holders on the occurrence of out-of-plane wrinkles. In all cases, simulation results were in good agreement with experimental observations. Since then, ESI Group released several versions of PAM-FORM. The software is nowadays used by several industrial companies in either a standalone software, i.e. PAM-FORM 2G, or a graphical interface, i.e. Visual-FORM. In the scope of a doctoral dissertation, Visual-FORM was recently applied at the *Chair of Carbon Composites* of the *Technical University of Munich* for the forming simulation of thick AFP laminates [127, 128].

ABAQUS, which is supplied by Dassault Systèmes Simulia, offers lots of flexibility for the simulation of thermoforming processes. For example, to model the behaviour of composite plies, the user can either consider a standard, already implemented, material model or develop his own model by implementing a customised constitutive law.

The standard material model, called FABRIC, has been developed to depict the behaviour of pre-impregnated woven fabrics during forming. As its name is referring to, FABRIC considers two distinct reinforcement directions, whose mechanical responses are assumed to be independent from each other. This anisotropic and non-linear material model requires the characterisation of in-plane tensile/compression properties for both fibre directions as well as intra-ply shear properties. Depending on material behaviour, different loading/unloading paths can be specified and strain-rate and/or temperature dependencies taken into account. This material model can only be applied to membranes and shell elements and used in dynamic explicit computations. [129]

In order to account for specific material behaviour, several researchers developed their own constitutive law. These can be implemented and integrated to ABAQUS via user subroutines. For example, Dong et al. implemented an updated material model based on an anisotropic elastic behaviour [130]. Based on the homogenisation approach published by Hsiao and Kikuchi [131], simulation models were also implemented by Peng and Cao [132] and Yu et al. [133]. The homogenisation technique aims to take into account the microstructure of the composite, e.g. fibre volume fraction, in the determination of macroscopic properties. Typically, this principle determines properties at large scales based on calculations performed on smaller scales [124].

Non-orthogonal methods were also implemented in ABAQUS. Xue et al. [134] and Harrison et al. [135] proposed models in which input parameters were determined by fitting experimental results. To overcome scattering issues caused by material characterisation, Harrison et al. developed a virtual testing tool able to depict, via a multi-scale energy approach, the intra-ply shear behaviour of fibre-reinforced textile thermoplastic composite materials [124]. In a subsequent study, Harrison et al. used this virtual testing approach to feed FE simulations [135]. In particular, the authors coupled it to a “stress power model” and applied it to the forming simulation of cross-plyed thermoplastic laminates [25]. Blanks were meshed with “mixed” elements composed of membranes and trusses. The “stress power model” was applied to membrane elements. Although encouraging results such as the prediction of intra-ply shear angle distributions were reported, the simulation was not able to simulate out-of-plane wrinkles because of the membrane type of elements.

ABAQUS supplies several friction models for isotropic interactions. They can be based on a Coulomb law or exhibit speed, pressure and temperature dependencies. Regarding anisotropic interactions, ABAQUS/Explicit does not have any built-in model. However, anisotropic friction models can be developed and implemented into customised subroutines [136].

Researchers from LaMCoS published so-called hyperelastic and hypoelastic approaches for the 3D simulation of forming processes. While the former is derived from potential energy, the latter relates an objective derivative of the Cauchy stress tensor to strain rate and constitutive tensors [35, 111, 137, 138]. Both approaches were implemented in ABAQUS/Explicit and validated with a dry unbalanced twill material (hyperelastic) and a commingled glass/polypropylene plain weave (hypoelastic) [139]. The hyperelastic approach was further extended to 3D-interlock reinforcements [140] and, more recently, to thermoplastic prepreg composite materials [141, 142]. Guzman-Maldonado et al. proposed a viscous-hyperelastic approach which assumes all mechanical properties to be uncoupled. Only intra-ply shear properties are considered viscoelastic. The model was implemented in PlasFib, which is a commercial software developed at LaMCoS. Results showed the approach to be able, using explicit dynamic computations, to depict proper non-linear viscoelastic behaviour of a five layers layup composite material composed of 8-HS glass/PA66 thermoplastic prepreg fabrics [141]. In a further study, this model was coupled to thermal computations to account for temperature variations during forming processes. Thermoforming simulations of an automotive component demonstrated the predictive capabilities of the tool [142].

Ten Thije et al. developed an innovative approach based on an updated Lagrangian FEM [143]. The application of their simulation model to materials of arbitrary degrees of anisotropy and deformations demonstrated to be robust and efficient. In a subsequent study, ten Thije and Akkerman developed a multi-layer triangular membrane element for the simulation of composite forming processes [144]. They showed the new element type to be able to predict the level at which out-of-plane wrinkles occurs.



However, due to the lack of bending stiffness in membrane elements, simulation results could not well predict the actual appearance of wrinkles. In a further release of the software, Haanappel et al. modelled the composite plies with an enhanced version of the multi-layer triangular element proposed by ten Thije and Akkerman [63, 66]. Each ply was represented by a layer of 2.5D three-node triangular elements consisting of a membrane element and a Discrete Kirchhoff Triangle (DKT). While in-plane properties, e.g. intra-ply shear, were managed by the membrane element, out-of-plane bending behaviour was described by the DKT. Forming simulations of a generic aerospace component with quasi-isotropic laminates composed of unidirectional UD-CF/PEEK plies, on the one hand, and woven 8-HS/PPS plies, on the other hand, led to satisfactory results. In particular, the intra-ply shear distribution proved to be in good agreement with experimental observations.

While in-plane properties, e.g. intra-ply shear, were managed by the membrane element, out-of-plane bending behaviour was described by the DKT. Forming simulations of a generic aerospace component with quasi-isotropic laminates composed of UD-CF/PEEK plies, on the one hand, and 8-HS/PPS plies, on the other hand, led to satisfactory results. In particular, the numerical intra-ply shear distribution proved to be in good agreement with experimental observations.

These studies, amongst others, contributed to the development of the AniForm simulation tool. Since 2014, this commercial software is available as AniForm Suite, which comprises a graphical interface for pre- and post-processing (AniForm PrePost) as well as an implicit FE solver dedicated to the 3D simulation of composite forming processes (AniForm Core). Ever since, the software is increasingly used by academics [59, 145] and undergoes adoption in automotive and aerospace industries.

The AniForm simulation tool offers the possibility to combine different constitutive laws and friction types to model specific material and interaction behaviour, respectively [146]. For example, Larberg and Akermo [24, 59] used a reinforced Kelvin-Voigt formulation model to depict intra-ply shear rigidity and a linear elastic model to represent in-plane tension. Regarding contacts, a combination of penalty Coulomb friction, viscous friction and adhesion was applied. The possibility for the user to combine different constitutive models, or friction types, enable the accurate modelling of complex behaviour. The investigations performed by Larberg and Akermo showed the ability of the software to predict intra-ply shear deformations of multi-ply layups composed of unidirectional thermoset prepreg composites when no fibre slippage occurs. In a recent study, Sjölander et al. used a similar formulation as Larberg and Akermo, with the exception that they include out-of-plane bending deformations in their analyses [145]. Out-of-plane bending was modelled by an orthotropic elastic model in order to account for different rigidities along and transverse to the fibre directions. The simulation of the forming process over a generic aerospace tool enabled the investigation of wrinkles development within multi-layer layups composed of unidirectional prepreg composites.

### 3.2.2 Mesoscopic Finite Element approaches

A major concern of mesoscopic simulations, i.e. analyses performed at the scale of yarns, lies in the selection of the type of finite elements. A compromise must be made between the level of detail and the computational cost. Depending on the application, woven and NCF reinforcements were discretised by 1D, 2D or 3D elements or a combination of these [139, 147, 148].

Mesoscopic simulations performed on elementary cells, i.e. representative parts of material internal structure, aim to investigate inter-yarn behaviour under different loading conditions, i.e. intra-ply shear, and determine corresponding mechanical and, for dry material, permeability properties. [35, 36, 111]

The development of mesoscopic simulation models requires the determination of specific properties, such as yarn/yarn friction. Yarn geometry and weave architecture must also be accurately characterised. The numerical representation of the internal material structure can be either generated from dedicated software, e.g. TexGen, or built from X-ray micro-computed tomography [111]. Most of constitutive laws have been implemented in ABAQUS [149] and LS-DYNA [147]. An application in PAM-CRASH [148] is also to be reported.

Cherouat and Billoët presented a mesoscopic model dedicated to the simulation of thermoset prepreg woven fabrics [149]. Their model accounted for both non-linear elastic fibre behaviour and viscoelastic matrix behaviour via a so-called “bi-component” element composed of two orthogonal trusses and a membrane element. The simulation model was validated by several bias-extension tests and deep-drawing experiments. The latter tests were performed for glass and carbon fibre fabric prepreg composites. Simulation results showed to be in good agreement with experimental observations, e.g. out-of-plane wrinkles.

### 3.2.3 Semi-discrete Finite Element approach

The semi-discrete Finite Element approach is an intermediate approach between macroscopic and mesoscopic methods and is dedicated to the simulation of textile composites. The model, which assumes no yarn slippage, is based on the principle of virtual work. For this approach, Hamila and Boisse introduced an innovative 3-node shell element composed of a set of unit cells. The approach requires the determination of in-plane tensile, intra-ply shear and out-of-plane bending rigidities. Based on experimental data, these are calibrated via virtual tests performed at the mesoscale. The constitutive model considers mechanical properties uncoupled and do not impose fibres to be aligned with element side lengths. The semi-discrete approach is nowadays commercially available via the FE software PlasFib. [35, 36, 150]

Semi-discrete simulations of molten fibre-reinforced thermoplastic materials have been performed over the last years [53, 151]. For example, Wang et al. simulated the punch forming of a multi-layer layup composed of 5-HS/PEEK prepreg composites [151]. Temperature-dependent material parameters were taken into account. Tool/ply and ply/ply interactions were managed by a viscous friction law. Results showed the ability of the simulation to predict temperature distributions within the composite stack and locations where out-of-plane wrinkles occur.

### 3.2.4 Microscopic Finite Element approach

Microscopic simulations are developed at the scale of the fibres [113, 152]. Although this type of simulations can supply important information about fibre rearrangements, especially under the combination of loads, these are rarely used because of their computational cost, on the one hand, and the difficulty to determine proper input parameters, e.g. characterisation of fibre/fibre contact behaviour.

Durville developed a microscopic model for plain weaves [113]. Based on an enhanced 3D beam formulation, the model showed to be able to consider planar cross-section variations. Computations were conducted with an implicit algorithm including three embedded loops accounting for non-linearities. Simulation output demonstrated the stability of the model and its ability to account for large deformations.

To the author's best knowledge, no full scale microscopic FE simulations of neither dry nor prepreg composite materials has been performed. Because of their computational cost, these are rather restrained to parts of reinforcements [111].

## 3.3 Selected approach

### 3.3.1 Motivation and goals

The approach considered for the simulation of thermoforming processes in the scope of this doctoral dissertation is selected based on the requirements set by the project funding this work, on the one hand, and the strategy of the *Chair of Carbon Composites* of the *Technical University of Munich*, on the other hand. Requirements are listed as follows:

- Development of 3D FE macroscopic simulation models,
- Selection of a commercially available software with dedicated support,
- Constitutive laws suitable for the modelling of molten unidirectional fibre-reinforced thermoplastic composite material must be “built-in” models,
- Pre- and post-processing must be accessible via graphical interfaces.

Because of their ability to account for all aspects of thermoforming processes, e.g. mechanical behaviour of materials, temperatures, pressures, etc., FE methods are preferred to kinematic ones.

The selection of macroscopic approaches is favoured over mesoscopic and microscopic ones because this work aims to simulate the complete thermoforming process of tailored thermoplastic composite blanks in order to predict the occurrence of potential defects, e.g. out-of-plane wrinkles. Continuum methods are found to be better candidates since they can be applied to large models and deliver, with regard to the objectives of this work, sufficient level of detail at reasonable computational effort.

Given that the results of this work aim to be implemented in an industrial environment, a commercial tool with suitable “built-in” material models and available support has to be considered. Three software correspond to the aforementioned requirements:

- ABAQUS (Dassault Systèmes Simulia),
- AniForm simulation tool (AniForm Engineering),
- PAM-FORM (ESI Group).

The software ABAQUS cannot be selected because its “built-in” material model FABRIC is only suited for fabric-reinforced thermoplastic composite materials. Because of their different deformation mechanisms, e.g. intra-ply shear, material model dedicated to fabric materials cannot be applied to unidirectional ones.

When this work started in 2013, AniForm simulation tool only consisted of a solver, i.e. AniForm Core. As graphical pre- and post-processing interfaces (AniForm Pre-Post) were not released at that time, the software was not eligible for this work.

The software selected in the scope of this work is PAM-FORM. The visual-based version Visual-FORM was favoured over the stand alone version PAM-FORM 2G because, ultimately, all ESI software will be transferred into this environment [153]. Besides, the Visual-Environment enables rapid and efficient data transfer for subsequent simulations [154]. Last but not least, one of the main advantages of Visual-FORM over PAM-FORM 2G is that the input file sent to the solver is an ASCII file, which can be edited by text editors, e.g. Notepad ++. Modifications are thus more efficient since the model does not have to be loaded into Visual-FORM. Simulation results presented in this doctoral dissertation are computed with solvers v.2012.0 and v.2013.0.

### 3.3.2 Software description

Most of the content of this section, including text and figures, is based on [P3].

The constitutive model of PAM-FORM dedicated to fibre-reinforced materials is composed of a thermo-visco-elastic matrix and elastic fibres. This material model, referred to as MAT 140, can only be applied to four-node shell elements. The constitutive law consists of three elements in parallel (see Fig. 3-3):

- A stabilising elastic “parent sheet”,
- A thermo-visco-elastic matrix component,
- Linear elastic springs.

The “parent sheet” behaves like an elastic material model dependent on the longitudinal shear modulus  $G$  and the Poisson’s ratio  $\nu$ . The “parent sheet” is also used to stabilise the behaviour of shell elements. The shear modulus can be defined either by a constant or a user-defined curve. For bidirectional materials, a locking angle  $\alpha_{lock}$  and a shear modulus to be considered once the locking angle has been reached  $G_{lock}$  can be selected. [155]

To avoid spurious stresses due to tensile and intra-ply shear behaviour coupling, the parent sheet was uncoupled from tensile properties.

The matrix is considered as a thermo-visco-elastic component. It is represented by a Maxwell element, i.e. a spring and a dashpot in series. The behaviour of this component is controlled by the largest tensile modulus ( $E_1$  or  $E_2$ ) and the viscosity  $\eta$ . Viscosity can be modelled as either a constant value or a Cross equation or a power-law equation. [155]

Linear springs  $E_1$  and  $E_2$  are the last component of MAT 140. These aim to depict material tensile behaviour. In the case of bidirectional reinforcements,  $E_1$  and  $E_2$  correspond to the mechanical behaviour of both family of fibres. For unidirectional fibre-reinforced materials,  $E_1$  represent the contribution of the fibres, while  $E_2$  corresponds to the transverse behaviour. Each tensile modulus property can be defined either by a constant value or a user-defined curve. [155]

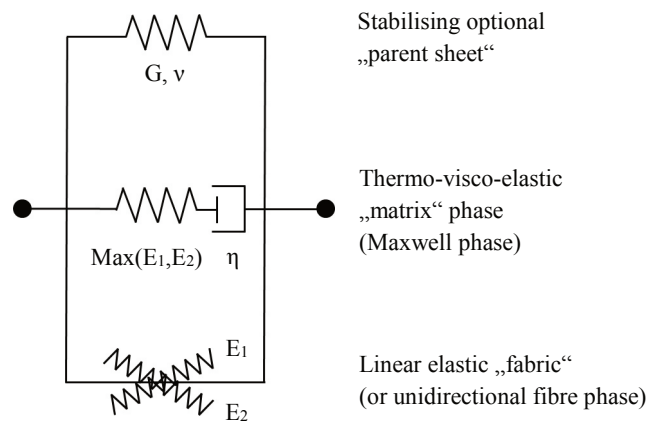


**Fig. 3-3: “Bi-phase” material model for fibre-reinforced materials (adapted from [155])**

The material model MAT 140 is composed of a stabilising parent sheet, a thermo-visco-elastic matrix and linear elastic springs representing the fibres.

To ease bending calibration and avoid coupling effects, longitudinal and transverse out-of-plane bending properties ( $B_1$  and  $B_2$ ) have been uncoupled from their respective tensile behaviour ( $E_1$  and  $E_2$ ). However, since out-of-plane bending properties are not coupled to the Maxwell element, these can only depict linear elastic behaviour. Bending properties cannot be defined by user-defined curves. Therefore, each bending property is defined by a constant value, referred to as bending modulus. [155]

In this simulation model, material viscous behaviour is managed by the viscosity  $\eta$ , which is a particularity of PAM-FORM. Other software, e.g. AniForm simulation tool, account for material viscous behaviour via input data, i.e. stress-strain, entered for different strain rates. In MAT 140, given that data can be entered for a single test speed only, i.e. strain rate, material viscous behaviour is managed via the consideration of a parameter representing composite viscosity.

The user has the possibility, via  $\alpha_1$  and  $\alpha_2$ , to select the original orientation of the first and second directions, respectively. In the scope of this work,  $\alpha_1$  was, as a convention, set to  $0^\circ$  since it corresponds to the orientation of the reinforcement. Since the second direction remains perpendicular to fibre orientations,  $\alpha_2$  was set to  $90^\circ$ . [155]

To account for specific behaviour of unidirectional and bidirectional composite materials, MAT 140 offers the possibility, via the parameter *RFLAG*, to specify whether the material model is unidirectional or bidirectional. As detailed in Chapter 2.2, both materials have different deformation mechanisms, especially in terms of intra-ply shear. Intra-ply shear of unidirectional materials can be seen as an inter-fibre sliding behaviour while this of bidirectional materials is related to a scissoring effect [109]. In the scope of this work, the unidirectional approach is considered, i.e. *RFLAG*=0. [156]

In PAM-FORM several other types of material models exist. For example, constitutive laws such as MAT 100 and MAT 101 can be selected for the modelling of isotropic materials, e.g. tooling. The only mechanical properties required for their implementation is a tensile modulus, a Poisson's ratio and a density. [157]

Different types of integration rules can be selected for shell elements [156]. These can be selected under *ISINT* and are summarised as follows:

- Belytschko-Tsay: uniform under integration rule (one integration point),
- Fully integrated Belytschko-Tsay (or Hughes-Tezduyar): full integration rule (four integration points), about 2.5 times more computational intensive than the default Belytschko-Tsay rule,
- Belytschko-Wong-Chiang: uniform under integration with anti-warping term rule (one integration point),
- Fully integrated Belytschko-Wong-Chiang: full integration with anti-warping term rule (four integration points), about 3.5 to 4 times more computational intensive than the default Belytschko-Wong-Chiang rule.

In the scope of this work, computations are performed with the default Belytschko-Tsay integration rule. Other options, such as hourglass prevention *ISHG* and internal damping  $\zeta$ , can also be selected [156].

Interactions between shell elements in thermoforming simulations are controlled by “contact cards” [157]. These are master-slave relations governed, for example, by:

- A symmetric node-to-segment with edge treatment algorithm,
- A non-symmetric node-to-segment with edge treatment algorithm,
- A self-impacting node-to-segment with edge treatment algorithm,
- A node-to-segment with smooth contact surface algorithm.

To each of these algorithms, several different types of contact models can be applied. Most of them, such as a Coulomb friction law or friction with pressure and/or velocity dependencies, are unfortunately restricted to isotropic contacts. Even user-defined contact models are restricted to isotropic contacts. For anisotropic contacts, PAM-FORM suggests two orthotropic Coulomb friction laws. While the first one enables the definitions of arbitrary directions, the second one considers the element side lengths as first and second directions. Since fibre orientations are initially oriented along element edges, the latter model is considered in the scope of this work. Interactions in PAM-FORM can only be modelled via constant friction parameters *FRICT*. For orthotropic contacts, one friction parameter per direction can be selected. [157]

A new version of PAM-FORM was released in 2015. Because this doctoral dissertation started in 2013, this version is not considered in this work. The new material card MAT 140 is a complete revision of the former model. In particular, all mechanical properties can now be selected in look-up tables. These are multi-curve editors which enable tensile, out-of-plane bending and intra-ply shear properties, i.e.  $E_1$ ,  $E_2$ ,  $B_1$ ,  $B_2$  and  $G$ , to be dependent on multiple parameters, such as strain rate for  $E_1$ ,  $E_2$  and  $G$  and curvatures for  $B_1$ ,  $B_2$ . Besides, to account for temperature variations in non-isothermal process simulations, all mechanical properties entered in look-up tables can be entered with temperature dependencies. As another noticeable effect, tensile and intra-ply shear behaviour have been totally uncoupled. Since the concept of “parent sheet” no longer exists, the Poisson’s ratio was deleted from the material model. [158]





## 4 Material characterisation

Material characterisation refers to the investigation of material behaviour and aim, in the field of FE modelling, to determine input for constitutive models. Given that simulation quality is mainly governed by the accuracy of the input parameters [66, 97], such investigations are essential in the development of FE models.

Material characterisation for FE thermoforming simulation is a twofold challenge: on the one hand, no test standard exists and, on the other hand, tests have to be conducted, to the best extent possible, under similar environmental conditions as forming occurs. In the present case, robust test methods able to characterise thermoplastic composites in their molten states have therefore to be developed.

Because of simulation considerations, both the unidirectional thermoplastic composite tape and the separation film considered for thermoforming experiments are characterised under environmental forming conditions. Investigations, which comprise the development of new test methods and the determination of material behaviour, are presented in the first and second parts of this chapter, respectively. The third section is dedicated to the characterisation of several contact properties. These are also conducted, to the best extent possible, under similar environmental conditions as forming occurs. To assess whether the test methods considered for molten thermoplastic materials are applicable to the characterisation of non-cured thermoset prepregs, a unidirectional thermoset composite tape is subsequently characterised under environmental forming conditions. Discussions about material characterisation test results and the presented test methods are finally held.

### 4.1 Characterisation of a unidirectional thermoplastic composite material

Based on material model requirements (see Chapter 3.3.2), intra-ply shear, longitudinal and transverse out-of-plane bending, longitudinal and transverse tensile and viscosity properties have to be characterised. Because MAT 140 does not account for in-plane compression and compaction, these deformation modes are not investigated. Characterisation analyses are conducted under forming temperature, i.e. 280°C (see Chapter 6.1.1), with the UD-CF/PA6 material presented in Tab. 1-1. Given that manufacturing processes are conducted at prescribed test speeds, experiments should also be conducted at constant test speeds. For simulation purposes, experimental results are thus expected as stress-strain curves for different test speeds, i.e. strain rates.

Most of the content of this part, including text and figures, is based on the final report supplied to one of the funding bodies of this work [159].

## 4.1.1 Intra-ply shear

Although unidirectional composite materials have two different intra-ply shear deformation modes (see Chapter 2.2.1), upon the requirements of the constitutive model (see Chapter 3.3.2), only longitudinal intra-ply shear behaviour is investigated.

### 4.1.1.1 Literature review

An exhaustive review of the state-of-the-art test methods applied to the characterisation of longitudinal intra-ply shear behaviour of unidirectional composite materials has been recently proposed by Haanappel and Akkerman [62, 66]. Hörmann subsequently completed it by adding Haanappel and Akkerman test method [160].

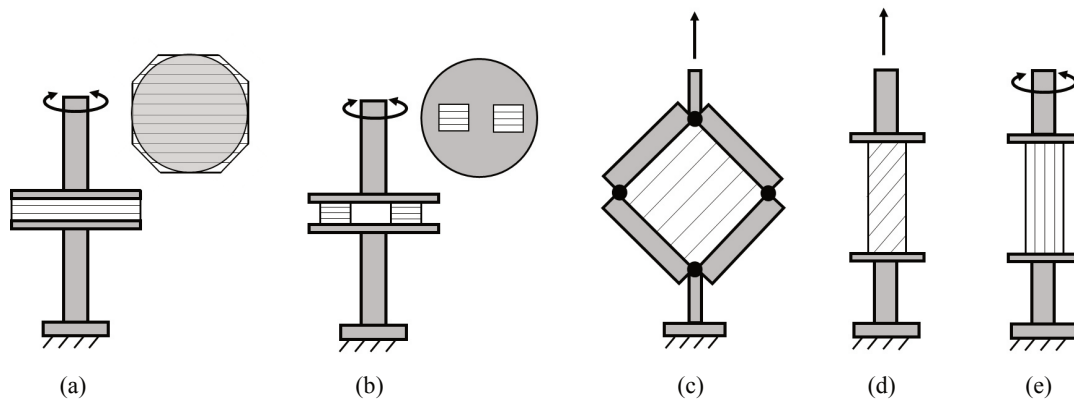


**Fig. 4-1: Schematic of state-of-the-art test methods for longitudinal intra-ply shear characterisation (adapted from [62] and [160])**

(a) and (b): Rotational parallel platens test method; (c): Picture-frame test setup, (d): Off-axis tension test setup; (e): Torsion bar test method.

In the 1990s, Groves presented different approaches to characterise intra-ply shear deformations of molten fibre-reinforced thermoplastic composites using a rotational rheometer. Specimens were positioned between two parallel platens and tested by means of torsion. In a first study [161], the platens were fully covered by either a unidirectional or a cross-ply laminate (see Fig. 4-1 a). Experimental results showed both arrangements to behave similarly. Subsequently, instead of covering whole platens, balanced pair of off-axis specimens were used to account for material anisotropy (see Fig. 4-1 b) [162]. With this configuration, Groves was able to investigate both longitudinal and transverse intra-ply shear behaviour based on the theory of Rogers [61]. Results, which were analysed using dynamic Maxwell parameters, highlighted the transverse Maxwell viscosity to be slightly higher than the longitudinal one for two different fibre-reinforced thermoplastic systems [162].

McGuinness and Ó Brádaigh developed a picture-frame test setup (see Fig. 4-1 c) [60]. This test apparatus, also referred to as “rhombus-shear”, is composed of four rigid bars used to clamp the specimen. While top and bottom points are connected to a universal testing machine, left and right ones can rotate within the plane of deformations. Based on this principle, when the top connection is pulled upwards, the initially square specimen deforms into a diamond shape. Experiments were performed with unidirectional CF/PEEK (APC-2) specimens. Because of material failure near attachment locations, tests had to be eventually carried out with unidirectional CF/PEEK (APC-2) specimens enclosed between two polymeric membranes. The influence of the membranes made, however, proper characterisation difficult. Further studies using cross-plyed specimens held between diaphragms were also conducted. Although encouraging results were obtained, cross-plyed specimens did not allow the derivation of convenient data for single plies. Under similar conditions of shear strain and shear rates, cross-plyed responses were about 25% larger than corresponding unidirectional experiments. This difference was assumed to be caused by some inter-ply movement.

Haanappel and Akkerman also reported picture-frame tests of unidirectional CF/PEEK specimens [62]. Specimens showed to be subjected to fibre tensioning because of small misalignments, which resulted in ply splitting. Similar observations were made from off-axis tests referred to as bias-extension tests (see Fig. 4-1 d). Because of low specimen integrity, strain localisation and fibre buckling occurred. Bias-extension tests performed on either single ply or cross-plyed non-cured thermoset prepreg materials delivered, however, satisfactory results [65, 163, 164].

More recently, Haanappel and Akkerman proposed a new test method to characterise longitudinal intra-ply shear properties of unidirectional fibre-reinforced thermoplastic composite materials (see Fig. 4-1 e) [62, 66]. This test method, referred to as “torsion bar test method”, consists on twisting a prismatic bar of rectangular cross-section. Specimens are clamped at room temperature in a rotational rheometer and tested dynamically under environmental forming conditions. Besides the presentation of a new test method, Haanappel and Akkerman also proposed a procedure for post-processing analyses. The authors applied a finite difference scheme introduced by Schwarzl et al. [165] and Schwarzl [166] to approximate the longitudinal intra-ply shear relaxation modulus. Material longitudinal intra-ply shear behaviour was subsequently determined by applying the theory of linear-viscoelasticity (LVE). Results were eventually presented as stress-strain curves for different shear rates. Although tests could only be conducted within material LVE region, the presented test method demonstrated good potential to become a standard in the characterisation of intra-ply shear properties of unidirectional CFRTP composites because of (i) simple specimen preparation, (ii) good reproducibility and (iii) tool availability.

### 4.1.1.2 Picture frame test setup

The experimental results presented in this section have been generated by S. Bel at the *Chair of Carbon Composites* of the *Technical University of Munich*.

#### Experimental method

First experiments to characterise longitudinal intra-ply shear behaviour of the UD-CF/PA6 material considered in the scope of this doctoral dissertation (see Tab. 1-1) are performed with the picture frame test setup of the TUM-LCC. The tool is composed of four rigid bars connected with ceramic bearings in order to minimise friction while testing [128]. The picture frame test setup is mounted in a universal testing machine and enclosed within an environmental chamber (see Fig. 4-2).

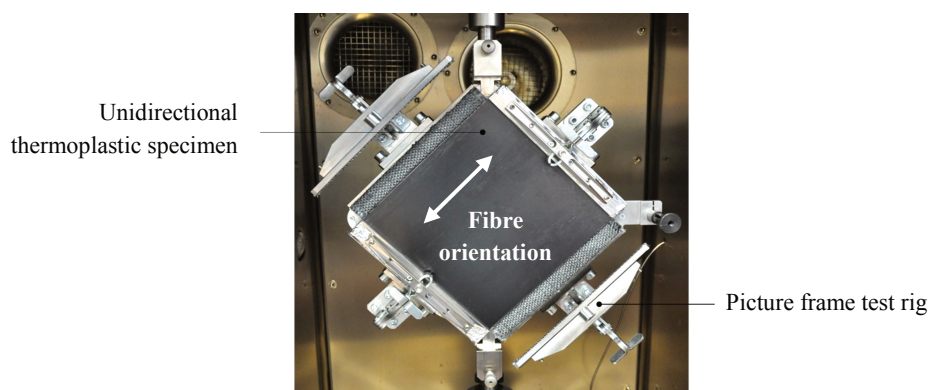


**Fig. 4-2:** Picture frame test setup enclosed within an environmental chamber and mounted in a universal testing machine [adapted from S.Bel]

Specimens are prepared from unidirectional plates of 1 mm thickness, brought into the frame at room temperature and tested at 280°C. A proper positioning is achieved when fibres are parallel to their respective side lengths. Given the lack of reinforcement in one direction, specimens are only clamped on two sides (these perpendicular to fibre direction). Once clamped, specimens have a free area of 200 x 200 mm<sup>2</sup>. Experiments are performed at a test speed of 50 mm/min.

#### Results

Because of the early occurrence of out-of-plane wrinkles (after about 10° of shear), picture frame test results cannot be used for characterisation purposes (see Fig. 4-3).

The onset of out-of-plane wrinkles is to be imputed to clamping. To enable the material to accommodate intra-ply shear deformations, fibres should have the possibility to rotate at their contact points with the frame [60]. In the present case, fibres cannot rotate. Because of clamping, these are forced to bend, which introduces tension. The combination of fibre stretching and weak transverse material behaviour leads to the occurrence of out-of-plane wrinkles. Specimen failure such as ply tearing was, however, not observed.

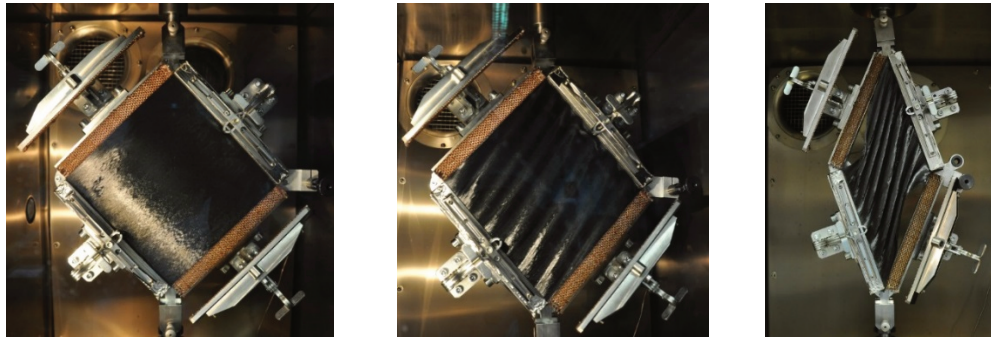


**Fig. 4-3:** Typical picture frame test results of a molten unidirectional fibre-reinforced thermoplastic composite material tested at 280°C [S. Bel]  
Left: Initial position; Middle: Wrinkles onset (20 mm displacement); Right: Final state.

#### 4.1.1.3 Development of a new test method using a rheometer

Given that picture frame test results cannot be regarded to characterise material intraply shear behaviour, an alternative test method using a rotational rheometer in a parallel platens configuration is considered. This approach, which has been originally applied to non-cured unidirectional thermoset pre-impregnated composite materials, has been developed in collaboration with Hörmann and published in [K7, K8, 160].

#### Experimental method

This innovative test method considers (i) the method of Rogers for the determination of storage and loss shear moduli from dynamic (oscillatory) experiments conducted with a rotational rheometer [61] and (ii) Haanappel and Akkerman post-processing method to convert results from frequency into time domain [62, 66]. Further details are given in Appendix b.

Experiments are conducted within an environmental chamber mounted on a rotational rheometer (MCR 302, Anton Paar). Based on machine supplier information, normal forces comprised between 0.005 and 50 N can be applied with a resolution 0.5 mN. Oscillatory experiments can be conducted up to a frequency of 100 Hz. [167]

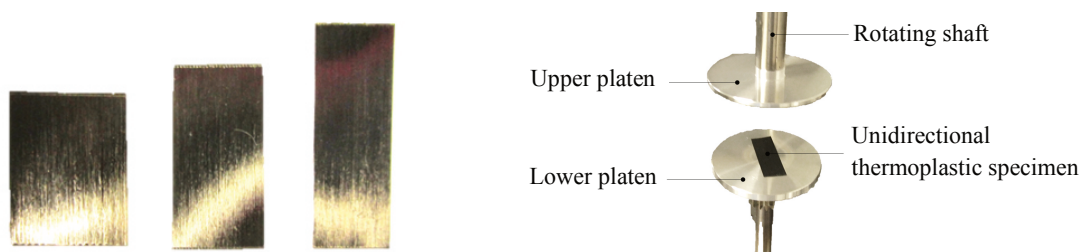


**Fig. 4-4:** (Left) Specimens of rectangular cross-section (from left to right: 20 x 15, 25 x 12 and 30 x 10 mm<sup>2</sup>, where the first value gives the dimension in fibre direction); (Right) Specimen positioned between two disposable circular platens

According to the method introduced in Appendix b, specimens of different aspect ratio are prepared (see Fig. 4-4 left). To prevent measurement inaccuracies caused by thermal expansion, the machine is tared once a homogeneous temperature distribution is reached. The specimen is subsequently placed onto the lower platen. A good positioning is achieved when the specimen is centred with the axis of rotation of the shaft (see Fig. 4-4 right). In the scope of this work, disposable circular platens of 50 mm diameter are used. Experiments are performed with flowing nitrogen to prevent material degradation [81].

## Results

Because of inconsistent test results, Digital Image Correlation (DIC) is used to investigate the quality of the disposable platens. Measurements are conducted with two cameras of 4 MP each and analysed with the software Aramis<sup>®</sup> supplied by GOM. Images, which have a resolution of about 47 pixels per millimetre, are treated over a diameter of 40 mm to avoid inaccuracies caused by edge effects.

Investigations using DIC demonstrated that both upper and lower circular disposable platens have significant thickness variations (see Fig. 4-5 left and Fig. 4-5 right, respectively). Because such irregularities introduce uneven shear distribution, the rotational parallel platens test setup cannot be considered to characterise the unidirectional thermoplastic composite material.

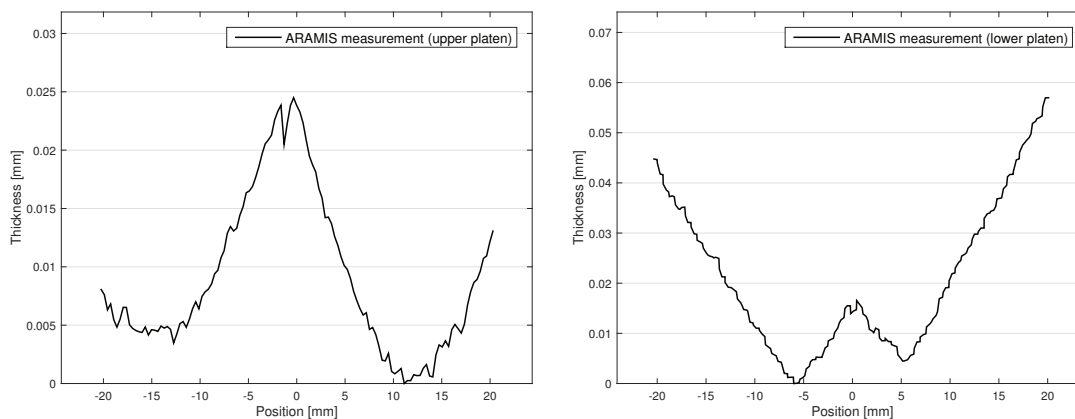


Fig. 4-5: Typical thickness variations of upper (left) and lower (right) disposable platens

### 4.1.1.4 Torsion bar test method

Given that previous test results cannot be used to characterise material intra-ply shear behaviour, a third approach is considered.

## Experimental method

The test method used for these investigations is similar to this described by Haanappel and Akkerman [62, 66]. Because the material investigated in the scope of this doctoral

dissertation is not available as plates of 11 mm thickness, experiments were performed with another UD-CF/PA6 prepreg material. The material, supplied by SGL Group, has very similar characteristics as this considered in this work and supplied by Celanese. For example, both materials have comparable fibre volume fraction (45% for the SGL material [168] against 48% for the Celanese material, see Tab. 1-1).

Investigations are conducted with the same rheometer as this presented in Chapter 4.1.1.3 (MCR 302, Anton Paar). In a similar manner, experiments are performed within an environmental chamber (see Fig. 4-6) with low flow of nitrogen in order to prevent material degradation [81]. As advised by Haanappel and Akkerman [62, 66], prismatic bars with rectangular cross-section are prepared. The dimensions of the specimens are 60 ( $L$ ) x 13 ( $W$ ) x 11 ( $T$ ) mm, where  $L$  is the dimension in fibre direction,  $W$  is the dimension transverse to the fibre direction and  $T$  is the thickness.

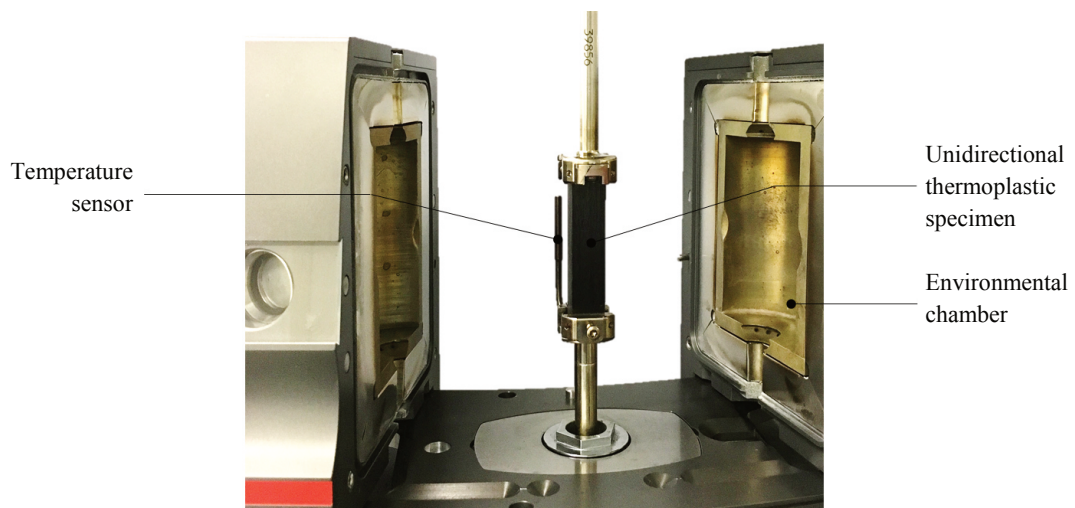


**Fig. 4-6: Unidirectional fibre-reinforced PA6 thermoplastic composite specimen enclosed within an environmental chamber and mounted on a rheometer**

To prevent issues caused by thermal expansion of the clamps, specimens are positioned while the environmental chamber is already at 280°C. A soaking of 10 minutes is observed before tightening the clamps to let the specimen accommodate with temperature. Experiments are started after another soaking time of 10 minutes to ensure homogenous temperature distribution. Proper soaking time is investigated with thermocouples positioned in the inner and outer sides of the specimens [S10].

Amplitude sweeps, i.e. variation of shear strain, are firstly performed to determine material LVE region. Frequency sweeps, i.e. variation of frequency, within material LVE region are secondly conducted. These results are eventually used within a finite difference scheme to approximate shear relaxation modulus.

## Results

The experimental results presented in this section have been generated in the context of the following Term Project [S10].

Amplitude sweeps are performed from  $10^{-4}\%$  to  $1\%$  of strain at three angular frequencies (1 rad/s, 10 rad/s and 100 rad/s). Results illustrated in Fig. 4-7 are the average values of the storage modulus calculated over five repetitions. Except for measurements performed at 1 rad/s below  $5 \cdot 10^{-4}\%$  of strain, an average error of 15% is to be reported.

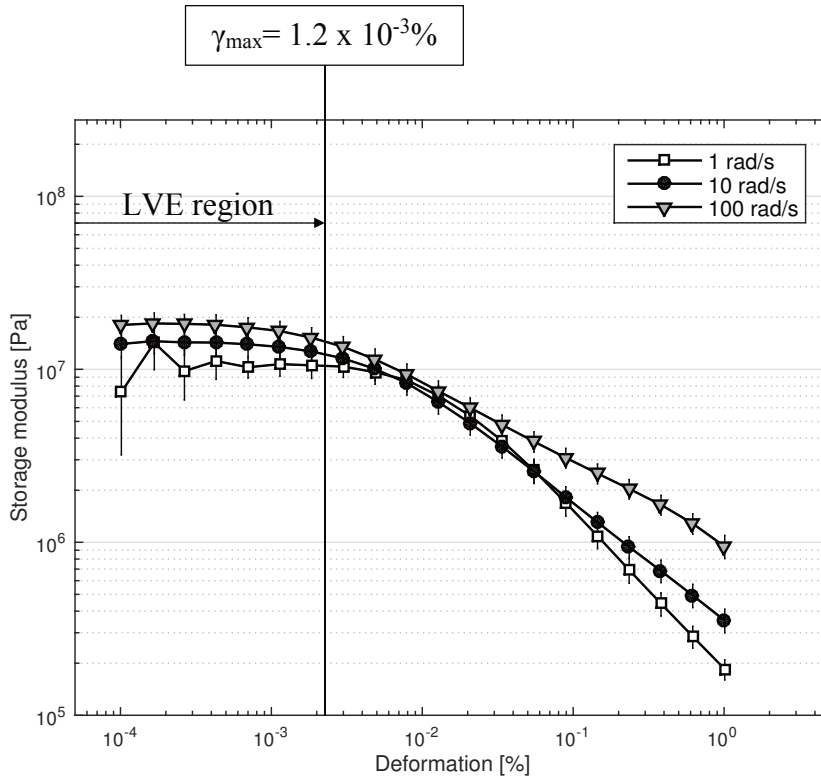


**Fig. 4-7:** Average amplitude sweep test results of molten UD-CF/PA6 specimens  
Investigations performed at 1 rad/s, 10 rad/s and 100 rad/s.

The LVE region ends when a dynamic viscoelastic function, e.g. storage modulus, deviates by maximum 10% from a constant value [169, 170]. The shear strain indicating the end of the LVE region  $\gamma_{max}$  is calculated for all angular frequencies. To be conservative, only the lowest value is eventually considered, i.e.  $1.2 \times 10^{-3}\%$  (see Fig. 4-7).

Once the limit of the LVE region is determined, frequency sweeps are carried out. To perform tests at the highest strain possible, experiments are performed at  $\gamma_{max}$ . Angular frequencies are varied from 0.1 rad/s to 500 rad/s. Results illustrated in Fig. 4-8 are the average values of the storage and loss moduli calculated over five repetitions. With an average error of 17.5% for the storage modulus and 19% for the loss moduli, an overall good reproducibility is to be reported.



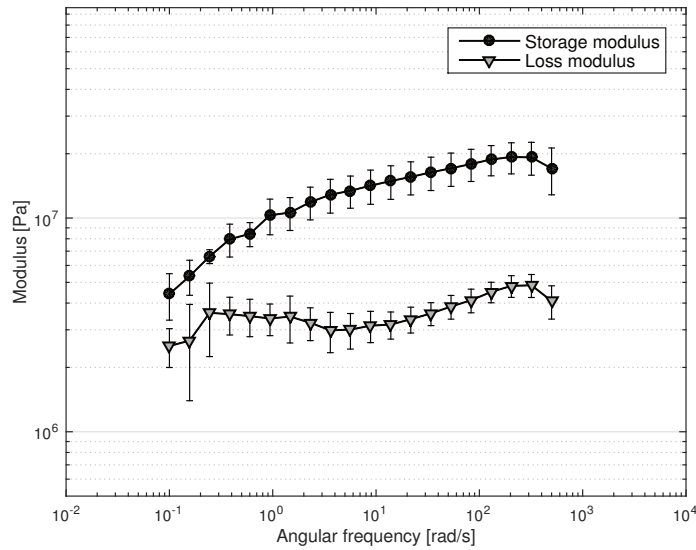


**Fig. 4-8:** Average frequency sweep test results of molten UD-CF/PA6 specimens  
Investigations performed at  $1.2 \times 10^{-3}\%$  of strain.

Following the method detailed in Appendix b and initially described by Haanappel and Akkerman [62, 66], frequency sweep results are subsequently used to determine the shear relaxation modulus  $G_r$  (see Fig. 4-9). To account for “true” material behaviour, loads caused by internal machine friction are subtracted from measurement data<sup>1</sup>. Also, to avoid boundary effects, measurements for both the lowest and highest angular frequencies are discarded. The longitudinal shear relaxation modulus is eventually calculated using the finite difference scheme introduced by Schwarzl et al. [165] and Schwarzl [166] (see equation (A-18) in Appendix b).

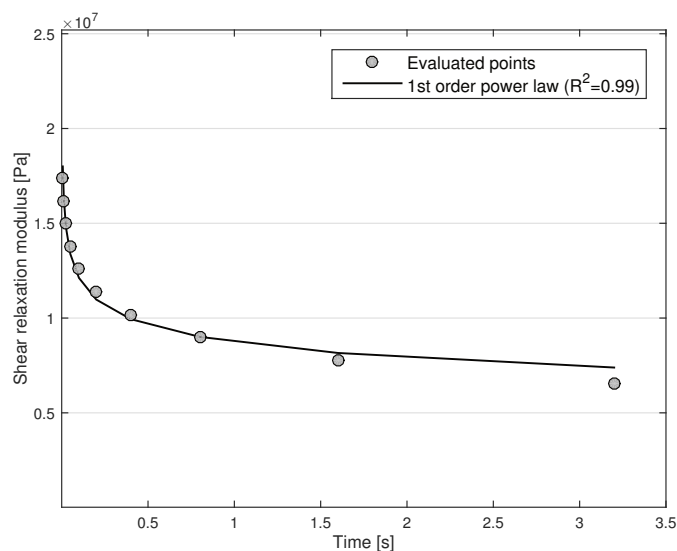


**Fig. 4-9:** Approximated shear relaxation modulus of a molten UD-CF/PA6 composite material

<sup>1</sup> Loads generated by internal machine friction are measured via “air sweeps”, which consist of frequency sweeps without specimen, i.e. in the air. These results are then subtracted from frequency sweep data.

Shear stresses are finally calculated according to equation (A-19) (see Appendix b). Results are presented in Fig. 4-10 for three different shear rates. The maximum shear rate is calculated using equation (A-20) (see Appendix b) with  $\gamma = \gamma_{\max}$  (end of the LVE region) and  $\omega = 320$  rad/s (sweeps are performed up to 500 rad/s but, to avoid boundary effects, first and last data are not taken into account).

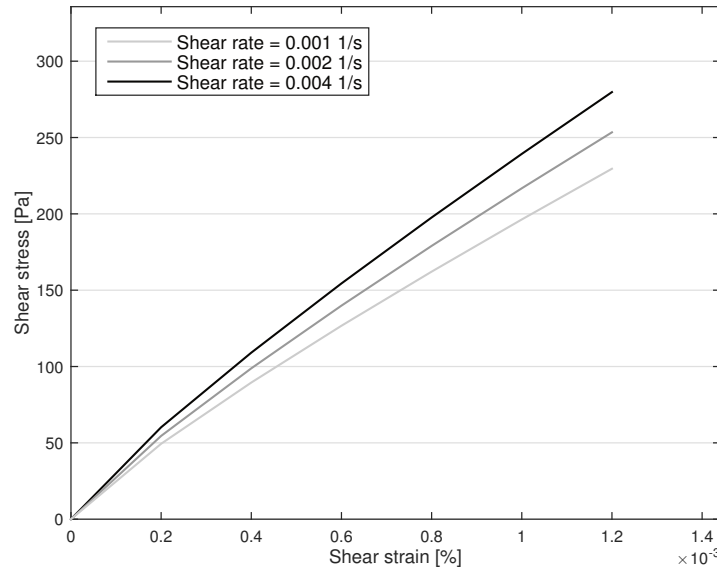


**Fig. 4-10:** Stress-strain response of a molten UD-CF/PA6 composite material subjected to longitudinal intra-ply shear deformations

Although a slight rate dependency is noticed, results highlight elastic dominated behaviour. Such observations are in good agreement with test results from Haanappel and Akkerman, who also tested a molten CF RTP composite material [62, 66].

## 4.1.2 Out-of-plane bending

Because of material orthotropy, on the one hand, and the possibility to implement two different out-of-plane bending parameters in MAT 140 (see Chapter 3.3.2), both longitudinal and transverse out-of-plane bending behaviour are investigated.

### 4.1.2.1 Longitudinal out-of-plane bending

Most of the content of this section, including text and figures, is based on [P2].

#### Literature review

Although some test methods developed at room temperature for dry reinforcements can easily be accommodated within environmental thermal chambers for pre-impregnated materials, e.g. picture frame/bias-extension tests [47, 54, 55], the adaptation of conventional bending test setups is more complicated. An overview of the main test methods developed to determine out-of-plane bending properties of dry reinforcement and pre-impregnated composites is presented in Tab. 4-1.

Tab. 4-1: Overview of the main test methods for out-of-plane bending characterisation

Ref.	Testing environment	Device	Load case	Material
Peirce et al. [171]	Room temperature	Cantilever test	Unique	-
Bilbao et al. [172]	Room temperature	Enhanced cantilever test	Multiple	Biaxial dry NCF
Liang et al. [83]	Up to 600°C	Cantilever test + thermal chamber	Multiple	5HS PEEK 5HS PPS Satin PA66
Soteropoulos et al. [173]	Room temperature	“Vertical” cantilever test	Multiple	0/90 glass fibre NCF
Lomov et al. [77]	Room temperature	Kawabata test	Multiple	Bi- and quadri-axial dry NCFs
Martin et al. [78]	Up to 170°C	Vee-bending test + thermal chamber	Multiple	UD glass fibre PP composite
University of Twente [174]	Up to 450°C	Rheometer + thermal chamber	Multiple	UD Carbon PEEK prepreg

Although various setups have been developed throughout the years, most of them are adapted from the cantilever test developed by Peirce [171]. In this test setup, a rectangular piece of material is laid on a support. The specimen is gradually pushed over an inclined plane. The test is over when the tip of the material comes into contact with the incline plane. Thanks to mechanical relationships, as well as the inherent properties of the specimen, the bending stiffness can be calculated. A variant of this test was proposed by Bilbao et al. in 2008 [172]. The device introduced by Bilbao et al. offers the main advantage to vary the load to which the specimen is subjected. To do so, the specimen is placed on top of a support composed of laths. By their removal, the overhang length of the specimen is subjected to gravity and thus bent under its own weight. As described by the authors, the test is a succession of quasistatic experiments with different load cases. The displacements of the specimen are successively recorded by a digital camera which enables to report the shape of the specimen. Until recently, all variants of cantilever tests were only suitable for tests performed at room temperature. In 2014, Liang et al. proposed an adaptation within an environmental thermal chamber [83]. Investigations proved the method to be applicable to the characterisation of thermoplastic composites through a control of the testing temperature. However, the usage of defined strain rates was not made possible since specimens were only subjected to gravity.

Soteropoulos et al. [37, 173] identified that the tips of the specimens tested with a cantilever setup are often twisted while bending due to non-linear loading effects. To evacuate this issue, Soteropoulos et al. designed a test in which specimens are hung vertically and thus aligned with gravity. In this setup, a load is attached to a string linked to the tip of the specimen. By using a digital camera and attaching different type of loads, the displacement of the specimen can be recorded and the bending stiffness determined. To the author's best knowledge, this method has not been applied under regulated environmental conditions yet. Other test setups, such as the Kawabata test, which are appropriate for the characterisation of out-of-plane bending properties at room temperature, have also never been used under regulated conditions [77]. In the middle of 1990s, Martin et al. proposed an innovative test method composed of a Vee-bending fixture mounted in a tensile testing machine and enclosed in a thermal chamber [78]. In a latter study, Dykes et al. proposed an enhanced version of this test setup. The new design of the fixture ensured constant shear deformation rates at the supports [79, 80]. However, the Vee-bending technique cannot be considered as a method used to characterise out-of-plane bending properties. In fact, the main goal of these analyses was to investigate the longitudinal and transverse viscosities of molten unidirectional thermoplastics. Therefore, bending tests were performed such that shear becomes the main deformation mode.

For the analysis of the bending behaviour of thermoplastic composites, a novel approach using a rheometer and a dedicated environmental chamber was suggested at the University of Twente [43, 66, 174]. The idea of the setup can be assimilated to a variant of the Kawabata test enclosed in a thermal chamber. The main difficulty of this method is to ensure pure bending. To describe a perfect circular path, the University of Twente developed customised clamps that do not hold tight the specimen. Sachs et al. explained that a good understanding of the boundary conditions and the deformation mechanisms is necessary to properly analyse the outcome of the tests [43].

Although test setups giving encouraging results were recently proposed, no method seems to be established for the characterisation of out-of-plane bending properties of unidirectional thermoplastic pre-impregnated composites in their molten configuration. A new approach using a DMA system is presented in the following section. This machine has the main advantage to offer a close control of the testing parameters, e.g. temperature and test speed. In this work, only standard test fixtures are considered in order to avoid complicated boundary conditions and ease the analysis of the testing outcomes.

## Development of a new test method using a DMA system

### *DMA system description*

The machine used in the scope of this work is a Q800 DMA system supplied by TA Instruments. A DMA system is a mechanical testing machine dedicated to fine measurements within a regulated environment. The Q800 enables analyses over an extended temperature range comprised between  $-145^{\circ}\text{C}$  and  $+600^{\circ}\text{C}$ . Heating rates from 0.1 up to  $20^{\circ}\text{C}/\text{min}$  can be applied. Under isothermal conditions, the temperature stability is claimed to be  $\pm 0.1^{\circ}\text{C}$  for experiments performed above  $50^{\circ}\text{C}$ . The machine can test samples of stiffness comprised between  $10^2$  and  $10^7$  N/m. [175]

Several different types of standard clamps can be adapted on the Q800 machine. Most common ones are these used to test in tension, compression and bending. Regarding standard bending test fixtures, single cantilever, double cantilever and three-point bending clamps are available. Although dynamic experiments are more often considered, both dynamic and quasistatic investigations can be performed with a DMA system [175, 176]. In the scope of this work, only quasistatic tests under isothermal conditions are considered and, while humidity of the test environment is not controlled, the moisture content is regulated by drying the specimens.

### *Specimen preparation*

Specimens are prepared from unidirectional plates of 1 mm thickness, which are prepared with the same material and the same method as this described in Chapter 1.1.

To ensure a homogeneous unidirectional fibre orientation, specimens are controlled using a ProFactor sensor [177]. This aspect is of particular importance because variations in the fibre orientation can lead to altered measurements. Specimens are prepared such that their side lengths are parallel to the fibre orientation (see Fig. 4-11). The dimensions of the specimens are  $25$  ( $L$ )  $\times$   $15$  ( $W$ )  $\times$   $1$  or  $2$  ( $T$ )  $\text{mm}^3$  where  $L$  is the dimension in fibre direction,  $W$  is the dimension transverse to the fibre direction and  $T$  is the thickness. Measurements of the specimen geometries are performed for every test with a  $1\ \mu\text{m}$  precision (see Tab. 4-2). All specimens are initially flat and considered as having uniform dimensions along their respective length and width and throughout their respective thickness.

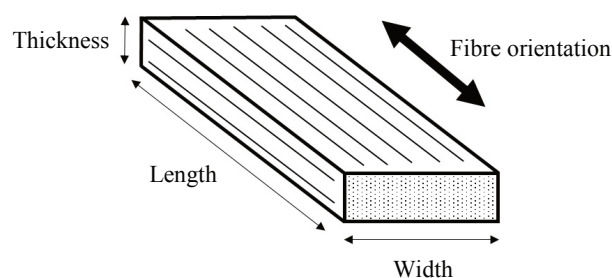


**Fig. 4-11:** Fibre orientation and geometry of specimens used for longitudinal bending tests

**Tab. 4-2: Average dimensions and standard deviations in millimetres of (a) the specimens used for preliminary investigations and (b) the specimens used for material characterisation**

	Single Cantilever	Double Cantilever	Three-point bending (20mm)	Three-point bending (50mm)
<b>Length [mm]</b>	(a) $17.621 \pm 0.130$	(a) $35 \pm 0$ (cantilever length)	(a) $20 \pm 0$ (b) $20 \pm 0$ (span length)	(a) $50 \pm 0$ (span length)
<b>Width [mm]</b>	(a) $14.851 \pm 0.106$	(a) $14.781 \pm 0.138$	(a) $14.759 \pm 0.266$ (b) $14.528 \pm 0.198$	(a) $14.857 \pm 0.112$
<b>Thickness [mm]</b>	(a) $0.966 \pm 0.085$ and (a) $1.957 \pm 0.041$	(a) $1.010 \pm 0.039$ and (a) $1.948 \pm 0.022$	(a) $1.016 \pm 0.035$ (b) $1.006 \pm 0.042$ and (a) $2.039 \pm 0.100$	(a) $1.944 \pm 0.112$

#### *Preliminary investigations*

Most of the content of this section, including text and figures, is based on [K3] and [S3].

Given that a DMA system offers different possibilities in the determination of out-of-plane bending properties, a screening of the different test methods is performed. Four standard test fixtures are evaluated: single cantilever, double cantilever, three-point bending 20 mm and three-point bending 50 mm. Tests are conducted for two specimen thicknesses (1 mm and 2 mm) at 200°C, 230°C and 260°C, i.e. far below, above, and far above melting temperature, respectively. For each configuration, three test speeds are applied: 10  $\mu\text{m}/\text{min}$ , 100  $\mu\text{m}/\text{min}$  and 500  $\mu\text{m}/\text{min}$ . [K3, S3]

The specimens are positioned in the machine at room temperature. The alignment of the sample is appropriate when the width of the specimens is parallel to the clamps/support. A good positioning is essential to avoid unsymmetrical loadings. Specimens mounted in different test fixtures are shown in Fig. 4-12.

Tests conducted with single- and double-cantilever fixtures are clamped at room temperature with a torque of 0.79 N.m (7 in.lb). Clamps are retightened using the same torque at 210°C (when applicable) to ensure a proper contact between the specimen and the tooling. Regarding three-point bending tests, a preload force of 0.001 N is applied. Specimens are then heated to testing temperature (200°C, 230°C or 260°C) at heating rates of 10 K/min and 20 K/min. Heating rates are found to have no noticeable effect on testing outcomes.

Flowing nitrogen is used to avoid polymer degradation [81]. For all four fixtures, the machine is forced to keep a neutral displacement while heating up in order not to alter the quality of the specimens.

To ensure a homogeneous temperature distribution within the specimen, tests are performed five minutes after isothermal conditions are reached. Finally, tests are executed with controlled displacement ramps, i.e. test speeds, over a displacement of 1500  $\mu\text{m}$ . Due to the stiffness limit of the machine, three-point bending tests of 50 mm span length cannot be conducted with specimens of 1 mm thickness.

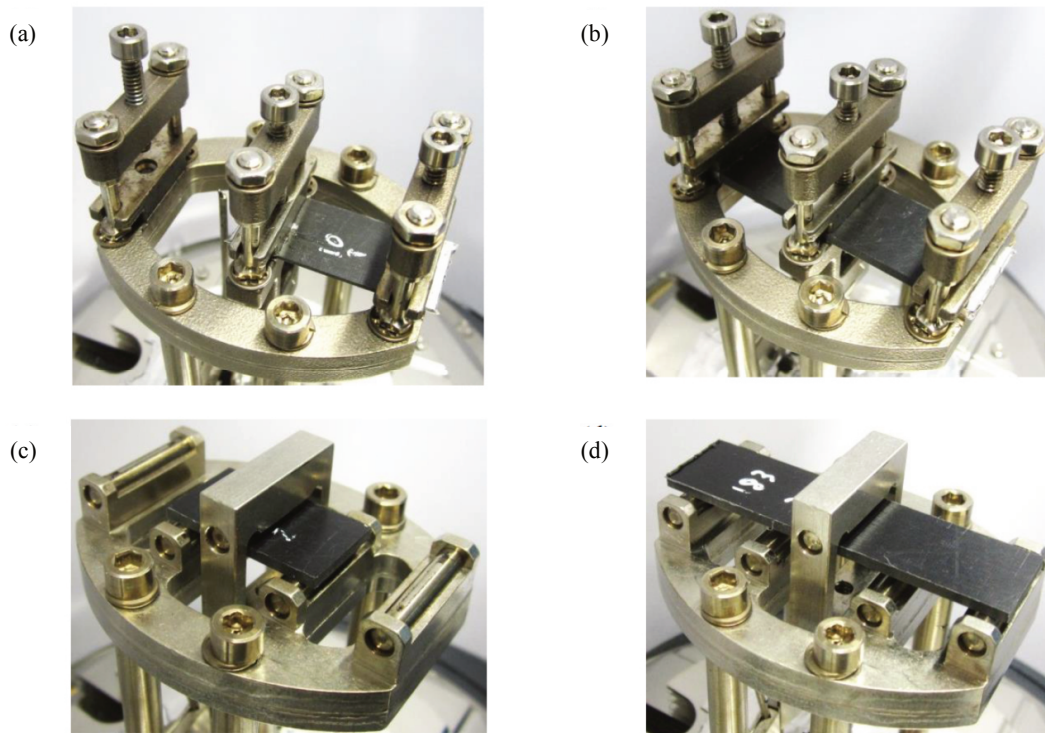


**Fig. 4-12:** Specimens mounted in different test fixtures: (a) Single cantilever; (b) Double cantilever; (c) Three-point bending (20 mm) and (d) Three-point bending (50 mm)

The outcome of the screening analysis is presented in Tab. 4-3. Both cantilever tests (single and double) are suitable for testing below melting temperature, i.e. 200°C, but not above, i.e. 230°C and 260°C. Both test fixtures appear to be unstable when composites are in their molten configuration. Their instability is caused by the lack of reactivity of the machine. The DMA system does not manage to take the phase transition of thermoplastics into account and simultaneously keep a neutral displacement. Relative displacements while heating up are caused by the interaction existing between the metallic fixtures of the DMA system and the thermoplastic specimen. Both have different coefficients of thermal expansions and therefore do not behave similarly when subjected to temperature variations.

To keep a neutral displacement while heating, the machine is forced to load the specimen. Because the transition between solid and molten states happens suddenly, the machine does not have enough time to adjust its parameters accordingly. As a consequence, when the melting temperature is reached, the sample is damaged due to the application of high forces. This issue can be overcome by forcing the machine to stay at an isothermal temperature below and close to melting temperature, e.g. 215°C, for a long period of time. Although this method gives satisfactory results, it is not suited for rapid testing. Besides, it is reported in the literature that the clamping of the cantilever tests has an undesirable effect on the experimental outcomes [178-180]. Therefore, cantilever tests are not selected for this work.

**Tab. 4-3: Outcome of screening investigations for longitudinal bending characterisation**

	Temperature [°C]	Cantilever (single and double)	Three-point bending (20mm)	Three-point bending (50mm)
<b>1 mm specimens</b>	200	Unstable above melting temperature	Selected method	Cannot be tested by DMA system
	230			
	260			
<b>2 mm specimens</b>	200	Interlaminar shear	Tooling limit	
	230			
	260			

On the other hand, all three-point bending configurations are stable below and above melting temperature for all test speeds. Although the norm ISO 14125 recommends to maximise the free span length to thickness ratio in order to minimise the occurrence of interlaminar shear within the specimen [181], the test method considering a three-point bending fixture of 50 mm span length does not show a good potential because of its tooling arrangement. Since both three-point bending setups are built in the same test rig (see Fig. 4-12 c) specimens tested with the three-point bending (50 mm) fixture can possibly enter into contact with the three-point bending (20 mm) tooling in case of important displacements. Such a risk is not acceptable and the consideration to select a three-point bending (50 mm) fixture is therefore discarded.

The assessment of three-point bending (20 mm) results can also be based on the norm ISO 14125. To maximise the free span length to thickness ratio, specimens of 1 mm thickness must be selected [181]. This choice is supported by the analysis of the specimen geometries after testing. As it can be seen in Tab. 4-4, the widths of the 2 mm thickness specimens were significantly modified at the location of the punch.



Such a phenomena is also reported by Martin et al. and characterised as transverse spreading [78]. Although transverse spreading is also observed for the specimens of 1 mm thickness, this phenomena can be neglected for this type of specimens (less than 3% variations). Similar deformations were also noticed at 260°C. Thickness measurements were not possible due to the deformed shape of the specimens.

**Tab. 4-4: Three-point bending (20 mm): specimen widths at punch location before and after testing for experiments performed at 230°C**

	Test speed [ $\mu\text{m}/\text{min}$ ]	Width before testing [mm]	Width before testing [mm]	Variation [%]
<b>1 mm specimens</b>	200	14.85	15.21	+2.42
	230	15.00	15.40	+2.67
	260	13.90	13.93	+0.22
<b>2 mm specimens</b>	200	14.66	17.27	+17.80
	230	14.65	16.99	+15.97
	260	14.73	16.42	+11.47

The analysis of the preliminary results and the indication given by the norm ISO 14125 tends eventually to favour the application of a three-point bending fixture of 20 mm span length and specimens of 1 mm thickness for the characterisation of unidirectional carbon fibre thermoplastic composites.

#### *Experimental method and results*

Having determined the most suitable test fixture and specimen geometry, additional quasistatic tests are carried out at 280°C for five different test speeds to characterise material longitudinal out-of-plane bending behaviour.

Specimens are positioned in the machine at room temperature (see Fig. 4-13). The alignment of the sample is appropriate when the width of the specimens is parallel to the clamps/support. A good positioning is essential to avoid unsymmetrical loadings. A preload force of 0.001 N is applied. Specimens are then heated to testing temperature, i.e. 280°C, at a heating rate of 10 K/min. Flowing nitrogen is used to avoid polymer degradation [81]. While heating up, the machine is forced to keep a neutral displacement in order not to alter the quality of the specimens. To ensure a homogeneous temperature distribution within the specimen, tests are performed ten minutes after isothermal conditions are reached. Finally, quasistatic tests are carried out at forming temperature for five different test speeds in order to characterise the longitudinal out-of-plane bending behaviour of the UD-CF/PA6 composite material.

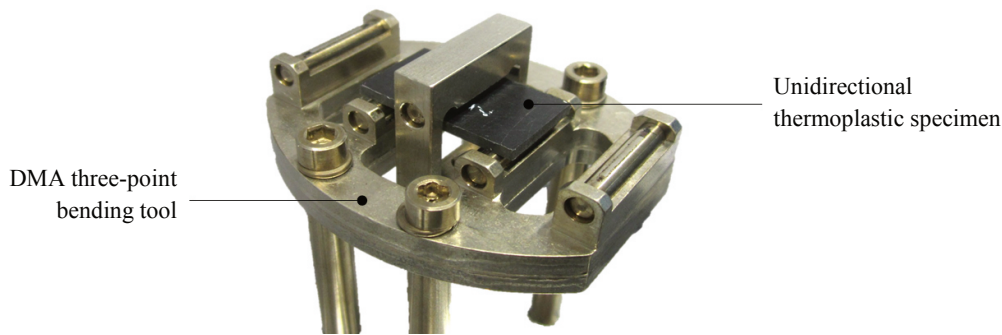


**Fig. 4-13: Unidirectional thermoplastic specimen mounted in a DMA three-point bending tool (20 mm)**

Measurements of the machine, i.e. force-displacement, are converted to stress-strain data using equation (4-1) and (4-2), respectively. Considering a span to thickness ratio of 20:1, the norm ISO 14125 [181] gives the expression of the stress in the outer fibre at mid-span  $\sigma_B$  in a beam of rectangular cross-section as:

$$\sigma_B = \frac{3FL}{2WT^2} \quad (4-1)$$

where  $F$  is the force applied at mid-span,  $L$  is the free specimen span length,  $W$  is the specimen width and  $T$  the specimen thickness.

The expression of the maximum strain in the outer fibre at mid-span  $\varepsilon_B$  is given as [181]:

$$\varepsilon_B = \frac{6DT}{L^2} \quad (4-2)$$

where  $D$  is the displacement at mid-span,  $T$  the specimen thickness and  $L$  the specimen free span length.

Stress-strain data presented in Fig. 4-14 indicate distinct viscous behaviour with a good result consistency. These are calculated as the average results over three repetitions, except for 2500  $\mu\text{m}/\text{min}$  where only two experiments were taken into consideration. This is due to the presence of an outlier in the data set caused by a test performed on a tooling soiled by some thermoplastic resin. The resin located on the support prevents a frictionless contact between the tooling and the specimen, which introduces additional stresses in the specimen and thus alter the testing outcome.

The standard deviations of the stresses presented in Fig. 4-14 are given in Tab. 4-5 for different strain values. An overall good reproducibility of the test method is to be acknowledged. The fluctuations registered for a test speed of 10000  $\mu\text{m}/\text{min}$  are due to the inability of the system to apply properly such a test speed [P2].

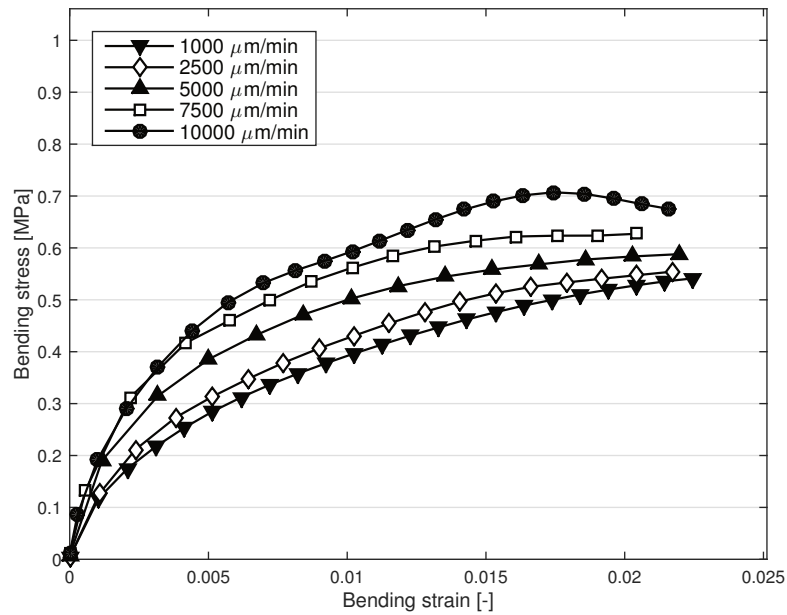


Fig. 4-14: Average bending stress-strain results of UD-CF/PA6 specimens (investigations performed at 280°C for different test speeds)

Tab. 4-5: Standard deviations of the stresses presented in Fig. 4-14

	1000 μm/min	2500 μm/min	5000 μm/min	7500 μm/min	10000 μm/min
<b>Stress standard deviation [%] at <math>\varepsilon = 0.0075</math></b>	7.763	4.960	7.275	5.040	1.895
<b>Stress standard deviation [%] at <math>\varepsilon = 0.015</math></b>	7.142	3.422	4.603	2.256	3.238
<b>Stress standard deviation [%] at <math>\varepsilon = 0.0225</math></b>	7.128	2.926	4.457	2.067	3.503

#### Out-of-plane bending modulus calculation

Out-of-plane bending moduli  $E_B$  are calculated to determine proper simulation input (see Chapter 3.3.2). Because all tests are performed for small deflections (maximum deflection corresponds to less than 10% of the free span length), bending moduli can be calculated as the ratio of equation (4-1) over equation (4-2) [P2]:

$$E_B = \frac{FL^3}{48ID} = K \frac{L^3}{48I} \quad (4-3)$$

where  $K$  is the specimen stiffness,  $I$  the second moment of inertia. The specimen stiffness  $K$  is defined as the ratio between the applied force  $F$  and the resulting displacement at mid-span  $D$ . Due to the acceleration of the machine, only the last third of data recorded by the DMA system, i.e.  $K$ , are used for analysis purposes [P2].

The evolution of the longitudinal out-of-plane bending modulus with respect to strain rates is displayed in Fig. 4-15. Strain rates  $\dot{\epsilon}_B$  are calculated as the time derivative of equation (4-2) :

$$\dot{\epsilon}_B = \frac{6\dot{D}t}{L^2} \quad (4-4)$$

where  $\dot{D}$  is the test speed.

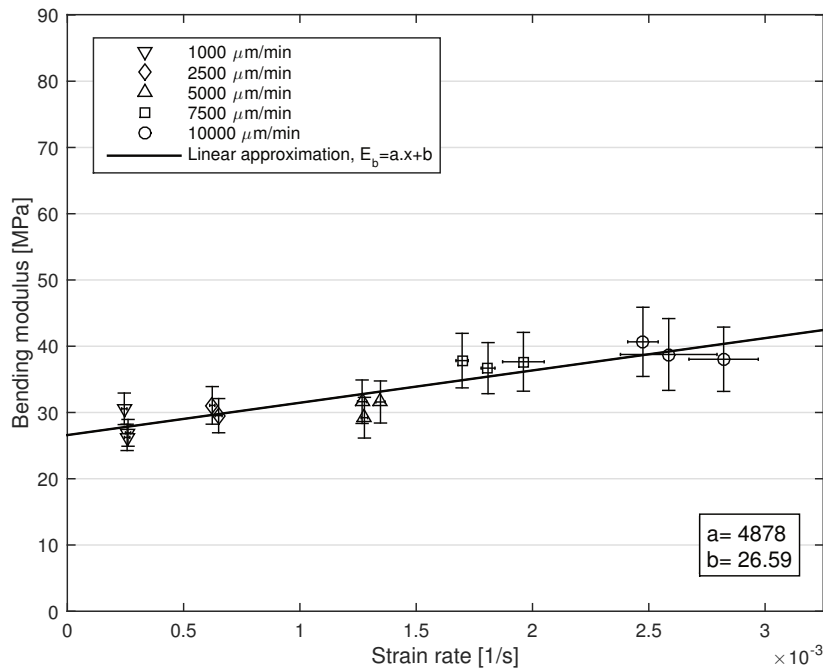


**Fig. 4-15: Strain rate dependency of the longitudinal out-of-plane bending modulus of a UD-CF/PA6 material (280°C)**

Correlations between test speeds (input given to the DMA system) and strain rates are presented in Tab. 4-6 for specimens of ideal geometries (20 mm length, 15 mm width and 1 mm thickness).

**Tab. 4-6: Equivalence between test speeds and strain rates for specimens of ideal geometry**

Test speed [μm/min]	1000	2500	5000	7500	10000
Strain rate [1/s]	$2.5 \times 10^{-4}$	$6.25 \times 10^{-4}$	$1.25 \times 10^{-3}$	$1.88 \times 10^{-3}$	$2.5 \times 10^{-3}$

The data recorded for similar test speeds are not all perfectly equivalent to their corresponding strain rates but rather spread around a value. This arises from the thickness variations existing between the specimens (several dozen micrometres).

Vertical errors are due to material non-linear stress behaviour (see Fig. 4-14) and the fact that calculations are performed over the last third of the measurements. A maximum error of 14% is to be reported. The relatively high horizontal standard deviations of the experiments performed at 10000  $\mu\text{m}/\text{min}$  reflect the difficulty encountered by the machine to control the application of such a test speed.

Results are found to satisfy a linear approximation within the range of data:

$$E_B = 4878 \cdot \dot{\epsilon}_B + 26.59 \quad (4-5)$$

Inaccuracies in the determination of the out-of-plane bending modulus can be caused by imprecisions in the measurement of specimen thicknesses. Since the value of the thickness is cubed in the calculation of the modulus (via the second moment of inertia), this parameter plays a rather important role. Each specimen was measured using a digital calliper with an accuracy of 1  $\mu\text{m}$ . Although the error arising from the thickness measurements cannot be precisely determined, it is expected to be rather small.

#### 4.1.2.2 Transverse out-of-plane bending

To assess whether the DMA test method is applicable to the characterisation of transverse out-of-plane bending properties, specimens of 1 mm and 2 mm thicknesses are positioned on top of a tray and enclosed for 15 minutes into an oven heated at 280°C.

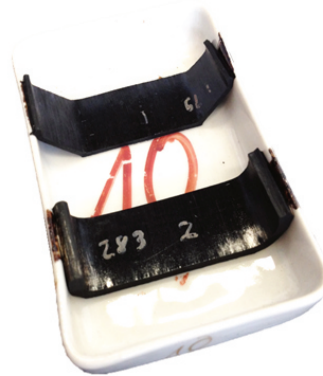


**Fig. 4-16: Transverse out-of-plane bending: specimen deformations after 15 minutes at 280°C**

Results show that both specimens are not able to withstand their own weights (see Fig. 4-16). Because of weak material behaviour caused by the lack of reinforcement, transverse out-of-plane bending properties cannot be investigated neither with a DMA system nor with other test methods.

#### 4.1.3 In-plane tension

In a similar manner as for out-of-plane bending properties, because of material orthotropy and the requirements of the material model (see Chapter 3.3.2), both longitudinal and transverse behaviour have to be investigated.

### 4.1.3.1 Longitudinal tension

In the scope of this doctoral dissertation, longitudinal in-plane tension behaviour is not investigated because:

- it is governed by fibre properties and as such, is not expected to vary with temperatures and strain rates (see Chapter 2.2.2),
- it is often scaled in explicit FE simulations to reduce computational effort (see Chapter 5.1.1).

A reference value of 200 GPa is considered [11].

### 4.1.3.2 Transverse tension

Most of the content of this section, including text and figures, is based on [P3].

#### Literature review

Since the 1960s the characterisation of transverse tensile properties of unidirectional composite materials has been considerably investigated in the field of fracture and damage mechanics [182-186]. Transverse tensile properties were also investigated in the analysis of intra-ply shear of unidirectional composite materials using off-axis tensile tests [187]. Released norms related to the characterisation of transverse tensile properties recommend the usage of universal testing machines and, if required, the application of an environmental chamber to control testing conditions [188, 189]. These norms were however originally developed for cured thermoset (and solid thermoplastic, i.e. non-molten) laminates. As such, they are not really suited for the characterisation of very soft materials like molten thermoplastic composite materials (thermoplastic materials tested above melting temperature). In the field of material forming, transverse tensile properties have already been investigated for a non-cured unidirectional thermoset pre-impregnated composite material.

In his study, Potter particularly showed that such materials are stiffer under intra-ply shear than transverse tension [65]. To the author's best knowledge, there has not been any published investigation reporting the characterisation of transverse tensile properties of molten thermoplastic composite materials.

In the following, a novel approach for the characterisation of the transverse tensile properties of molten unidirectional pre-impregnated composite materials is presented using a DMA system in a quasi-static manner. First unsuccessful attempts conducted within an environmental chamber mounted on a universal testing machine are used as motivation for this work.

#### Initial situation

First attempts for the characterisation of transverse tensile properties have been performed by S. Bel at the *Chair of Carbon Composites* of the *Technical University of*

*Munich* using a universal testing machine (UPM 250kN, Hegewald and Peschke). Tests are carried out within an environmental chamber in order to reproduce similar conditions as during forming (280°C). Specimens of 200 (L) x 50 (W) x 1 (T) mm<sup>3</sup> where  $L$  is the length in fibre direction,  $W$  is the dimension transverse to fibre direction and  $T$  is the thickness, are tested at 10 mm/min, 50 mm/min and 100 mm/min. A good positioning of the specimens is achieved when an initial free test length of 20 mm is reached (15 mm clamping on each side) and when the specimen's fibre orientation was parallel to the side length of the clamps (see Fig. 4-17).

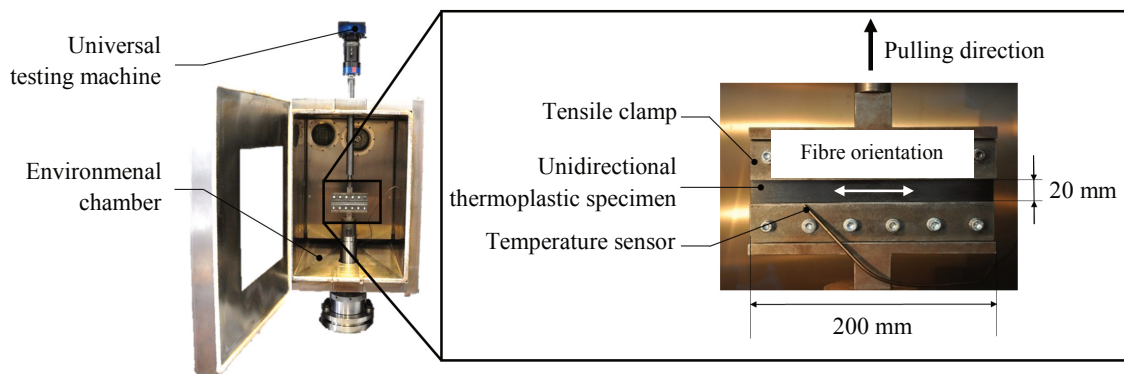


**Fig. 4-17:** Thermoplastic specimen mounted in a universal testing machine and enclosed within an environmental chamber [adapted from S. Bel]

Although few pretrials delivered encouraging results, additional investigations showed a lack of reproducibility. Difficulties are mainly caused by the thermal expansion of the metallic clamps and their interactions with the thermoplastic composite specimens. By heating up the environmental chamber to such an elevated temperature, the alignment of the clamps undergoes significant variations which influenced the initial specimen free length and therefore, the initial specimen stress state.

The expansion of the clamps directly introduce forces (mainly compressive) which make the specimen buckle. Approaches considered to counteract thermal expansion such as (i) commanding the tensile testing machine to remain at zero force while heating up and, (ii) eliminating the buckle by straightening the specimen, are not satisfactory. The unsymmetrical and rather unpredictable aspects of the variations make them particularly difficult to anticipate.

Because of severe thermal expansion issues, the method considered here, using a universal testing machine and an environmental chamber, appears not to be suitable for the characterisation, under environmental forming conditions (280°C), of the transverse tensile properties of a unidirectional thermoplastic material. Besides, the usage of a relatively large environmental chamber raise uncertainties regarding temperature distribution. Although air circulation is managed by a fan, homogeneous temperature is difficult to achieve. To prevent temperature distribution issues, significant soaking time have to be applied, which, in return, leads to relatively long testing time.

For the investigation of transverse tensile properties of a molten thermoplastic material, a simple and robust test method which enables fine measurements as well as a close control of environmental conditions is needed. The selected test method should also permit efficient testing, via e.g. high heating rates, and rapid data analyses. To fulfil these requirements, a new approach using a DMA system in a quasi-static manner has been developed. In particular, preliminary analyses performed with a control material showed its potential and relevance to characterise transverse tensile properties of soft/molten composite materials (see Chapter 4.4.3).

## Development of a test method using a DMA system

### *Specimen preparation*

Specimens of  $6.5 (L) \times 23 (W) \times 2 (T) \text{ mm}^3$ , where  $L$  is the length in fibre direction,  $W$  is the dimension transverse to fibre direction and  $T$  is the thickness, are prepared from unidirectional blanks of 1 mm thickness. These are laid and consolidated in the same manner as presented in Chapter 1.1. To protect DMA clamps, specimen tips are wrapped in aluminium tapes (see Chapter 4.4.3). The outer layers of some specimens are examined using an optical measuring system (ProFactor sensor [177]) to control whether they have a homogeneous unidirectional fibre orientation perpendicular to the specimen side length. Although measurements are not performed for all specimens, results are assumed to be representative. An average fibre orientation of  $87.80^\circ (\pm 3.08^\circ)$  with respect to the specimen side length is to be reported. Deviations are mainly caused by the consolidation process. The effect of such fibre reorientations is not considered in the present study.

### *Experimental methods and results*

Specimens are positioned at room temperature and clamped with a torque of 3 in.lb (0.34 N.m). The alignment of the sample is appropriate when the specimen fibre orientation is parallel to the side length of the clamps (see Fig. 4-18). Specimens have an initial free length of about 10 mm. The furnace is eventually closed and heated up to  $280^\circ\text{C}$  at a heating rate of  $10^\circ\text{C}/\text{min}$ . During the heating up phase, the actuator is blocked to avoid undesirable effects. To ensure homogeneous temperature distribution, tests are performed ten minutes after isothermal conditions are reached.

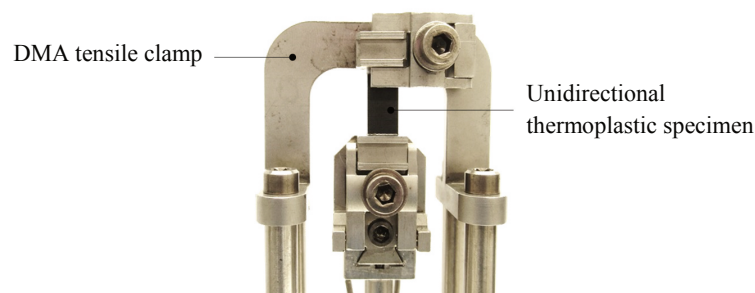


**Fig. 4-18:** Unidirectional thermoplastic specimen mounted in a DMA tensile clamp



Due to unsuccessful attempts at constant test speeds, tests are conducted at constant loading rates (0.025 N/min, 0.05 N/min, 0.075 N/min, 0.100 N/min and 0.125 N/min). Difficulties encountered with tests conducted at prescribed test speeds is due to the working principle of the machine and the weak behaviour of the material. Unlike tensile testing machines, DMA systems apply forces and measure displacements [176]. For tests performed at prescribed test speeds, the machine must reach selected test speeds by applying forces and measuring resulting displacements. This iterative process appears to be especially complicated to manage with weak materials, such as a molten thermoplastic composites.

Force-displacement data recorded by the DMA systems are converted to strains  $\varepsilon_t$  and stresses  $\sigma_t$  using equations (4-6) and (4-7), respectively:

$$\varepsilon_t = \frac{D}{L_0} \quad (4-6)$$

where  $D$  is the displacement of the crosshead (universal testing machine) / actuator (DMA system) and  $L_0$  is the initial specimen free length,

$$\sigma_t = \frac{F}{A_0} = \frac{F}{W * T} \quad (4-7)$$

where  $F$  is the measured force and  $A_0$  the initial specimen cross-section calculated by multiplying  $W$  and  $T$ , the specimen width and thickness, respectively.

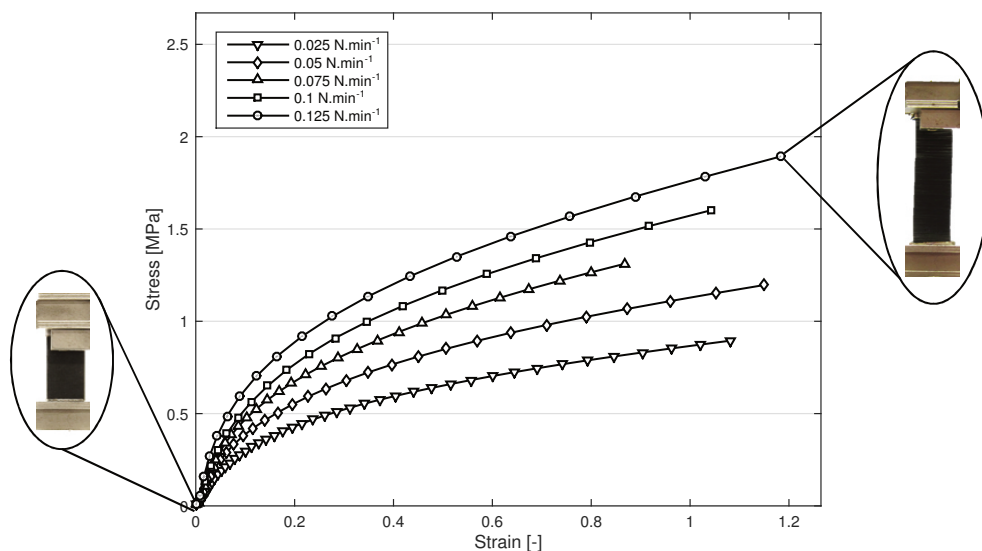


**Fig. 4-19: Average stress-strain transverse tensile test results of UD-CF/PA6 specimens (investigations performed at 280°C with a DMA system)**

Results presented in Fig. 4-19 are the average stress-strain data calculated over three repetitions. Standard deviations, which are not plotted for clarity purposes, remain always smaller than 2%.

The small scatter of the data indicates the overall good reproducibility of the presented test method. Variations in the end strain values are due to different initial specimen free lengths (from about 10 mm to 13 mm). No failure of specimens is observed at the end of the tests. The material exhibits clear viscous behaviour under environmental forming conditions.

## 4.1.4 Viscosity

As detailed in Chapter 3.3.2, material viscous behaviour in MAT 140 is managed by a parameter representing composite viscosity. Because of the influence of the fibres, viscosity has to be characterised for the composite and not for the unfilled polymer resin [81]. This section aims therefore to characterise composite viscous behaviour under thermoforming conditions.

### 4.1.4.1 Literature review

The usage of standard apparatus applied to unfilled polymers, e.g. rotational and capillary rheometers, have shown to be limited to melts reinforced with fillers of small aspect ratio<sup>2</sup>. In particular, the usage of rotational rheometers for the characterisation of continuous fibre-reinforced melts seems to be restricted to small deformations in order not to change sample configuration and fibre orientations. Other studies considering capillary rheometers showed the high volume fraction of continuous fibre-reinforced composites to prevent proper characterisation. [81]

Because no capillary rheometer is available at the *Chair of Carbon Composites* of the *Technical University of Munich*, on the one hand, and the limits of rotational rheometers, none of the aforementioned methods is considered to characterise the viscosity of the unidirectional fibre-reinforced composite material presented in Tab. 1-1. Instead, an analytical method based on transverse tensile test results is derived and applied to results presented in Fig. 4-19.

### 4.1.4.2 Method and results

The instantaneous transverse composite viscosity  $\eta_t$  can be calculated from transverse tensile tests via the equation (4-8). Derivation details are given in Appendix c.

$$\eta_t = \frac{\sigma_t(L_0 + D)}{2\dot{D}} \quad (4-8)$$

where  $\sigma_t$  is the transverse tensile stress,  $L_0$  is the initial specimen free length,  $D$  is the displacement and  $\dot{D}$  is the speed.

---

<sup>2</sup> Ratio between the largest and the shortest lengths of the filler.

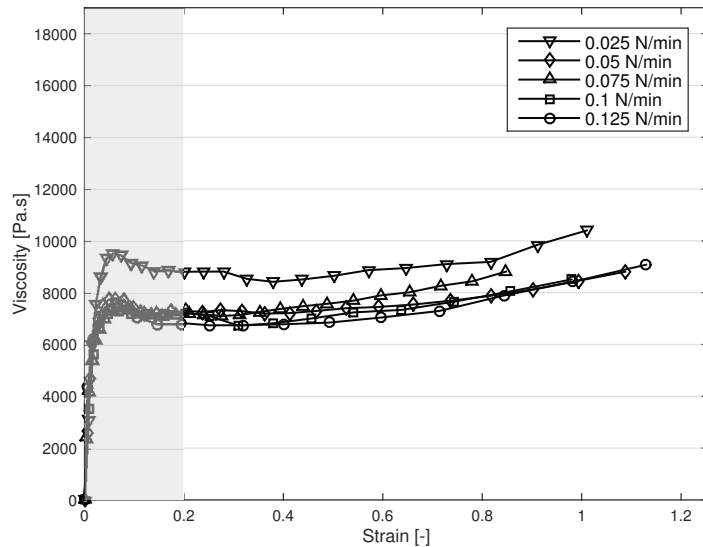


**Fig. 4-20:** Average composite viscosities calculated according to equation (4-8) for different loading rates

Results presented in Fig. 4-20 are the average viscosity values calculated according to equation (4-8) over three transverse tensile tests. Standard deviations, which are not plotted for clarity purposes, remain smaller than 15% in average. Most of data scattering occurs within the first 0.2 value of strain (see grey zone in Fig. 4-20) with a maximum error of about 37% for 0.025 N/min.

That scattering is larger below the first 0.2 value of strain is due to flow initiation. Flow initiation, which is characterised by a slight viscosity overshoot (see grey zone in Fig. 4-20), is reported to be influenced by local fibre reorientation [81] and molecular entanglement [190]. Although it can be observed for all test series, the overshoot is more distinct for 0.025 N/min because fibres can rearrange more easily at low rates.

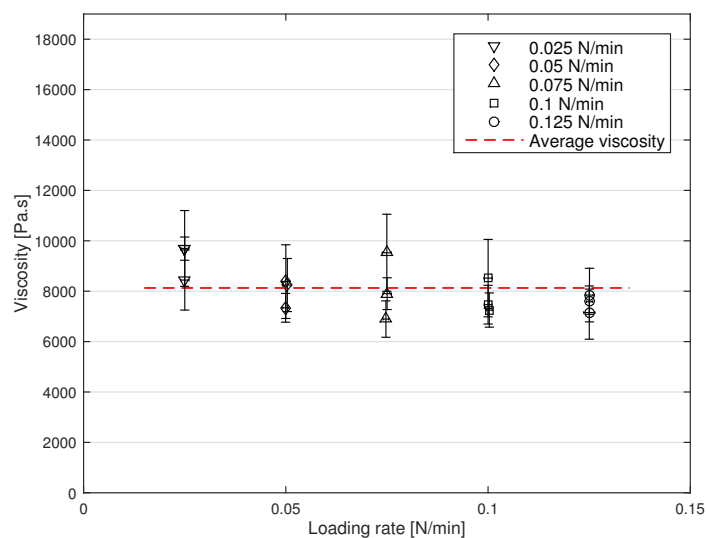


**Fig. 4-21:** Evolution of composite viscosity over the investigated range of loading rates. Viscosities are calculated after 0.2 value of strain (see Fig. 4-20).

To avoid effects of flow initiation, only data after 0.2 value of strain are considered for analysis purposes. Despite transverse tensile tests are performed at constant loading rates and thus, varying test speeds (see Chapter 4.4.3 and Fig. 5-2), viscosity appears to remain rather constant within the range of data (see Fig. 4-20). The relatively low standard deviations indicate that the viscosity does not vary significantly during testing (see Fig. 4-21). An average composite viscosity of 8129 Pa.s is approximated within the range of data. Because of the presence of reinforcing fibres, composite viscosity is found to be larger than neat PA6, which has a viscosity of about 200 Pa.s at 280°C [191]. In fact, composite viscosities are reported to be dependent on the viscosity of the neat resin, the fibre volume fraction and the fibre array packing geometry [81].

Because MAT 140 considers viscous fluids to be dependent on deviatoric stresses rather than Cauchy stresses [155], a specific composite viscosity  $\eta_{PAM}$  has to be calculated for simulation purposes. According to equation (A-32)<sup>3</sup>, composite viscosity reads:

$$\eta_{PAM} \approx 4065 \text{ Pa.s} \approx 0.004 \text{ GPa.ms} \quad (4-9)$$

## 4.2 Characterisation of a separation film

Most of the content of this section, including text and figures, is based on [K10].

In the scope of this work, thermoforming experiments are performed with layups composed of tailored thermoplastic composite blanks and separation films (see Chapter 6.1.1). The latter, which are located at the interface between composite and tooling, aim to (i) ease part removal after forming and (ii) enhance forming quality by decreasing tool/ply friction. Within this work, a heat-resistant polyimide film supplied by Airtech, also referred to as kapton film, is considered (see Tab. 4-7) [192].

**Tab. 4-7: Main properties of the polyimide film supplied by Airtech [192]**

<b>Material type</b>	<b>Maximum use temperature [°C]</b>	<b>Thickness [µm]</b>	<b>Colour</b>
Polyimide	405	50	Amber

In FE thermoforming simulations, auxiliary materials are usually only taken into account within interaction properties. Typically, separation films are not modelled “explicitly” but their influence is considered within tool/ply friction coefficients. In the scope of this doctoral dissertation, an innovative approach in which each separation film is modelled by a layer of shell elements is introduced (see Chapter 6.1.4).

<sup>3</sup> Details of the derivation are given in Appendix c.

For simulation purposes, the separation film must thus be characterised. As an isotropic material, the film is modelled with MAT 101. Besides the density, two input parameters are required (see Chapter 3.3.2):

- Poisson's ratio,
- Young's modulus.

In the scope of this work, the Poisson's ratio of the separation film is assumed to be strain rate and temperature independent. According to [193], a Poisson's ratio  $\nu_{film}$  of 0.33 is considered.

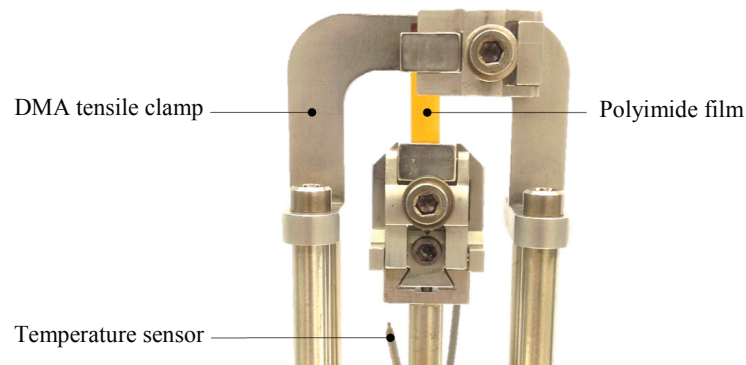


**Fig. 4-22: Polyimide film mounted in a DMA tensile clamp**

Because of the lack of material data at forming temperature, a series of tensile tests are performed at 280°C. For accuracy purposes, investigations are conducted with a DMA system (see Chapter 4.1.2.1). Specimens are positioned at room temperature and clamped with a torque of 5 in.lb, i.e. 0.565 N.m (see Fig. 4-22). To prevent slippage, a higher torque than this prescribed by TA Instruments is applied. Specimens have an initial free length of about 10 mm. The furnace is eventually closed and heated up to 280°C at a heating rate of 10°C/min.

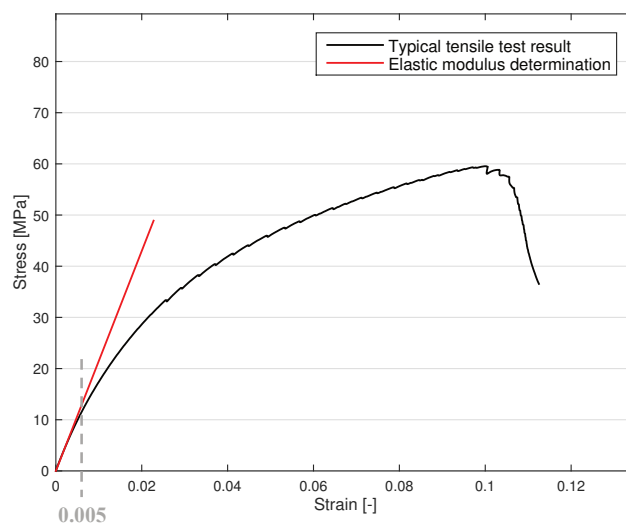


**Fig. 4-23: Typical stress-strain tensile test response of a polyimide film (investigation performed at 280°C with a DMA system)**

Tensile tests are carried out at a prescribed test speed of 100  $\mu\text{m}/\text{min}$ . A typical test result is presented in Fig. 4-23. The elastic modulus is determined as the tangent of the initial stress-strain response (see red line in Fig. 4-23). Although further investigations would be necessary to confirm pure elasticity, e.g. load release tests, mechanical behaviour is assumed to be elastic up to a strain value of 0.5%. An average Young's modulus of about  $2.1 \pm 0.2$  GPa is calculated over six repetitions.

### 4.3 Characterisation of contact properties

Based on the experimental thermoforming setup considered in this work (see Chapter 6.1.1), tool/film, ply/ply and film/ply interactions need to be characterised. For these purposes, a novel friction test setup, which enables investigations at different test speeds, temperatures, pressures and fibre orientations, is introduced. Characterisation analyses are eventually conducted, to the best possible extent, under similar environmental conditions as forming occurs, at different test speeds, pressures and, if applicable, fibre orientations to identify potential dependencies.

#### 4.3.1 Literature review

A review of the state-of-the-art test methods for the characterisation of contact properties (tool/ply and ply/ply) has been recently proposed by Sachs et al. [43, 93]. Further details can also be found in [37, 44, 94, 194].

Unlike investigations at room temperature [195, 196], no test standard exists for the characterisation of tool/ply and ply/ply interactions under regulated environmental conditions. Despite this lack, most wet friction analyses, i.e. tests performed with molten thermoplastic materials, have been conducted with similar test setups. Investigations have been typically carried out with variants of the pull-out and pull-through test setups (see Fig. 4-24 left and right, respectively) [43, 67, 82, 90, 93, 94].

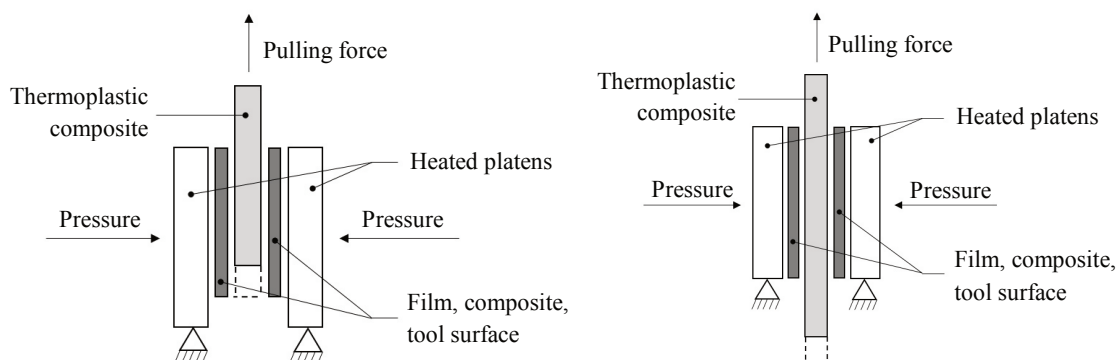


Fig. 4-24: Schematic of a pull-out (left) and pull-through (right) test setup

Pull-out and pull-through test setups are both based on the same working principle. Contact properties are characterised by pulling a ply out or through two others, respectively. Depending on the configuration, these apparatus can be used to investigate tool/ply or ply/ply interactions. The main difference between both test setups lies in the fact that, in pull-out experiments, contact area decreases during testing, whereas it remains constant in pull-through analyses. To control testing conditions, each test setup can regulate test speeds, temperatures and applied pressures.

The characterisation of wet friction properties has been a popular field of research over the last years. In particular, an international benchmark led by the University of Twente was conducted [93]. The goal of this collaborative work was “to clarify whether design differences (between test setups) have a significant effect on measurement results”. For comparison purposes, each participant characterised the same thermoplastic composite material using its own test apparatus. In their conclusion, Sachs et al. emphasised the importance of temperature and pressure distributions and recommended to pay particular attention to these in the development of new test setups [43, 93].

For tool-ply friction, Harrison et al. proposed an innovative approach using a rotational rheometer [194]. Investigations were conducted with a customised test rig. According to the authors, the consideration of a rheometer enables more efficient testing than classical pull-out and pull-through test setups. Results, which were analysed using a dedicated post-processing method, showed a similar trend than measurements performed with pull-out and pull-through test apparatus. Discrepancies were assumed to be caused by an unverified assumption used for data analysis (constant film thickness).

Although several test setups were proposed over the years, no method seems to be established for the characterisation of contact properties. Therefore, a new approach based on the test setup introduced in the norm DIN 14882 [195] has been developed to meet wet friction requirements and recommendations of Sachs et al. [93].

### **4.3.2 Development of a new friction test setup**

Most of the content of this section, including text and figures, is based on [K11 and S6].

The norm DIN 14882 [195] presents an efficient test method, referred to as “carrier test setup”, to characterise contact properties at room temperature. Interactions between material A and material B are investigated when a carrier, below which is fixed a piece of material B, is pulled over a support, on top of which lays a piece of material A (see Fig. 4-25). Depending on materials A and B, different types of interactions can be investigated.

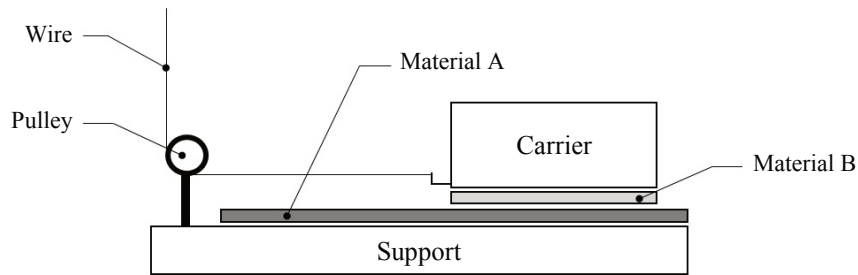


**Fig. 4-25:** Schematic of the “carrier test setup” introduced by DIN 14882 (adapted from [195])

In the scope of this doctoral dissertation, the original concept presented in DIN 14882 [195] is modified to meet wet friction requirements. The new “carrier test setup” must:

- Offer the possibility to perform experiments at different temperatures, pressures and test speeds,
- Enable efficient specimen replacement,
- Be connected to a load cell to measure frictional forces,
- Be lightweight to ease mounting/dismounting operations.

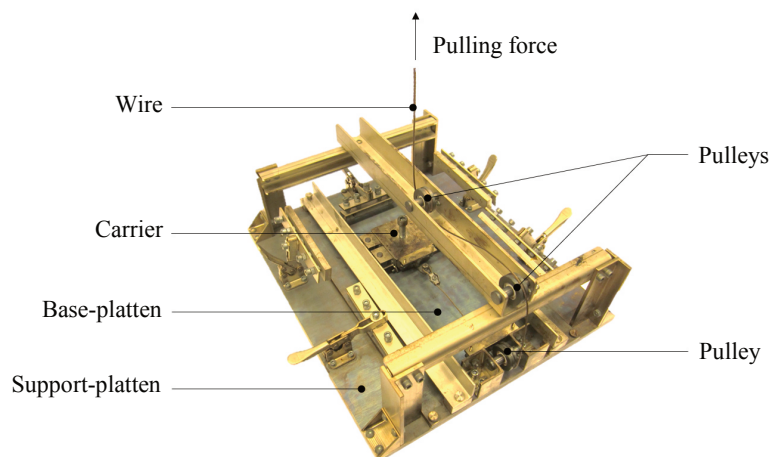


**Fig. 4-26:** Enhanced “carrier test setup” suitable for wet friction characterisation

In order to control testing environment, the new test setup (see Fig. 4-26) can be mounted on a universal testing machine and enclosed within an environmental chamber. This enables the application of test speeds up to 400 mm/min and temperatures up to 350°C. The load applied on the carrier can also be varied. Three levels can be selected: about 5 kPa (basic configuration), about 8 kPa (intermediate configuration) and about 11 kPa (full configuration). Frictional forces can be accurately measured via a load cell connected to the universal testing machine. To ensure efficient specimen replacement, as well as easy mounting/dismounting operations, the new test setup has a modular assembly composed of three distinct bodies:

- The base-plate body,
- The specimen-plate body,
- The carrier body.



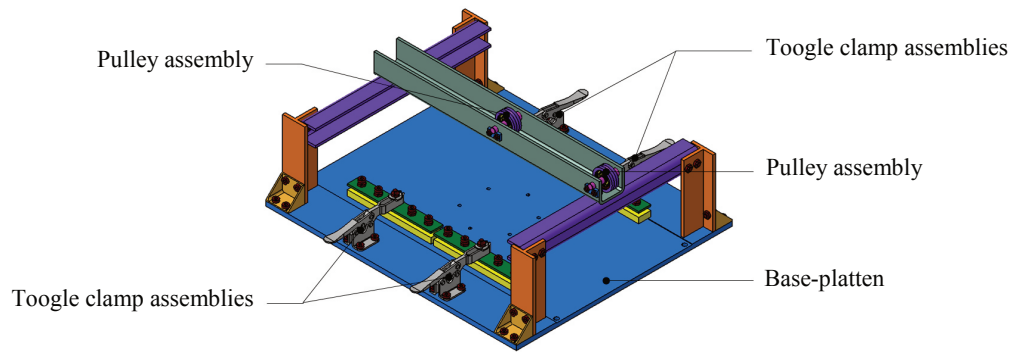


**Fig. 4-27: Isometric view of the base-plate body (adapted from [S6])**

The base-plate body consists of a base-platen, four pull-push toggle clamp assemblies, and two pulley assemblies (see Fig. 4-27). The base-plate body aims to carry both the specimen-plate and the carrier bodies. Once mounted on the universal testing machine, the base-plate body remains fix, even during specimen replacement. To lightweight the assembly, the bottom side of the base-platen is machined with cut-outs (see Fig. A-7 left in Appendix d).

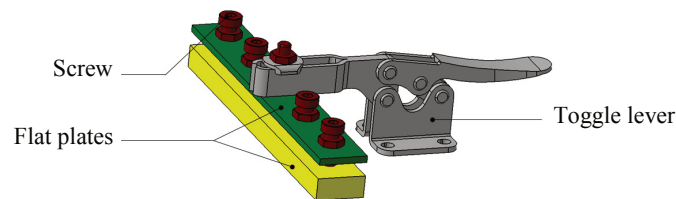


**Fig. 4-28: Isometric view of the pull-push toggle clamp assembly (adapted from [S6])**

Pull-push toggle clamp assemblies are composed of a commercially available toggle lever [197] and two plates screwed together (see Fig. 4-28). Their role is to clamp specimens laying on the specimen-platen (see Fig. 4-30). Their design enables (i) rapid load application/release via toggle levers and (ii) clamp height adjustments via a simple but efficient concept consisting of two plates screwed together. Clamp height adjustments are essential to ensure optimum contact with specimens.

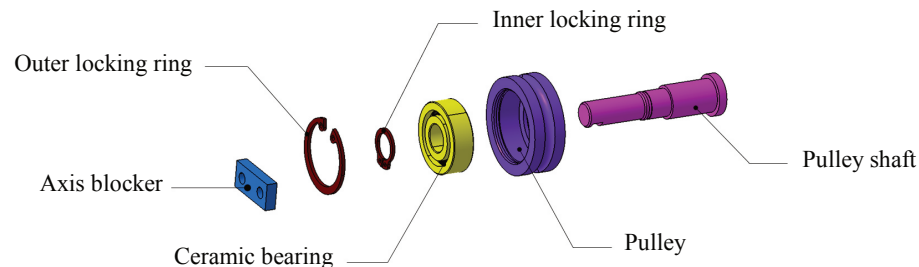


**Fig. 4-29: Exploded view of the pulley assembly (adapted from [S6])**

Pulley assemblies are composed of a shaft, a pulley, a bearing, outer and inner rings and an axis blocker (see Fig. 4-29). In the scope of this work, commercially available

ceramic bearings are considered because of (i) their heat-resistance capabilities (up to 400°C) and (ii) their low friction [198]. To ensure the pulley assembly not to twist and thus, remain straight, axis blockers are used.

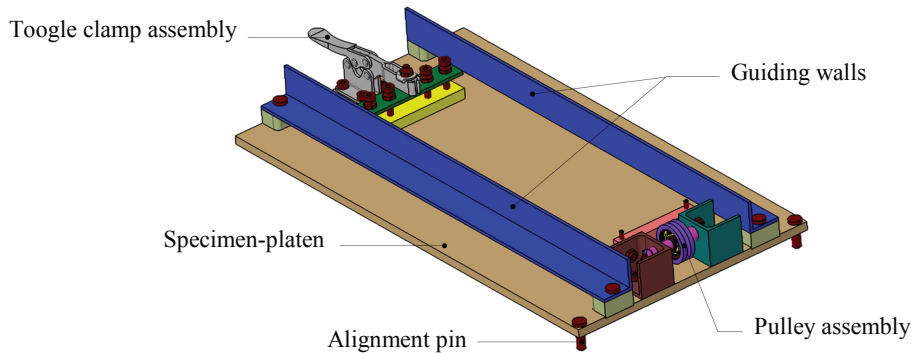


**Fig. 4-30: Isometric view of the specimen-plate body (adapted from [S6])**

The specimen-plate body consists of a base-platen, referred to as specimen-platen, a pull-push toggle clamp assembly, two guiding walls and a pulley assembly for the wire (see Fig. 4-30). The role of the specimen-plate body is to hold the specimen located onto the specimen-platen and support the carrier while sliding. One of the particularities of this body is the presence of guiding walls. These ensure the carrier to be pulled straight during testing. To ease sliding on the walls, the carrier is equipped with four “wheels” (see Fig. 4-31 and Fig. 4-32). In a similar manner as for the base-platen, the bottom side of the specimen-platen is machined with cut-outs to reduce weight (see Fig. A-7 right in Appendix d).

For specimen replacement, the whole specimen-plate body needs to be taken out of the environmental chamber. The specimen positioned on top of the specimen-platen is replaced after having dismantled guiding walls, which are just fixed by pins. The toggle clamp onto the platen ensures the specimen not to move during transfers. Once the specimen-platen is properly mounted onto the base-platen (alignment is verified by two pins), the four toggle clamps located on the base-platen are lowered onto the specimen located onto the specimen-platen.

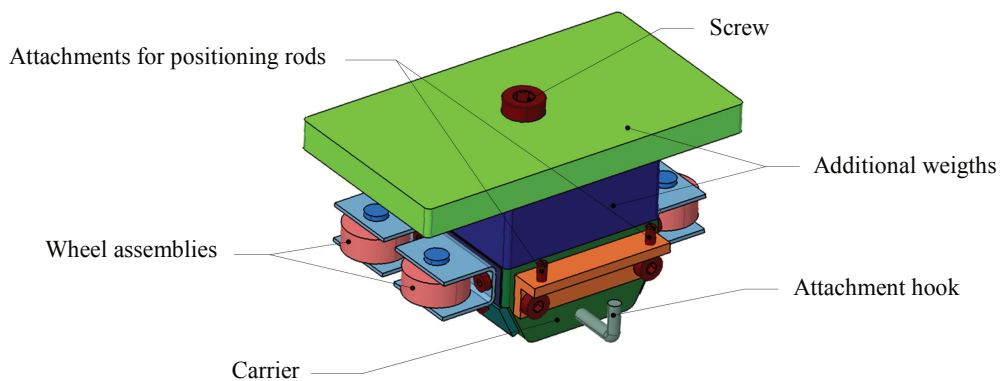


**Fig. 4-31: Isometric view of the carrier body (adapted from [S6])**

The carrier body is composed of a carrier, an attachment hook to connect the wire, four wheel assemblies, two attachments for positioning rods, two additional weights and a screw (see Fig. 4-31). By considering the carrier as such or adding additional weights, three different load levels can be selected. Wheel assemblies are developed similarly to pulley assemblies (see Fig. 4-29). In particular, ceramic bearings are also used. To ensure the carrier to be placed in a reproducible manner, positioning rods are also foreseen (not shown in Fig. 4-31). Their usage is illustrated in Fig. A-8 (see Appendix d) when the carrier body is positioned on top of the specimen-platen. The role of the carrier body is to carry the specimen located below the carrier. As shown in Fig. 4-32, the specimen is fixed by means of attachment plates.

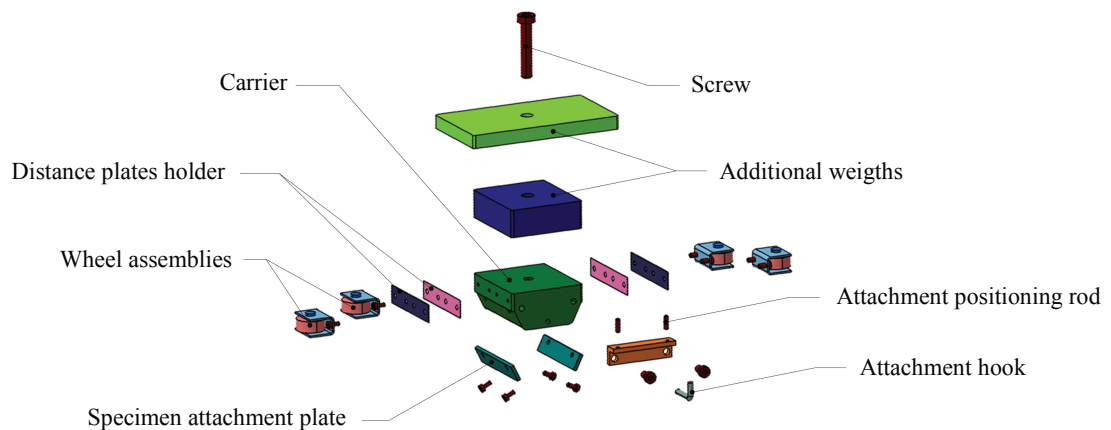


**Fig. 4-32: Exploded view of the carrier body (adapted from [S6])**

In order to be mounted below the carrier, the specimen needs to be formed into carrier geometry. To ease preparation and ensure good reproducibility, a dedicated tooling is developed (see Fig. 4-33). The specimen is formed when the flat piece of material is forced by a hood, which has female carrier geometry, to comply with carrier shape. Specimens of different thicknesses can be prepared by adjusting the distance between the hood and the male mould with a screw. Energy to heat thermoplastic specimens needs to be brought externally, e.g. by means of a heat gun (see Appendix e).

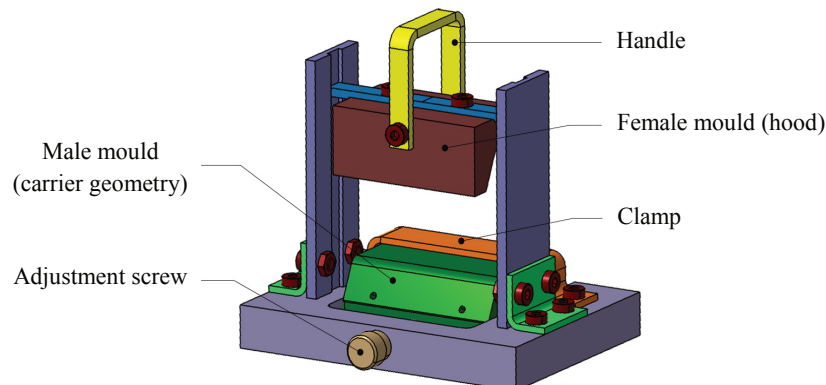


**Fig. 4-33: Tooling for specimen preparation (adapted from [S6])**

To prevent corrosion, the new friction test setup and specimen preparation tooling are manufactured with stainless steel. The wire used to pull the carrier, as well as the toggle levers, is also made out of stainless steel.

Given that the presented test setup meets both wet friction requirements and recommendations made by Sachs et al. [93], it is applied to the characterisation of tool/film, ply/ply and film/ply interactions. Investigations are conducted, to the best possible extent, under similar environmental conditions as forming occurs.

### 4.3.3 Experimental results

According to the thermoforming process considered in Chapter 6.1.1, contacts between treated separation film/tool surface, thermoplast/thermoplast and treated separation film/thermoplast have to be investigated. Most of the content of this section, including text and figures, is based on [K11 and S8].

#### 4.3.3.1 Treated separation film/tool

Separation film specimens are prepared from the same polyimide film [192] and treated with the same release agent as used for thermoforming experiments [199] (see Chapter 6.1.1). The tool surface is represented by the stainless steel bottom surface of the carrier.

Given that treated separation film/tool interactions are isotropic, tests are conducted with and without guidance walls to investigate their influence on measurement results. Experiments are also performed at different test speeds and pressure levels. Because of inaccuracies in the manufacturing of some wheel shafts (component similar to this presented in Fig. 4-29), wheels located on the right hand side of the carrier do not roll on the wall, but block and slide, which generates significant friction. To overcome this issue within a limited amount of time, tests with guidance walls are not performed with two but only one guidance wall, i.e. this located on the left-hand side of the carrier. The test matrix is presented in Tab. 4-8.

**Tab. 4-8: Test matrix for treated separation film/tool contact characterisation**

	<b>4.83 kPa</b>	<b>7.98 kPa</b>	<b>11.14 kPa</b>
<b>Without walls</b>	100 mm/min	100 mm/min	100 mm/min
	300 mm/min	300 mm/min	200 mm/min
			300 mm/min
<b>With left wall</b>	Not investigated	100 mm/min	100 mm/min
		300 mm/min	300 mm/min

Each configuration is tested after five minutes soaking time at 280°C and repeated three times. Release agent is applied only once per configuration. Therefore, only the first experiments can be used to describe the frictional behaviour seen by the tooling during thermoforming. The other two repetitions can be used to investigate the influence of release agent on contact behaviour.

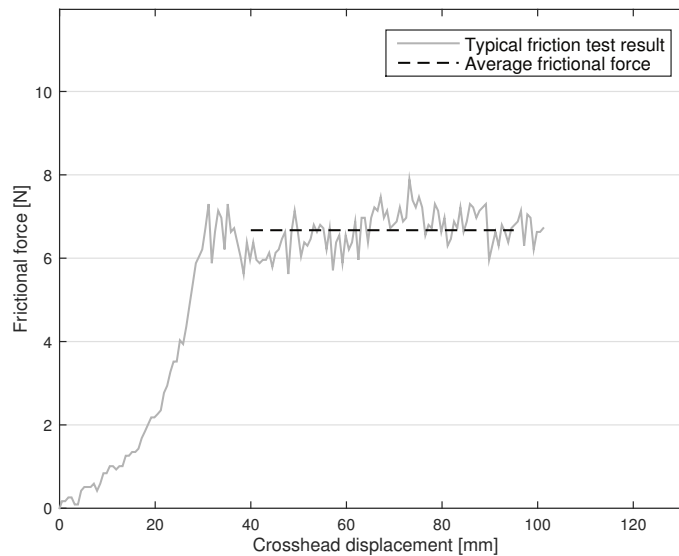


**Fig. 4-34:** Typical outcome of a treated separation film/tool surface friction test

A typical outcome of a friction test performed between a metallic tool surface and a treated separation film is presented in Fig. 4-34. Experimental results show that the frictional force increases until it reaches a sort of steady state. Since no distinct peak is observed, both static and kinetic friction coefficients seem to be in the same order of magnitude. Therefore, friction coefficient  $\mu_{tool}$  is derived according to equation (2-1), i.e. as the ratio of the average force measured by the load cell  $F_{ave}$  and the normal force acting on the carrier  $N$ :

$$\mu_{tool} = \frac{F_{ave}}{N} \quad (4-10)$$

Experimental results presented as friction coefficients calculated according to equation (4-10) are presented in Tab. 4-9. All friction coefficients increase with the number of repetitions. This increase is correlated with the reduction of release agent quantity. Every time the carrier slides on the film, the amount of release agent diminishes because some of it remains on the bottom of the carrier. Therefore, the more tests, the less release agent and thus, the higher the friction. Interactions involving treated surfaces were also investigated by Murtagh and Mallon who reported that the application of release agent eases interactions [82]. Although the authors investigated the contact between a treated metallic surface and a molten thermoplastic composite material, their observations are in good agreement with these presented in this study. However, the authors also showed friction coefficients to increase with test speeds. This effect,

which is not noticed in the present case, is assumed to be solely due to the presence of molten thermoplastic resin in their experiments. Given that no clear correlation with test speed and pressure is observed, friction coefficients presented in Tab. 4-9 are considered to be test speed and pressure independent.

**Tab. 4-9: Friction coefficients between treated separation film and tool surface calculated according to equation (4-10) for experiments performed without wall. Numbers in brackets correspond to the friction coefficients calculated for experiments performed with the left wall**

		<b>4.83 kPa</b>	<b>7.98 kPa</b>	<b>11.14 kPa</b>
<b>100 mm/min</b>	Test #1	0.199	0.244 (0.234)	0.117 (0.133)
	Test #2	0.291	0.305 (0.341)	0.138 (0.215)
	Test #3	0.311	0.344 (0.373)	0.251 (0.208)
<b>200 mm/min</b>	Test #1			0.195
	Test #2	Not investigated	Not investigated	0.241
	Test #3			0.286
<b>300 mm/min</b>	Test #1	0.212	0.127 (0.200)	0.101 (0.190)
	Test #2	0.242	0.166 (0.289)	0.107 (0.230)
	Test #3	0.285	0.180 (0.366)	0.184 (0.285)

Because release agent is applied once per configuration, only results obtained with “fresh” release agent can be taken into account for characterisation purposes. Therefore, only results referred to as “Test #1” are considered. To investigate the influence of guidance wall on measurements, average friction coefficients calculated for experiments performed with and without walls are presented in Tab. 4-10.

**Tab. 4-10: Average friction coefficients between treated separation film and tool surface calculated for “fresh” friction test results (tests #1 in Tab. 4-9)**

	<b>Without wall</b> [-]	<b>With left wall</b> [-]	<b>Influence</b> [%]
<b>Average friction coefficient (standard deviation)</b>	0.171 (±0.055)	0.189 (±0.042)	+10.84

Results obtained for tests performed with a guidance wall overestimate the actual friction coefficient. This effect, which has to be taken into account in the analysis of subsequent friction test results, is to be imputed to the contact existing between the wheels of the carrier and the wall.

### 4.3.3.2 Thermoplast/thermoplast

Investigations of the inter-ply slip in unidirectional thermoplastic laminates require intensive specimen preparation. In a first step, flat specimens are prepared from consolidated tailored thermoplastic composite blanks (see Chapter 1.1). While specimens to be clamped onto the specimen-platen are flat, specimens to be fixed below the carrier must be formed (see Appendix e).

Pretrials performed above melting temperature showed that the carrier specimen ripped off because of (i) insufficient clamping force and (ii) important adhesion with the other molten specimen. Modifications made to prevent specimen slippage and improve clamping capabilities consisted in the addition of a metallic plate behind the carrier and supplementary screws on the specimen attachment plates (see Appendix e). Despite these improvements, only experiments with the lowest pressure could be properly conducted (about 5.15 kPa). To investigate fibre orientation and test speed dependencies, experiments are performed with three different pairs of fibre orientations and test speeds. Orientations are given with respect to the movement of the carrier, i.e. pulling direction. When the fibre direction is aligned with the carrier motion, this is considered as “0°”. Each configuration is repeated three times with new specimens for each repetition. Tests are carried out after five minutes soaking time at 280°C with only one guidance wall. The test matrix is presented in Tab. 4-11.

**Tab. 4-11: Test matrix for inter-ply contact characterisation**

	0°/0°	0°/90°	90°/90°
	100 mm/min	100 mm/min	100 mm/min
<b>5.15 kPa</b>	200 mm/min	200 mm/min	200 mm/min
	300 mm/min	300 mm/min	300 mm/min

A typical outcome of a friction test performed between two molten thermoplastic specimens is presented in Fig. 4-35. The weak behaviour within the first 30 mm of the crosshead displacement corresponds to the straightening of the stainless steel wire. Once the wire is under tension, experimental results show that the force reaches a peak before decreasing to a constant level. Such behaviour is in good agreement with observations made by other researchers [43, 67, 82, 90, 200]. According to Murtagh and Mallon [82], who investigated interactions between molten thermoplastic composite materials and a metallic surface, this overshoot reflects the development of an adhesive bond created by the combination of heat and pressure. In the present study, such a phenomenon is also assumed to occur because of the pressure applied on the specimens during heat up, which lasts for at least 30 minutes. However, as reported by Sachs [43], the force overshoot could also be due to non-linear viscoelastic effects caused by flow start-up [81] or slip relaxation effects [201].

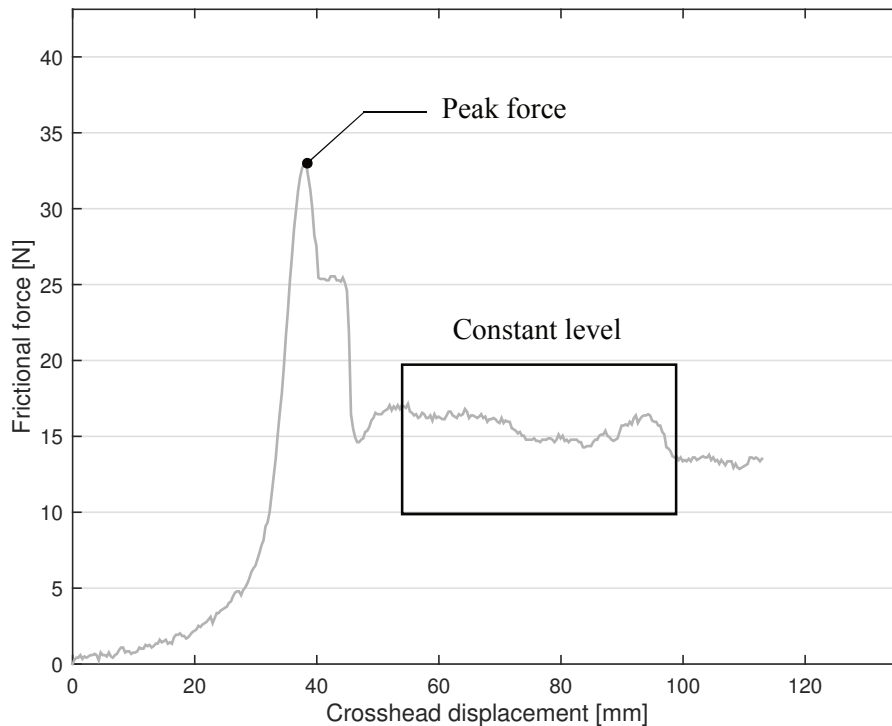


**Fig. 4-35: Typical outcome of a molten thermoplastic/molten thermoplastic friction test**  
Example given for 0°/0° and a test speed of 200 mm/min.

If the peak force is associated with a yield shear stress calculated according to equation (4-11) [43, 67, 82, 90, 200], this value can be associated to the shear strength required to break such adhesive bonds and thus, initiate motion (see Chapter 2.2.5). Inter-ply shear stresses  $\tau_{fric}$  are calculated as the ratio between the frictional force measured by the load cell  $F_{fric}$  and nominal specimen area  $A$  ( $77 \times 40 \text{ mm}^2$ ):

$$\tau_{fric} = \frac{F_{fric}}{A} \quad (4-11)$$

In the following, peak and steady-state shear stresses calculated according to equation (4-11) are analysed separately, in particular their dependencies to test speeds and fibre orientations. Because of experimental difficulties, only two out of three repetitions are considered for tests performed at 100 mm/min.

### Peak shear stress

The evolutions of peak shear stresses with respect to test speeds for different fibre orientations are presented in Fig. 4-36 and Fig. 4-37. For all configurations, peak shear stresses increase with test speeds. This is in good agreement with observations made by Sachs [43] and Vanclooster [200]. The dependency of peak shear stresses to test speeds is assumed to be mainly due to the viscous behaviour of the adhesive bonds described by Murtagh and Mallon [90].



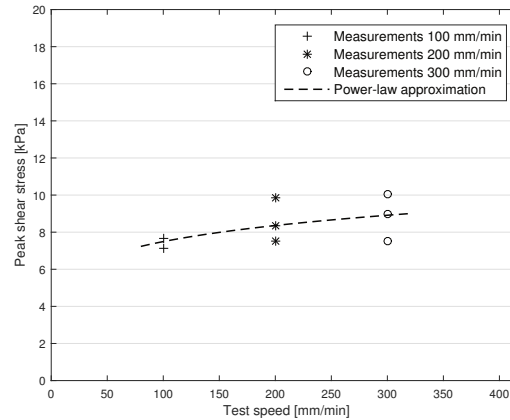


**Fig. 4-36:** Evolution of peak shear stresses with respect to test speed in a  $0^\circ/0^\circ$  configuration

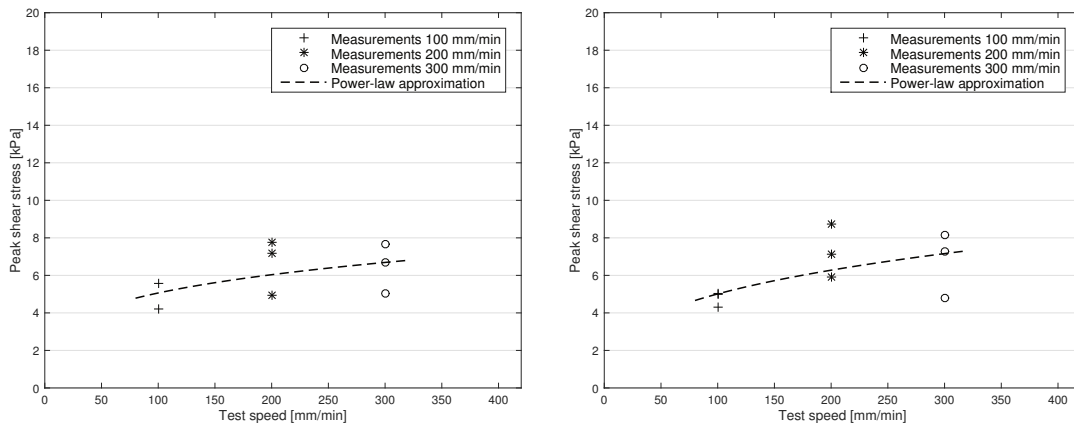


**Fig. 4-37:** Evolution of peak shear stresses with respect to test speed  
Left:  $0^\circ/90^\circ$  configuration; Right:  $90^\circ/90^\circ$  configuration.

While peak shear stresses measured for  $0^\circ/90^\circ$  and  $90^\circ/90^\circ$  configurations have similar order of magnitudes, these are quantitatively smaller than the peak shear stresses measured for the  $0^\circ/0^\circ$  configuration. In a similar manner as for adhesive joints [202], weaker behaviour observed for configurations with at least one  $90^\circ$  specimen is assumed to be caused by the lack of reinforcement in strain direction, i.e. no fibre aligned with load introduction.

### Steady-state shear stress

The evolutions of steady-state shear stresses with respect to test speeds are presented in Fig. 4-38 and Fig. 4-39 for different fibre orientations. For all configurations, these decrease and level off as test speeds increase. This behaviour is in good agreement with literature for tests conducted at low pressure values [43]. Sachs, who investigated interactions between a metallic foil and molten thermoplastic composite materials, attributed this decrease to a contraction and/or discontinuity of the inter-layer resin film [43]. If experiments would be performed at higher pressures, steady-state shear stresses would rather increase before levelling off [43, 82].

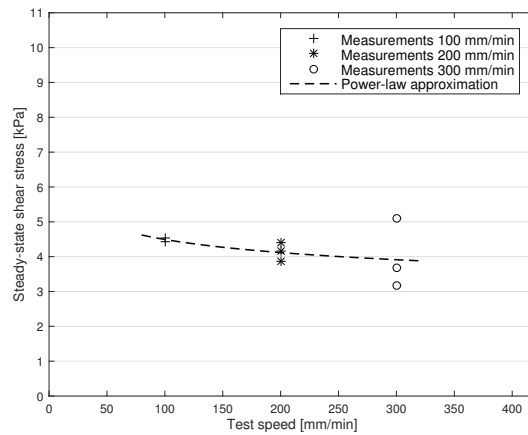


**Fig. 4-38:** Evolution of steady-state shear stresses with respect to test speed in a 0°/0° configuration

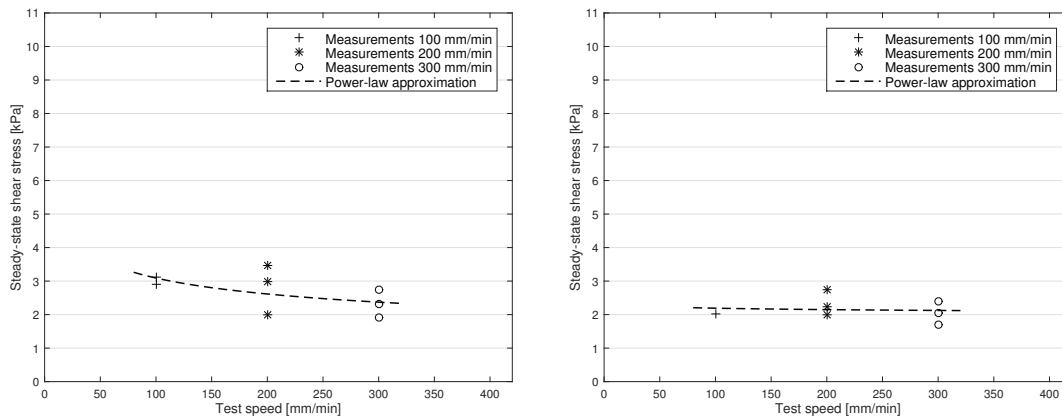


**Fig. 4-39:** Evolution of steady-state shear stresses with respect to test speed  
Left: 0°/90° configuration; Right: 90°/90° configuration.

Steady-state shear stresses for 0°/0° tests are found to be higher than these measured for 0°/90° and 90°/90° experiments. Murtagh and Mallon, who investigated interactions between molten thermoplastic composites, related this behaviour to the viscosity of the arrangement, which is larger in parallel-ply layups (0°/0°) than in 0°/θ° configurations (with θ ≠ 0) [82]. That parallel ply layups are more resistant to slip than 0°/90° configurations was also reported by Scherer and Friedrich [67].

Scherer and Friedrich reported that frictional forces in 90°/90° configurations were higher than these in 0°/0° configurations [67], which is inconsistent with the test results illustrated in Fig. 4-38 and Fig. 4-39. However, presented measurement data for 90°/90° and, to some extent, for 0°/90° should be considered carefully. Because of the lack of reinforcement in strain direction and the motion of the carrier, local ply tearing in 90° specimens is observed (see Chapter 4.5). Such “bulk” deformations, which were also evidenced by Scherer and Friedrich for 90°/90° configurations [67], complicate and influence the characterisation of configurations having at least one 90° specimen.

### Input for thermoforming simulation

Because interactions in PAM-FORM cannot be modelled via force-displacement curves such as these presented in Fig. 4-34 and Fig. 4-35 but can only be implemented via constant parameters *FRICT* (see Chapter 3.3.2), friction coefficients must be determined. According to Lebrun et al. [90], friction coefficients  $\mu$  can be calculated as follows:

$$\mu = \frac{\tau_{fric}}{\sigma_{fric}} = \frac{F_{fric}}{N} \quad (4-12)$$

where  $\sigma_{fric}$  is the pressure applied on the carrier (about 5.15 kPa),  $F_{fric}$  is the frictional force and  $N$  is the normal force, i.e. carrier load.

Results displayed in Tab. 4-12 present static and kinetic friction coefficients corresponding to peak and steady-state shear stresses, respectively (see Chapter 2.2.5). These are calculated according to the regressions determined from experimental test results for the same test speed as this used for thermoforming experiments, i.e. 50 mm/min (see Chapter 6.1.1). Results reflect “true” inter-ply friction coefficients since friction generated by carrier wheels during motion have been taken into account and subtracted from measurement data (10.84%, see Chapter 4.3.3.1).

**Tab. 4-12: Inter-ply static and kinetic friction coefficients calculated for 50 mm/min**

	0°/0°	0°/90°	90°/90°
<b>Static friction coefficient [-]</b>	1.303	0.824	0.776
<b>Kinetic friction coefficient [-]</b>	0.956	0.709	0.436

#### 4.3.3.3 Treated separation film/thermoplast

Separation film specimens are prepared from the same polyimide film [192] and treated with the same release agent as these used for thermoforming experiments [199] (see Chapter 6.1.1). Thermoplastic specimens are fixed below the carrier and prepared as presented in Appendix e.

The strong adhesion between molten thermoplastic specimens and treated films prevent proper characterisation. Although the carrier has been reworked to enhance clamping capabilities (see Chapter 4.3.3.2), none of the experiments can be successfully conducted. Based on the maximum force recorded by the load cell before the specimens rip off, static friction coefficient, calculated according to equation (4-12), can be assumed to be at least equal to 2.5.

## 4.4 Characterisation of a non-cured unidirectional thermoset composite material

According to the goals of this doctoral dissertation (see Chapter 1.2), a non-cured thermoset composite tape is tested under environmental forming conditions to assess whether the test methods considered for molten thermoplastic materials are also suitable for the characterisation of this type of materials. Investigations are performed using similar procedures as detailed in Chapter 4.1.

In the scope of this study, a non-cured unidirectional carbon fibre thermoset pre-impregnated tape qualified for aerospace applications supplied by Hexcel is considered and tested under environmental forming conditions, i.e. 60°C. The material has a nominal thickness of about 0.26 mm. In a similar manner as thermoplastic tapes, specimens are prepared from unidirectional tailored blanks laid by an ATL machine.

### 4.4.1 Intra-ply shear

Intra-ply shear investigations are conducted with the same three approaches as these considered in Chapter 4.1.1: (i) a picture frame test setup, a rotational rheometer using (ii) a parallel platens measuring system and (iii) a torsion bar arrangement.

#### 4.4.1.1 Picture frame test setup

Single layer specimens are brought into the frame at room temperature and tested at 60°C (see Fig. 4-40). A proper positioning is achieved when fibres are parallel to their respective side lengths. Given the lack of reinforcement in one direction, specimens are only clamped on two sides, i.e. perpendicular to fibre direction. Once clamped, specimens have a free area of 200 x 150 mm<sup>2</sup>. Experiments are performed at test speeds of 50, 100 and 200 mm/min.

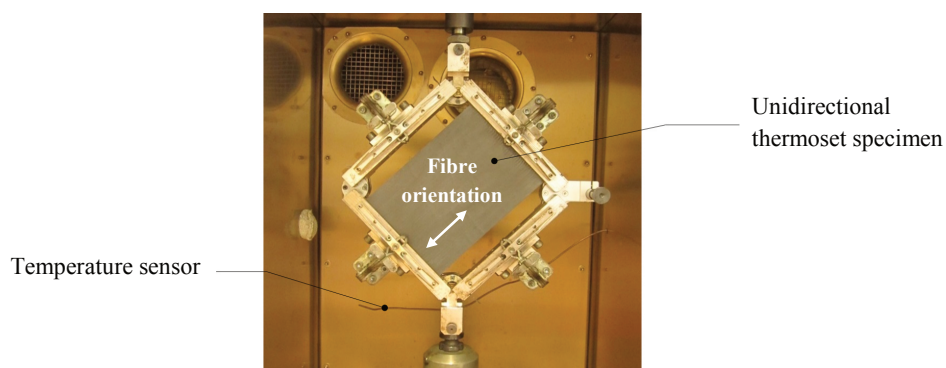


**Fig. 4-40:** Non-cured unidirectional thermoset specimen clamped in a picture frame setup, mounted in a testing machine and enclosed within an environmental chamber

In a similar manner as for unidirectional thermoplastic specimens (see Chapter 4.1.1.2), picture frame tests lead to the early occurrence of out-of-plane wrinkles. For

large displacements, i.e. shear angles, specimen failure is even observed. In particular, transverse ply tearing is noticed (see Fig. 4-41). Such observations are in good agreement with investigations performed by Leutz [128]. Winkles and failure are due to clamping, which prevents fibres to rotate (see Fig. 4-41), and weak specimen integrity. The typical evolution of a picture frame test is presented in Fig. 4-42.

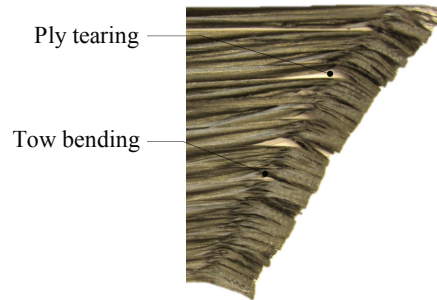


**Fig. 4-41: Transverse ply tearing and tow bending within a sheared specimen (final state)**

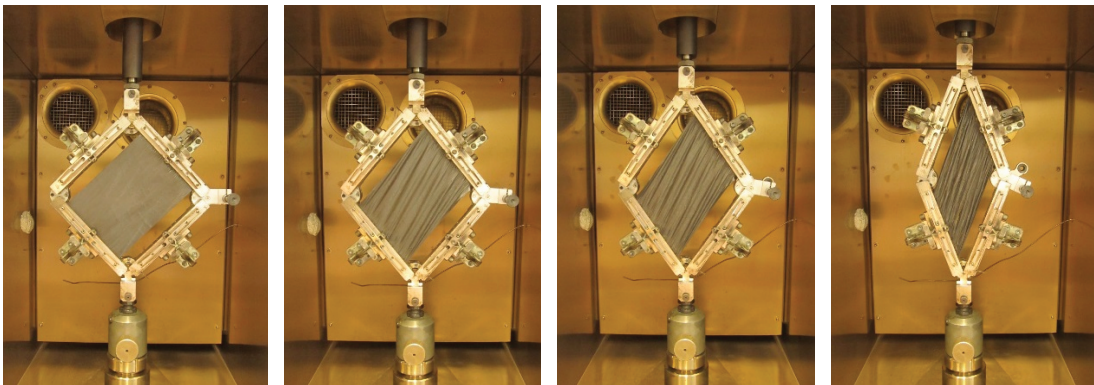


**Fig. 4-42: Typical evolution of a picture frame test of a non-cured unidirectional thermoset specimen**

From left to right: specimen at rest, specimen after about 5 mm displacement, specimen after about 40 mm displacement, final position.

#### 4.4.1.2 New rotational parallel platens test setup

The experimental results presented in this section have been generated in the context of the following Term Project [S7].

Investigations are conducted with the same rotational rheometer as this introduced in Chapter 4.1.1.3 (MCR 302, Anton Paar) and the same test method as presented in Appendix b. Compared to these experiments, few differences are, however, to be noticed:

- Instead of an environmental chamber, experiments are performed with a Peltier temperature control unit (see Fig. 4-43),
- Instead of laying specimens on a bottom platen, specimens are laid inside a cup,
- Top platen and lower cup are not changed after every test.

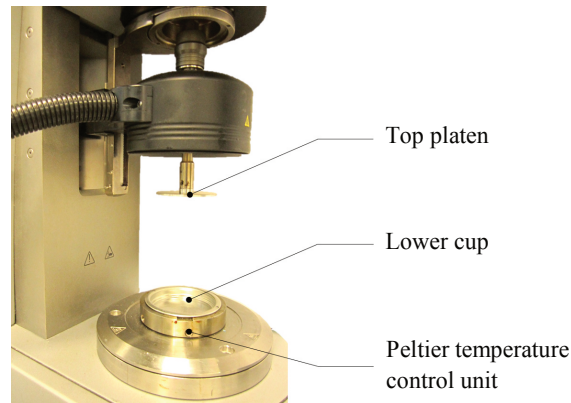


**Fig. 4-43: Rotational rheometer used with a Peltier temperature control unit**

Rectangular single layer specimens are laid onto the lower cup while temperature is already at 60°C. Once isothermal conditions are reached, the top platen is lowered to a specific gap thickness, i.e. 0.16 mm, to ensure good contact with the specimen. Oscillatory tests are started five minutes after the selected gap thickness is reached.

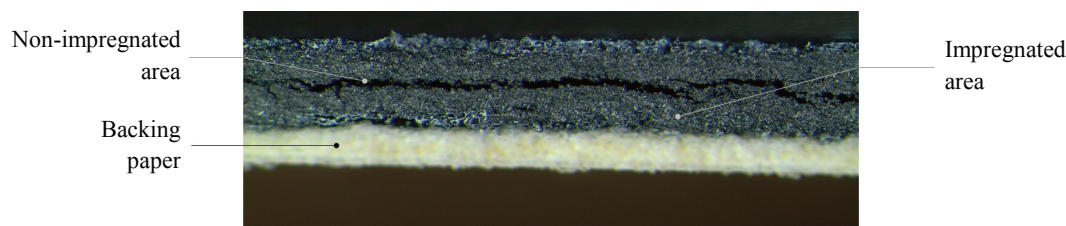


**Fig. 4-44: Microscopy from a non-cured unidirectional thermoset specimen [S7]**

Because of inconsistent test results, material microstructure is investigated using a stereo microscope (SZX10, Olympus). Microscopy analysis highlights non-uniform material through-thickness impregnation (see Fig. 4-44). Given that such material configuration prevents the even distribution of shear deformations throughout the specimens, the rotational parallel platens test setup cannot be considered to characterise this non-cured unidirectional thermoset pre-impregnated composite material.

#### 4.4.1.3 Torsion bar test method

The experimental results presented in this chapter have been generated in the context of the following Term Project [S10].

Investigations are conducted with the same rheometer as this presented in Chapter 4.1.1.3 (MCR 302, Anton Paar). Experiments are performed within an environmental chamber with low flow of nitrogen. Prismatic bars with rectangular cross-section are prepared. The dimensions of the specimens are 60 ( $L$ ) x 13 ( $W$ ) x 12 ( $T$ ) mm, where  $L$  is the dimension in fibre direction,  $W$  is the dimension transverse to the fibre direction and  $T$  is the thickness. Because material is soft and tacky at room temperature, specimens are prepared when material is still in its frozen state. Despite this precaution, local inter-ply shear is noticed at specimen edges (see Appendix f).

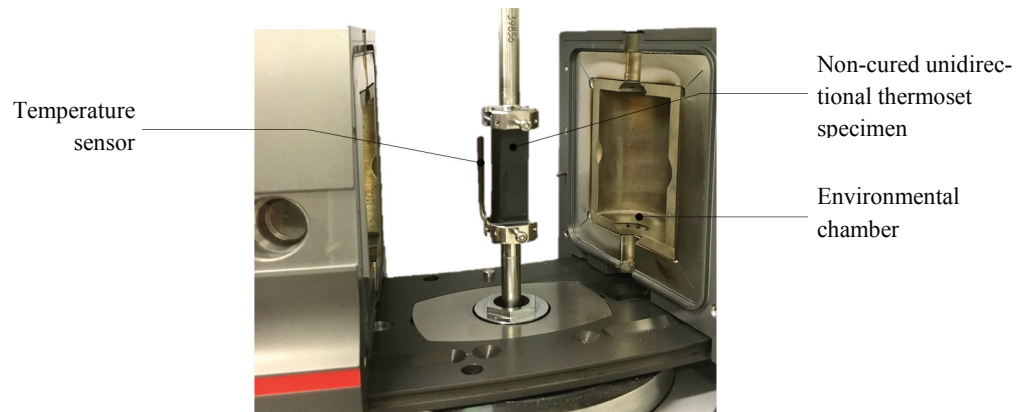


**Fig. 4-45: Unidirectional fibre-reinforced thermoset composite specimen enclosed within an environmental chamber and mounted in a rheometer for torsion tests**

Specimens are positioned while the environmental chamber is already at testing temperature, i.e. 60°C (see Fig. 4-45). Investigations performed with thermocouples positioned in the inner and outer sides of the specimens showed a soaking time of ten minutes to be sufficient to reach isothermal conditions.

Amplitude sweeps are performed from 10<sup>-4</sup>% to 1% of strain at three angular frequencies (1 rad/s, 10 rad/s and 100 rad/s). Results illustrated in Fig. 4-46 are the average values of the storage modulus calculated over five repetitions. An average error of about 22% is to be reported. The LVE region ends when a dynamic viscoelastic function, e.g. storage modulus, deviates by maximum 10% from a constant value [169, 170]. To be conservative, although the shear strain indicating the end of the LVE region  $\gamma_{max}$  is calculated for all angular frequencies, only the lowest value is eventually considered, i.e. 1.5 x 10<sup>-3</sup>%.

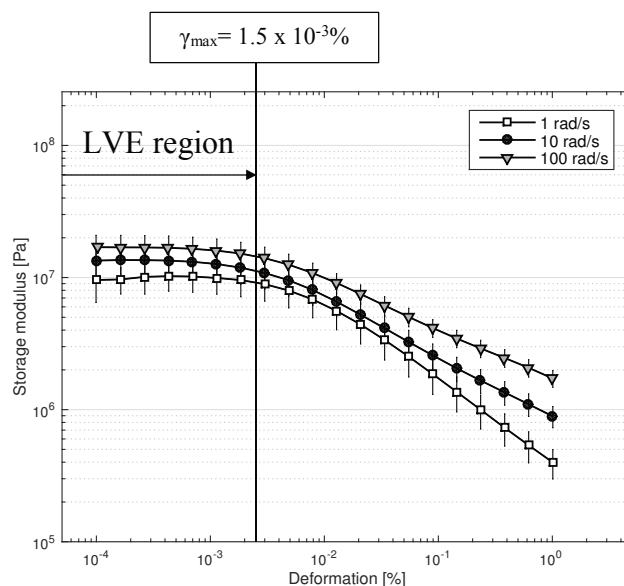


**Fig. 4-46: Average amplitude sweep test results of non-cured unidirectional thermoset pre-impregnated composite specimens**

Investigations performed at 1 rad/s, 10 rad/s and 100 rad/s.

Once the limit of the LVE region is determined, frequency sweeps are carried out. To perform tests at the highest strain possible, experiments are performed at  $\gamma_{max}$ . Angular frequencies are varied from 0.1 rad/s to 500 rad/s. Results illustrated in Fig. 4-47 are the average values of the storage and loss moduli calculated over five repetitions. With an average error of 9% for the storage modulus and 7% for the loss moduli, an overall good reproducibility is to be reported.

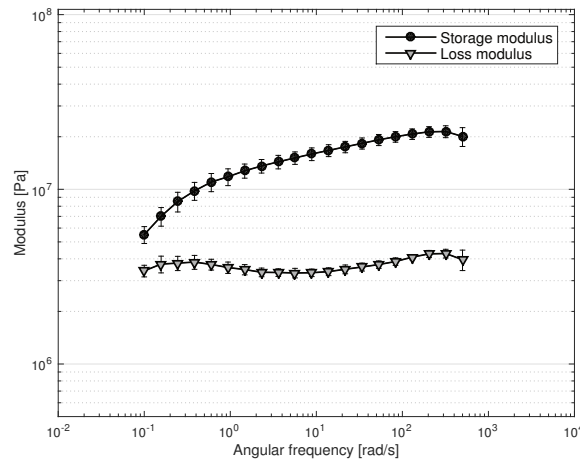


**Fig. 4-47: Average frequency sweep test results of non-cured unidirectional thermoset pre-impregnated composite specimens**

Investigations performed at  $1.5 \times 10^{-3}\%$  of strain.

Following the method detailed in Appendix b and initially described by Haanappel and Akkerman [62, 66], frequency sweep results are used to determine shear relaxation modulus  $G_r$  (see Fig. 4-48). To account for “true” material behaviour, loads caused by internal machine friction are subtracted from measurement data. Measurement data for both the lowest and highest angular frequencies are discarded to avoid boundary effects. The longitudinal shear relaxation modulus is eventually calculated using the finite difference scheme introduced by Schwarzl et al. [165] and Schwarzl [166] (see equation (A-18) in Appendix b).

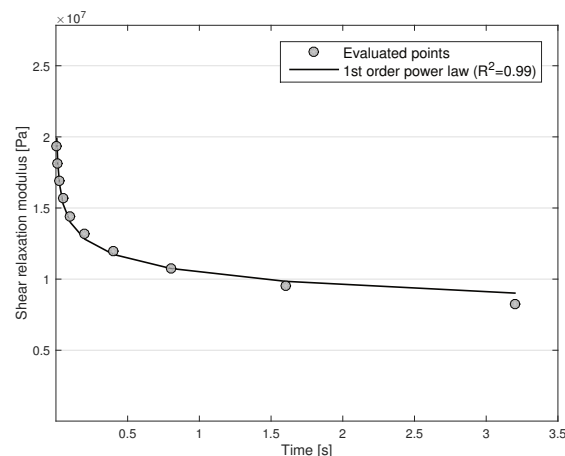


**Fig. 4-48: Approximated shear relaxation modulus of a non-cured composite material**



Shear stresses are eventually calculated according to equation (A-19) (see Appendix b). Results are presented in Fig. 4-49 for three different shear rates. The maximum shear rate is calculated using equation (A-20) (see Appendix b) with  $\gamma = \gamma_{max}$  (end of the LVE region) and  $\omega = 320$  rad/s (sweeps are performed up to 500 rad/s but, to avoid boundary effects, first and last data are not taken into account). Although a slight rate dependency is noticed, results highlight elastic dominated behaviour. These observations are similar to these reported for the thermoplastic material (see Chapter 4.1.1.4).

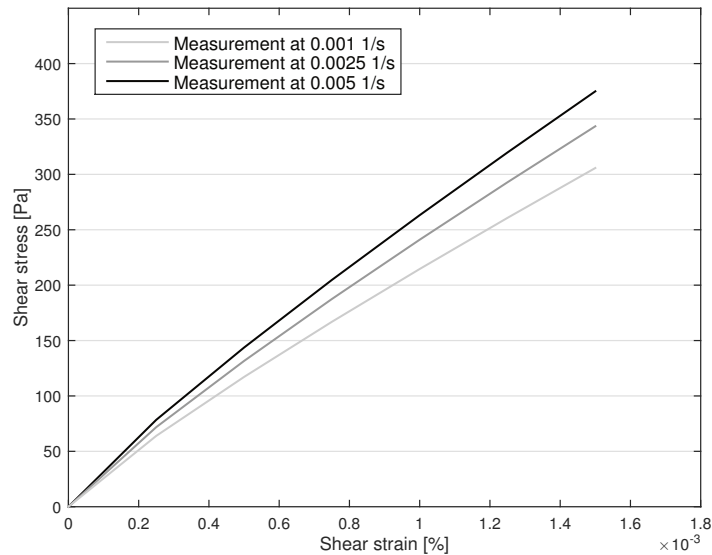


**Fig. 4-49:** Stress-strain response of a non-cured unidirectional thermoset pre-impregnated tape subjected to longitudinal shear deformations

## 4.4.2 Out-of-plane bending

According to preliminary experimental (see Chapter 4.1.2.1), longitudinal out-of-plane bending behaviour is investigated using a DMA system with a three-point bending fixture of 20 mm span length and specimens of 1 mm thickness.

Specimens are positioned in the machine at room temperature (see Fig. 4-50). The alignment of the sample is appropriate when the width of the specimens is parallel to the clamps/support. A good positioning is essential to avoid unsymmetrical loading. A preload force of 0.001 N is applied. Specimens are then heated to testing temperature, i.e. 60°C, at a heating rate of 10 K/min. Flowing nitrogen is used to regulate temperature. While heating up, the machine is forced to keep a neutral displacement in order not to alter the quality of the specimens. To ensure a homogeneous temperature distribution within the specimen, tests are performed ten minutes after isothermal conditions are reached. Finally, quasistatic tests are carried out at forming temperature for four different test speeds comprised between 500  $\mu\text{m}/\text{min}$  and 4000  $\mu\text{m}/\text{min}$  in order to characterise the longitudinal out-of-plane bending behaviour of this non-cured unidirectional carbon fibre-reinforced thermoset pre-impregnated composite material.

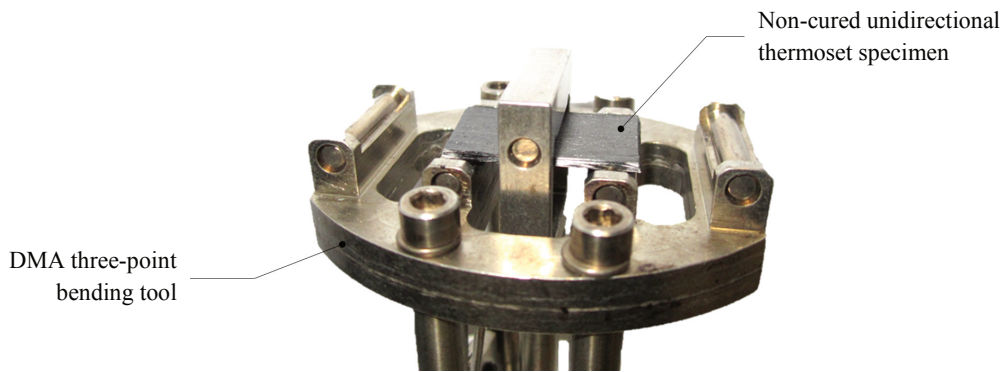


**Fig. 4-50: Non-cured unidirectional thermoset specimen mounted in a DMA three-point bending tool (20 mm)**

Stress-strain data are determined according to equations (4-1) and (4-2), respectively. Results presented in Fig. 4-51, which highlight slight viscous behaviour, are the average values calculated over at least five repetitions. Inconsistencies for low strain values, e.g. stresses calculated for 4000  $\mu\text{m}/\text{min}$  are smaller than these calculated for 2000  $\mu\text{m}/\text{min}$ , are caused by machine acceleration. Details about machine acceleration can be found in [P2].

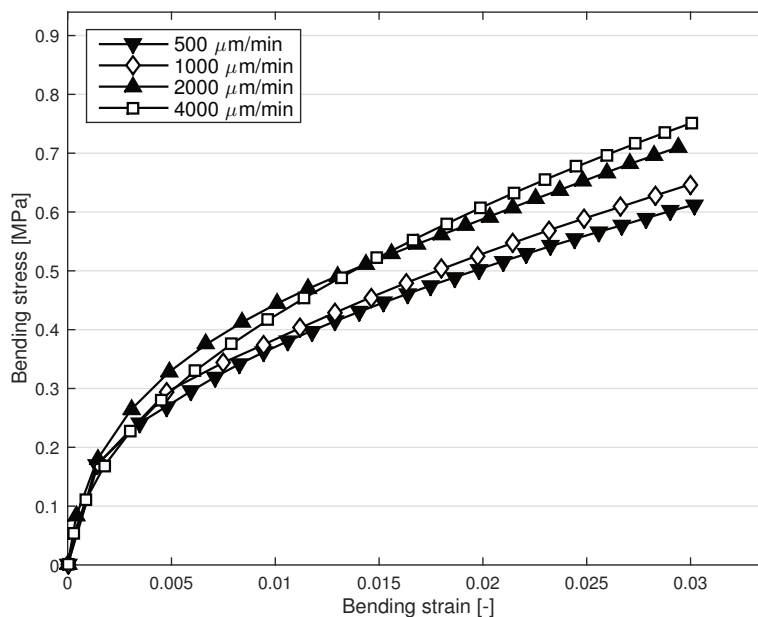


**Fig. 4-51: Average bending stress-strain results of non-cured unidirectional thermoset specimens (investigations performed at 60°C for different test speeds)**

Standard deviations of the stresses presented in Fig. 4-51 are given in Tab. 4-13 for different strain values. An overall good reproducibility is to be acknowledged, although standard deviations are slightly larger than for thermoplastic specimens. This is to be imputed to specimen preparation. Because material is soft and tacky at room temperature, specimens are more subjected to fibre reorientations (see Appendix g).

Tab. 4-13: Standard deviations of the stresses presented in Fig. 4-51

	500 $\mu\text{m}/\text{min}$	1000 $\mu\text{m}/\text{min}$	2000 $\mu\text{m}/\text{min}$	4000 $\mu\text{m}/\text{min}$
Stress standard deviation [%] at $\varepsilon = 0.0075$	9.681	7.387	15.096	18.645
Stress standard deviation [%] at $\varepsilon = 0.015$	9.094	8.140	10.668	9.774
Stress standard deviation [%] at $\varepsilon = 0.0225$	8.338	7.837	10.872	8.552

Due to the acceleration of the machine, only the last third of data recorded by the DMA system are used to calculate out-of-plane bending moduli [P2]. Calculations are performed according to equation (4-3).

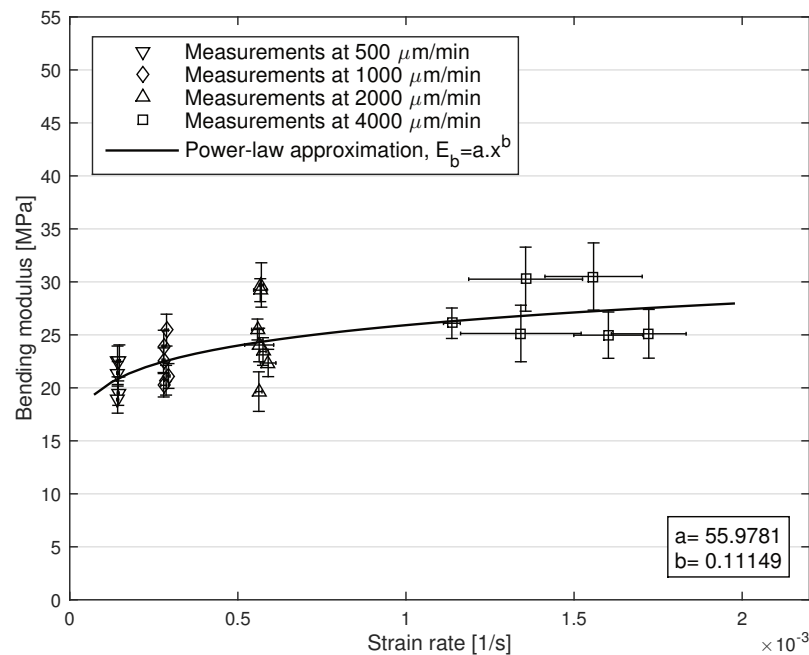


Fig. 4-52: Strain rate dependency of the longitudinal out-of-plane bending modulus of a non-cured unidirectional thermoset composite material (60°C)

The evolution of the longitudinal out-of-plane bending modulus with respect to strain rates is displayed in Fig. 4-52. Correlations between test speeds (input given to the DMA system) and strain rates are calculated according to equation (4-4) and presented in Tab. 4-14 for specimens of ideal geometries (20 mm length, 15 mm width and 1 mm thickness). Data scattering and standard deviations for tests conducted at 4000  $\mu\text{m}/\text{min}$  indicate the difficulty encountered by the machine to accurately apply such a test speed. This test speed seems to be the limit of the machine.

**Tab. 4-14: Equivalence between test speeds and strain rates for specimens of ideal geometry**

Test speed [ $\mu\text{m}/\text{min}$ ]	500	1000	2000	4000
Strain rate [1/s]	$1.25 \times 10^{-4}$	$2.5 \times 10^{-4}$	$5 \times 10^{-4}$	$1 \times 10^{-3}$

Vertical errors are due to the material non-linear stress behaviour (see Fig. 4-51) and the fact that calculations are performed over the last third of the measurements. A maximum error of 11% is to be reported. Results are found to satisfy a power-law approximation within the range of data:

$$E_B = 55.98 \cdot \dot{\epsilon}_B^{0.11} \quad (4-13)$$

### 4.4.3 Transverse tension

Most of the content of this section, including text and figures, is based on [P3].

In-plane transverse tensile properties are characterised using a universal testing machine, on the one hand, and a DMA system, on the other hand. The aim is to assess the relevance of the DMA test method introduced in Chapter 4.1.3.2. For comparison purposes, experiments are conducted under similar environmental conditions, i.e. 60°C.

Specimens of 200 (L) x 40 (W) x 1 (T) mm<sup>3</sup> for the tensile testing machine and of 6.5 (L) x 23 (W) x 1 (T) mm<sup>3</sup> for the DMA system, where  $L$  is the length in fibre direction,  $W$  is the dimension transverse to fibre direction and  $T$  is the thickness, are prepared at room temperature from defrosted unidirectional tailored blanks. To protect DMA clamps, specimen tips are wrapped in aluminium tapes (see Fig. 4-53 left). Because of the soft and tacky aspects of the material at room temperature, specimens are subjected to fibre reorientations (see Appendix h). This effect is, however, not further investigated in the present study.

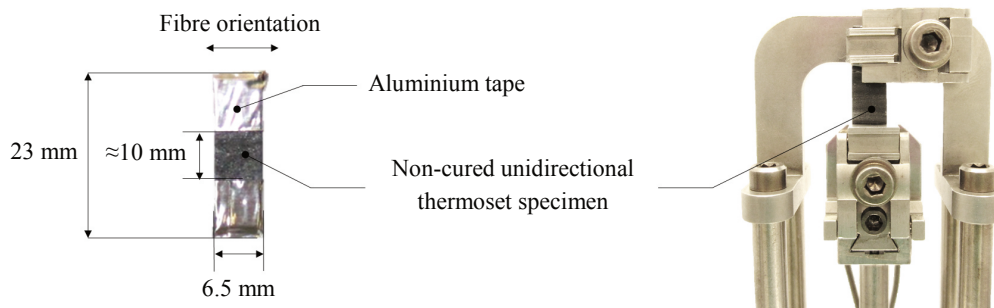


**Fig. 4-53: Non-cured unidirectional thermoset specimen whose tips are wrapped in aluminium tapes (left) and non-cured unidirectional thermoset specimen mounted in a DMA system (right)**

The universal testing machine and the environmental chamber considered for these analyses are the same ones as those used for the investigations detailed in Chapter 4.1.3.2. To avoid the introduction of any pre-tension, specimens are clamped at room temperature on the upper clamp. They are subsequently brought into the environmental chamber and fixed to the lower clamp. A good positioning of the specimen is achieved when an initial free test length of 20 mm is achieved (10 mm clamping on each side) and when the specimen's fibre orientation is parallel to the side length of the clamps. When testing temperature is reached, an appropriate soaking time (evaluated using thermocouples) of ten minutes is applied. Quasi-static tests are eventually carried out at 5 mm/min, 25 mm/min, 75 mm/min, 150 mm/min and 300 mm/min. For each test speed, five repetitions are performed.

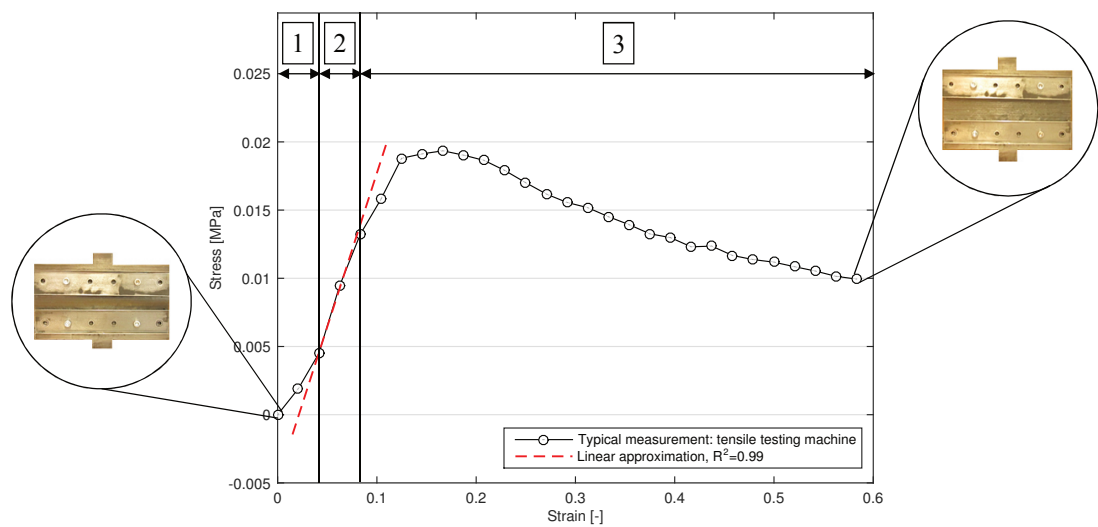


**Fig. 4-54: Typical stress-strain result of a non-cured unidirectional thermoset composite material tested at 60°C with a universal testing machine (example given for 25 mm/min)**

Specimens are positioned in the DMA system at room temperature and clamped with a torque of 3 in.lb (0.34 N.m). The alignment of the sample is appropriate when the specimen's fibre orientation is parallel to the side length of the clamps (see Fig. 4-53 right). An initial free length of about 10 mm is to be reported. The furnace is subsequently closed and heated up to 60°C at a rate of 10°C/min. During the heating up phase, the actuator is blocked to avoid undesirable effects. To ensure a homogeneous temperature distribution, tests are performed ten minutes after isothermal conditions are reached. In a similar manner as for molten thermoplastic specimens, due to unsuccessful attempts at constant test speeds, tests are conducted at constant loading rates (0.025 N/min, 0.05 N/min, 0.075 N/min, 0.100 N/min and 0.125 N/min). At least five repetitions are performed for every configuration.

Typical results obtained with the universal testing machine and the DMA system are presented in Fig. 4-54 and Fig. 4-55, respectively. Stresses and strains are calculated according to equations (4-7) and (4-6), respectively.

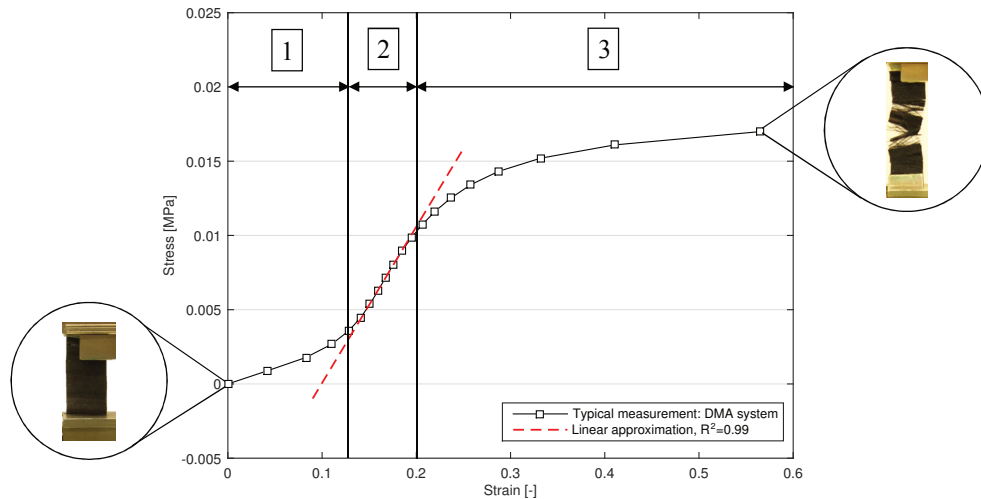


**Fig. 4-55: Typical stress-strain result of a non-cured unidirectional thermoset composite material tested at 60°C with a DMA system (example given for 0.1 N/min)**

Regarding measurements performed with the DMA system, although specimens always have an initial stiffness within the measuring range of the machine (see Chapter 4.1.2.1), their stiffness happen to drop below  $10^2$  N/m during testing. However, based on the excellent reproducibility and consistency of the results, the introduced error is assumed to be negligible.

Results illustrated in Fig. 4-54 and Fig. 4-55 depict similar material behaviour, which can be split in three regions. The early weak behaviour is assumed to be caused by several phenomena like (i) specimen straightening and/or (ii) specimen slippage. The second zone corresponds to the actual phase where the material is characterised. The third and last part coincides with failure. Deteriorations of the specimen's integrity are particularly well depicted by the change of slope (failure initiation) and the drop of force, which eventually indicates specimen failure (see Fig. 4-54). Similar observations are made in Fig. 4-55, although the change of slope is not followed by a drop of force but by a levelling off. This is due to the manner with which the DMA system is controlled, i.e. constant loading rate (instead of constant test speed). The material depicts linear stress-strain response within regions 2 in Fig. 4-54 and Fig. 4-55. As the ratio between engineering stress and engineering strain (see equations (4-7) and (4-6), respectively) within linear regions, moduli are approximated as the slope of the tangent of stress-strain curves. For comparison purposes between results obtained with the universal testing machine and the DMA system, such moduli are derived as function of test speeds and loading rates, respectively.

A particular drawback of performing experiments at constant loading rates is that test speeds vary over time. For comparison purposes with results obtained at constant test speeds (universal testing machine), “equivalent” test speeds have thus to be determined. To do so, test speeds measured by the DMA system over the region considered for the determination of the moduli, i.e. regions 2 in Fig. 4-55, are averaged and con-

verted to strain rates using the geometry of the specimens (measured with a 1  $\mu\text{m}$  accuracy). A mean error of about 11% is to be reported for such averaging operations. Strain rates are subsequently averaged per test configuration (see Tab. 4-15 and horizontal standard deviations in Fig. 4-56 right). For tests performed with the universal testing machine, strain rates calculations are easier since experiments are performed at constant test speeds (see Tab. 4-15).

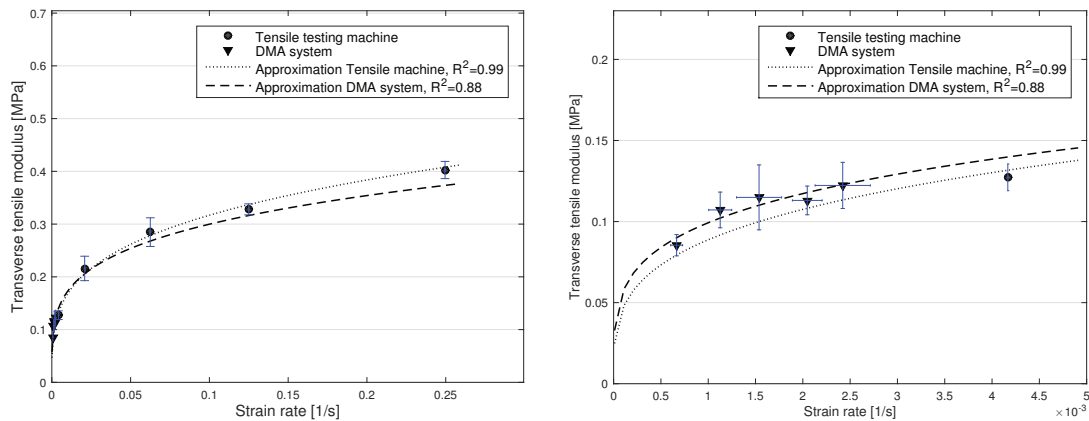


**Fig. 4-56: Evolution of transverse tensile modulus with respect to strain rate of a non-cured unidirectional thermoset composite material tested at 60°C**

Full curve (left) and close-up (right) comparison between results obtained with a universal testing machine and a DMA system.

The evolution of moduli with respect to strain rates is used as basis for comparison. As it can be seen in Fig. 4-56 left, both test methods produce similar results and depict a distinct strain rate dependency. The maximum discrepancy between both methods remains smaller than 10% for a strain rate of 0.25 1/s. Given that experiments obtained with the DMA system are restrained to small strain rates (maximum 2.42 E-3 1/s, see Fig. 4-56 right and Tab. 4-15), the error grows as data are extrapolated. This is a drawback of the presented test method since strain rates occurring during industrial thermoforming processes, and thus strain rates at which material characterisation tests must be performed for the development of FE thermoforming simulations, can be particularly high. This disadvantage could be overcome by reducing the initial specimen free length. Further analyses would be however necessary to investigate the influence of clamping on such short specimens.

Results obtained by both test methods are globally consistent with each other and show good reproducibility (see vertical standard deviations in Fig. 4-56). Inaccuracies introduced by test speed averaging do not seem to have much influence on experimental results. Although strain rates at which experiments can be conducted appear to be limited, the presented test method shows good potential for the characterisation of transverse tensile properties. The DMA system also proved to be a more efficient test method offering a better control of environmental test conditions. Time saving is mainly due to reduced efforts to mount/unmount specimens.

**Tab. 4-15: Average strain rates for investigations conducted on a non-cured unidirectional thermoset composite material at constant loading rates (DMA system) and constant test speeds (universal testing machine) – Standard deviations are also plotted in Fig. 4-56 (see horizontal bars)**

	Test speed [mm/min]	Loading rate [N/min]	Average strain rate [1/s]	Standard deviation [%]
<b>DMA system</b>	-	0.025	6.66 E-4	9.51
	-	0.05	1.13 E-3	10.76
	-	0.075	1.54 E-3	15.48
	-	0.100	2.05 E-3	7.66
	-	0.125	2.42 E-3	12.03
<b>Universal testing machine</b>	5	-	4.17 E-3	< 0.01
	25	-	2.08 E-2	< 0.01
	75	-	6.25 E-2	< 0.01
	150	-	1.25 E-1	0.051
	300	-	2.50 E-1	0.106

#### 4.4.4 Inter-ply slip

Inter-ply slip experiments are conducted with the test setup developed in the scope of this doctoral dissertation and presented in Chapter 4.3.2. Investigations are performed at 60°C for three different test speeds (25 mm/min, 100 mm/min and 300 mm/min) and fibre orientations (0°/0°, 0°/90° and 90°/90°). Because thermoset composite materials are soft at room temperature, specimen preparation is more efficient than with their thermoplastic counterparts.

None of the experiments performed with the new friction test setup work properly. As the pulling force increases, the carrier starts rotating around its attachment hook instead of sliding (see Fig. 4-57). This behaviour, which becomes more significant as test speed increases, is due to the high tackiness of the material and the usage of an attachment hook. To prevent the development of a bending moment at the attachment hook, the latter should be ideally located in the same plane as contact occurs. However, since this is practically unachievable for “carrier test setups”, other approaches, e.g. pull-out and pull-through apparatus, should be considered for the inter-ply slip characterisation of non-cured thermoset materials.



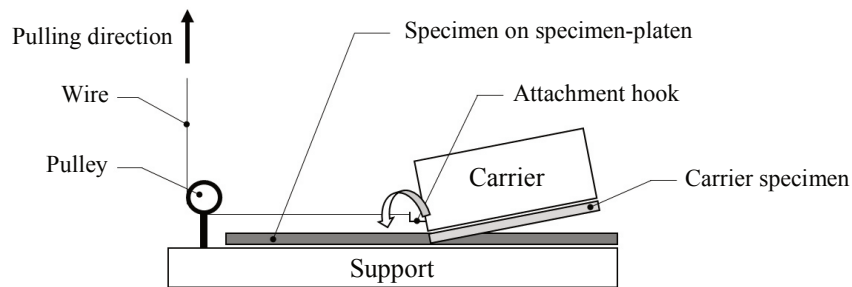


Fig. 4-57: Schematic of typical carrier rotation observed during inter-ply slip investigations

Experiments performed at *Fraunhofer Institute* (Augsburg, Germany) with horizontal pull-out and pull-through test setups give satisfactory results for certain configurations. Results can, however, not be presented because investigations are still on-going.

## 4.5 Discussion

The work presented in this chapter aimed to:

- characterise under environmental forming conditions the intrinsic behaviour of a unidirectional thermoplastic composite tape (UD-CF/PA6) as well as a polyimide separation film and their respective interactions,
- assess whether the test methods applied to the molten fibre-reinforced thermoplastic composite material are appropriate for a non-cured unidirectional thermoset composite tape.

### 4.5.1 Benefits and limits of presented test methods

To determine proper input parameters for the development of FE thermoforming simulations, the (i) intra-ply shear, (ii) out-of-plane bending and (iii) in-plane tensile behaviour of the unidirectional thermoplastic composite material considered in this study (UD-CF/PA6) were investigated under environmental forming conditions. The composite viscosity was subsequently determined using an analytical approach based on transverse tensile test results. Because of the lack of methods and test standards published in literature, several new test methods were developed.

First intra-ply shear investigations were performed with a picture frame test setup. Because of the early occurrence of out-of-plane wrinkles, no test results could be accounted for material characterisation. In a second approach, experiments were conducted with a rotational rheometer and a parallel platens test setup. Because of poor equipment quality, test results could not be used for material characterisation. The consideration of high-precision disposable platens should, however, enable the proper application of this test method. In a third and last approach, the torsion bar test method introduced by Haanappel and Akkerman [62, 66] was considered. The regulation of a temperature of 280°C in a nitrogen-enriched atmosphere appeared to be difficult to achieve because of equipment limits. Tests performed with sensors measured an actual

specimen temperature of about 272°C [S10]. Although the resulting error cannot be quantified, it can be considered negligible. Test results are in good agreement with literature [62, 66] and highlight that material behaviour is dominated by elastic deformations within the range of data. However, squeeze-out effects caused by clamping conditions might have altered test results (see Fig. 4-58) [S10]. Future studies should analyse these phenomena and precisely determine their influence.



**Fig. 4-58:** Typical resin squeeze-out observed at the tip of a thermoplastic composite material specimen after testing [S10]

Shear stress-strain results obtained for different shear rates at forming temperature are well suited for the development of FE thermoforming simulations. Nevertheless, the torsion bar test method should be extended to large deformations to investigate material behaviour at high shear rates and shear strain values.

Out-of-plane bending investigations were conducted with a new test method using a DMA system in a quasi-static manner. The presented test method gave satisfactory results, although only longitudinal out-of-plane bending behaviour could be characterised. Experiments performed with a three-point-bending test setup highlighted clear material viscous behaviour within the range of data. Despite inaccuracies at low strain values caused by machine acceleration, the presented test method offered good control of testing parameters, i.e. temperature and test speeds. According to PAM-FORM requirements, test results were eventually expressed as out-of-plane bending moduli. Future investigations should focus on the feasibility to carry out tests at higher strain rates and strain values. In this respect, dynamic testing could be considered.

Because longitudinal tensile properties do not need to be characterised, only transverse tensile tests were carried out. Experiments were conducted with a new test method using a DMA system in a quasi-static manner. Test results highlighted clear material viscous behaviour within the range of data. In a similar manner as for out-of-plane bending analyses, the machine demonstrated good ability to control testing parameters, i.e. temperature and loading rates. However, because the DMA system was not able to perform experiments at prescribed test speeds, characterisation had to be conducted at prescribed loading rates. To be considered for FE thermoforming simulations, stress-strain results will have thus to be converted to test speeds. Future studies should focus on the feasibility to carry out tests at prescribed test speeds and, to the best possible extent, at similar test speeds, i.e. strain rates, as these encountered during thermoforming processes. In this respect, dynamic testing could also be considered.

Transverse tensile test results were eventually used to evaluate composite viscosity. Based on experimental evidences, the viscosity was assumed constant within the range of data. The calculated viscosity will be considered for the development of FE thermoforming simulations, although it does not correspond to the shear viscosity (as required by PAM-FORM) but to the transverse elongational viscosity.

The method considering a DMA system to carry out quasi-static tensile tests was also applied to characterise, under environmental forming conditions, the mechanical behaviour of the separation film considered in this study (polyimide film). Given that the material was considered isotropic elastic, only tensile tests were performed. Although the global response was non-linear, a Young's modulus was derived from the early linear, and assumed elastic, behaviour.

For the investigation of contact properties under regulated environmental conditions, a new test apparatus based on the "carrier test setup" illustrated in [195] was developed. The equipment can be mounted on a universal testing machine and enclosed within an environmental chamber. This enables the application of test speeds up to 400 mm/min and temperatures up to 350°C. The load applied on the carrier can also be varied. The modular assembly of the new test setup ensures efficient specimen replacement as well as easy mounting/dismounting operations.

Film/tool, ply/ply and film/ply interactions were investigated. Experiments performed between a treated separation film and a tool surface gave satisfactory results. No particular dependency was observed. However, resistance to motion, i.e. friction, was noticed to increase as the quantity of release agent decreased. Inter-ply investigations highlighted a clear test speed dependency. However, because of clamping deficiency, experiments could not be carried out with different levels of pressure. Also because of clamping deficiency, frictional behaviour between treated separation films and thermoplastic plies could not be characterised.

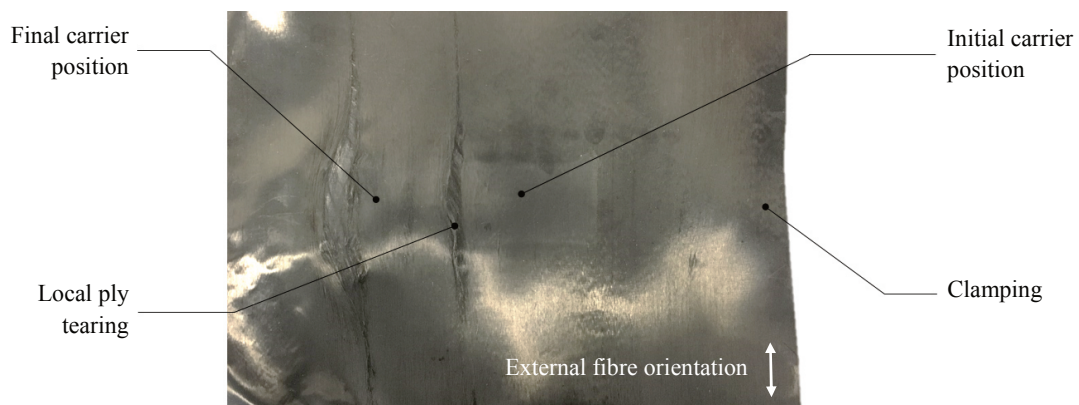


**Fig. 4-59:** Typical ply tearing observed in a 90° specimen-platen specimen (tearing on the left hand side of the plate are caused by specimen removal after testing)

To increase the integrity of the specimens, tests were conducted with cross-plyed layups, i.e.  $[90_2 0_2]_s$ . Nevertheless, because of the lack of reinforcement in strain direction and the motion of the carrier, local ply tearing in  $90^\circ$  specimens was observed (see Fig. 4-59). Kinetic frictional behaviour of  $0^\circ/90^\circ$  and  $90^\circ/90^\circ$  configurations could thus only be evaluated over limited range of data.

Investigations performed in the same environmental conditions as friction tests occurred, i.e. after five minutes soaking time at  $280^\circ\text{C}$ , evidenced a specimen temperature of about  $235^\circ\text{C}$ . This discrepancy is assumed to have only limited influence because temperature was still about  $15^\circ\text{C}$  above material melting point.

Future developments should focus on the improvement of clamping capabilities by adding, for example, a subsequent component able to increase local pressure on the carrier specimen. To carry out experiments at higher test speeds than  $400\text{ mm/min}$  without replacing the actual universal testing machine, a multi-step pulley assembly system could be developed. To gain a better understanding of the mechanisms occurring during inter-ply slip, microscopic analyses could be considered. Such investigations should give interesting information regarding the evolution of the inter-layer resin film thickness and the potential inter-fibre contacts. Static and kinetic friction coefficients, which were eventually derived from experimental results, can be used for the development of FE thermoforming simulations.

## 4.5.2 Investigation of a non-cured unidirectional thermoset composite material

A non-cured unidirectional carbon-fibre thermoset pre-impregnated composite tape qualified for aerospace applications was investigated using the same test methods as these applied to the molten unidirectional thermoplastic composite tape (UD-CF/PA6) to assess whether these are also appropriate for such materials. Experiments were carried out under environmental forming conditions, i.e.  $60^\circ\text{C}$ .

First intra-ply shear investigations were conducted with a picture frame test setup. In a similar manner as for its thermoplastic counterpart, the thermoset material started rapidly wrinkling. Ply failure (tearing) was even observed for large displacements. The method using a rotational rheometer and a parallel platens test setup was also considered. Because of material non-homogeneous through-thickness impregnation, no proper characterisation could be carried out. Eventually, experiments conducted with the torsion bar test method were satisfactory. Like for the thermoplastic prepreg, results highlighted an elastic dominated behaviour within the range of data. However, investigations performed within a benchmark<sup>4</sup> showed that clamping conditions might alter test results. This aspect should be further investigated in future studies.

---

<sup>4</sup> Bilateral benchmark conducted between the *Chair of Carbon Composites* of the *Technical University of Munich* and the *Thermoplastic Research Center* located in Enschede, the Netherlands.

The test methods developed with the DMA system for longitudinal out-of-plane and transverse tensile investigations were properly applied to the non-cured unidirectional thermoset material. Experimental results highlighted smaller strain rate dependency than for the thermoplastic material. These observations reflect the respective viscosities of the composite materials. Under environmental forming conditions, thermoset resins are much less viscous than their thermoplastic counterparts [11].

Investigations of the inter-ply slip in non-cured unidirectional thermoset laminates were conducted with the friction test setup developed in the scope of this doctoral dissertation. Because of material tackiness and the occurrence of a bending moment at the attachment hook, “carrier” test setups are not good candidates for such investigations. Other apparatus, such as pull-out and pull-through test setups, should be rather considered.

Because of their soft and tacky aspects at room temperature, thermoset specimens were more difficult to prepare than their thermoplastic counterparts. In particular, they were found to be more subjected to defects induced by cutting and handling, e.g. local fibre reorientation.

All experimental test results presented in this chapter, except those of the thermoset material, will be used for the development of FE thermoforming simulations. They will be essentially considered in Chapter 5 to calibrate, via an inverse method, material and friction models.



## 5 Calibration of simulation models

Characterisation results presented in Chapter 4 are essential for the development of thermoforming simulations. However, prior to modelling complete processes, convenient material model parameters need to be identified. Although ESI Group ensures mechanical properties of its material model MAT 140 to be uncoupled (see Chapter 3.3.2), experience proves that coupling still occurs. As a consequence, characterisation results cannot be directly considered as simulation input. Instead, experimental data are used in an inverse approach. These analyses, also called “calibration analyses”, aim to identify simulation input parameters which depict best material behaviour. To apprehend the occurrence of potential coupling, deformation mechanisms are examined separately. This is achieved by simulating same tests as these performed for material characterisation, e.g. three-point bending test for out-of-plane bending.

The first part of this chapter details the identification of composite material model parameters (MAT 140). Investigations to identify MAT 101 parameters are subsequently described. This material model is applied to separation films. Before results are eventually discussed, identification of tool/ply and ply/ply interaction parameters are presented.

### 5.1 Calibration of composite material model

The identification of composite material model parameters comprises longitudinal and transverse tension, viscosity, longitudinal and transverse out-of-plane bending and intra-ply shear properties.

#### 5.1.1 Longitudinal tension and density

The software PAM-FORM is based on an explicit integration scheme. Unlike the implicit approach, the explicit method considers a finite central difference rule to integrate the equation of motion [114, 148]:

$$[M]\{\ddot{u}\}_n + [K]\{u\}_n = \{P\}_n \quad (5-1)$$

where  $[M]$  is the mass matrix,  $[K]$  is the stiffness matrix,  $\{\ddot{u}\}$  is the acceleration vector,  $\{u\}$  is the nodal displacement vector,  $\{P\}$  is the force vector and  $n$  is the number of cycle at time  $T_n$  (after  $n\Delta t$  time steps).

In PAM-FORM, the time step  $\Delta t$  for shell elements is calculated as follows [157]:

$$\Delta t = K \cdot \frac{l}{c} \quad (5-2)$$

where  $K$  is a constant scale factor equal to 0.9,  $l$  is the element side length and  $c$  is the sound speed, which depends on the Young's modulus  $E$  and the mass density  $\rho$  [157]:

$$c = \sqrt{\frac{E}{\rho}} \quad (5-3)$$

In the case of composite materials, where two tensile moduli are considered, the sound speed  $c$  is dependent on the largest tensile modulus, i.e. the longitudinal one  $E_l$ .

The time step plays a major role in explicit FE simulations. It governs the convergence of the simulation model and the accuracy of the results. The smallest the time step, the more accurate the results but also the longer the computational time. The selection of a time step is therefore a trade-off between accuracy and computational effort. As first assumptions,  $E_l$  and  $\rho$  are considered as:

$$E_l = 10 \text{ GPa} \quad \text{and} \quad \rho = 1.14 \times 10^{-4} \text{ kg/mm}^3 \quad (5-4)$$

Longitudinal tensile properties  $E_l$  are governed by tensile behaviour of carbon fibres (about 200 GPa [11]). Since  $E_l$  is much stiffer than all other material properties (see Chapter 2.2.2), it can be scaled down, up to a certain extent, to decrease computational time without influencing global mechanical behaviour. The density  $\rho$  presented in (5-4) has been scaled by 100 compared to the value reported in the material data sheet [31]. In explicit thermoforming simulations, the density does not play an important role in the description of material behaviour. Therefore, it can be scaled, up to a certain extent, to decrease computational time.

The relevance of both parameters will be further investigated once material model parameters have been identified (see Chapter 5.1.5).

## 5.1.2 Transverse tension and viscosity

Most of the content of this section, including text and figures, is based on [P3].

The identification of viscosity  $\eta$  and transverse tensile parameter  $E_2$  is performed by modelling DMA tensile tests (see Chapter 4.1.3.2). A unidirectional sample of 6.5 (L) x 10 (W) x 2 (T) mm<sup>3</sup>, where  $L$  is the length in fibre direction,  $W$  is the dimension transverse to fibre direction and  $T$  is the thickness, is clamped on one side and pulled on the other (see Fig. 5-1). In this model, fibres are oriented perpendicular to pulling direction.



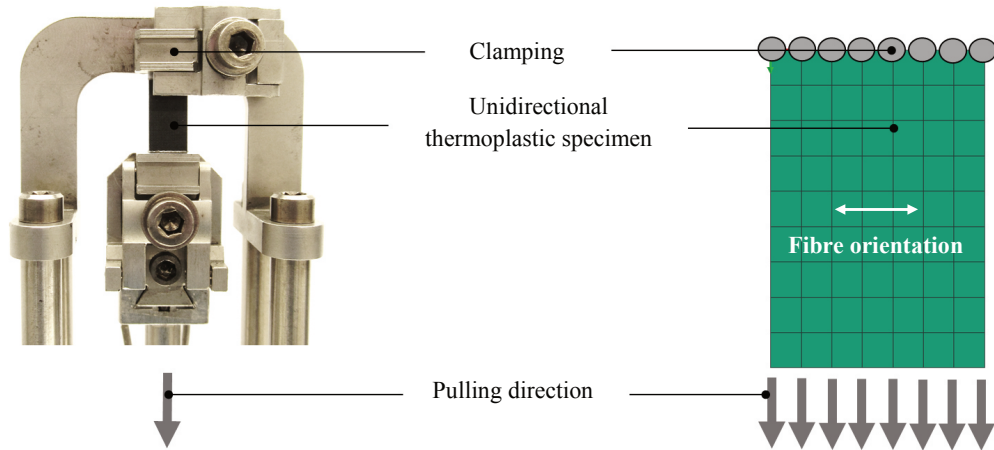


**Fig. 5-1: Experimental (left) and numerical (right) transverse tensile tests of a UD-CF/PA6 specimen**

Boundary conditions are chosen in accordance with experimental data. In a first step, virtual tests are performed at constant loading rates. During such experiments, test speeds are not constant but vary (see Fig. 8).

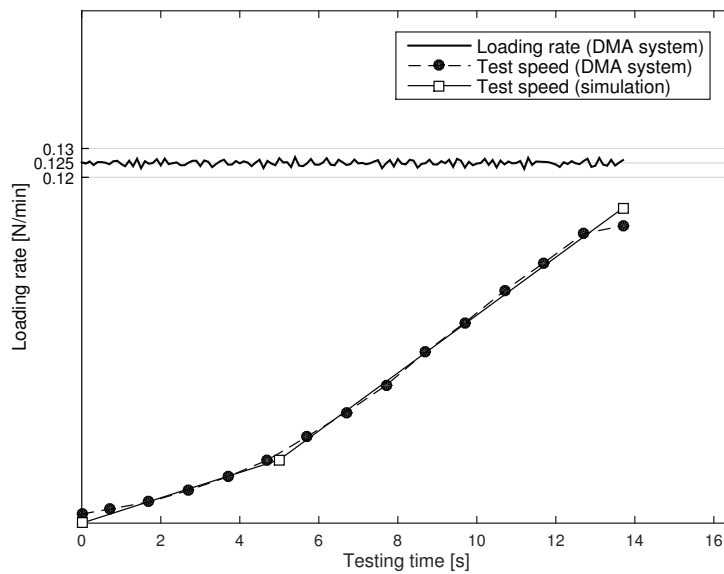


**Fig. 5-2: Typical test speed evolution of a transverse tensile test performed at a constant loading rate with a DMA system**  
Example given for 0.125 N/min.

For each loading rate, experimental test speeds are approximated by bilinear curves (see Fig. 5-2), imported into simulation models and used as kinematic boundary conditions (see bottom nodes in Fig. 5-1 right).

As mentioned in Chapter 3.3.2, viscous behaviour is managed by a Maxwell element. The identification of the viscosity  $\eta$  is performed via a sensitivity analysis based on 0.025 N/min test results. Viscosity was varied from 0.0001 to 0.004 GPa.ms, which is the PAM-FORM viscosity calculated in equation (4-9).

As it can be seen in Fig. 5-3, the higher the viscosity, the more non-linear material behaviour. The viscosity seems to mainly influence the initial step up of the curve. Based on a trial-by-error approach, a value of 0.0012 GPa.ms was selected. Since transverse viscosity can be considered as rate-independent (see Chapter 4.1.4.2), this value is kept constant for the identification of  $E_2$  parameters.

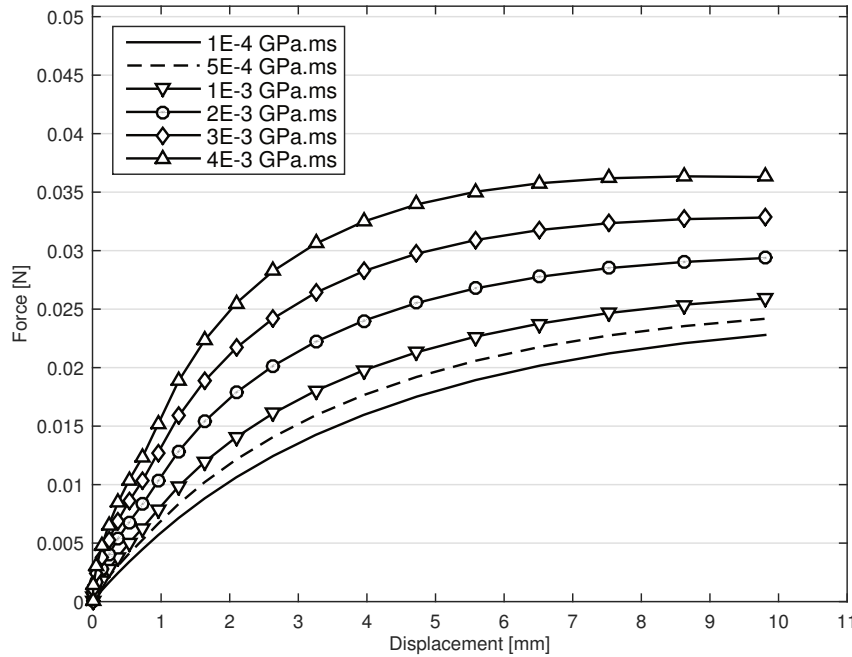


**Fig. 5-3:** Sensitivity analysis performed for the identification of the viscosity parameter

The objective of this analysis is to identify, for each loading rate, the value of  $E_2$  which provides best fit of experimental data presented in Fig. 4-19. PAM-FORM offers the possibility to treat  $E_2$  as a curve or a constant value. In this study, to ease parameter identification, constant  $E_2$  values are sought. Investigations are conducted using a dichotomy approach with a step of 0.05 GPa. Results are compared using the least square method, i.e. minimisation of the residual sum of squares  $SS_{res}$  which is calculated as the squared sum of the difference between experimental data  $y_i$  and simulation values  $f_i$ :

$$SS_{res} = \sum_i (y_i - f_i)^2 \quad (5-5)$$

Stress-strain experimental data are converted to force-displacement via equations (4-7) and (4-6), respectively. Comparison between simulation and experimental results are presented in Fig. 5-4. Simulation succeeds in depicting material behaviour tendencies (including rate dependencies). Discrepancies especially occur for high loading rates at the beginning of the curves (displacement smaller than 5% of total displacement). A maximum error of about 15% is otherwise to be reported.

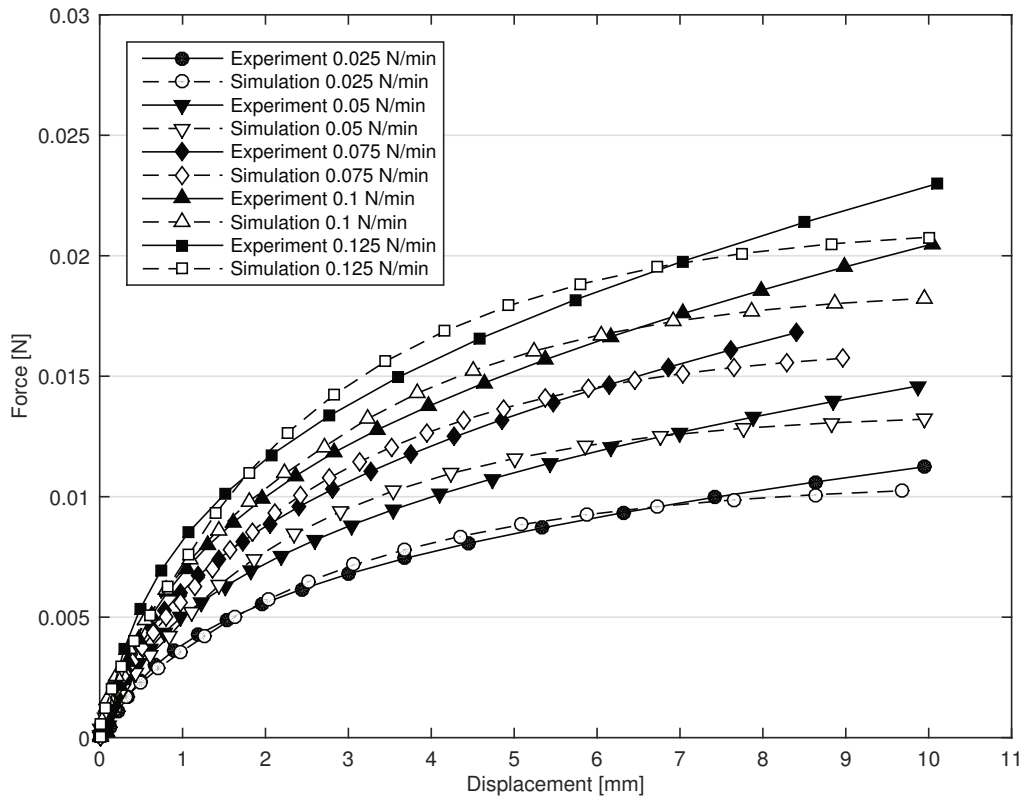


**Fig. 5-4: Simulation of transverse tensile tests of molten UD-CF/PA6 specimens – Comparison between experimental and simulation results (constant loading rates)**

Industrial thermoforming processes are conducted at prescribed test speeds. In order to be able to determine simulation input for any process speeds, simulation input parameters have to be correlated to test speeds.

In a first approach, “equivalent” constant test speeds, i.e. strain rates, were determined by averaging, i.e. in the same manner as for thermoset composites (see Chapter 4.4.3). But when these test speeds were used as kinematic boundary conditions, simulation results showed important discrepancies compared to experimental data. Because of clear viscous material behaviour, averaging has indeed to be performed over a large period of time which leads to important inaccuracies. The larger the test period, the less accurate the approximation by averaging.

To reduce these inaccuracies, the determination of “equivalent” test speeds is rather performed numerically. These investigations are performed with the previously identified parameters  $E_2$  and  $\eta$ . Investigations are conducted using a dichotomy approach with a test speed step of 0.005 mm/ms, i.e. 5 mm/s. Results are compared using the least square method, i.e. minimisation of the squared sum of the subtractions between experimental and simulation data performed at constant test speeds.

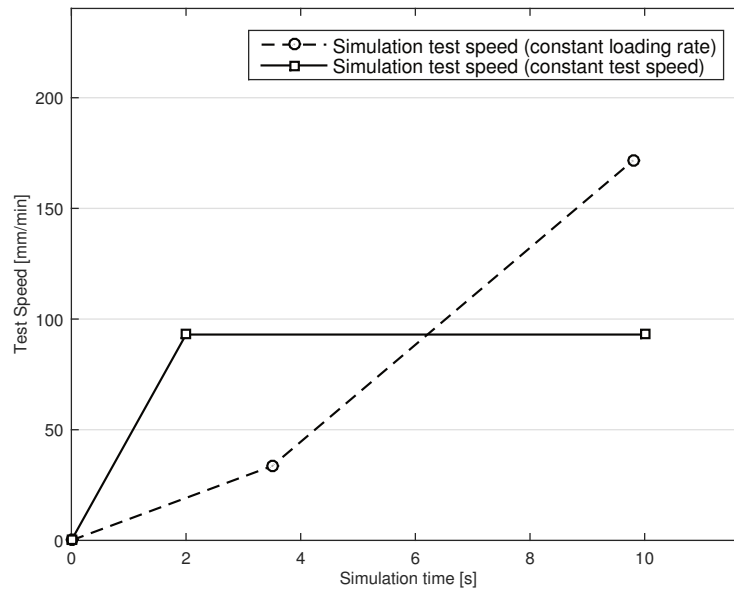


**Fig. 5-5: Typical “equivalent” test speed of experiments performed at constant loading rates**  
Example given for 0.125 N/min.

The determination of “equivalent” constant test speeds introduces additional errors between simulation and experimental results. These especially occur for displacements smaller than 1.5 mm, i.e. up to a simulation time of two seconds in Fig. 5-5. The over-estimation of transverse tensile forces are caused by viscous effects (up to 1.5 mm, simulation test speeds are much higher than experimental ones). A maximum error of about 25% is otherwise to be reported. A typical outcome of the identification is presented in Fig. 5-6 for a loading rate of 0.125 N/min.

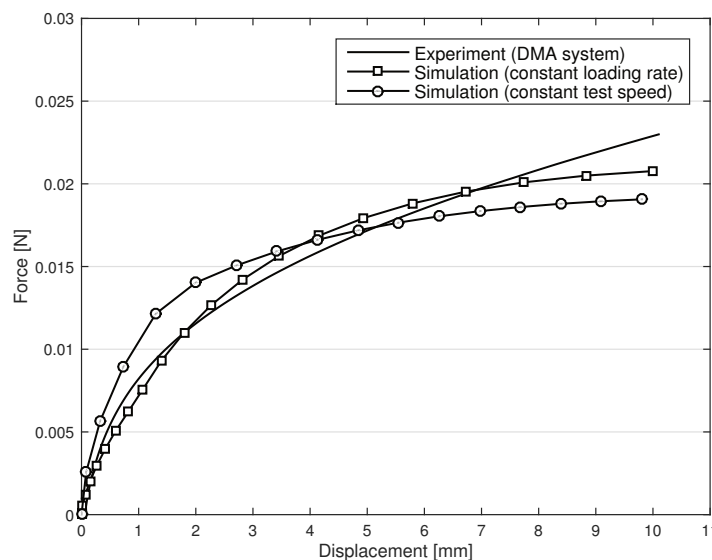


**Fig. 5-6: Simulation of transverse tensile tests of molten UD-CF/PA6 specimens – Comparison between experimental, simulation at a constant loading rate and simulation at a constant test speed results**  
Example given for 0.125 N/min.

The values of the viscosity, the transverse tensile parameters and the “equivalent” test speeds are presented in Tab. 5-1 for all loading rates.

**Tab. 5-1: Results of the identification analysis performed to determine material model parameters (viscosity, transverse tensile moduli and “equivalent” test speeds)**

Loading rate [N/min]	Viscosity [GPa.ms]	Simulation input $E_2$ [GPa]	“Equivalent” test speed [mm/min]
0.025	0.0012	$1.9 \times 10^{-6}$	39
0.05		$2.3 \times 10^{-6}$	63
0.075		$2.85 \times 10^{-6}$	75
0.1		$3.2 \times 10^{-6}$	87
0.125		$3.7 \times 10^{-6}$	93

The correlation between test speeds and simulation parameters appears to be particularly important for the development of thermoforming simulations since manufacturing processes are always conducted at prescribed speeds. Based on the correlation presented in equation (5-6), simulation input can be determined for any thermoforming process speeds (see Fig. 5-7).

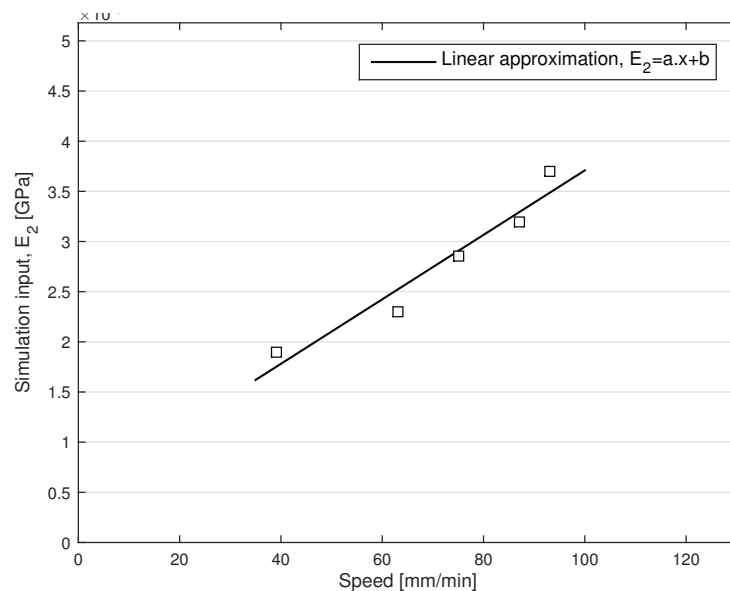


**Fig. 5-7: Correlation between simulation input  $E_2$  and speed**

$$E_2 = 3.21 \times 10^{-8} \cdot V + 4.96 \times 10^{-7} \quad (5-6)$$

where  $V$  is the speed [mm/min], e.g. thermoforming speed.

### 5.1.3 Out-of-plane bending

The identification of material model parameter  $B_1$ , which governs longitudinal out-of-plane bending behaviour, is performed by modelling three-point bending tests performed for material characterisation (see Chapter 4.1.2.1). Because transverse out-of-plane bending properties could not be characterised, only longitudinal out-of-plane bending is treated within this part. Model parameter  $B_2$ , which controls transverse out-of-plane behaviour, is identified in a different manner (see Chapter 5.1.4).

As for experiments, a unidirectional sample of 20 ( $L$ ) x 15 ( $W$ ) x 1 ( $T$ ) mm<sup>3</sup>, where  $L$  is the free span length in fibre direction,  $W$  is the dimension transverse to fibre direction and  $T$  is the thickness, is supported on both sides and loaded at mid-span (see Fig. 5-8). In this model, fibres are perpendicular to loading direction.

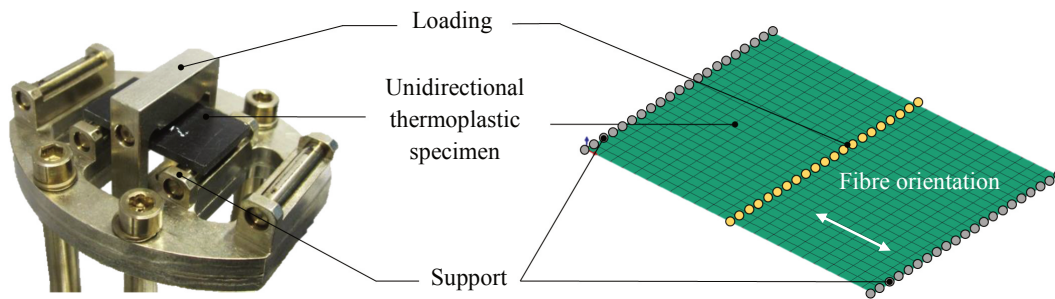


**Fig. 5-8:** Experimental (left) and numerical (right) longitudinal three-point bending tests of a UD-CF/PA6 specimen

For each case, experimental test speeds are approximated by bilinear curves, imported into simulation models (see Fig. 5-9) and used as kinematic boundary conditions on nodes at middle-span (see yellow nodes in Fig. 5-8 right).

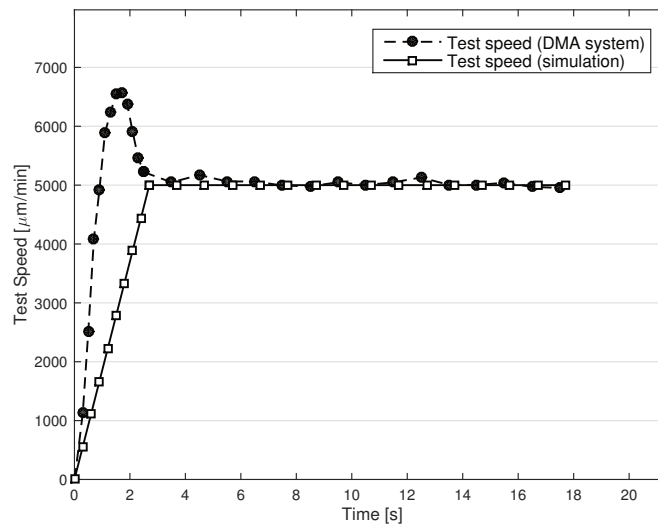


**Fig. 5-9:** Typical test speed evolution of a three-point bending test performed at a constant test speed with a DMA system  
Example given for 5000 μm/min.

The aim of the inverse approach is to identify, for each test speed, values of  $B_I$  which fit the best out-of-plane bending moduli presented in Fig. 4-15. Such moduli were derived because of the limits of MAT 140, which can only depict linear elastic out-of-plane bending behaviour. Optimisation analyses are performed until simulation output deviate less than 0.1% from experimental data (see Tab. 5-2).

**Tab. 5-2: Experimental and numerical longitudinal out-of-plane bending moduli after parameter identification**

Test speed [ $\mu\text{m}/\text{min}$ ]	Experimental data [MPa]	Simulation data [MPa]	Absolute error [%]
1000	28.63	28.62	0.016
2500	30.34	30.34	0.001
5000	33.18	33.20	0.07
7500	36.03	36.02	0.009
10000	38.89	38.85	0.060

A typical comparison between characterised and simulated material behaviour is presented in Fig. 5-10. Because non-linearities cannot be taken into account, MAT 140 depicts rather “smeared” than “exact” behaviour. In particular, longitudinal out-of-plane bending properties are underestimated at low strain values.

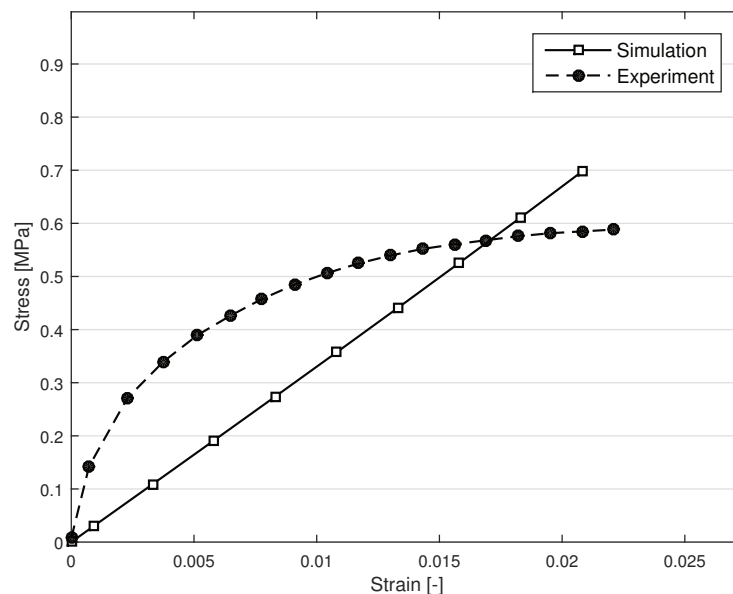


**Fig. 5-10: Comparison between experimental and numerical longitudinal out-of-plane bending behaviour**  
Example given for 5000  $\mu\text{m}/\text{min}$ .

Identification results are presented in Tab. 5-3 and Fig. 5-11. The identification of longitudinal out-of-plane bending properties enables the derivation of a correlation between test speeds and simulation input required to depict, to the best extent possible, proper mechanical behaviour.

**Tab. 5-3: Results of the identification analysis performed to determine material model longitudinal out-of-plane bending parameters**

Test speed [ $\mu\text{m}/\text{min}$ ]	Simulation input ( $B_1$ ) [GPa]
1000	0.02845
2500	0.03015
5000	0.03300
7500	0.03580
10000	0.03860

The correlation between test speeds and simulation parameter  $B_1$  appears to be particularly important for the development of thermoforming simulations since manufacturing processes are always conducted at prescribed speeds. Based the correlation presented in equation (5-7) (see Fig. 5-11), simulation input can be determined for any thermoforming process speeds.

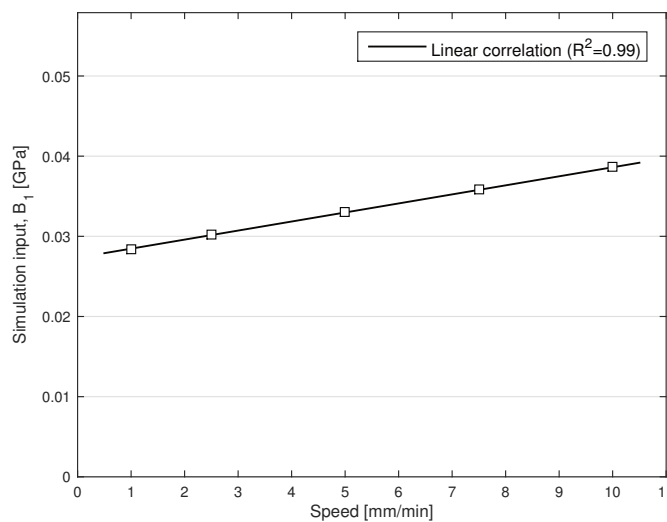


**Fig. 5-11: Correlation between simulation input  $B_1$  and speed**

$$B_1 = 1.13 \times 10^{-3} \cdot V + 2.73 \times 10^{-2} \quad (5-7)$$

where  $V$  is the speed [mm/min], e.g. thermoforming speed.



### 5.1.4 Intra-ply shear

The identification of the intra-ply shear parameter  $G$  is performed by modelling picture frame tests rather than torsion bar tests. Thick bar specimens, for which solid elements are required [S9], can indeed not be modelled using MAT 140, whose usage is restricted to shell elements (see Chapter 3.3.2).

A benefit of considering picture frame tests is also that, instead of one, two material model parameters can be identified. Because of the occurrence of out-of-plane wrinkles (see Fig. 4-3), the virtual behaviour of picture frame tests is controlled by  $G$  and  $B_2$ , which govern intra-ply shear and transverse out-of-plane bending properties, respectively. The investigations presented in this section aim to identify these parameters via an inverse approach such that:

- Onset of out-of-plane wrinkles (after about 20 mm displacement)
  - Six starting wrinkles can be identified,
  - All starting wrinkles run from one clamp to another and follow the same orientation (a bit bias compared to side frame),
  - Only starting wrinkles are out-of-plane. Other deformations, e.g. material sides, remain in-plane.
- Final position (after about 90 mm displacement)
  - Six distinct wrinkles with similar dimensions (height and width) can be identified,
  - All wrinkles have similar spacing and follow the same orientation,
  - Material sides behave in an anti-symmetric manner,
  - On the same free side, two distinct behaviour are noticed: localised compression and slight out-of-plane behaviour,
  - Height of wrinkles is comprised between 15 mm and 20 mm.

Numerical investigations are performed based on the model developed by Santner [203]. The frames of the picture frame setup are modelled with beam elements (see Fig. 5-12). These are governed by a dedicated linear elastic material model (MAT 201) in which damping is considered to prevent the occurrence of dynamic effects. In a similar manner as in experimental tests, the specimen is only clamped in fibre direction. Clamping is managed by connecting beams to shell elements. In transverse direction, since the material is not clamped, beams and shell elements are not connected. The picture frame setup is clamped on its lowest node and pulled on its top node (red and green nodes in Fig. 5-12, respectively). Simulations are performed at 50 mm/min like experimental tests. To save computational time, the simulation velocity is scaled with a factor 10 (see Appendix i).

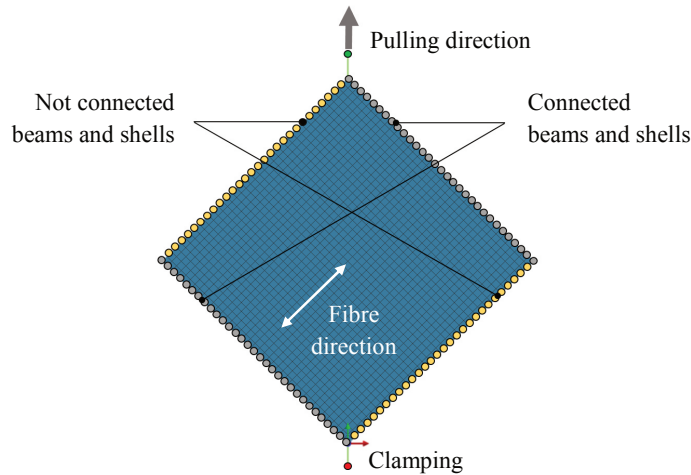


**Fig. 5-12: Picture frame simulation model applied to the identification of  $G$  and  $B_2$  parameters**

Investigations are conducted with the latest version of the material model, which comprises the identified values of  $\rho$ ,  $E_1$ ,  $E_2$  and  $B_1$  parameters. The intra-ply shear modulus  $G$  is assumed to be equal to about 8 GPa (see Appendix i), while the initial transverse out-of-plane bending modulus  $B_2$  is considered to be equal to about 1% of the longitudinal value.

First simulation attempts showed the material model to be unstable. Computational stability was brought by reducing the intra-ply shear modulus. Once a convenient intra-ply shear modulus was identified, a sensitivity analysis was performed to determine a suitable transverse out-of-plane bending parameter. Despite the effort, simulation outcomes did not match experimental results:

- Onset of out-of-plane wrinkles (after about 20 mm displacement)
  - No distinct out-of-plane wrinkles ,
  - Both specimen sides exhibit significant out-of-plane deformations (five to ten times larger than the heights of starting wrinkles).
- Final position (after about 90 mm displacement)
  - Although six wrinkles with similar orientation are obtained, their widths as well as their spacing are not regular,
  - Both specimen sides exhibit out-of-plane displacements about twice the heights of the wrinkles.

The inability of the model to depict proper material behaviour, as well as the occurrence of computational instabilities, are due to weak longitudinal out-of-plane bending properties. As detailed in Chapter 5.1.3, because non-linearities cannot be taken into account, MAT 140 underestimates such properties at low strain values, which is precisely the range of strain at which out-of-plane wrinkles are initiated. The disregard of viscous longitudinal out-of-plane bending properties leads to weak material behaviour, which consequently causes numerical instabilities and unrealistic material deformations.

To overcome these issues, longitudinal out-of-plane bending properties were scaled up and new sensitivity analysis was performed. Investigations showed the weaker the in-plane shear modulus, the earlier the appearance of out-of-plane wrinkles. On this basis, an intra-ply shear modulus of 5 MPa was found to lead to an onset of wrinkles after 20 mm displacement. In a second step, once the parameter  $G$  was identified, transverse out-of-plane bending modulus was investigated. Sensitivity analysis showed the weaker this property, the more numerous out-of-plane wrinkles. Such observations are in accordance with analyses reported by other researchers [66, 83, 97]. A transverse out-of-plane bending modulus equal to about 1.4% of the longitudinal one was found to be give satisfactory results. Comparisons between experimental picture frame test results and simulation outcomes are presented in Fig. 5-13 and Fig. 5-14 for a displacement of 20 mm and 90 mm, respectively.

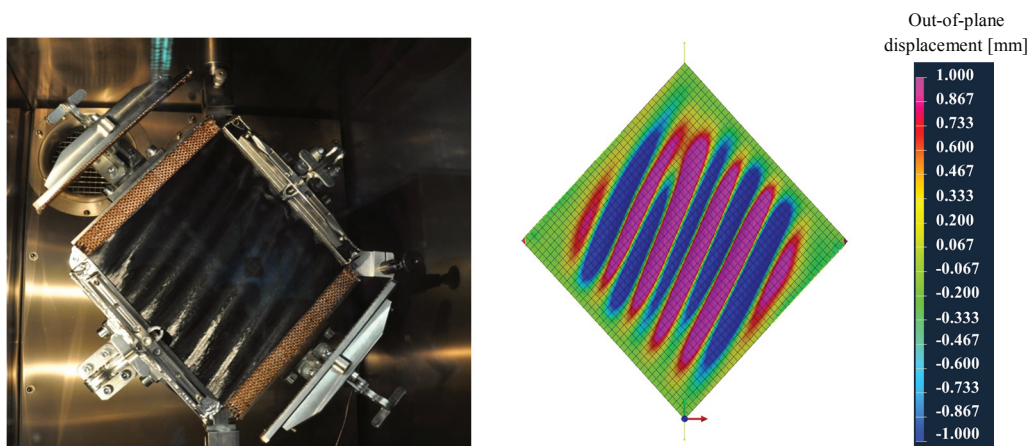


**Fig. 5-13:** Experimental (left) and simulation (right) results after 20 mm displacement

Simulation results regarding the onset of out-of-plane wrinkles (after 20 mm displacement) are in very good agreement with experiments (see Fig. 5-13). In particular, the amount and the orientation of starting wrinkles are similar. Also, like in experiments, all deformations, except wrinkles, remain in-plane.

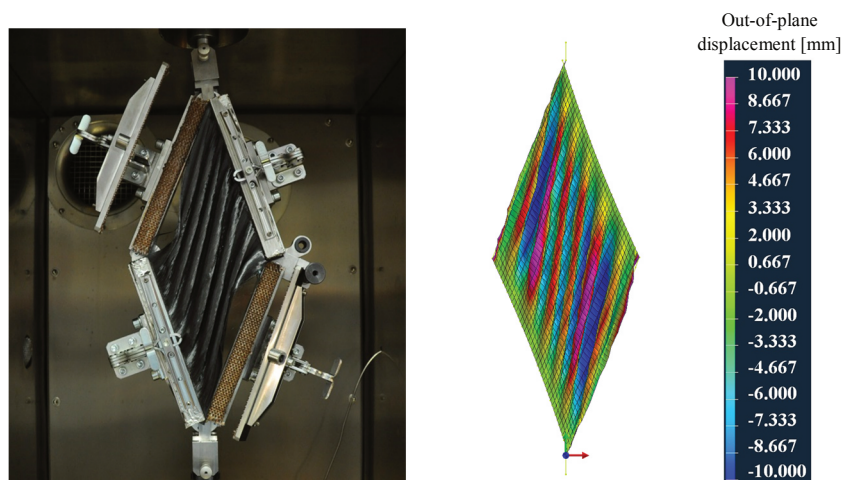


**Fig. 5-14:** Experimental (left) and simulation (right) results after 90 mm displacement

Simulation results after 90 mm displacement (final position) are in overall good agreement with experimental observations (see Fig. 5-14). In particular, specimen free sides behave in an anti-symmetric manner. The amount (six), the orientation (a bit bias compared to side frames) and the regularity of the wrinkles are properly depicted. The height peak-to-peak measured in the simulation model, i.e. 14 mm and 23 mm, is also in reasonable accordance with experimental results, i.e. 15 mm and 20 mm.

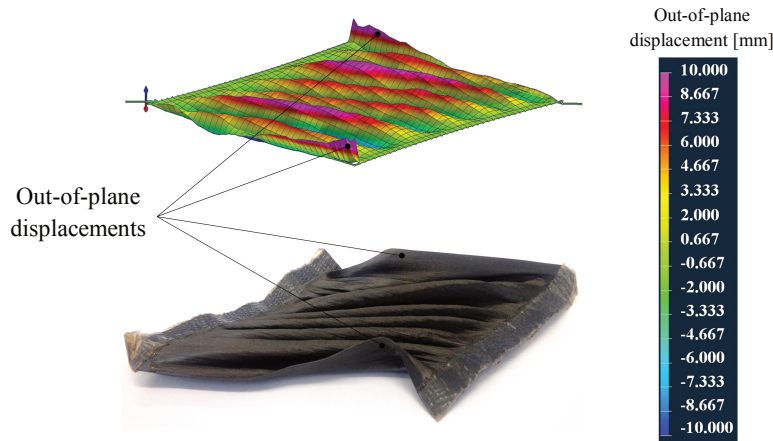


**Fig. 5-15:** Side view - Simulation (top) and experimental (bottom) final shapes of a specimen tested with a picture frame test setup

However, some differences are also to be reported. Free edges from picture frame specimens showed to undergo slight out-of-plane behaviour and localised draw-in displacements (see Fig. 5-15 and Fig. 5-16). Simulation succeeds in predicting the localisation of out-of-plane displacements (see Fig. 5-15) but fails in predicting their order of magnitudes. Numerical out-of-plane displacements are significantly larger than these observed experimentally. Furthermore, simulation shows not to be able to depict the occurrence of localised draw-in displacements (see Fig. 5-16). Discrepancies between simulation and experimental results are assumed to be caused by boundary conditions.

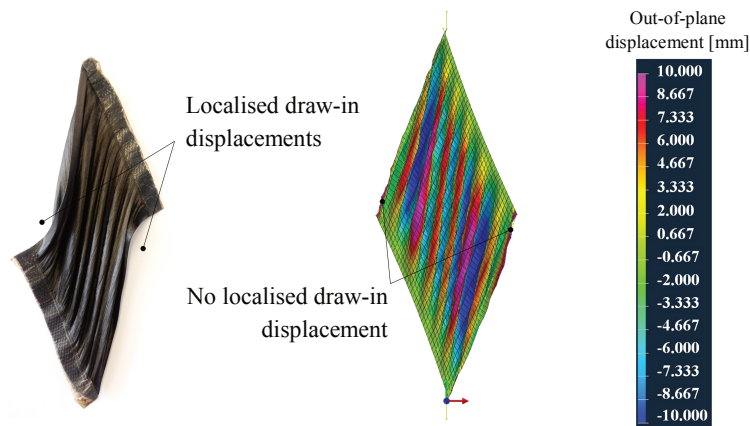


**Fig. 5-16:** Front view - Simulation (top) and experimental (bottom) final shapes of a specimen tested with a picture frame test setup

### 5.1.5 Sensitivity analysis

Sensitivity analysis is conducted when all parameters of the material model are identified. Its aim is to investigate the stability, the convergence and the accuracy of the material model. For these purposes, the simulation time step is varied via  $E_I$ ,  $\rho$  and the mesh size (see equation (5-2)). Investigations are carried out for transverse tension and longitudinal out-of-plane bending simulations.

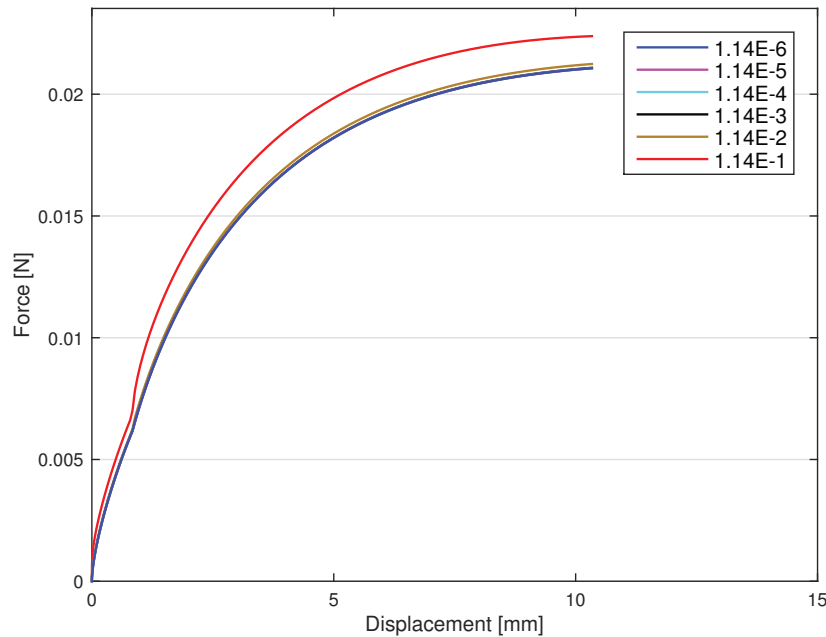


**Fig. 5-17: Typical outcome of a sensitivity analysis (investigated parameter: density)**

Results presented in this figure are obtained for transverse tensile tests performed at a loading rate of 0.125 N/min.

Detailed results are presented in Appendix j. As an example, the outcome of a typical analysis, in which the value of the density is varied from  $1.14\text{E-}6$  to  $1.14\text{E-}1$   $\text{kg/mm}^3$ , is presented in Fig. 5-17. As the density is reduced, accuracy is increased. However, as the density is reduced, computational time is also increased. This is to be imputed to a reduction of the time step. In the present case, densities equal to or lower than  $1.14\text{E-}3$   $\text{kg/mm}^3$  are found to be suitable.

Sensitivity analysis showed initial values of  $E_I$  and  $\rho$  to be convenient parameters (see Chapter 5.1.1.).

## 5.2 Calibration of separation film material model

The identification of MAT 101 parameters is performed by modelling DMA tensile tests (see Chapter 4.2). A kapton film specimen of  $6.5$  (L)  $\times$   $10$  (W)  $\times$   $0.05$  (T)  $\text{mm}^3$ , where  $L$  is the length,  $W$  is the width and  $T$  is the thickness, is clamped on one side and pulled on the other (see Fig. 5-18).

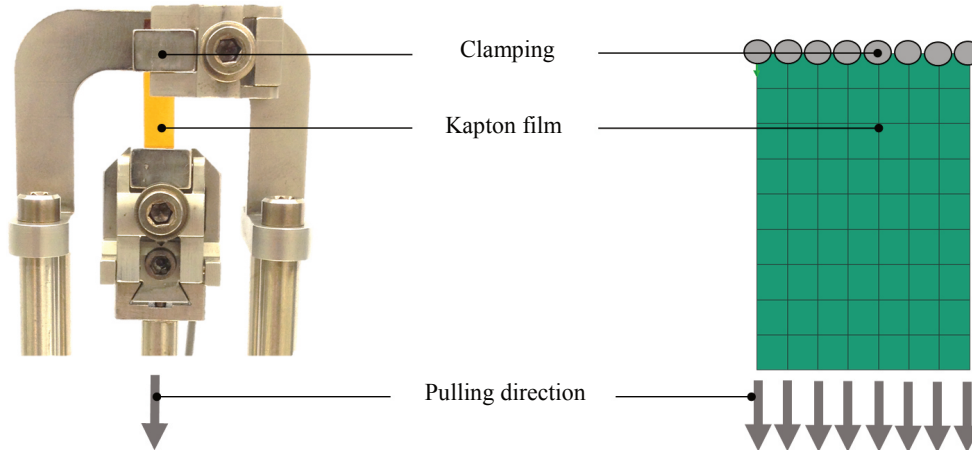


Fig. 5-18: Experimental (left) and numerical (right) tensile tests of a polyimide film

In a similar manner as for the thermoplastic composite material, the density  $\rho$  is scaled down by 100. As already mentioned in Chapter 5.1, this scaling increases computational efficiency with no influence on simulation accuracy:

$$\rho = 1.10^{-4} \text{ kg/mm}^3 \quad (5-8)$$

To reduce computational effort, a different test speed than this applied during material characterisation is applied as boundary condition. Such a scaling does not influence parameter identification since kapton film is modelled with linear elastic isotropic material behaviour.

For consistency purposes with longitudinal tensile behaviour of the fibre-reinforced thermoplastic composite material, kapton film tensile properties are scaled down by 20. Based on material characterisation test results (see Chapter 4.2), the goal of the calibration is to identify  $E$  such that a modulus of 0.1 GPa is reached.

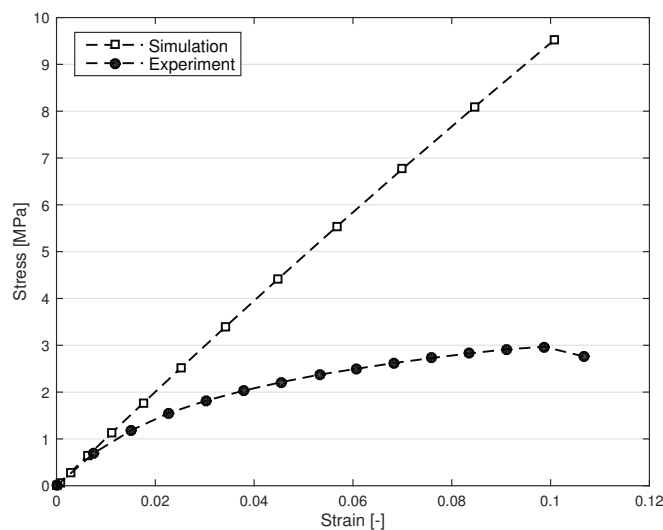


Fig. 5-19: Comparison between experimental and numerical tensile test results of a polyimide film (280°C)

The outcome of the inverse approach gives:

$$E = 0.1 \text{ GPa} \quad (5-9)$$

A comparison between simulation and experimental results (scaled down by 20) is presented in Fig. 5-19. Only early material behaviour, i.e. elasticity, is properly depicted since material plasticity and failure are not taken into account by the simulation model. This simplification is, however, not expected to influence thermoforming simulation results since kapton film is assumed to undergo only minor deformations during manufacturing processes (see Chapter 6.1.1).

### 5.3 Calibration of contact properties

The identification of proper friction coefficients concern both tool/ply and ply/ply interactions (see Tab. 5-4). Because no experimental value for treated film/ply interactions is available, this configuration is not considered in this section. A dedicated friction coefficient will be selected in a subsequent step, i.e. during the development of thermoforming process simulation models (see Chapter 6.1.4).

**Tab. 5-4: Configurations investigated for the identification of simulation friction coefficients**

<b>Configuration 1</b>	<b>Configuration 2</b>	<b>Configuration 3</b>	<b>Configuration 4</b>
Tool / Treated kapton film	Ply/ply (0/0)	Ply/ply (0/90)	Ply/ply (90/90)

Investigations are performed by modelling a similar “carrier test” as this used for material characterisation (see Fig. 5-20). This simulation model can be applied to all configurations depending on sliding directions and/or the material models applied to the carrier and the support. To ease post-processing, a 10 x 10 mm<sup>2</sup> carrier, on which a uniform normal pressure of 0.01 MPa is applied, is considered. The dimensions of the support are sufficient to ensure proper parameter identification.

In this work, a symmetric node-to-segment with edge treatment algorithm is selected (CNTAC 33 in PAM-FORM [157]). This contact model is based on a master/slave approach. For all configurations, the carrier is set as master and the support as slave. As recommended by Santner [203] to prevent the occurrence of oscillations in simulation outcomes, different mesh sizes for carrier and support are used and, carrier and support element edges are not facing each other. Santner reported a decrease of frictional force when element edges were positioned on top of each other [203]. To further prevent the occurrence of dynamic effects, contact damping, via the parameter *XDMP1*, is also considered.

In the model presented in Fig. 5-20, the carrier is free to move along all directions while the support is fixed. For configurations in which thermoplastic composites are involved (configurations 2 to 4), fibres are aligned with direction 1.

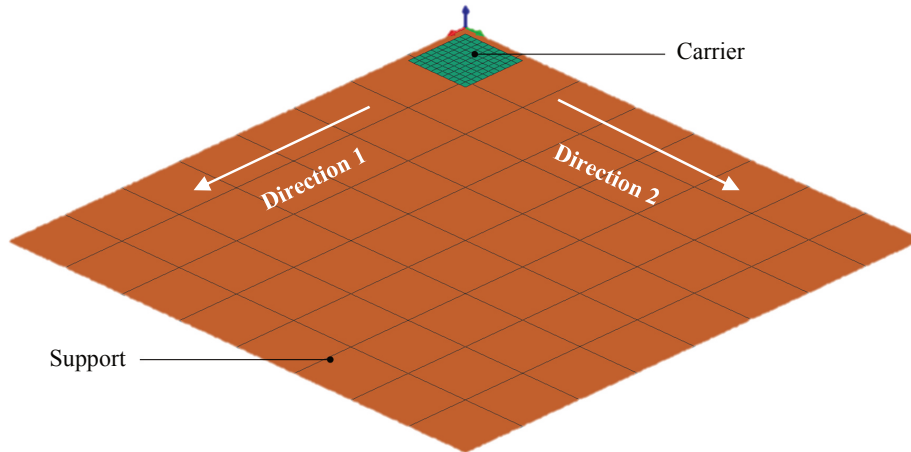


**Fig. 5-20: Simulation model applied to the identification of friction coefficients**

Orthotropic friction coefficients can be identified using the presented model. Depending on the configuration, the carrier can be pulled either along or transverse to fibre direction, i.e. along the 1- or 2-direction, respectively.

As detailed in Chapter 3.3.2, PAM-FORM offers numerous contact models for isotropic friction. Orthotropic interactions can, however, only be modelled by means of Coulomb friction laws. Given that dependency with respect to fibre direction is more important than others, e.g. test speed, an orthotropic Coulomb based friction model is considered for configurations 2 to 4. For contacts between treated kapton film and tool surface (configuration 1), an isotropic Coulomb friction law is considered. To reduce computational time and given that velocity independent friction laws are considered, investigations are performed with a velocity of 0.05 mm/ms.

Interactions in PAM-FORM can only be modelled via constant friction coefficients [157]. Curves such as these obtained during material characterisation (see Fig. 4-35) cannot be implemented. For orthotropic contacts, one friction coefficient per direction can be selected. For identification purposes, the user must thus choose based on process and material considerations whether static or kinetic friction coefficients should be taken into account. Because treated films are expected to slide against tool surface during thermoforming, kinetic friction coefficient<sup>1</sup> should be considered (configuration 1). For contacts between molten thermoplastic layers, since only limited slip is expected to occur, static friction coefficients should be taken into account (configurations 2, 3 and 4) [43].

<sup>1</sup> In the present case, static and kinetic friction coefficients are similar since experimental results showed both parameters to be the same (see Chapter 4.3.3.1).



Identification results are presented in Tab. 5-5. Because of orthotropy, parameters of configuration 2 and configuration 4 are identical. Comparisons between simulation and experimental results are presented in Fig. 5-21 left for interactions between a treated kapton film and a tool surface and in Fig. 5-21 right for interactions between two 0° UD-CF/PA6 layers. Experimental data have been adapted for visualisation purposes.

**Tab. 5-5: Results of the identification analysis performed to determine simulation friction coefficients**

	Parameters [-]	Experimental data [-]	Simulation data [-]	Error [%]
<b>Configuration 1</b>	$\mu_{d,tool}$	0.171	0.170	< 0.1%
<b>Configuration 2</b>	$\mu_{s,0/0}$	1.303	1.299	< 0.1%
<b>Configuration 4</b>	$\mu_{s,90/90}$	0.776	0.779	< 0.1%
<b>Configuration 3</b>	$\mu_{s,0/90}$	0.824	0.822	< 0.1%

The slack caused by the straightening of the stainless steel wire and observed during material characterisation tests is not depicted by the simulation. Instead, contact occurs as soon as interactions are initiated (see Fig. 5-21).

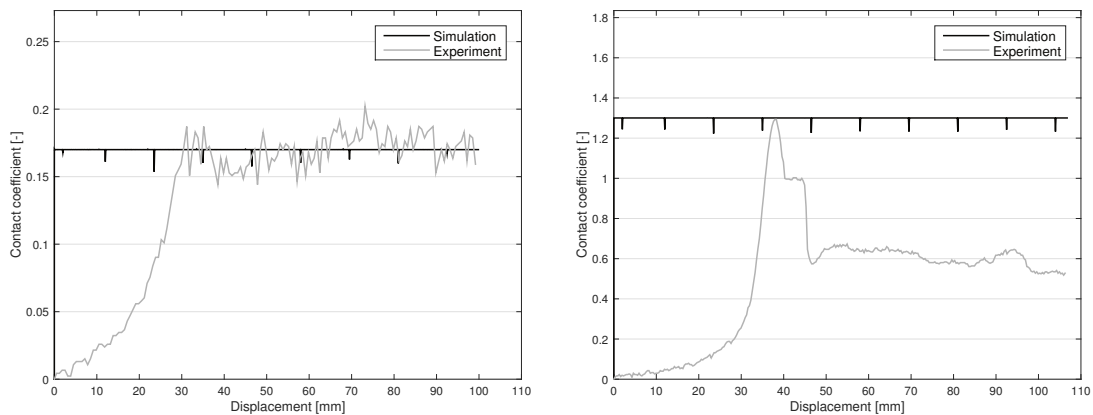


**Fig. 5-21: Comparison between experimental and simulation test results for interactions occurring between a tool surface and a treated kapton film (left) and two 0° molten UD-CF/PA6 plies (right)**

## 5.4 Results and discussion

The goal of this chapter was to determine, using models from Visual-FORM, simulation input parameters which depict best material behaviour. All parameters, except the Poisson's ratio (see Appendix k), were identified using an inverse method based on material characterisation test results (see Chapter 4).

Results presented in Fig. 5-22 and Fig. 5-23 can be used as input for the simulation of thermoforming processes performed at 280°C (see Chapter 6.1.4). The thermoplastic composite material model can, however, only be applied with processes conducted at 50 mm/min. This restriction lies in the fact that intra-ply shear and transverse out-of-plane bending parameters were identified using picture frame test results performed at this specific test speed.

Due to some material model specificities, identified simulation parameters appeared to be rather different from experimental data. Difficulties encountered in the identification of MAT 140 parameters were caused (i) by the limits of the characterisation test method and (ii) by the restrictions of the material model.

	IDMAT	MATYP	RHO	ISINT	ISHG	ISTRAT	IFROZ			
MATER/	XX	140	1.14E-4	0	0					
BLANK	AUXID1	AUXID2	AUXID3	AUXID4	AUXID5	AUXID6	QVM	THDID	IDMP	AND
	0	0	0	0	0	0	1		0	0
	TITLE									
NAME	Carbon Fibre UD PA6 tape									
BLANK	BLANK	HGM	HGW	HGQ	As					
E1option	E1	BLANK	Fb1	Fs1	ALPHA1	B1				
E1	10		STIF_CONST		0	2,514				
E2option	E2	BLANK	Fb2	Fs2	RFLAG	Alpha2	B2			
E2	2,10E-06		STIF_CONST		0	90	0.035			
G_option	LCS	NUEp	ALPHlock	G_lock	Fbm	Fsm	SRFIL			
G	0.005	0.3468								
Eta_optn	ETA	BLANK	T							
Eta	0.0012									
OPTION	Ro	B	n	thk_elim	thk_mult	thk_cut				
BLANK										
a0	b0	w0	phi	lunc	ZHI	f				
				1	0.5	0				

**Fig. 5-22: Material model of a molten UD-CF/PA6 tape (MAT 140)**

This material model was calibrated based on characterisation tests performed at 280°C and 50 mm/min. Its application is thus restricted to these specific temperature and speed.

Experimental transverse tensile test results prevented the efficient and accurate identification of  $E_2$  parameters. Because data were function of loading rates, intensive investigations had to be conducted to determine “equivalent” test speeds. For out-of-plane bending properties, difficulties in the identification of suitable parameters were caused by the limits of MAT 140, which can only depict linear elastic bending behaviour. The identification of intra-ply shear properties, via the modelling of torsion bar tests, could also not be carried out because of material model limits. Regarding transverse out-of-plane bending, identification analysis based on an elementary test setup could not be conducted because no experimental data was available. An alternative, via the modelling of a picture frame test, was found to determine both  $G$  and  $B_2$  parameters. However, the main drawback of this approach is that identified material model parameters can only be used for a single test speed, i.e. the test speed at which the picture frame test was performed. Difficulties encountered in identification analysis were eventually due to the lack of documentation available. In particular, the role and the influence of the viscosity  $\eta$  on other mechanical parameters should be clarified.

Identification analyses would be more intuitive if data entry would be different. For example, it would be more convenient if the user, for each deformation mode, could enter material data such as they are obtained from characterisation tests, i.e. stress-strain curves for given strain rates and/or temperatures. In the latest version of the material model (v. 2015), such data entry is now possible [158].

In comparison to the investigations conducted for MAT 140, analyses performed for MAT 101 (the material model of the kapton film) were rather simple. In particular, the identification of a proper elastic modulus could be performed without difficulty since the aimed elastic modulus corresponded to the entered value (see Fig. 5-23).

	IDMAT	MATYP	RHO	ISINT	ISHG	ISTRAT	IFROZ			
MATER/	XX	101	1,00E-04	0	0					
BLANK	AUXID1	AUXID2	AUXID3	AUXID4	AUXID5	AUXID6	QVM	THDID	IDMP	AND
	0	0	0	0	0	0	1		0	0
	TITLE									
NAME	Kapton film									
E	BLANK	NU	ALPHA	HGM	HGW	HGQ	As			
0.1		0.33								
BLANK	KSI	Fo.								
	0.5	0								

**Fig. 5-23: Material model of a polyimide film (MAT 101)**  
 This material model was calibrated characterisation tests performed at 280°C. Its application is thus restricted to this specific temperature.

The identification of friction coefficients was rather simple because, like for MAT 101, simulation output corresponded to entered values. To complete the development of contact models, further parameters, such as non-linear contact penalty stiffness (*FSVNL*), are determined in Chapter 6.1.4.

The parameters identified within this chapter will be used in Chapter 6 for the development of FE thermoforming simulation models.



## 6 Validation and applications

Before supporting industrial decision making regarding the design of new components and the development of new manufacturing techniques, the reliability of FE thermoforming simulations must be demonstrated on generic components, referred to as demonstrators. The aim of these investigations is to validate their predictive quality by comparing computed results to experimental measurements. Such investigations are typically performed on components, which have similar geometrical features as industrial parts and are formed under comparable environmental conditions.

Details about the validation are presented in the first part of this chapter. Once validated, two case studies are considered. The first one analyses the benefit of accounting for separation films in FE thermoforming simulations, while the second investigates, via a sensitivity study, the influence of the transverse tensile properties of composite tapes on simulation outcomes.

### 6.1 Validation

This section details the validation of the FE simulation approach. In a first part, the thermoforming process and the demonstrators considered for validation purposes are described. Once comparison criteria and methods have been introduced, experimental and computed results are presented. Comparisons are eventually held accordingly.

#### 6.1.1 Thermoforming process and demonstrators

Most of the content of this section, including text and figures, is based on [K10].

The thermoforming process considered in the scope of this work is a laboratory variant of an industrial thermoforming process. The material is not formed by a thermoforming press but by a universal testing machine. The main difference between both methods lies in the forming (or stamping) speed. To control forming environment, experiments are performed within an environmental chamber. All experiments are carried out at 50 mm/min and 280°C, i.e. above material melting temperature (see Tab. 1-1).

The demonstrator considered in the scope of this doctoral dissertation is a generic part with a double-curved geometry. Its shape follows the intersection of two sinusoidal waves. As such, it is commonly referred to as “double-sinus wave” component (see Fig. 6-1) [128]. The basis of the tooling has a square cross-section of about 150 mm side length. The heights at points A and B are of about 40 mm and 35 mm, respectively.

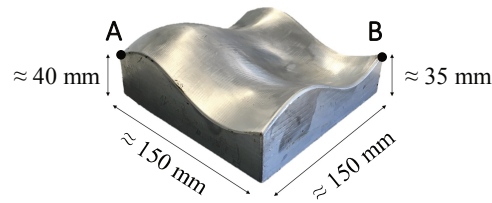


**Fig. 6-1: Demonstrator (or “double-sinus wave” component) considered for validation**

The stack, composed of two polyimide separation films [192] and a composite layup in-between, is placed between male and female moulds at room temperature (see Fig. 6-2). A circumferential blankholder of rectangular cross-section with a weight of 2.5 kg is positioned on top of the film-composite-film stack. Forming occurs when the stack, pushed by the stamp, is forced to comply with mould geometry. Experiments are performed after at least ten minutes soaking time to ensure homogeneous temperature distribution.

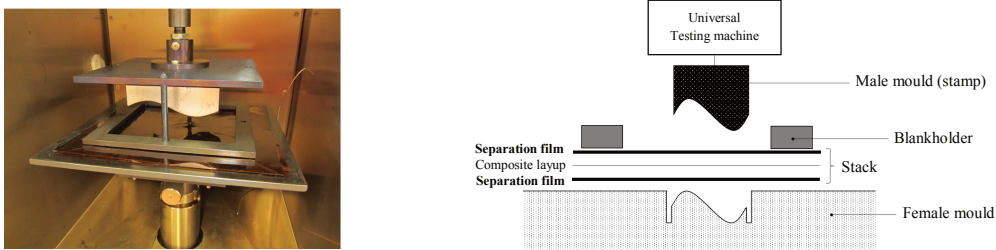


**Fig. 6-2: Double-sinus wave tooling mounted on a universal testing machine and enclosed in an environmental chamber (left) and schematic of the thermoforming process (right)**

The validation is carried out with different composite layups:

- $[0_8]$  with a blank size of  $300 \times 300 \text{ mm}^2$ ,
- $[0_8]$  with a blank size of  $350 \times 350 \text{ mm}^2$ ,
- $[0_2 90_2]_S$  with a blank size of  $350 \times 350 \text{ mm}^2$ .

Composite blanks are composed of eight layers, i.e. about 1.2 mm thickness, of unidirectional carbon fibre-reinforced PA6 tapes (see Chapter 1.1). Tailored layups are laid using a FiberForge RELAY 2000 station and consolidated using a mechanical press, as described in Chapter 1.1. As separation film, a heat-resistant polyimide film is considered [192]. Such films aim to ease part removal after forming and enhance forming quality by decreasing tool/ply friction. Before being applied to thermoforming applications, separation films are treated with a release agent (Release All 45<sup>®</sup>, Airtech [199]), and cut into “star shapes” (see Fig. 6-3). Such cut-outs aim to ease the deformations of the films during forming by preventing the occurrence of large strains. After forming, demoulding occurs when the temperature is stabilised below 70°C.

Mechanical properties of the unidirectional thermoplastic composite tape and the separation film under environmental forming conditions are presented in Chapters 4.1 and 4.2, respectively.

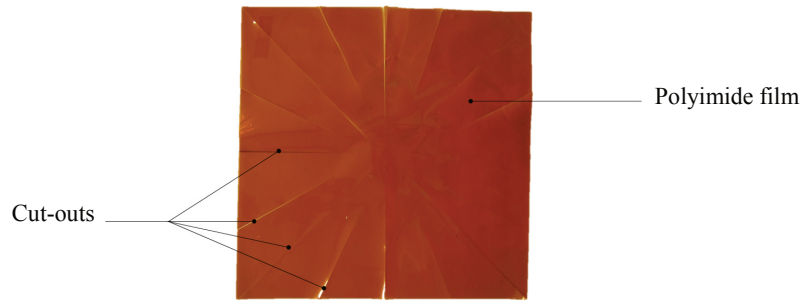


**Fig. 6-3:** Cut-outs of a treated polyimide film

## 6.1.2 Validation criteria and comparison methods

The validation of the simulation approach is carried out by comparing experimental results to simulation outcomes. For a proper assessment, three particular aspects are considered:

- Preform geometries,
- Out-of-plane wrinkles,
- Fibre orientations on the external layer of the preforms.

Comparisons of preform geometries are based on six different lengths measured manually using a ruler. The aim is to evaluate the ability of the simulation to predict final preform shapes. The accuracy of such predictions is of particular importance for industrial applications since preforms will be assembled with other components. Deviations in preform geometries might lead to important shimming operations. Besides their time and cost intensive concerns, such operations can also significantly increase the global weight of the structure.

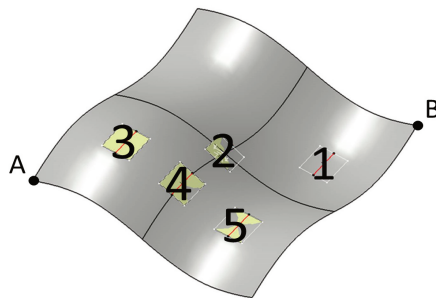


**Fig. 6-4:** Position of the five regions of interest (ROI) considered for validation  
Points A and B are given for orientation purposes (see Fig. 6-1).

The simulation approach is also evaluated on its ability to locate and depict (quantity and shape) out-of-plane wrinkles. Investigations are conducted visually without the assistance of any optical system and measurements are performed manually using a ruler. The accuracy with which out-of-plane wrinkles can be predicted is of great interest for industrial applications since such defects influence assembly operations and mechanical properties of final components [37, 99].

Measured and computed fibre orientations are compared via a Matlab routine [127, 128, 204]. Investigations are conducted on five regions of interest (see Fig. 6-4). Each ROI represents an area of about  $20 \times 20 \text{ mm}^2$ . Computed results are extracted from simulation output and imported as *.pc* files, which contain XYZ-coordinates of fibre orientations. Experimental measurements are performed with an optical sensor mounted on an automated robot to ensure good reproducibility. The sensor, supplied by ProFactor [177], measures one fibre orientation per pixel, which corresponds to a value every  $35 \mu\text{m}$ , and has an accuracy of about  $1^\circ$  [205]. Measurement data are imported into the Matlab routine as *.mat* files. After comparisons, results are plotted on 3D models in which colour scales indicate whether deviations are small or large. The goal of these analyses is to assess the potential of the simulation to predict fibre orientations after forming. Such ability is essential for industrial applications since fibre orientations play a major role in the performance of composite components [206].

### 6.1.3 Experimental results

Thermoforming outcomes for the  $[0]_8 300 \times 300 \text{ mm}^2$ ,  $[0]_8 350 \times 350 \text{ mm}^2$  and  $[0_2 90_2]_8 350 \times 350 \text{ mm}^2$  tailored blanks are presented in Fig. 6-5 left, Fig. 6-5 right and Fig. 6-6, respectively.

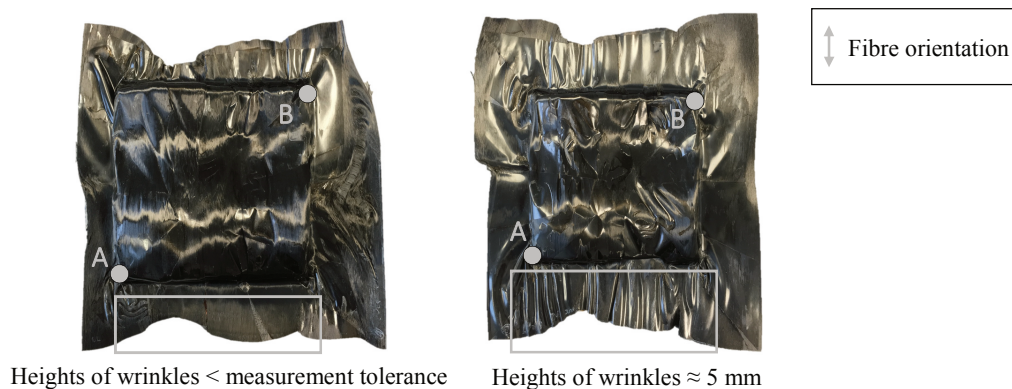


**Fig. 6-5: Thermoforming outcomes of  $[0]_8$  tailored blanks**

Left: Initial blank size of  $300 \times 300 \text{ mm}^2$ ; Right: Initial blank size of  $350 \times 350 \text{ mm}^2$ . Points A and B are given for orientation purposes (see Fig. 6-1).

Both unidirectional tailored blanks exhibit similar shapes after forming (see Fig. 6-5). Draw-in displacements, which only occur along fibre direction, are caused by stiff fibre tensile behaviour (see Chapter 2.2.2). The occurrence of compressive forces perpendicular to fibre direction, combined with weak transverse behaviour, leads to the development of out-of-plane wrinkles. These are found to have different heights in both preforms because (i) the  $300 \times 300 \text{ mm}^2$  blank has been mispositioned in the environmental chamber and (ii) smaller blanks are less subjected to wrinkling [27]. Tearing observed on the right hand side of the  $300 \times 300 \text{ mm}^2$  preform is due to an unexpected contact between the tool surface and the molten blank. Since it only occurred at the end of the thermoforming process, its influence is assumed to be negligible.



Draw-in displacements on the four edges of the cross-plyed blank are similar. This is due to the presence of two families of fibres oriented perpendicular to each other (see Fig. 6-6). Preform geometries of all three layups are discussed in more details in Chapter 6.1.5.1.



**Fig. 6-6: Thermoforming outcome of the  $[0_2 90_2]_s$  tailored blank**  
Points A and B are given for orientation purposes (see Fig. 6-1).

The unevenness of the surface of the demonstrators is caused by interactions between blanks and separation films (see Fig. 6-7). Poor surface finish is imputed to air entrapment due to the non-compaction of the film-composite-film stacks prior to forming.

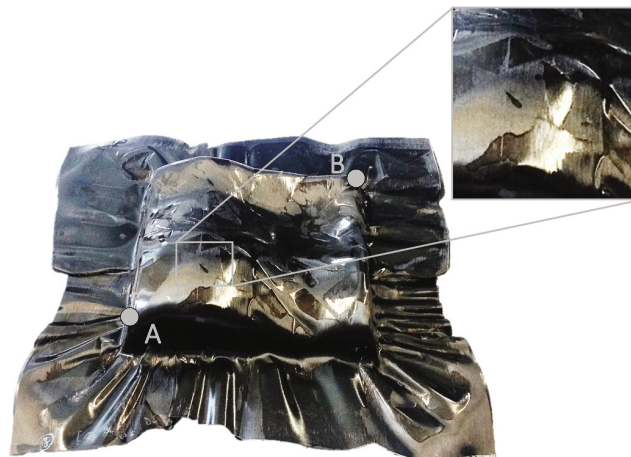


**Fig. 6-7: Influence of separation films on surface finish**  
Example given for the cross-plyed stack.  
Points A and B are given for orientation purposes (see Fig. 6-1).

According to the method presented in Chapter 6.1.2, the outer layers of the demonstrators are scanned with a ProFactor sensor [177]. Measurements are performed using an automated robot and achieved for the five ROIs illustrated in Fig. 6-4. The arrangement of the setup is presented in Fig. 6-8.

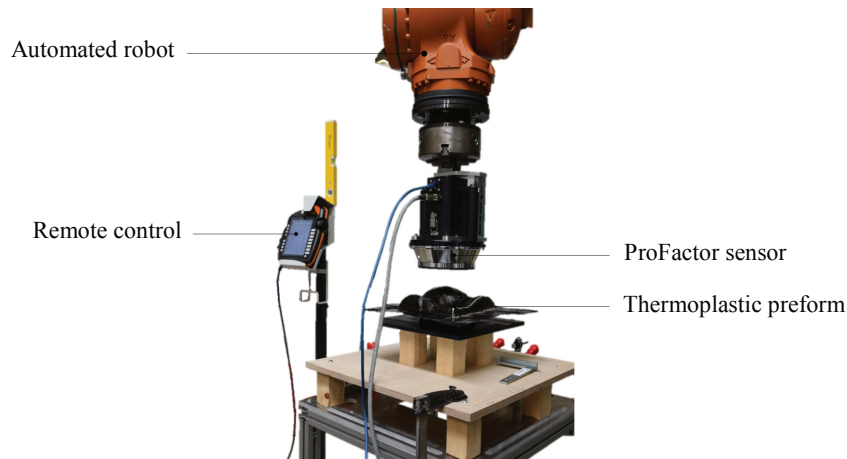


Fig. 6-8: Setup for fibre orientation measurements

### 6.1.4 Simulation modelling

Simulation models are developed according to the thermoforming setup presented in Chapter 6.1.1. As a macroscopic FE simulation approach, every component is modelled, i.e. stamp, mould, blankholder and composite stack. Separation films are also modelled “explicitly”<sup>1</sup> since these seem to influence forming outcomes (see Chapter 6.1.3). To prevent the occurrence of dynamic effects, these are modelled as plain plies, i.e. without cut-outs. All parts are meshed with four-node shell elements (see Fig. 6-9). Three integration points are considered within their thicknesses. For the application of smooth contact properties [203], layers of shell elements are slightly disorganised (see Appendix 1). Composite layers are meshed with elements of 4 mm side length and eventually oriented either at 0° or 90°. Depending on the configuration, blanks have an initial size of either 300 x 300 mm<sup>2</sup> or 350 x 350 mm<sup>2</sup>.

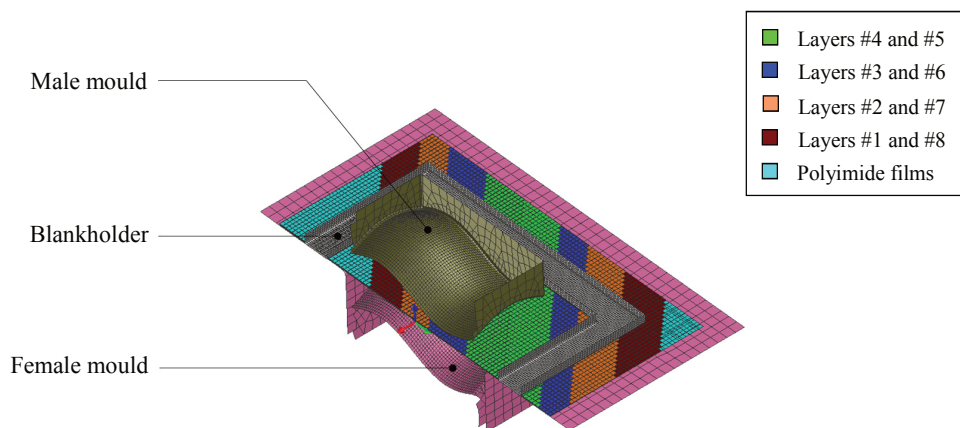


Fig. 6-9: Macroscopic FE simulation model used for validation

<sup>1</sup> The “explicit” modelling of the separation films is an innovative approach considered in the scope of this doctoral dissertation. Its benefits are demonstrated in Chapter 6.2.1.

Stamp, mould and blankholder components are modelled as rigid bodies since their geometries are not expected to vary during thermoforming. Thermoplastic composite layers are represented by the viscous material model MAT 140 introduced in Chapter 5.4 and polyimide separation films are described by the isotropic material model MAT 101 presented in Chapter 5.4. Both material models are suitable to simulate the thermoforming processes presented in Chapter 6.1.1 since they have been calibrated for a temperature of 280°C and a test speed of 50 mm/min.

Interactions between components are managed by a symmetric node-to-segment with edge treatment algorithm (CNTAC 33 in PAM-FORM [157]). Friction coefficients for the interactions between treated films/tool and plies/plies are these identified in Chapter 5.4. Regarding the interactions between treated films and thermoplastic plies, a user-defined coefficient of 5 is selected in accordance with experimental results (see Chapter 4.3.3.3). To prevent dynamic effects caused by contact initiation, non-linear contact penalty stiffness parameters (*FSVNL*) are considered. These are defined based on a trial-by-error approach<sup>2</sup>. A coefficient of 100 is implemented for contacts with polyimide separation films, while a value of 5 is accounted for contacts with thermoplastic plies. The parameter which governs the amount of stress necessary to separate two objects (*SEPSTR*) is also selected via a trial-by-error approach. This property is of particular importance in the modelling of inter-ply interactions since it represents the tackiness and “consolidated” aspect of the tailored thermoplastic blanks. Because this property was not characterised, first investigations were conducted with 0.1 MPa [63]. After several attempts, a value of 0.01 MPa is eventually considered. For the sake of simplicity, all contacts are initiated when two objects come at a distance of 0.13 mm.

To decrease computational effort, models are developed with mass and velocity scaling. These are introduced in accordance with results presented in Chapter 5 as well as in Appendix i and j. To prevent dynamic effects, kinematic damping (*KINDA*) is applied to separation films and composite plies. For best efficiency, the application of this parameter is managed by the solver. Computations conducted on eight processors and 24 GB of RAM last between eight and a half hours and twelve and a half hours depending on the size of the model.

## 6.1.5 Results

### 6.1.5.1 Preform geometries and out-of-plane wrinkles

Computed and measured preform geometries are compared for six distinct characteristic lengths. The ability of the simulation to depict proper amount and shapes of out-of-plane wrinkles is assessed for each edge of the preforms.

---

<sup>2</sup> Parameters determined via a trial-by-error approach are determined by comparing experimental and computed data for several values of the investigated parameters. Comparisons, which are not presented in this doctoral dissertation, were performed according to the criteria presented in Chapter 6.1.2.

### Unidirectional tailored blank (300 x 300 mm<sup>2</sup>)

Preform geometries after forming are illustrated in Fig. 6-10. Some measurements are also presented in Tab. 6-1. Computed lengths aligned with fibre direction are in good agreement with measured ones (error smaller than 2.5%).

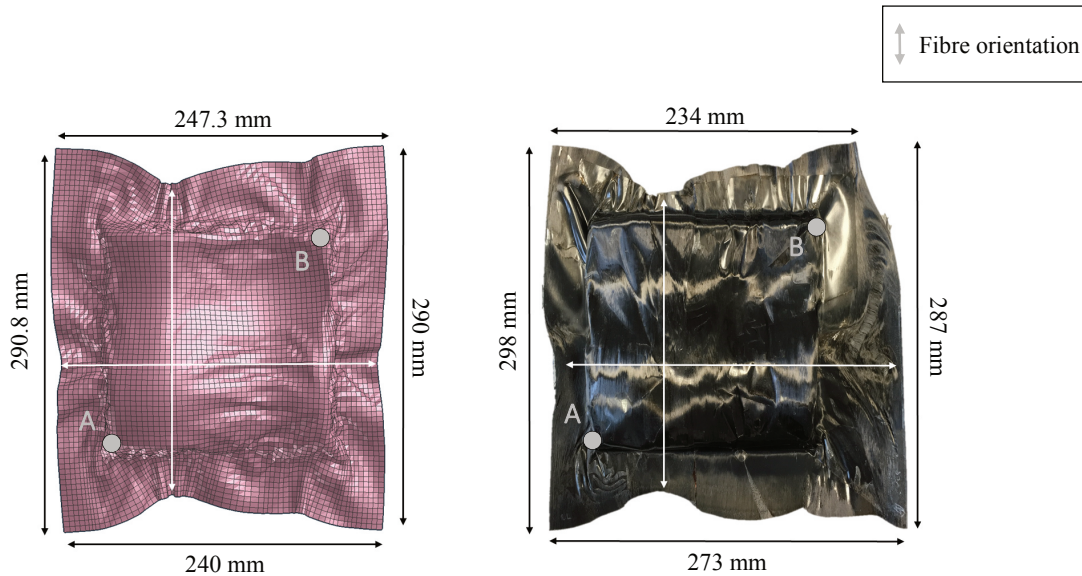


**Fig. 6-10: Preform geometries after forming for the [0]<sub>8</sub> tailored blank (300 x 300 mm<sup>2</sup>)**  
 Left: Simulation; Right: Experiment. The lengths of the white arrows are given in Tab. 6-1. Points A and B are given for orientation purposes (see Fig. 6-1).

The lengths perpendicular to fibre direction computed by the simulation deviate from those measured experimentally. This is due to the unexpected contact which occurred between the blank and the tool at the end of the thermoforming process (see Chapter 6.1.3). The high frictional forces (tool/ply contact, see Chapter 4.3.3.3) and the lack of reinforcement in the direction of motion led to the tearing of the laminate.

**Tab. 6-1: Lengths and widths indicated by white arrows in Fig. 6-10**

	Simulation	Experiment
Vertical length [mm]	235.3	234
Horizontal length [mm]	238	266

Comparisons between computed and observed out-of-plane wrinkles are presented in Tab. 6-2. The ability of the simulation to predict the (i) quantity, (ii) shape (width and peak-to-peak heights) and (iii) location of out-of-plane wrinkles is assessed for each side of the demonstrator.

**Tab. 6-2: Comparisons between computed and observed out-of-plane wrinkles for the [0]<sub>s</sub> tailored blank (300 x 300 mm<sup>2</sup>)**

<b>Location</b>	<b>Simulation</b>	<b>Experiment</b>
Bottom side	Quantity: 8 Height: < 12 mm Width: from 7 mm to 30 mm Location: mainly where draw-in displacements occur	Quantity: Numerous Height: < measurement tolerance Width: < 5 mm Location: mainly where draw-in displacements occur
Right hand side	Quantity: 5 Height: from 3 mm to 10 mm Width: from 15 mm to 45 mm Location: along the edge	Fibre tearing
Top side	Quantity: 7 Height: from 8 mm to 10 mm Width: from 3 mm to 30 mm Location: mainly where draw-in displacements occur	Quantity: Numerous Height: < 5 mm Width: < 6 mm Location: along the edge
Left hand side	Quantity: 4 Height: from 5 mm to 10 mm Width: from 10 mm to 40 mm Location: along the edge	Rather flat

The simulation globally succeeds in identifying the occurrence of out-of-plane wrinkles at the corners of the “double-sinus wave” component. Comparisons on the edges are made rather difficult because of material tearing and the mispositioning of the blank in the environmental chamber (see Chapter 6.1.3).

### Unidirectional tailored blank (350 x 350 mm<sup>2</sup>)

Preform geometries after forming are illustrated in Fig. 6-11. Some measurements are also presented in Tab. 6-3.

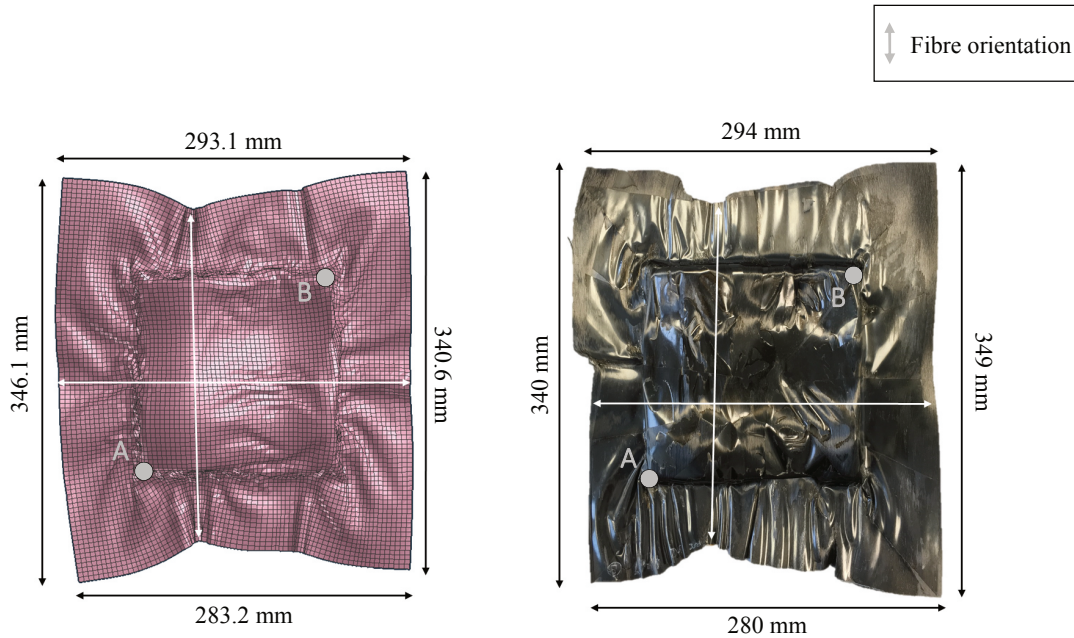


**Fig. 6-11:** Preform geometries after forming for the  $[0]_8$  tailored blank (350 x 350 mm<sup>2</sup>)  
 Left: Simulation; Right: Experiment.  
 Points A and B are given for orientation purposes (see Fig. 6-1).

All computed lengths are in good agreement with measured ones. A maximum error of about 6.6% is to be reported.

**Tab. 6-3:** Lengths and widths indicated by white arrows in Fig. 6-11

	Simulation	Experiment
Vertical length [mm]	284.6	283
Horizontal length [mm]	299.6	281

Comparisons between computed and observed out-of-plane wrinkles located on the edges of the preforms are presented in Tab. 6-4.

**Tab. 6-4: Comparisons between computed and observed out-of-plane wrinkles for the [0]<sub>s</sub> tailored blank (350 x 350 mm<sup>2</sup>)**

<b>Location</b>	<b>Simulation</b>	<b>Experiment</b>
Bottom side	Quantity: 6 Height: from 8 mm to 15 mm Width: from 5 mm to 22 mm Location: mainly where draw-in displacements occur	Quantity: Numerous Height: < 5 mm Width: from 5 mm to 20 mm Location: along the edge
Right hand side	Quantity: 5 Height: from 5 mm to 12 mm Width: from 15 mm to 50 mm Location: along the edge	Rather flat
Top side	Quantity: 6 Height: from 8 mm to 13 mm Width: from 4 mm to 50 mm Location: mainly where draw-in displacements occur	Quantity: Numerous but less than on the bottom side Height: < 5 mm Width: from 5 mm to 20 mm Location: mainly where draw-in displacements occur
Left hand side	Quantity: 5 Height: from 5 mm to 10 mm Width: from 10 mm to 40 mm Location: all along the edge	Only one wrinkle, otherwise rather flat

The simulation globally succeeds in identifying the occurrence of out-of-plane wrinkles at the corners of the “double-sinus wave” component. On the edges, the simulation appears to be able to determine critical areas where out-of-plane wrinkles can potentially occur, although their exact shape and amount cannot be predicted. Deviations between computed and experimental results are assumed to be mainly caused by a too coarse mesh size. According to ten Thije [144], “the element size should not exceed one third of the smallest wrinkle” to enable proper depiction. In this work, shell elements of 4 mm side length are considered for wrinkles of maximum about 5 mm heights. For finer predictions, a finer mesh should be considered. However, for computational efficiency purposes, the mesh size of the models presented in this doctoral dissertation has not been modified.

### Cross-plyed tailored blank

Preform geometries after forming are illustrated in Fig. 6-12. Some measurements are also presented in Tab. 6-5. All computed lengths are in good agreement with measured ones. A maximum error of about 4% is to be reported.

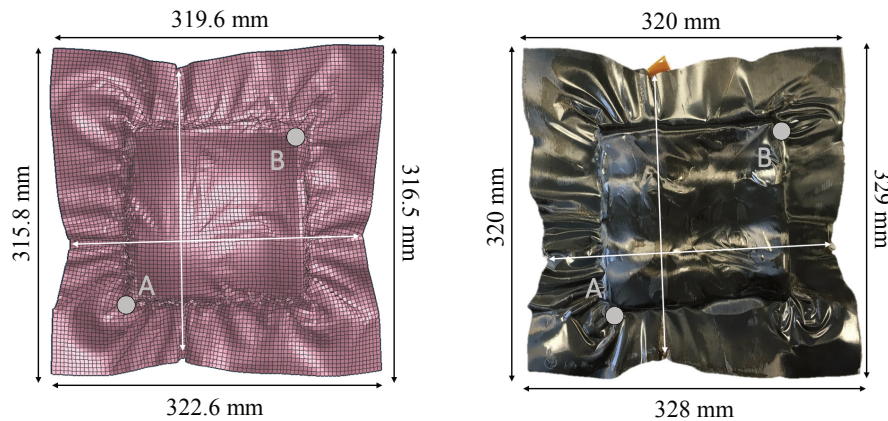


**Fig. 6-12: Preform geometries after forming for the  $[0_2 90_2]_s$  tailored blank**  
 Left: Simulation; Right: Experiment.  
 Points A and B are given for orientation purposes (see Fig. 6-1).

Comparisons between computed and observed out-of-plane wrinkles located on the edges of the preforms are presented in Tab. 6-6.

**Tab. 6-5: Lengths and widths indicated by white arrows in Fig. 6-12**

	Simulation	Experiment
Vertical length [mm]	281	281
Horizontal length [mm]	282.1	279

The simulation globally succeeds in identifying the occurrence of out-of-plane wrinkles at the corners of the “double-sinus wave” component. The simulation also appears to be able to locate and, to some extent, determine the proper amount of out-of-plane wrinkles. However, it does not seem to be able to accurately identify their shapes. In a similar manner as for the previous layup, deviations between experimental and computed results are assumed to be caused by a too coarse mesh size. Discrepancies are also assumed to be due to post-forming deformations<sup>3</sup>, which are reflected in experimental measurements but not in computed ones.

<sup>3</sup> Deformations which occur during consolidation or demoulding operations.



**Tab. 6-6: Comparisons between computed and observed out-of-plane wrinkles for the [0<sub>2</sub> 90<sub>2</sub>]<sub>s</sub> tailored blank**

<b>Location</b>	<b>Simulation</b>	<b>Experiment</b>
Bottom side	Quantity: Numerous	Quantity: Numerous
	Height: from 5 mm to 15 mm	Height: < 3 mm
	Width: from 9 mm to 30 mm	Width: < 10 mm
	Location: along the edge but mainly where draw-in displacements occur	Location: along the edge but concentrated where draw-in displacements occur
Right hand side	Quantity and location: similar as bottom side	Quantity: Numerous
	Height: from 8 mm 15 mm	Height: < measurement tolerance
	Width: from 13 to 50 mm	Width: < 10 mm
		Location: along the edge
Top side	Quantity and location: similar as bottom side	Quantity and location: similar as bottom side
	Height: from 7 mm to 16 mm	Height: < 3 mm
	Width: from 10 mm to 45 mm	Width: < 10 mm
Left hand side	Quantity and location: similar as bottom side	Quantity and location: similar as bottom side
	Height: from 4 to 15 mm	Height: from 5 mm to 13 mm
	Width: from 15 mm to 35 mm	Width: < 10 mm

## Conclusion

The simulation shows to be able to properly predict preform geometries. Although it cannot precisely depict the amount and shape of out-of-plane wrinkles, it demonstrated the ability to identify critical regions where they can potentially occur, e.g. corners and locations at maximum draw-in displacements. Deviations between computed and experimental results are assumed to be caused by a too coarse mesh size as well as some inaccuracies in the positioning of the blanks (blanks could not be positioned with the same accuracy in the environmental chamber and in the simulation). Discrepancies are also assumed to be due to post-forming deformations, which are reflected in experimental measurements but not in computed ones.

### 6.1.5.2 Fibre orientations

Computed and measured fibre orientations are compared according to the method introduced in Chapter 6.1.2. Deviations presented in Tab. 6-7 and Fig. 6-13 are determined by subtracting measured fibre orientations from computed ones. Calculations are performed with average measured and average computed fibre orientations [204], which are determined for each ROI as the mean values of the data measured by the sensor and computed by the simulation, respectively.

Tab. 6-7: Deviations in degree (°) between computed and measured fibre orientations

ROI	$[0]_s$ 300 x 300 mm <sup>2</sup>	$[0]_s$ 350 x 350 mm <sup>2</sup>	$[0_2 90_2]_s$ 350 x 350 mm <sup>2</sup>
1	-0.95°	0.70°	-0.83°
2	-0.75°	-0.65°	-2.34°
3	-2.86°	2.53°	2.55°
4	1.24°	3.67°	0.73°
5	0.43°	5.77°	-0.95°

Computed fibre orientations are in good agreement with measured ones. The Matlab routine considered for comparison purposes appears to be an efficient tool to analyse both data sets [204]. Inaccuracies in the calculation of average measured fibre orientations caused by the unevenness of preform surfaces (see Fig. 6-7) have been overcome by discarding spurious measurement data (see Appendix m). Other experimental aspects, e.g. blank mispositioning (see Chapter 6.1.3) and part distortions caused by consolidation and demoulding operations, might also have introduced some inaccuracies.

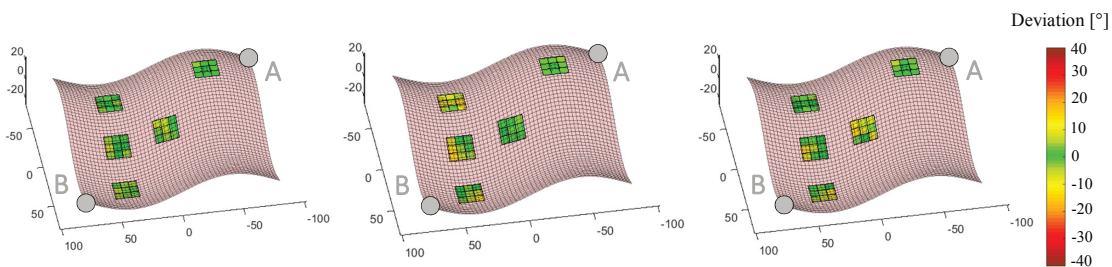


Fig. 6-13: Deviations between computed and measured fibre orientations (3D visualisation)  
 Left:  $[0]_s$  tailored blank (300 x 300 mm<sup>2</sup>); Middle:  $[0]_s$  tailored blank (350 x 350 mm<sup>2</sup>);  
 Right:  $[0_2 90_2]_s$  tailored blank.  
 Points A and B are given for orientation purposes (see Fig. 6-1).

## 6.2 Applications

Comparisons conducted between computed and experimental results have validated the presented FE simulation approach. In this section, this approach is used to investigate two case studies. The first one assesses the benefit of accounting for separation films in FE thermoforming simulations, while the second analyses, via a sensitivity study, the influence of the transverse tensile properties of the composite tape on simulation outcomes.

### 6.2.1 Influence of separation films on thermoforming simulation results

Most of the content of this section, including text and figures, is based on [K10].

To assess whether it is important to model separation films in the same manner as composite plies, i.e. with shell elements and a dedicated material model, the approach presented in this doctoral dissertation is compared to the “classical” modelling method, in which separation films are not modelled as such but their influence is only considered in friction properties. Two approaches are thus considered in this case study:

- Approach 1: separation films are modelled “explicitly” (see Chapter 6.1.4),
- Approach 2: the influence of separation films is only considered within tool/ply interactions (see Fig. 6-14).

Apart from the modelling of their separation films, models developed for the first and second approaches are identical. According to material characterisation test results, a tool/ply friction coefficient of 0.171 is considered in the second approach (see Chapter 4.3.3.1).

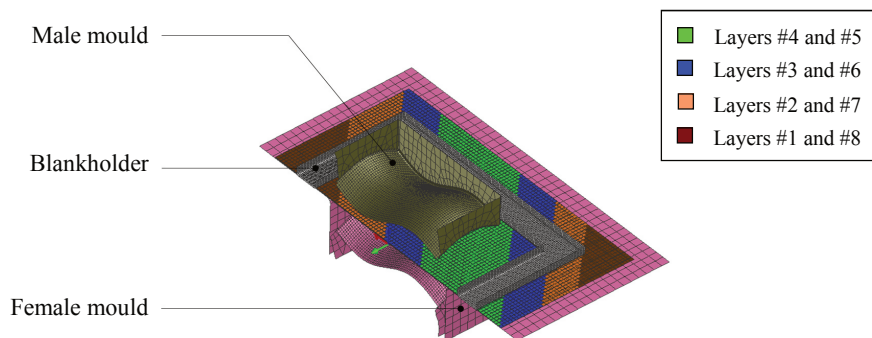


**Fig. 6-14:** “Classical” macroscopic FE simulation model in which separation films are not modelled “explicitly” (approach 2)

Both simulation approaches are assessed on their ability to predict preform geometries, out-of-plane wrinkles and external fibre orientations. Comparisons are conducted for the three layups introduced in Chapter 6.1.1 and with the same methods as presented in Chapter 6.1.2.

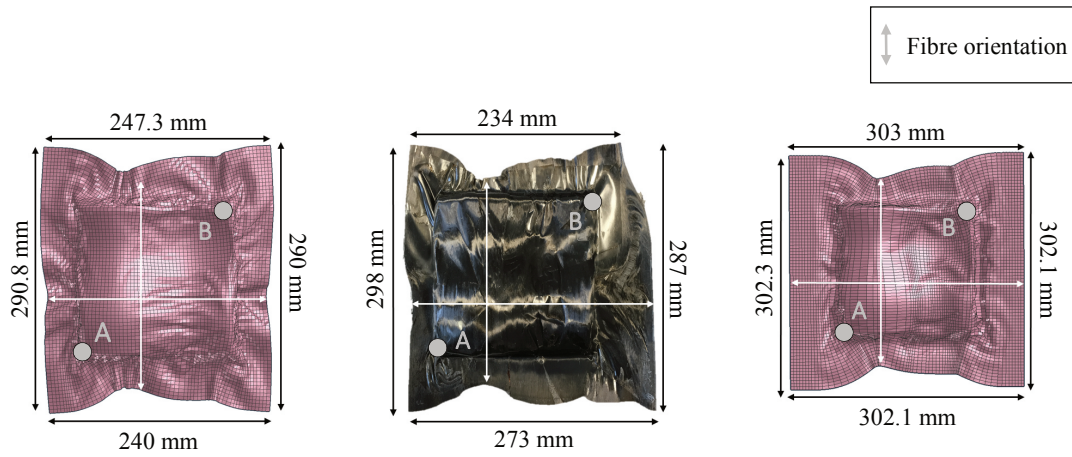


**Fig. 6-15: Preform geometries after forming for the  $[0]_8$  tailored blank (300 x 300 mm<sup>2</sup>)**  
 Left: Approach 1; Middle: Experiment; Right: Approach 2. Points A and B are given for orientation purposes (see Fig. 6-1).

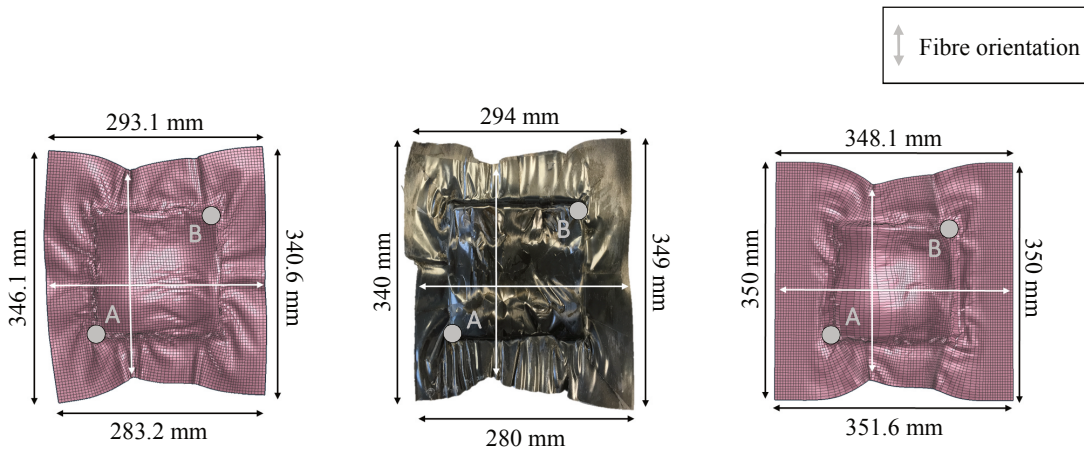


**Fig. 6-16: Preform geometries after forming for the  $[0]_8$  tailored blank (350 x 350 mm<sup>2</sup>)**  
 Left: Approach 1; Middle: Experiment; Right: Approach 2. Points A and B are given for orientation purposes (see Fig. 6-1).

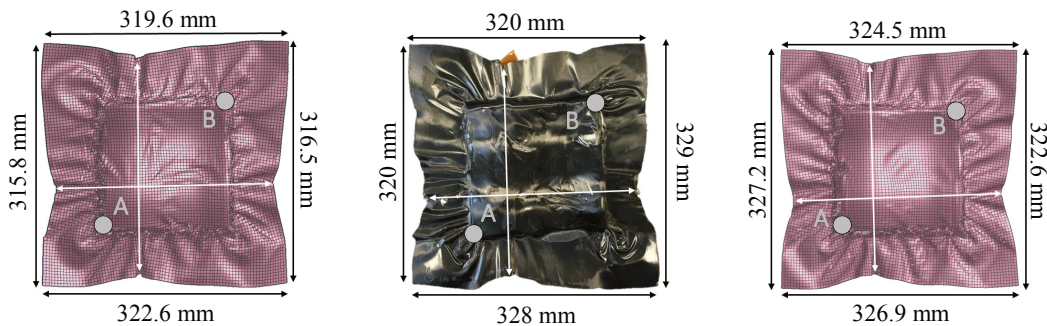


**Fig. 6-17: Preform geometries after forming for the  $[0_2 90_2]_s$  tailored blank**  
 Left: Approach 1; Middle: Experiment; Right: Approach 2. Points A and B are given for orientation purposes (see Fig. 6-1).

Preform geometries after forming are illustrated in Fig. 6-15, Fig. 6-16 and Fig. 6-17. Some measurements are also presented in Tab. 6-8. Although the second simulation approach can globally predict the geometry of the cross-plyed layup, it cannot determine the proper geometry of the unidirectional blanks. The capabilities of the second approach seems to be limited because it does not take into account the mechanical aspect of the separation films. Due to their significant stiffness (see Chapter 4.2) and the fact that they stick to the blanks during forming (see Chapter 4.3.3.3), separation films stiffen and thus, influence composite behaviour. It can be noticed that when the films are modelled “explicitly” (approach 1), unidirectional blanks slip over the mould in a similar manner as in the experiments (see widths in Fig. 6-15 and Fig. 6-16), while when their influence is only taken into account in tool/ply interactions (approach 2), blanks do not slip but rather undergo severe transverse deformations. For a unidirectional layup, the maximum transverse strain computed by a model developed according to the second approach is indeed more than twice the value computed by a model developed according to the first approach (about 1.55 compared to 0.62).

**Tab. 6-8:** Lengths and widths indicated by white arrows in Fig. 6-15, Fig. 6-16 and Fig. 6-17. The first values correspond to simulation results for approach 1, the second to the experimental measurements and the third to simulation results for approach 2

	[0] <sub>8</sub> 300 x 300 mm <sup>2</sup>	[0] <sub>8</sub> 350 x 350 mm <sup>2</sup>	[0 <sub>2</sub> 90 <sub>2</sub> ] <sub>s</sub> 350 x 350 mm <sup>2</sup>
Vertical length [mm]	235.3 / 234 / 241.5	284 / 283 / 288.2	280.7 / 281 / 288.9
Horizontal length [mm]	238.6 / 266 / 303	299.8 / 281 / 350	281.3 / 279 / 287.7

Because the development of out-of-plane wrinkles is related to blank deformations, conclusions drawn about preform geometries also apply to out-of-plane wrinkles. In particular, although both simulation approaches depict similar outcomes for the cross-plyed layup, discrepancies occur for the unidirectional blanks. After comparison with experimental outcomes, results computed with the first simulation approach appear to be more accurate than those computed with the second approach.

To complete the assessment, the external fibre orientations computed by both simulation approaches are compared to experimental measurements using the Matlab routine introduced in Chapter 6.1.2. Results, which consist in cumulative errors<sup>4</sup>, are presented in Tab. 6-9. For all three layups, the first approach demonstrates a better ability to predict external fibre orientations.

<sup>4</sup> Cumulative errors are calculated by adding up the absolute deviations of each ROI, which are determined by subtracting measured fibre orientations from computed ones.

**Tab. 6-9: Evaluation of both simulation approaches: cumulative errors between measured and computed fibre orientations**

	[0] <sub>s</sub> 300 x 300 mm <sup>2</sup>	[0] <sub>s</sub> 350 x 350 mm <sup>2</sup>	[0 <sub>2</sub> 90 <sub>2</sub> ] <sub>s</sub> 350 x 350 mm <sup>2</sup>
<b>Approach 1</b>			
Cumulative error [°]	6.22	13.32	7.40
<b>Approach 2</b>			
Cumulative error [°]	10.28	15.08	10.35

The first approach, which consists in the “explicit” modelling of separation films, appears to be better suited than the second approach, which only considers the influence of separation films within tool/ply interactions, to predict proper forming behaviour. The importance to model such films as composite plies is due to their substantial stiffness (see Chapter 4.2) and the fact that they stick to the blanks during thermoforming (see Chapter 4.3.3.3). Therefore, they do not only influence tool/ply interactions but also stiffen composite behaviour.

## 6.2.2 Influence of composite transverse tensile properties on thermoforming simulation results

To investigate the influence of the transverse tensile properties of the composite tape on simulation outcomes, in particular on (i) preform geometries, (ii) out-of-plane wrinkles and (iii) fibre orientations, three macroscopic FE thermoforming simulation models are considered. These are developed according to the approach presented in Chapter 6.1.4, i.e. the separation films are modelled with shell elements and a dedicated material model. Analyses are conducted by comparing the outcomes of a reference simulation, which considers the composite material model calibrated in Chapter 5, with those of simulations having transverse tensile properties  $E_2$  ten times smaller or larger. Sensitivity analysis is carried out for the three layups introduced in Chapter 6.1.1.

Preform geometries after forming are illustrated in Fig. 6-18, Fig. 6-19 and Fig. 6-20. Some measurements are also presented in Tab. 6-10. The influence of transverse tensile properties on final preform shapes appears to be negligible for all types of blanks, although a larger influence on unidirectional layups is noticed (variations up to maximum about 4%). This was to be expected since unidirectional blanks are only reinforced in one direction. The lack of load carrier in the other direction makes them more sensitive to transverse loads. On the contrary, cross-ply tailored blanks are more stable because of their layup arrangement and the presence two families of fibres.

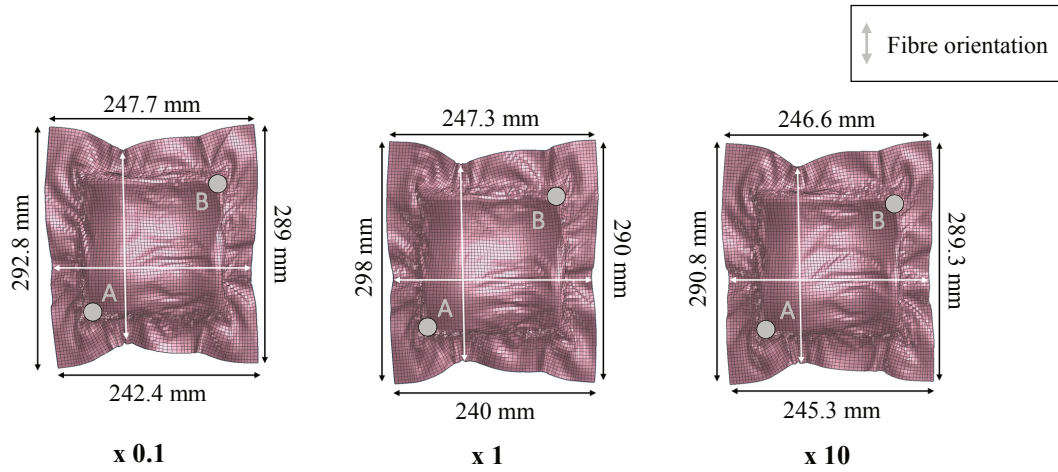


**Fig. 6-18: Preform geometries after forming for the  $[0]_8$  tailored blank ( $300 \times 300 \text{ mm}^2$ )**  
 Left:  $E_2$  multiplied by 0.1; Middle: Original  $E_2$ ; Right:  $E_2$  multiplied by 10. Points A and B are given for orientation purposes (see Fig. 6-1).

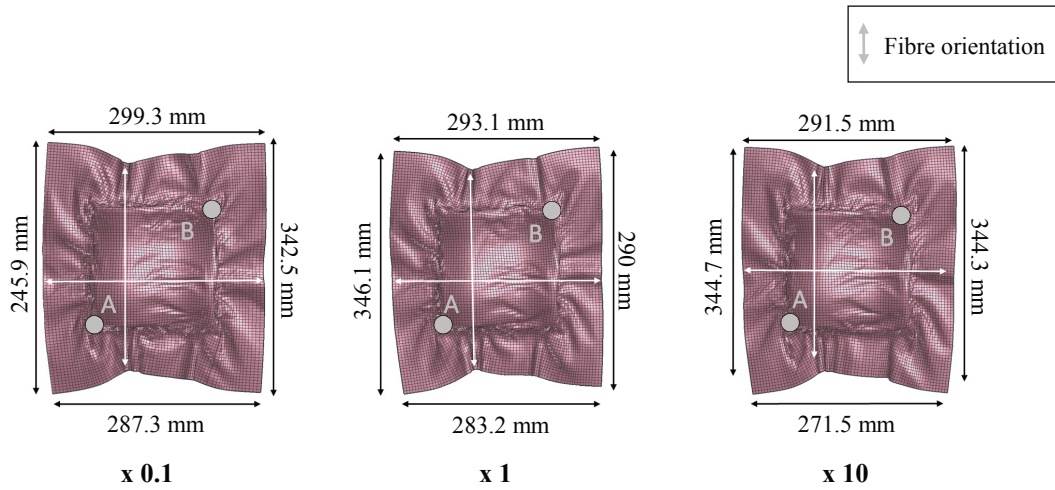


**Fig. 6-19: Preform geometries after forming for the  $[0]_8$  tailored blank ( $350 \times 350 \text{ mm}^2$ )**  
 Left:  $E_2$  multiplied by 0.1; Middle: Original  $E_2$ ; Right:  $E_2$  multiplied by 10. Points A and B are given for orientation purposes (see Fig. 6-1).

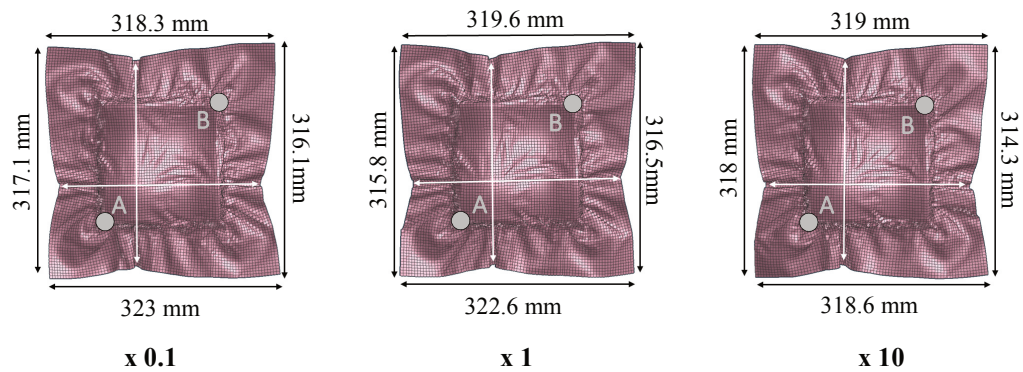


**Fig. 6-20: Preform geometries after forming for the  $[0_2 90_2]_s$  tailored blank**  
 Left:  $E_2$  multiplied by 0.1; Middle: Original  $E_2$ ; Right:  $E_2$  multiplied by 10. Points A and B are given for orientation purposes (see Fig. 6-1).

For all three layups, the variation of transverse tensile properties do not have a considerable influence on the overall location of out-of-plane wrinkles. The amount and shapes of major wrinkles are also found not to be much influenced (few millimetres variations).

**Tab. 6-10:** Lengths and widths indicated by white arrows in Fig. 6-18, Fig. 6-19 and Fig. 6-20. The first values correspond to simulation results for  $E_2$  multiplied by 0.1, the second to simulation results for original  $E_2$  and the third to simulation results for  $E_2$  multiplied by 10

	[0] <sub>8</sub> 300 x 300 mm <sup>2</sup>	[0] <sub>8</sub> 350 x 350 mm <sup>2</sup>	[0 <sub>2</sub> 90 <sub>2</sub> ] <sub>s</sub> 350 x 350 mm <sup>2</sup>
Vertical length [mm]	233.1 / 235.3 / 236.5	285.3 / 284 / 282.7	280.5 / 280.7 / 280.3
Horizontal length [mm]	242.9 / 238.6 / 241.5	305.3 / 299.8 / 293.7	280.3 / 281.3 / 278.1

To complete the assessment, the computed fibre orientations are compared to experimental measurements using the Matlab routine introduced in Chapter 6.1.2. Results, which consist in cumulative errors, are presented in Tab. 6-11.

**Tab. 6-11:** Influence of transverse tensile properties on computed fibre orientations: cumulative error between measured and computed fibre orientations. The first values correspond to comparisons performed with  $E_2$  multiplied by 0.1, the second to comparisons performed with original  $E_2$  and the third to comparisons performed with  $E_2$  multiplied by 10

	[0] <sub>8</sub> 300 x 300 mm <sup>2</sup>	[0] <sub>8</sub> 350 x 350 mm <sup>2</sup>	[0 <sub>2</sub> 90 <sub>2</sub> ] <sub>s</sub> 350 x 350 mm <sup>2</sup>
Cumulative error [°]	7.60 / 6.22 / 8.44	15.40 / 13.32 / 15.61	6.68 / 7.40 / 6.68

For the cross-plyed layup, discrepancies (about 0.72°) are considered to be rather due to inaccuracies in the measurements than to some influence of transverse tensile properties. Measurement inaccuracies are likely caused by post-forming deformations and approximations in the positioning of the robot [204].

Deviations observed for unidirectional blanks are slightly more significant (up to 2.5°). These can therefore not only be imputed to measurement inaccuracies. However, given their small values, transverse tensile properties only seem to have a very limited influence on thermoforming simulation outcomes.



According to the investigations presented in this section (preform geometries, out-of-plane wrinkles and fibre orientations), the transverse tensile properties of the composite tape do not seem to have considerable influence on simulation results.

## 6.3 Conclusion

The goal of this chapter was to validate and subsequently apply the FE thermoforming simulation approach presented in this doctoral dissertation.

The validation was performed with a laboratory-scale thermoforming process and a generic double-curved demonstrator. Investigations were conducted with three different tailored blanks, which varied in sizes and layup arrangements. Comparisons between computed and experimental results demonstrated the quality and accuracy of the presented approach. For all three blanks, the simulation appeared to be able to predict proper preform geometries and external fibre orientations. Results also demonstrated the ability of the simulation to determine critical areas where out-of-plane wrinkles can potentially occur, although their exact shape and amount could not be predicted.

Once validated, the simulation approach was applied to two case studies. The first one highlighted the benefit of accounting for separation films in FE thermoforming simulations. Because separation films stiffen composite behaviour, they must be modelled in the same manner as composite plies, i.e. with shell elements and a dedicated material model. Further analyses with other types of films and demonstrator geometries would be, however, necessary to generalise this outcome to other applications. The second case study investigated the influence of the transverse tensile properties of the composite tape on thermoforming simulation results. Results demonstrated, via a sensitivity analysis, that they only have a limited influence.

According to the results presented in this chapter, the simulation approach presented in this doctoral dissertation can now be used in an industrial context to support decision making regarding, for example, the development and optimisation of manufacturing techniques or the design of new components.



## 7 Conclusions and recommendations

The principal aim of the work presented in this doctoral dissertation was to develop macroscopic FE thermoforming simulation models able to predict the potential occurrence of defects, such as out-of-plane wrinkles and fibre reorientations. The detection of such defects is particularly important for quality and performance purposes since they alter the shapes and the mechanical properties of final components. In industrial applications, FE thermoforming simulations can enable significant cost and time saving by supporting early decision making regarding the design of new components and the development of new manufacturing techniques.

The development of thermoforming simulations consists in the characterisation of materials and the elaboration of appropriate simulation approaches. Before simulations can be considered for industrial applications, the reliability of their predictions must be validated. To be relevant, such investigations are performed with processes and components which have similar features as in the industry. In the scope of this work, the presented simulation approach was validated based on a laboratory-scale thermoforming process and a generic double-curved component. Tailored composite blanks were manufactured according to industrial standards. These, which are composed of continuous unidirectional carbon fibre-reinforced PA6 tapes, were prepared by an ATL technology and consolidated using a mechanical press.

In the following, the main achievements of this doctoral dissertation with respect to (i) material characterisation, (ii) thermoforming simulation and (iii) validation and applications are highlighted and discussed. Recommendations for further investigations and future applications are also made according to the goals listed in Chapter 1.2.

### 7.1 Material characterisation

Material characterisation aims to investigate material behaviour in order to determine proper input parameters for the development of FE thermoforming simulations. With this respect, both the unidirectional thermoplastic composite material and the separation film considered in this work were characterised. In a subsequent step, different types of interactions were investigated.

Given that the behaviour of the thermoplastic composite material is much dependent on temperature and thermoforming takes place under specific environmental conditions, investigations were conducted, to the best possible extent, under similar environmental conditions as forming occurs.

Because of the lack of methods and test standards available in the literature regarding the intra-ply characterisation of molten thermoplastic composite materials, two test methods were developed. These methods, which consider the application of a DMA system in a quasi-static manner, aim to characterise longitudinal out-of-plane bending and transverse tensile behaviour. Although three different approaches were considered for intra-ply shear investigations, only the outcomes obtained from a rotational rheometer with a torsion bar test method [62, 66] could be accounted for characterisation purposes. The DMA system and the rheometer showed to be well suited to characterise molten unidirectional thermoplastic materials. In particular, they demonstrated good ability to control testing parameters such as temperatures and test speeds.

Under longitudinal out-of-plane bending and transverse tensile loading, the molten unidirectional thermoplastic composite material exhibited clear viscous behaviour. Under intra-ply shear loading, an elastic dominated response with limited viscous effects was observed. This particular behaviour might be due to the fact that intra-ply shear investigations were only conducted within material LVE region.

The main drawback of the presented test methods lies in the test speeds at which experiments are performed and thus, strain rates at which specimens are characterised. These might be limited for some industrial applications, in particular, for those carried out at high forming speeds, e.g. 100 mm/s. To extend their testing capabilities, the DMA system and the rheometer should be used dynamically outside material LVE region rather than quasi-statically for the DMA system and dynamically within material LVE region for the rheometer.

The test methods developed and/or presented in this doctoral dissertation were successfully applied to a non-cured unidirectional thermoset prepreg material, which showed to have less viscous behaviour than its thermoplastic counterpart. However, future studies should address the effect of clamping on characterisation test results.

The method considering a DMA system to carry out quasi-static tensile tests was also applied to characterise, under environmental forming conditions, the mechanical behaviour of the separation film considered in this study (polyimide film). Given that the material was considered isotropic elastic, only tensile tests were performed. Although test results were globally non-linear, a Young's modulus was derived from the early linear, and assumed elastic, behaviour.

For the characterisation of contact properties under regulated environmental conditions, a new test setup based on the "carrier test setup" was developed. With this equipment, experiments can be performed at different temperatures, test speeds and load levels. The presented apparatus showed to be able to characterise inter-ply slip in molten unidirectional thermoplastic laminates for different test speeds and interactions between treated films and tool for different test speeds and pressure values. Inter-ply slip at high pressure values and contact between treated films and molten thermoplastic

plies could not be characterised because of experimental issues. With this respect, the design of the carrier should be modified in order to improve clamping capabilities.

Inter-ply slip in non-cured unidirectional thermoset laminates could not be characterised with the developed friction test setup because of material tackiness and the occurrence of a bending moment at the attachment hook. Future studies should consider other types of apparatus, such as pull-out and pull-through test setups, rather than the “carrier” approach. These appear to be better candidates because of their different working principles and thus, the absence of bending moment at their attachment point.

## 7.2 Thermoforming simulation

The development of thermoforming simulation comprises both the calibration of the material models and the preparation of thermoforming process simulation models.

The simulations presented in the scope of this doctoral dissertation were developed using the commercial software Visual-FORM supplied by ESI Group and computed with the solver PAM-FORM v.2012.0 and v.2013.0.

To model the molten thermoplastic composite tape, a constitutive model composed of a thermo-visco-elastic matrix and elastic fibres was considered (MAT 140) and applied to four-node shell elements. This model was selected because of its ability to depict the specific, i.e. viscous, behaviour of the material. Because of some model specificities, e.g. parameter coupling, characterisation test results could not be directly considered as simulation input. Instead, experimental data were used in an inverse approach to identify suitable simulation parameters.

This identification process appeared to be rather difficult because of the limits of the characterisation test method (transverse tensile tests were conducted for constant loading rates rather than constant strain rates) and the restrictions of the material model. One of the main drawbacks of this identification process, besides the effort, is that identified parameters can significantly differ from experimental data. Therefore, these parameters can only be regarded as simulation input without clear scientific significance. The identification process would be more intuitive if the user could, for each deformation mode, enter material data as they are obtained from characterisation tests, i.e. stress-strain curves for given strain rates and/or temperatures. Based on the feedbacks of their customers, ESI Group has made available this type of data entry in the latest version of the material model MAT 140 (v.2015) [158].

Regarding the modelling of the polyimide separation film, an isotropic material model (MAT 101) was considered and applied to four-node shell elements. In comparison to the identification analysis conducted for MAT 140, investigations were easier since the aimed value of the elastic modulus corresponded to the entered one.

Contacts were managed by a symmetric node-to-segment with edge treatment algorithm. All contacts were developed according to material characterisation test results, except for the interactions between treated films and composite plies which could not be characterised and for which a user-defined value was considered. In a similar manner as for MAT 101, the identification of suitable friction coefficients was rather simple since simulation output corresponded to entered values. The interaction between the tool and the separation film was modelled with an isotropic Coulomb model according to characterisation test results. Although a speed dependency was experimentally observed, inter-ply slip behaviour was modelled with a simple orthotropic Coulomb law because of the restriction of the simulation software. With this respect, the development of a more elaborated contact model, which can account for actual temperatures, fibre orientations, speeds and if required, pressures, should be addressed in future work.

Thermoforming simulation models were developed according to the experimental forming process. Similar blank geometries, layup arrangements, test speed and pressure were considered. The only difference between the experimental process and the simulation models lies in the modelling of the separation films. To prevent the occurrence of dynamic effects, separation films were modelled as plain plies, i.e. without cut-outs. This simplification is, however, not expected to influence simulation results since, during forming, polyimide films stick to the blanks and are only subjected to small deformations.

### 7.3 Validation and applications

The validation aims to demonstrate the potential of the presented simulation approach. For this purpose, computed and experimental results are compared according to several criteria. By analogy with industrial applications, validation was conducted with a laboratory-scale thermoforming process and a generic double-curved demonstrator. The simulation approach was assessed according to its ability to predict preform geometries, external fibre orientations and out-of-plane wrinkles. Comparisons regarding preform geometries (maximum 7% deviation) and external fibre orientations (maximum 6° deviation) demonstrated the quality and accuracy of the presented simulation approach. Results also showed the ability of the simulation to determine critical areas where out-of-plane wrinkles can potentially occur, although their quantity and shapes could not be exactly predicted. For finer predictions, a finer mesh should be considered. However, for computational efficiency purposes, the mesh size of the models presented in this doctoral dissertation was not modified. To enhance actual validation methods, future work should consider comparing the fibre orientations of all composite plies, rather than for the external layer only, and for the entire component, rather than for limited regions of interest. Comparisons could also be conducted according to other types of criteria, such as fibre strains.

Once validated, the simulation approach was applied to two use cases. The first one highlighted the benefit of modelling separation films in the same manner as composite plies, i.e. with a layer of shell elements and a dedicated material model, in FE thermoforming simulations. The second application showed, via a sensitivity analysis, that the transverse tensile properties of the composite tape only have limited influence on simulation results. This result might be of particular importance for the development of future thermoforming simulations.

For future work, the modelling of non-isothermal thermoforming processes could be considered. These processes occur in some industrial applications when the temperature of the mould is around thermoplastic glass transition temperature to enable rapid cooling and consolidation. For the development of such FE thermoforming simulations, new material characterisation test methods, e.g. characterisation of thermal conductivities, and material modelling approaches, e.g. implementation of thermal-mechanical constitutive laws, should be investigated.





## References

- [1] United Nations Framework Convention on Climate Change (UNFCCC) - Conference of the Parties (COP), “Adoption of the Paris Agreement. Proposal by the President”, 12/12/2015, p. 21. [Online]. Available: [https://unfccc.int/documentation/documents/advanced\\_search/items/6911.php?priref=600008831](https://unfccc.int/documentation/documents/advanced_search/items/6911.php?priref=600008831)
- [2] Intergovernmental Panel on Climate Change (IPCC), “Climate Change 2014: Mitigation of Climate Change”, 2014, p. 44. [Online]. Available: <https://www.ipcc.ch/report/ar5/wg3/>
- [3] United States Environmental Protection Agency, “Global Greenhouse Gas Emissions Data”, 2015. [Online]. Available: <http://www3.epa.gov/climatechange/ghgemissions/global.html>
- [4] International Transport Report, “Reducing transport greenhouse gas emissions: trends and data, in Background for the 2010 International Transport Forum (Transport and Innovation: Unleashing the Potential)”, 2010. [Online]. Available: [www.itf-oecd.org/sites/default/files/docs/10ghgtrends.pdf](http://www.itf-oecd.org/sites/default/files/docs/10ghgtrends.pdf)
- [5] European Commission, “Reducing CO2 emissions from passenger cars”, 2015. [Online]. Available: [http://ec.europa.eu/clima/policies/transport/vehicles/cars/index\\_en.htm](http://ec.europa.eu/clima/policies/transport/vehicles/cars/index_en.htm)
- [6] International Air Transport Association (IATA), “A global approach to reducing aviation emissions”, 2009. [Online]. Available: [http://corporate.airfrance.com/fileadmin/dossiers/img\\_rte\\_fr/IATA.pdf](http://corporate.airfrance.com/fileadmin/dossiers/img_rte_fr/IATA.pdf)
- [7] European Commission, “Reducing car weight and cutting down greenhouse gas emissions”, 20/02/2012. [Online]. Available: [http://ec.europa.eu/research/transport/projects/items/reducing\\_car\\_weight\\_and\\_cutting\\_down\\_greenhouse\\_gas\\_emissions\\_en.htm](http://ec.europa.eu/research/transport/projects/items/reducing_car_weight_and_cutting_down_greenhouse_gas_emissions_en.htm)
- [8] DuPont, “Vehicle Weight Reduction for Optimal Performance”, 2016. [Online]. Available: <http://www.dupont.com/industries/automotive/articles/lightweighting.html>
- [9] H. Helms and U. Lambrecht, “The Potential Contribution of Light-Weighting to Reduce Transport Energy Consumption”, *Int J LCA*, vol. 12, no. 1, pp. 58-64, 2007. [Online]. Available: [http://www.ifeu.org/verkehrundumwelt/pdf/Helms%282006%29\\_light-weighting.pdf](http://www.ifeu.org/verkehrundumwelt/pdf/Helms%282006%29_light-weighting.pdf)
- [10] Dry Composites, “BMW i3: first mass produced composite car in production”, 03/10/2013. [Online]. Available: <http://www.drycomposites.com/bmw-i3-first-mass-produced-composite-car-in-production/>
- [11] B.T. Åström, *Manufacturing of Polymer Composites*. London: Chapman and Hall, 1997.

- [12] S.W. Tsai, *Theory of Composites Design (third edition)*. Stanford: Think Composites, 2008.
- [13] F. Campbell, *Manufacturing Processes for Advanced Composites*. Oxford: Elsevier, 2004.
- [14] A. Brent Strong, *Fundamentals of Composites Manufacturing - Materials, Methods and Applications*. Dearborn: Society of Manufacturing Engineers, p. 161, 2005. [Online]. Available: <https://books.google.fr/books?id=aCm9yvodiJcC&pg>
- [15] BASF, “Ultracom - thermoplastic composite system”, 2014. [Online]. Available: <http://www.standort-ludwigshafen.basf.de/group/corporate/site-ludwigshafen/en/brand/ULTRACOM>
- [16] TenCate, “TenCate Cetex Thermoplastic Composites”, 2015. [Online]. Available: <http://www.tencate.com/advancedcomposites/products/thermoplastic/default.aspx>
- [17] Celanese, “Celstran CFR-TP continuous fibre reinforced thermoplastic”, 2016. [Online]. Available: <http://www.celanese.com/engineered-materials/products/Celstran-CFRT.aspx>
- [18] F.N. Cogswell, *Thermoplastic aromatic polymer composites*. Oxford: Butterworth Heinemann, 1992.
- [19] T.G. Gutowski, “Cost, Automation, and Design” in *Advanced Composites Manufacturing*, T.G. Gutowski, Ed, New York: John Wiley & Sons, 1997, pp. 513-570.
- [20] D. Lukaszewicz, C. Ward and K. Potter, “The engineering aspects of automated prepreg layup: History, present and future”, *Compos Part B-Eng*, vol. 43, no. 3, pp. 997-1009, 2012.
- [21] R.S. Moon, C.C. Johnson and R.D. Hale, “Nondestructive evaluation and mechanical testing of steered fiber composites” in *Proceedings of 47<sup>th</sup> International SAMPE symposium*, Long Beach, USA, 2002.
- [22] A. Burkhart and D. Cramer, “Continuous-fibre reinforced thermoplastic tailored blanks”, *JEC Composites Magazine*, vol. 43, no. 22, pp. 41-43, 2006.
- [23] K. Potter, “Beyond the pin-jointed net: maximizing the deformability of aligned continuous fibre reinforcements”, *Compos Part A-Appl S*, vol. 33, no. 5, pp. 677-686, 2002.
- [24] Y.R. Larberg, “Forming of Stacked Unidirectional Prepreg Materials”, doctoral dissertation, Royal Institute of Technology, 2012.

- [25] P. Harrison, R. Gomas and N. Currado-Correia, "Press forming a 0/90 cross-ply advanced thermoplastic composite using the double-dome benchmark geometry", *Compos Part A-Appl S*, vol. 54, no. 0, pp. 56-69, 2013.
- [26] R.K. Okine, "Analysis of Forming Parts from Advanced Thermoplastic Composite Sheet Materials", *SAMPE Journal*, vol. 25, no. 3, pp. 9-19, 1989.
- [27] K. Friedrich, M. Hou and J. Krebs, "Thermoforming of continuous fibre/thermoplastic composite sheets" in *Composite Sheet Forming*, D. Bhattacharya, Ed, Amsterdam: Elsevier, 1997, pp. 91-162.
- [28] T. Creasy, "Sheet forming in polymer matrix composites" in *Manufacturing Techniques for Polymer Matrix Composites*, S. Advani and K.T. Hsiao, Ed, Philadelphia: Woodhead Publishing Ltd, 2012, pp. 123-138.
- [29] Dutch Thermoplastic Components, *Aerospace structures*, 2011. [Online]. Available: <http://www.composites.nl/products/aerospace-structures/>
- [30] T.A. Martin and D. Bhattacharyya, "Squeeze flow in thermoplastic composites" in *Polypropylene: An A-Z reference*, J. Karger-Kocsis, Ed, Dordrecht: Springer, 1999, pp. 776-782.
- [31] Celanese Chemicals Europe GmbH, "Standard product values of Celstran CFR-TP PA6 CF60-01", *Product technical Datasheet*, July 2014.
- [32] FibreForge, *RELAY Station brochure*, 2014. [Online]. Available: <http://www.fiberforge.com/documents/2.%20Fiberforge%20RELAY%20Station%20brochure.pdf>
- [33] M. Biron, "Outline of the actual situation of plastics compared to conventional materials" in *Thermoplastics and Thermoplastic Composites*, M. Biron, Ed, Oxford: Elsevier, 2013, pp. 1-29.
- [34] C.L. Tucker, "Forming of Advanced Composites" in *Advanced Composites Manufacturing*, T.G. Gutowski, Ed, New York: John Wiley & Sons, 1997, pp. 297-372.
- [35] P. Boisse, "Finite element analysis of composite forming" in *Composite forming technologies*, A.C. Long, Ed, Cambridge: Woodhead Publishing Ltd, 2007, pp. 46-79.
- [36] T. Gereke, O. Döbrich, M. Hübner and C. Cherif, "Experimental and computational composite textile reinforcement forming: a review", *Compos Part A-Appl S*, vol. 46, no. 0, pp. 1-10, 2013.
- [37] J.A. Sherwood, K.A. Fetfatsidis, J.L. Gorczyca and L. Berger, "Fabric thermo-stamping in polymer matrix composites", in *Manufacturing Techniques for Polymer Matrix Composites*, S. Advani and K.T. Hsiao, Ed, Philadelphia: Woodhead Publishing Ltd, 2012, pp. 139-179.

- [38] R. Akkerman and S.P. Haanappel, "Thermoplastic composites manufacturing by thermoforming" in *Advances in Composites Manufacturing and Process Design*, P. Boisse, Ed, Cambridge: Woodhead Publishing Ltd, 2015, pp. 111-129.
- [39] R. Brooks, "Forming technology for thermoplastic composites" in *Composites forming technologies*, A. C. Long, Ed, Cambridge: Woodhead Publishing Ltd, 2015, pp. 256-276.
- [40] J. Krebs, K. Friedrich and D. Bhattacharyya, "A direct comparison of matched-die versus diaphragm forming", *Compos Part A-Appl S*, vol. 29, no. 1-2, pp. 183-188, 1998.
- [41] M. Hou and K. Friedrich, "3-D Stamp Forming of Thermoplastic Matrix Composites", *Appl Compos Mater*, vol. 1, no. 2, pp. 135-153, 1994.
- [42] Rucks, *Our Presses - Plastics and Composites*, 17/02/2016. [Online]. Available: [http://www.rucks.de/en\\_234\\_plastics\\_and\\_composites.html](http://www.rucks.de/en_234_plastics_and_composites.html)
- [43] U. Sachs, "Friction and bending in thermoplastic composites forming processes", doctoral dissertation, University of Twente, 2014.
- [44] A.C Long and M.J. Clifford, "Composite forming mechanisms and materials characterisation" in *Composites forming technologies*, A. C. Long, Ed, Cambridge: Woodhead Publishing Ltd, 2007, pp. 1-21.
- [45] S. Bel, P. Boisse and F. Dumont, "Analyses of the Deformation Mechanisms of Non-Crimp Fabric Composite Reinforcements during Preforming", *Appl Compos Mater*, vol. 19, no. 3, pp. 513-528, 2012.
- [46] S.B. Sharma, M.P.F. Sutcliffe and S.H. Chang, "Characterisation of material properties for draping of dry woven composite material", *Compos Part A-Appl S*, vol. 34, no. 12, pp. 1167-1175, 2003.
- [47] J. Cao, R. Akkerman, P. Boisse, J. Chen, H.S. Cheng, E.F. de Graaf et al., "Characterization of mechanical behavior of woven fabrics: Experimental methods and benchmark results", *Compos Part A-Appl S*, vol. 39, no. 6, pp. 1037-1053, 2008.
- [48] H. Kong, A.P. Mouritz and R. Paton, "Tensile extension properties and deformation mechanisms of multiaxial non-crimp fabrics", *Compos Struct*, vol. 66, no. 1-4, pp. 249-259, 2004.
- [49] J. Launay, G. Hivet, A.V. Duong and P. Boisse, "Experimental analysis of the influence of tensions on in plane shear behaviour of woven composite reinforcements", *Compos Sci Technol*, vol. 68, no. 2, pp. 506-515, 2008.
- [50] S.V. Lomov, M. Barburski, T. Stoilova, I. Verpoest, R. Akkerman, R. Loendersloot and R.H.W. ten Thije, "Carbon composites based on multiaxial

- multiply stitched preforms: Part 3: Biaxial tension, picture frame and compression tests of the preforms”, *Compos Part A-Appl S*, vol. 36, no. 9, pp. 1188-1206, 2005.
- [51] U. Mohammed, C. Lekakou, L. Dong and M.G. Bader, “Shear deformation and micromechanics of woven fabrics”, *Compos Part A-Appl S*, vol. 31, no. 4, pp. 299-308, 2000.
- [52] P. Potluri, D.A. Perez Ciurezu and R.B. Ramgulam, “Measurement of meso-scale shear deformations for modelling textile composites”, *Compos Part A-Appl S*, vol. 37, no. 2, pp. 303-314, 2006.
- [53] P. Wang, N. Hamila, P. Pineau and P. Boisse, “Thermomechanical analysis of thermoplastic composite prepregs using bias-extension test”, *J Thermoplast Compos*, vol. 27, no. 5, pp. 1-20, 2012.
- [54] G. Lebrun, M. Bureau and J. Denault, “Evaluation of bias-extension and picture-frame test methods for the measurement of intraply shear properties of PP/glass commingled fabrics”, *Compos Struct*, vol. 61, no. 4, pp. 341-352, 2003.
- [55] P. Harrison, M.J. Clifford and A.C. Long, “Shear characterisation of viscous woven textile composites: a comparison between picture frame and bias extension experiments”, *Compos Sci Technol*, vol. 64, no. 10-11, pp. 1453-1465, 2004.
- [56] D. Lussier and J. Chen, “Material Characterization of Woven Fabrics for Thermoforming of Composites”, *J Thermoplast Compos*, vol. 15, no. 6, pp. 497-509, 2002.
- [57] C.E. Wilks, C.D. Rudd, A.C. Long and C.F. Johnson, “Rate dependency during processing of glass/thermoplastic composites” in *Proceedings of 12<sup>th</sup> International Conference on Composite Materials (ICCM)*, Paris, France, 1999.
- [58] K. Drechsler, R. Hinterhölzl and A. Margossian, “Draping Simulation” in *Lecture for Process Simulation and Material Modelling*, Technical University of Munich, 2015.
- [59] Y. Larberg and M. Akermo, “In-plane deformation of multi-layered unidirectional thermoset prepreg - Modelling and experimental verification”, *Compos Part A-Appl S*, vol. 56, no. 0, pp. 203-212, 2014.
- [60] G.B. McGuinness and C.M. Ó Brádaigh, “Characterisation of thermoplastic composite melts in rhombus-shear: the picture-frame experiment”, *Compos Part A-Appl S*, vol. 29, no. 1-2, pp. 115-132, 1998.
- [61] T.G. Rogers, “Rheological characterization of anisotropic materials”, *Composites*, vol. 20, no.1, pp. 21-27, 1989.

- [62] S.P. Haanappel and R. Akkerman, "Shear characterisation of uni-directional fibre reinforced thermoplastic melts by means of torsion", *Compos Part A-Appl S*, vol. 56, no. 0, pp. 8-26, 2014.
- [63] S.P. Haanappel, R.H.W. ten Thijsse, U. Sachs, B. Rietman and R. Akkerman, "Formability analyses of uni-directional and textile reinforced thermoplastics", *Compos Part A-Appl S*, vol. 56, no. 0, pp. 80-92, 2014.
- [64] R. Akkerman, B. Rietman, S. Haanappel and U. Sachs, "Towards Design for Thermoplastic Composites Manufacturing Using Process Simulation" in *Proceedings of 1<sup>st</sup> International Conference and Exhibition on Thermoplastic Composites (ITHEC)*, Bremen, Germany, 2012.
- [65] K. Potter, "In-plane and out-of-plane deformation properties of unidirectional preimpregnated reinforcement", *Compos Part A-Appl S*, vol. 33, no. 11, pp. 1469-1477, 2002.
- [66] S.P. Haanappel, "Forming of UD fibre reinforced thermoplastics: a critical evaluation of intra-ply shear", doctoral dissertation, University of Twente, 2013.
- [67] R. Scherer and K. Friedrich, "Inter- and intraply-slip flow processes during thermoforming of CF/PP-laminates", *Compos Manuf*, vol. 2, no. 2, pp. 92-96, 1991.
- [68] K. Buet-Gautier and P. Boisse, "Experimental Analysis and Modeling of Biaxial Mechanical Behavior of Woven Composite Reinforcements", *Exp Mech*, vol. 41, no. 1, pp. 260-269, 2001.
- [69] P. Boisse, A. Gasser and G. Hivet, "Analyses of fabric tensile behaviour: determination of the biaxial tension-strain surfaces and their use in forming simulations", *Compos Part A-Appl S*, vol. 32, no. 10, pp. 1395-1414, 2001.
- [70] P. Boisse, M. Borr, K. Buet and A. Cherouat, "Finite element simulations of textile composite forming including the biaxial fabric behaviour", *Compos Part B-Eng*, vol. 28, no. 4, pp. 453-464, 1997.
- [71] S.V. Lomov, A. Willems, I. Verpoest and Y. Zhu, "Picture Frame Test of Woven Composite Reinforcements with a Full-Field Strain Registration", *Text Res J*, vol. 76, no. 3, pp. 243-252, 2006.
- [72] A. Gasser, P. Boisse and S. Hanklar, "Mechanical behaviour of dry fabric reinforcements. 3D simulations versus biaxial tests", *Comp Mater Sci*, vol. 17, no. 1, pp. 7-20, 2000.
- [73] P. Grosberg and G.M. Abbott, "The Fabric Cantilever", *Text Res J*, vol. 36, no. 10, pp. 930-932, 1966.

- [74] T.K. Ghosh, S.K. Batra and R.L. Barker, "The Bending Behaviour of Plain-woven Fabrics Part I: A Critical Review", *J Text I*, vol. 81, no. 3, pp. 245-254, 1990.
- [75] W.R. Yu, M. Zampaloni, F. Pourboghrat, K. Chung and T.J. Kang, "Analysis of flexible bending behavior of woven preform using non-orthogonal constitutive equation", *Compos Part A-Appl S*, vol. 36, no. 6, pp. 839-850, 2005.
- [76] E. de Bilbao, D. Soulat, G. Hivet and A. Gasser, "Experimental Study of Bending Behaviour of Reinforcements", *Exp Mech*, vol. 50, no. 3, pp. 333-351, 2010.
- [77] S.V. Lomov, I. Verpoest, M. Barburski and J. Laperre, "Carbon composites based on multiaxial multiply stitched preforms: Part 2: KES-F characterisation of the deformability of the preforms at low loads", *Compos Part A-Appl S*, vol. 34, no. 4, pp. 359-370, 2003.
- [78] T.A. Martin, D. Bhattacharyya and I.F. Collins, "Bending of fibre-reinforced thermoplastic sheets", *Compos Manuf*, vol. 6, no. 3-4, pp. 177-187, 1995.
- [79] T.A. Martin, S.J. Mander, R.J. Dykes and D. Bhattacharya, "Bending of Continuous Fibre-Reinforced Thermoplastic Sheets" in *Composite Sheet Forming*, D. Bhattacharya, Ed, Amsterdam: Elsevier, 1997, pp. 371-401.
- [80] R.J. Dykes, T.A. Martin and D. Bhattacharyya, "Determination of longitudinal and transverse shear behaviour of continuous fibre-reinforced composites from vee-bending", *Compos Part A-Appl S*, vol. 29, no. 1-2, pp. 39-49, 1998.
- [81] S.G. Advani, T.S. Creasy and S.F. Schuler, "Rheology of Long Fiber-Reinforced Composites in Sheet Forming" in *Composite Sheet Forming*, D. Bhattacharya, Ed, Amsterdam: Elsevier, 1997, pp. 323-369.
- [82] A.M. Murtagh and P.J. Mallon, "Characterisation of Shearing and Frictional Behaviour during Sheet Forming" in *Composite Sheet Forming*, D. Bhattacharya, Ed, Amsterdam: Elsevier, 1997, pp. 163-216.
- [83] B. Liang, N. Hamila, M. Peillon and P. Boisse, "Analysis of thermoplastic prepreg bending stiffness during manufacturing and of its influence on wrinkling simulations", *Compos Part A-Appl S*, vol. 67, no. 0, pp. 111-122, 2014.
- [84] B. Chen and T-W Chou, "Compaction of woven-fabric preforms: nesting and multi-layer deformation", *Compos Sci Technol*, vol. 60, no. 12-13, pp. 2223-2231, 2000.
- [85] A.C Long, P. Boisse and F. Robitaille, "Mechanical analysis of textiles" in *Design and manufacture of textile composites*, A. C. Long, Ed, Cambridge: Woodhead Publishing Ltd, 2005, pp. 62-109.

- [86] S.V. Lomov and I. Verpoest, "Compression of Woven Reinforcements: A Mathematical Model", *J Reinf Plas Comp*, vol. 19, no. 16, pp. 1329-1350, 2000.
- [87] S.V. Lomov, I. Verpoest, T. Peeters, D. Roose and M. Zako, "Nesting in textile laminates: geometrical modelling of the laminate", *Compos Sci Technol*, vol. 63, no. 7, pp. 993-1007, 2003.
- [88] P. Hubert and A. Poursartip, "A method for the direct measurement of the fibre bed compaction curve of composite prepregs", *Compos Part A-Appl S*, vol. 32, no. 2, pp. 179-187, 2001.
- [89] K.L. Sundarkrishnaa, *Friction Material Composites: Materials Perspective*. Berlin Heidelberg: Springer, 2012.
- [90] G. Lebrun, M.N. bureau and J. Denault, "Thermoforming-Stamping of Continuous Glass Fiber/Polypropylene Composites: Interlaminar and Tool-Laminate Shear Properties", *J Thermoplast Compos*, vol. 17, no. 2, pp. 137-165, 2004.
- [91] B. Cornelissen, B. Rietman and R. Akkerman, "Frictional behaviour of high performance fibrous tows: Friction experiments", *Compos Part A-Appl S*, vol. 44, no. 0, pp. 95-104, 2013.
- [92] R.H.W ten Thije, R. Akkerman, M. Ubbink and L. van der Meer, "A lubrication approach to friction in thermoplastic composites forming processes", *Compos Part A-Appl S*, vol. 42, no. 8, pp. 950-960, 2011.
- [93] U. Sachs, R. Akkerman, K. Fetfasidis, E. Vidal-Sallé, J. Schumacher, G. Ziegmann et al., "Characterization of the dynamic friction of woven fabrics: Experimental methods and benchmark results", *Compos Part A-Appl S*, vol. 67, no. 0, pp. 289-298, 2014.
- [94] J.L. Gorczyca, J.A. Sherwood, L. Liu and J. Chen, "Modeling of Friction and Shear in Thermoforming of Composites - Part I", *J Compos Mater*, vol. 38, no. 21, pp. 1931-1947, 2004.
- [95] R. Paton, "Forming technology for thermoset composites" in *Composites forming technologies*, A. C. Long, Ed, Cambridge: Woodhead Publishing Ltd, 2015, pp. 256-276.
- [96] C.M. Ó Brádaigh, R. B. Pipes and P.J. Mallon, "Issues in Diaphragm Forming of Continuous Fiber Reinforced Thermoplastic Composites", *Polym Compos*, vol. 12, no. 4, pp. 246-256, 1991.
- [97] P. Boisse, N. Hamila, E. Vidal-Sallé and F. Dumont, "Simulation of wrinkling during textile composite reinforcement forming. Influence of tensile, in-plane shear and bending stiffnesses", *Compos Sci Technol*, vol. 71, no. 5, pp. 683-692, 2011.



- [98] P. Hallander, M. Akermo, C. Mattei, M. Petersson and T. Nyman, "An experimental study of mechanisms behind wrinkle development during forming of composite laminates", *Compos Part A-Appl S*, vol. 50, no. 0, pp. 54-64, 2013.
- [99] G.R. Christie, I.F. Collins and D. Bhattacharyya, "Out-of-plane buckling of fibre reinforced thermoplastic sheets under homogeneous biaxial conditions", *J Appl Mech*, vol. 62, no. 4, pp. 834-840, 1995.
- [100] M.R. Monaghan, P.J. Mallon, C.M. Ó Brádaigh and R.B. Pipes, "The Effect of Diaphragm Stiffness on the Quality of Diaphragm Formed Thermoplastic Composite Components", *J Thermoplast Compos*, vol. 3, no. 3, pp. 202-215, 1990.
- [101] B.D. Hull, T.G. Rogers and A.J.M. Spencer, "Theory of fibre buckling and wrinkling in shear flows of fibre-reinforced composites", *Compos Manuf*, vol. 2, no. 3-4, pp. 185-191, 1991.
- [102] T.A. Martin, G.R. Christie and D. Bhattacharyya, "Grid Strain Analysis and its Application in Composite Sheet Forming" in *Composite Sheet Forming*, D. Bhattacharya, Ed, Amsterdam: Elsevier, 1997, pp. 163-216.
- [103] G. Dillon, P. Mallon and M. Monaghan, "The Autoclave Processing of Composites" in *Advanced Composites Manufacturing*, T.G. Gutowski, Ed, New York: John Wiley & Sons, 1997, pp. 207-258.
- [104] P.J. Joyce and T.J. Moon, "Compression Strength Reduction in Composites with In-Plane Fiber Waviness" in *Composite Materials: Fatigue and Fracture (7<sup>th</sup> volume)*, R.B. Bucinell, Ed, West Conshohoscken: ASTM, 1998, pp. 76-96.
- [105] F. Van der Weeën, „Algorithms for draping fabrics on doubly-curved surfaces“, *Int J Numer Meth Eng*, vol. 31, no. 7, pp. 1415-1426, 1991.
- [106] R. Akkerman and E.A.D. Lamers, "Constitutive modelling for composite forming", in *Composites forming technologies*, A. C. Long, Ed, Cambridge: Woodhead Publishing Ltd, 2015, pp. 22-45.
- [107] C. Mack and H.M. Taylor, „39-The fitting of Woven Cloth to Surface“, *J Text I*, vol. 47, no. 9, pp. 477-487, 1956.
- [108] A.C. Long, B.J. Souter, F. Robitaille and C.D. Rudd, „Effects of fibre architecture on deformation during preform manufacture“ in *Proceedings of 12<sup>th</sup> International Conference on Composite Materials (ICCM)*, Paris, France, 1999.
- [109] J.W. Klintworth and A.C. Long, "The use of draping simulation in composite design" in *Composite forming technologies*, A.C. Long, Ed, Cambridge: Woodhead Publishing Ltd, 2007, pp. 277-292.
- [110] J.E. Flaherty and A. Eaton, "Finite Element Analysis" in *Lecture in Computer Science (CSCI, MATH 6860)*, Rensselaer Polytechnic Institute, 2000.

- [111] P. Boisse, N. Nouar and A. Charmetant, "Finite element analysis of composite forming at macroscopic and mesoscopic scale", in *Advances in Composites Manufacturing and Process Design*, P. Boisse, Ed, Cambridge: Woodhead Publishing Ltd, 2015, pp. 297-315.
- [112] P. Boisse, B. Zouari and A. Gasser, "A mesoscopic approach for the simulation of woven fibre composite forming", *Compos Sci Technol*, vol. 65, no. 3-4, pp. 429-436, 2005.
- [113] D. Durville, "Simulation of the mechanical behaviour of woven fabrics at the scale of fibers", *Int J Mater Form*, vol. 3, no. 2, pp. 1241-1251, 2010.
- [114] T-C. Lim, S. Ramakrishna, "Modelling of composite sheet forming: a review". *Compos Part A-Appl S*, vol. 33, no. 4, pp. 515-537, 2002.
- [115] A.J.M. Spencer, "Constitutive theory for strongly anisotropic solids", in *Continuum Theory of the Mechanics of Fibre-Reinforced Composites*, A.J.M. Spencer, Ed, Wien: Springer Verlag, 1984, pp. 1-32.
- [116] X. Yu, B. Cartwright, D. McGuckin, L. Ye, Y.W. Mai, "Intraply shear locking in finite element analyses of woven fabric forming processes", *Compos Part A-Appl S*, vol. 37, no. 5, pp. 790-803, 2006.
- [117] N. Hamila and P. Boisse, "Locking in simulation of composite reinforcement deformations. Analysis and treatment", *Compos Part A-Appl S*, vol. 53, no. 0, pp. 109-117, 2013.
- [118] C.M. Ó Brádaigh and R.B. Pipes, „Finite Element Analysis of Composite Sheet-Forming Processes“ in *Proceedings of the 2<sup>nd</sup> International Conference of on Flow Processes in Composite Materials (FPCM)*, Limerick, Ireland, 1991, vol. 2, no. 3-4, pp. 161-170.
- [119] C.M. Ó Brádaigh, G.B. McGuinness and S.P. McEntee, "Implicit Finite Element Modelling of Composite Sheet Forming Processes" in *Composite Sheet Forming*, D. Bhattacharya, Ed, Amsterdam: Elsevier, 1997, pp. 247-322.
- [120] P. Harrison and M. Clifford, "Rheological behaviour of pre-impregnated textile composites" in *Design and manufacture of textile composites*, A. C. Long, Ed, Cambridge: Woodhead Publishing Ltd, 2005, pp. 110-148.
- [121] A.F. Johnson, "Rheological model for the forming of fabric-reinforced thermoplastic sheets", *Compos Manuf*, vol. 6, no. 3-4, pp. 153-160, 1995.
- [122] G.B. McGuinness and C.M. Ó Brádaigh, "Development of rheological models for forming flows and picture-frame shear testing of fabric reinforced thermoplastic sheets", *J Non-Newton Fluid*, vol. 73, no. 1-2, pp. 1-28, 1997.
- [123] A.J.M. Spencer, "Theory of fabric-reinforced viscous fluids", *Compos Part A-Appl S*, vol. 31, no. 12, pp. 1311-1321, 2000.

- [124] P. Harrison, M.J. cliffors, A.C. Long and C.D. Rudd, "A constituent-based predictive approach to modelling the rheology of viscous textile composites", *Compos Part A-Appl S*, vol. 35, no. 7-8, pp. 915-931, 2004.
- [125] A.K. Pickett, T. Queckboerner, P. de Luca and E. Haug, "An explicit finite element solution for the forming prediction of continuous fibre-reinforced thermoplastic sheets", *Compos Manuf*, vol. 6, no. 3-4, pp. 237-243, 1995.
- [126] P. de Luca, P. Lefébure and A.K. Pickett, "Numerical and experimental investigation of some press forming parameters of two fibre reinforced thermoplastics: APC2-AS4 and PEI-CETEX", *Compos Part A-Appl S*, vol. 29, no. 1-2, pp. 101-110, 1998.
- [127] D. Leutz, M. Vermilyea, S. Bel and R. Hinterhölzl, "Forming Simulation of Thick AFP Laminates and Comparison with Live CT Imaging", *Appl Compos Mater*, pp. 1-18, 2016.
- [128] D. Leutz, "Forming simulation of AFP material layups: Material characterization, simulation and validation", doctoral dissertation, Technical University of Munich, 2016.
- [129] ABAQUS (6.11), "ABAQUS Documentation", *Dassault Systèmes Simulia Corp.*, Providence, RI, USA, 2011.
- [130] L. Dong, C. Lekakou and M.G. Bader, "Processing of Composites: Simulations of the Draping of Fabrics with Updated Material Behaviour Law", *J Compos Mater*, vol. 35, no. 2, pp. 138-163, 2001.
- [131] S-W. Hsiao, N. Kikuchi, "Numerical analysis and optimal design of composite thermoforming process", *Comput Meth Appl Mech Eng*, vol. 177, no. 1-2, pp. 1-34, 1999.
- [132] X. Peng and J. Cao, "A dual homogenization and finite element approach for material characterization of textile composites", *Compos Part B-Eng*, vol. 33, no. 1, pp. 45-56, 2002.
- [133] W-R. Yu, F. Pourboghrat, K. Chung, M. Zampaloni and T.J. Kang, "Non-orthogonal constitutive equation for woven fabric reinforced thermoplastic composites", *Compos Part A-Appl S*, vol. 33, no. 8, pp. 1095-1105, 2002.
- [134] P. Xue, X. Peng, J. Cao, "A non-orthogonal constitutive model for characterizing woven composites", *Compos Part A-Appl S*, vol. 34, no. 2, pp. 183-193, 2003.
- [135] P. Harrison, W-R. Yu and A.C. Long, "Rate dependent modelling of the forming behaviour of viscous textile composites", *Compos Part A-Appl S*, vol. 42, no. 11, pp. 1719-1726, 2011.

- [136] J.L. Gorczyca-Cole, J.A. Sherwood and J. Chen, “A friction model for thermo-stamping commingled glass-polypropylene woven fabrics”, *Compos Part A-Appl S*, vol. 38, no. 2, pp. 393-406, 2007.
- [137] Y. Aimène, E. Vidal-Sallé, B. Hagège, P. Sidoroff and P. Boisse, “A hyperelastic approach for composite reinforcement large deformation analysis”, *J Compos Mater*, vol. 44, no. 1, pp. 5-26, 2010.
- [138] P. Badel, S. Gauthier, E. Vidal-Sallé and P. Boisse, “Rate constitutive equations for computational analyses of textile composite reinforcement mechanical behaviour during forming”, *Compos Part A-Appl S*, vol. 40, no. 8, pp. 997-1007, 2009.
- [139] P. Boisse, Y. Aimène, A. Dogui, S. Dridi, S. Gatouillat, N. Hamila et al., “Hypoelastic, hyperelastic, discrete and semi-discrete approaches for textile composite reinforcement forming”, *Int J Mater Form*, vol. 3, no. 2, pp. 1229-1240, 2010.
- [140] A. Charmetant, J.G. Orliac, E. Vidal-Sallé and P. Boisse, “Hyperelastic model for large deformation analyses of 3D interlock”, *Compos Sci Technol*, vol. 72, no. 12, pp. 1352-1360, 2012.
- [141] E. Guzman-Maldonado, N. Hamila, P. Boisse and J. Bikard, “Thermomechanical analysis, modelling and simulation of the forming of pre-impregnated thermoplastics composites”, *Compos Part A-Appl S*, vol. 78, no. 0, pp. 211-222, 2015.
- [142] E. Guzman-Maldonado, N. Hamila, N. Nouar, G. Moulin and P. Boisse, “Simulation of thermoplastic prepreg thermoforming based on a visco-hyperelastic model and a thermal homogenization”, *Mater Design*, vol. 93, no. 0, pp. 431-442, 2016.
- [143] R.H.W. ten Thije, R. Akkerman and J. Huétink, “Large deformation simulation of aniso-tropic material using an updated Lagrangian finite element method”, *Comput Method Appl M*, vol. 196, no. 33-34, pp. 3141-3150, 2007.
- [144] R.H.W. ten Thije and R. Akkerman, “A multi-layer triangular membrane finite element for the forming simulation of laminated composites”, *Compos Part A-Appl S*, vol. 40, no. 6-7, pp. 739-753, 2009.
- [145] J. Sjölander, P. Hallander and M. Akermo, “Forming induced wrinkling of composite laminates: A numerical study on wrinkling mechanisms”, *Compos Part A-Appl S*, vol. 81, no. 0, pp. 41-51, 2016.
- [146] AniForm simulation tool, “Help-manual”, *AniForm Engineering B.V.*, 2016.
- [147] D. Jauffrès, J.A. Sherwood, C.D. Morris and J. Chen, “Discrete mesoscopic modeling for the simulation of woven-fabric reinforcement forming”, *Int J Mater Form*, vol. 3, no.2, pp. 1205-1216, 2010.

- [148] A.K. Pickett, G. Creech and P. de Luca, "Simplified and Advanced Simulations Methods for Prediction of Fabric Draping", *Eur J Comp Mech*, vol. 14, no. 6-7, pp. 677-691, 2005.
- [149] A. Cherouat and J-L. Billoët, "Mechanical and numerical modelling of composite manufacturing processes deep-drawing and laying-up of thin pre-impregnated woven fabrics", *J Mater Process Tech*, vol. 118, no.1-3, pp. 460-471, 2001.
- [150] N. Hamila, P. Boisse, F. Sabourin and M. Burin, "A semi-discrete shell finite element for textile composite reinforcement forming simulation", *Int J Numer Meth Eng*, vol. 79, no.12, pp. 1443-1466, 2009.
- [151] P. Wang, N. Hamila and P. Boisse, "Thermoforming simulation of multilayer composites with continuous fibres and thermoplastic matrix", *Compos Part B-Eng*, vol. 52, no. 0, pp. 127-136, 2013.
- [152] G. Zhou, X. Sun and Y. Wang, "Multi-chain digital element analysis in textile mechanics", *Compos Sci Technol*, vol. 64, no. 2, pp. 239-244, 2004.
- [153] Personal communication with ESI Group, 2016.
- [154] ESI Group, "Visual-Environment", 2016. [Online]. Available: <https://www.esi-group.com/fr/solutions-logicielles/plate-forme-dintegration-virtuelle/simulation-multi-domaines/visual-environment>
- [155] ESI Group, "Solver Notes - Material Type 140", 2009.
- [156] ESI Group, "Solver Reference - Material Type 140", 2012.
- [157] ESI Group, "VPSolution - Solver Reference Manual", 2011.
- [158] ESI Group, "Composite Simulation Solution 2015 - Release Notes & Installation Guide", 2015.
- [159] A. Margossian, "Umformsimulation von thermoplastischen Laminaten (AP2.1, AP4.2)" in *Lehrstuhl für Carbon Composites - TU München, Abschlussbericht des MAIdesign Projekts*, German National Library of Science and Technology, Hannover, 2015.
- [160] P. Hörmann, "Thermoset automated fibre placement - on steering effects and their prediction", doctoral dissertation, Technical University of Munich, 2016.
- [161] D.J. Groves, "A characterization of shear flow in continuous fibre thermoplastic laminates", *Composites*, vol. 20, no. 1, pp. 28-32, 1989.
- [162] D.J. Groves, A.M. Bellamy, and D.M. Stocks, "Anisotropic rheology of continuous fibre thermoplastic composites", *Composites*, vol. 23, no. 2, pp. 75-80, 1992.

- [163] K. Potter, "Bias extension measurements on cross-plyed unidirectional prepreg", *Compos Part A-Appl S*, vol. 33, no. 1, pp. 63-73, 2002.
- [164] Y. R. Larberg, M. Akermo and M. Norrby, "On the in-plane deformability of cross-plyed unidirectional prepreg", *J Compos Mater*, vol. 46, no. 8, pp. 929-939, 2011.
- [165] F.R. Schwarzl and L.C.E. Struik, "Analysis of relaxation measurements", *Adv Mol Relax Process*, vol. 1, no. 3, pp. 201-255, 1968.
- [166] F.R. Schwarzl, "Numerical calculation of stress relaxation modulus from dynamic data for linear viscoelastic materials", *Rheol Acta*, vol. 14, no. 7, pp. 581-590, 1975.
- [167] Anton Paar, "Instruction Manual MCR Series", 2011.
- [168] SGL Group, "Carbon fiber organic sheet with thermoplastic matrix", 2015.
- [169] T.G. Mezger, *Das Rheologie Handbuch (fourth edition)*. Hannover: Vincentz Network, 2012.
- [170] TA Instruments, "Rheology solutions: Determining the linear viscoelastic region in polymers", 2016. [Online]. Available: [http://www.tainstruments.co.jp/application/pdf/Rheology\\_Library/Solutions/RS023.PDF](http://www.tainstruments.co.jp/application/pdf/Rheology_Library/Solutions/RS023.PDF)
- [171] F.T. Peirce, "26-The "Handle" of Cloth as a Measurable Quantity", *J Text I*, vol. 21, no. 9, pp. 377-416, 1930.
- [172] E. de Bilbao, D. Soulat, G. Hivet, J. Launay and A. Gasser, "Bending tests of composite reinforcements", *Int J Mater Form*, vol. 1, no. 1, pp. 835-838, 2008.
- [173] D. Soteropoulos, K.A. Fetfatsidis, J.A. Sherwood and J. Langworthy, "Digital Method of Analyzing the Bending Stiffness of Non-Crimp Fabrics" in *Proceedings of the 14<sup>th</sup> International ESAFORM Conference on Material Forming*, Belfast, UK, 2011.
- [174] C.H. ten Hove, "Bending of CF/PEEK prepregs", Master's thesis, University of Twente, 2012.
- [175] TA Instruments, "DMA Q Series™ Getting Started Guide", Revision H, 2007.
- [176] K.P. Menard, *Dynamic mechanical analysis: a practical introduction*. Boca Raton: CRC Press, 1999.
- [177] W. Palfinger, S. Thumfart and C. Eitzinger, "Photometric stereo on carbon fiber surfaces" in *Proceedings of the 35<sup>th</sup> Workshop of the Austrian Association for Pattern Recognition*, Graz, Austria, 2011.
- [178] S. Deng, M. Hou and L. Ye, "Temperature-dependent elastic moduli of epoxies measured by DMA and their correlations to mechanical testing data", *Polym Test*, vol. 26, no. 6, pp. 803-813, 2007.

- [179] S.J. Hwang, R.F. Gibson and J. Singh, "Decomposition of coupling effects on damping of laminated composites under flexural vibration", *Compos Sci Technol*, vol. 43, no. 2, pp. 159-169, 1992.
- [180] J.D.D. Melo and D.W. Radford, "Time and temperature dependence of the viscoelastic properties of CFRP by dynamic mechanical analysis", *Compos Struct*, vol. 70, no. 2, pp. 240-253, 2005.
- [181] Norm DIN EN ISO 14125, "Fibre-reinforced plastic composites - Determination of flexural properties", 1998.
- [182] D.F. Adams and D.R. Doner, "Transverse Normal Loading of a Unidirectional Composite", *J Compos Mater*, vol. 1, no. 2, pp. 152-164, 1967.
- [183] E.S. Folias, "On the prediction of Failure at a Fiber/Matrix in a Composite Subjected to a Transverse Tensile Load", *J Compos Mater*, vol. 25, no. 7, pp. 869-886, 1991.
- [184] J. Koyanagi, S. Yoneyama, A. Nemoto and J.D.D. Melo, "Time and temperature dependence of carbon/epoxy interface strength", *Compos Sci Technol*, vol. 70, no. 9, pp. 1395-1400, 2010.
- [185] L. Yang, Y. Yan, Y. Liu and Z. Ran, "Microscopic failure mechanisms of fiber-reinforced polymer composites under transverse tension and compression", *Compos Sci Technol*, vol. 72, no. 15, pp. 1818-1825, 2012.
- [186] Z. Tang, C. Wang and Y. Yu, "Failure response of fiber-epoxy unidirectional laminate under transverse tensile/compressive loading using finite-volume micromechanics", *Compos Part B-Eng*, vol. 79, pp. 331-341, 2015.
- [187] C.C. Chamis and J.H. Sinclair, "Ten-deg off-axis test for shear properties in fiber composites", *Exp Mech*, vol. 17, no. 9, pp. 339-346, 1977.
- [188] Norm ASTM D 3039/D 3039M, "Standard Test Method for Tensile Properties of Polymer Matrix Composite Materials", 2000.
- [189] Norm DIN EN ISO 527-5, "Plastics - Determination of tensile properties - Part 5: Test conditions for unidirectional fibre-reinforced plastic composites", 1997.
- [190] T.A. Oswald and N. Rudolph, *Polymer Rheology: Fundamentals and Applications*. Munich: Hanser Publishers, 2015.
- [191] L. Bottenbruch and R. Binsack, *Polyamide: Kunststoff Handbuch 3/4. Technische Thermoplaste*. München: Carl Hanser Verlag, 1998.
- [192] Airtech Europe SARL, "Thermalimide E - Ultra high temperature bagging film", 2015. Online. [Available]: [http://catalogue.airtech.lu/product.php?product\\_id=663&lang=EN](http://catalogue.airtech.lu/product.php?product_id=663&lang=EN).
- [193] S.M. Lee, *Reference book for composites technology*. Boca Raton: CRC Press, 1989. Online. [Available]: <http://books.google.de/books?id=SSIDWXXa0xQC>.

- [194] P. Harrison, R.T. Thije, R. Akkerman and A. Long, “Characterising and modelling tool-ply friction of viscous textile composites”, *World J Eng*, vol. 7, no. 1, pp. 5-22, 2010.
- [195] Norm DIN EN 14882, “Determination of the static and dynamic coefficient of friction”, 2005.
- [196] Norm ASTM D 1894-01, “Standard Test Method for Static and Kinetic Coefficients of Friction of Plastic Film and Sheeting”, 2001.
- [197] Destaco, “Horizontal Hold Down Clamps (215 USS)”, 2016. [Online]. Available: <http://www.destaco.com/assets/docs/en/ds/215.pdf>
- [198] Sturm Präzision, “Ceramic Bearing”, 2016. [Online]. Available: <https://www.sturm-kugellager-shop.de/keramik-lager/ker-zro2/757/keramik-rillenkugellager-6000-ker-zro2>
- [199] Airtech Europe SARL, “Release All 45 - Semi-permanent release agent”, 2015. Online. [Available]: [http://catalogue.airtech.lu/category.php?category\\_id=5&](http://catalogue.airtech.lu/category.php?category_id=5&)
- [200] K. Vanclooster, S.V. Lomov and I. Verpoest, “Investigation of interply shear in composite forming” in *Proceedings of the 17<sup>th</sup> International ESAFORM Conference on Material Forming*, Lyon, France, 2008.
- [201] B. Kazatchkov and S. G. Hatzikiriakos, “Relaxation effects of slip in shear flow of linear molten polymers”, *Rheologica Acta*, vol. 49, no. 3, pp. 267-274, 2010.
- [202] G. Kelly, “Joining of Carbon Fibre Reinforced Plastics for Automotive Applications”, doctoral dissertation, Royal Institute of Technology, 2004.
- [203] U.J. Santner, “FE Simulation of Composite Textile Tests for Setting up Material Cards”, Diploma’s thesis, Technical University of Munich, 2013.
- [204] A. Schug, “Validation Method for Evaluating Forming Simulations of Composite Textiles”, Diploma’s thesis, Technical University of Munich, 2013.
- [205] S. Thumfart, W. Palfinger, M. Stöger and C. Eitzinger, “Accurate Fibre Orientation Measurement for Carbon Fibre Surfaces” in *Proceedings of the 15<sup>th</sup> International Conference on Computer Analysis of Images and Patterns (CAIP)*, York, UK, 2013.
- [206] S. Bagherpour, “Fibre Reinforced Polyester Composites” in *Polyester*, H.E-D.M. Saleh, Ed, Online: InTech, 2012. Available: <http://www.intechopen.com/books/polyester/fibre-reinforced-polyester-composites>
- [207] WolframAlpha, “Computational knowledge engine”, 18/04/2016. [Online]. Available: <https://www.wolframalpha.com/>.



- 
- [208] Professional Plastics, “Mechanical Properties of Plastic Materials”, 19/03/2016. [Online]. Available: <http://www.professionalplastics.com/professionalplastics/MechanicalPropertiesofPlastics.pdf>
- [209] S.A. Hussain, B. Sidda Reddy and V. Nageswara Reddy, “Prediction of Elastic Properties of FRP Composite Lamina for Longitudinal Loading”, *J Eng Appl Sci*, vol. 3, no. 6, pp. 70-75, 2008.



# A Appendix

## a Appendix to Chapter 1.1



**Fig. A-1:** Thermoforming unit belonging to the *Chair of Carbon Composites of the Technical University of Munich (TUM-LCC)* [S3]

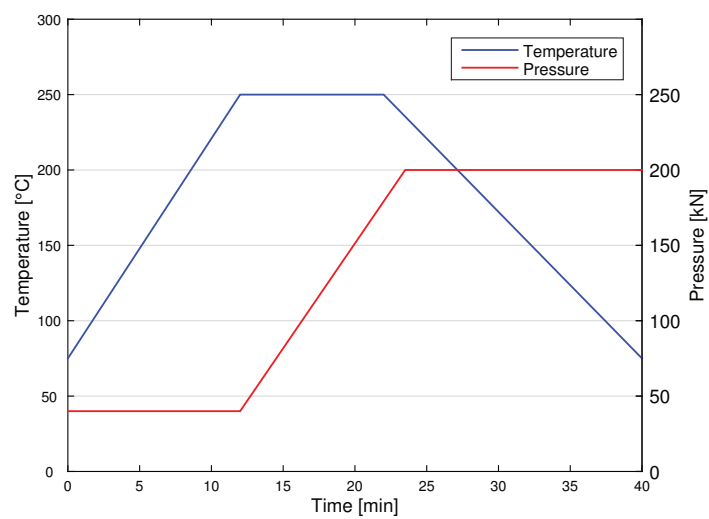


**Fig. A-2:** Typical cycle applied to the consolidation of tailored thermoplastic composite blanks

## b Appendix to Chapter 4.1.1.3

The approach presented in this appendix has been developed in collaboration with Hörmann and published in [K7, K8, 160].

### Basics about dynamic (oscillatory) tests

Most of the content of this section, including text and figures, is based on [K8] and [190].

In oscillatory experiments, the material is subjected to a sinusoidal shear deformation of angular frequency  $\omega$  and amplitude  $\gamma_0$ :

$$\gamma(t) = \gamma_0 \sin(\omega t) \quad (\text{A-1})$$

where  $\gamma_0$  must be kept reasonably small to ensure to stay within material LVE region. Correspondingly, the stress response has a sinusoidal form:

$$\tau(t) = \tau_0 \sin(\omega t + \delta) \quad (\text{A-2})$$

where  $\tau_0$  is the stress amplitude and  $\delta$  the phase lag. The phase lag characterises material viscoelasticity. As illustrated in Fig. A-3, the stress response has the particularity not be in-phase with the entry signal.

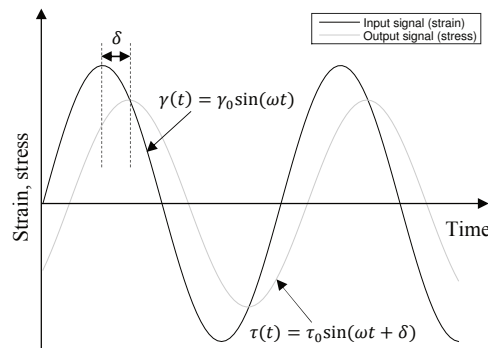


Fig. A-3: Typical sinusoidal strain and stress signals during dynamic experiments

Given that strain and stress signals are sinusoidal, the resulting shear modulus is complex and denoted  $G^*$ :

$$G^* = \frac{\tau(t)}{\gamma(t)} = G' + i \cdot G'' \quad (\text{A-3})$$

As a complex number,  $G^*$  consists of a real part  $G'$  called storage and an imaginary part  $G''$  called loss modulus. While the former represents elastic contributions, i.e. amount of energy stored during the deformation, the latter represents viscous aspects, i.e. amount of energy dissipated during the deformation [190]. The expressions of storage and loss moduli are given in equation (A-4):

$$G' = \frac{\tau_0}{\gamma_0} \cos(\delta) \quad G'' = \frac{\tau_0}{\gamma_0} \sin(\delta) \quad \tan(\delta) = \frac{G''}{G'} \quad (\text{A-4})$$

### New test method using a rheometer in a parallel platens configuration

Most of the content of this section, including text and figures, is based on [K8].

The innovative test method presented in this section considers (i) the method of Rogers for the determination of storage and loss shear moduli from dynamic (oscillatory) experiments conducted with a rotational rheometer [61] and (ii) Haanappel and Akkerman post-processing method to convert results from frequency into time domain [62, 66]. Further details are given in Appendix b.

#### Rogers' method

The presented test method considers a rotational rheometer and a parallel platens test setup. Experiments are carried out with centred single ply specimens of rectangular cross-section (see Fig. A-4). Unlike Groves, these do not cover the whole platens (see Chapter 4.1.1.1). To ensure good adhesion, some normal force  $F_N$  is applied. During testing, the gap thickness  $d$  remains constant. The contact between the specimen and the platens is assumed to be perfect (no slippage). The specimen is twisted when the upper platen starts oscillating at a frequency  $f$ . These experiments are conducted at a prescribed angle of twist signal  $\theta(t)$ . The torque signal  $M(t)$  is measured as response. Expressions of the twist and torque signals can be written as follows:

$$\theta(t) = \theta_0 \sin(\omega t) \quad (\text{A-5})$$

$$M(t) = M_0 \sin(\omega t + \delta) \quad (\text{A-6})$$

where  $\theta_0$  is the amplitude of the angle of twist,  $M_0$  is the amplitude of the torque,  $\omega$  is the angular frequency,  $\delta$  is the phase lag and  $t$  is the time.

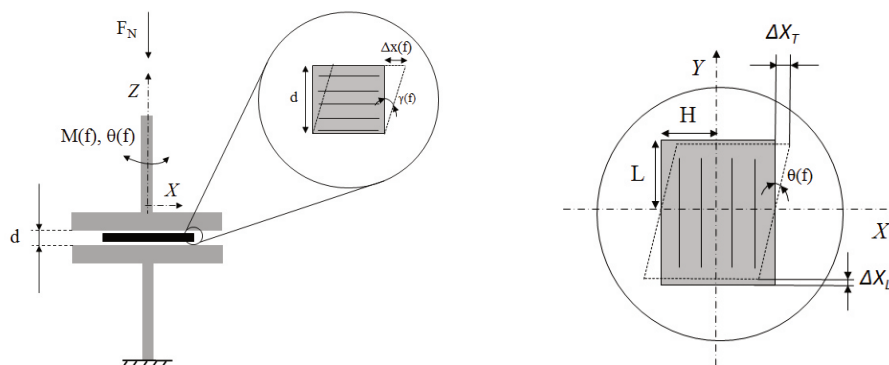


Fig. A-4: Front view (left) and top view (right) of a rectangular unidirectional composite specimen subjected to shear in a parallel platens test setup mounted on a rotational rheometer

In 1989, Rogers correlated longitudinal and transverse shear behaviour of molten uni-directional CFRTM materials with the output of oscillatory experiments conducted with a parallel platens test setup [61]. Rogers particularly derived that, when a viscoelastic material is twisted, the amplitude of the torque  $M_0$  and the phase lag  $\delta$  can be related to the transverse  $G'_T$  and longitudinal  $G'_L$  storage shear moduli and transverse  $G''_T$  and longitudinal  $G''_L$  loss shear moduli, the amplitude of the angle of twist  $\theta_0$  and the gap thickness  $d$  through the relations presented in equations (A-7) and (A-8). The geometry of the specimens is accounted via the second moments of inertia  $I_1$  and  $I_2$ .

$$M_0 \cos \delta = (I_y G'_L + I_x G'_T) \frac{\theta_0}{d} \quad (\text{A-7})$$

$$M_0 \sin \delta = (I_y G''_L + I_x G''_T) \frac{\theta_0}{d} \quad (\text{A-8})$$

If specimens of rectangular cross-section measuring  $2L \times 2H$ , where  $2L$  is the dimension along fibre direction and  $2H$  is the dimension transverse to fibre direction, are considered (see Fig. A-4 right), equations (A-7) and (A-8) can be rewritten as:

$$\frac{3M_0 d \cos \delta}{4\theta_0 L H^3} = G'_L + G'_T \left(\frac{L}{H}\right)^2 \quad (\text{A-9})$$

$$\frac{3M_0 d \sin \delta}{4\theta_0 L H^3} = G''_L + G''_T \left(\frac{L}{H}\right)^2 \quad (\text{A-10})$$

As shown in equations (A-9) and (A-10), if tests are conducted with specimens of different aspect ratios  $(L/H)$  and subsequently plotted against  $(L/H)^2$ , results should be aligned with a first order polynomial regression of the form  $a\left(\frac{L}{H}\right)^2 + b$ , in which the slope  $a$  represents the loss (or storage) transverse shear modulus and the intercept with the y-axis  $b$  the loss (or storage) longitudinal shear modulus (see Fig. A-5). [61]

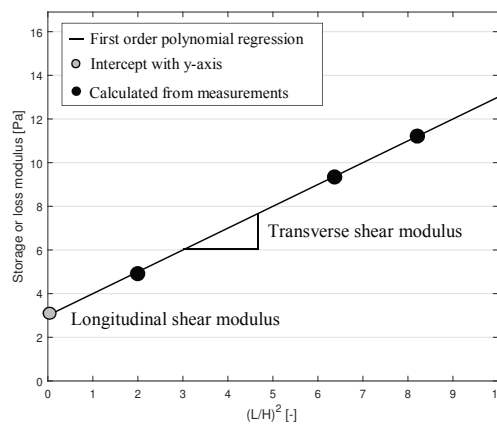


**Fig. A-5:** Typical determination of storage/loss transverse and longitudinal shear moduli using the method introduced by Rogers

In a parallel platens test setup, specimens are subjected to transverse  $\Delta X_T$  and longitudinal  $\Delta X_L$  displacements (see Fig. A-4 right). Because the amplitudes of the angle of twist  $\theta_0$  remain small, maximum displacements at their tips are expressed as follows:

$$\Delta X_T = L \cdot \tan(\theta_0) \approx L \cdot \theta_0 \quad (\text{A-11})$$

$$\Delta X_L = H \cdot \tan(\theta_0) \approx H \cdot \theta_0 \quad (\text{A-12})$$

Based on Fig. A-4 left, maximum transverse  $\gamma_T$  and longitudinal  $\gamma_L$  shear strains at the tip of the specimens can be also approximated as follows:

$$\gamma_{T,max} \approx \frac{L \cdot \theta_0}{d} \quad (\text{A-13})$$

$$\gamma_{L,max} \approx \frac{H \cdot \theta_0}{d} \quad (\text{A-14})$$

Shear rates in parallel platens experiments varies from zero at the centre of the specimen to a maximum value at the tip of the specimen. Maximum transverse and longitudinal shear rates at the tip of the specimens can be calculated as follows:

$$\dot{\gamma}_{T,max} = \omega \cdot \gamma_{T,max} = 2 \cdot \pi \cdot f \gamma_{T,max} \quad (\text{A-15})$$

$$\dot{\gamma}_{L,max} = \omega \cdot \gamma_{L,max} = 2 \cdot \pi \cdot f \gamma_{L,max} \quad (\text{A-16})$$

#### *Analysis of experimental test results*

The presented test method has been developed for experiments performed within material LVE region. In the scope of this work, only longitudinal shear is investigated.

Based on the LVE theory, transient shear stresses  $\tau$  can be calculated according to Boltzmann integral [190]:

$$\tau(t) = \int_{s=-\infty}^t G_r(t-s) \dot{\gamma}(s) ds \quad (\text{A-17})$$

where  $G_r$  is the shear relaxation modulus and  $\dot{\gamma}$  is the shear rate.

As recently detailed by Haanappel and Akkerman [62, 66], the longitudinal shear relaxation modulus can be approximated using Schwarzl and Struik [165] and Schwarzl [166] finite difference scheme:

$$G_r(t) = G'_L(\omega) - 0.528 G''_L \left( \frac{\omega}{2} \right) + 0.112 G''_L(\omega) + 0.0383 G''_L(2\omega) \quad (\text{A-18})$$

where  $t = 1/\omega$ .

Haanappel and Akkerman [62, 66] reported that if experiments are performed at constant shear rates  $\dot{\gamma}$  and the shear relaxation modulus  $G_r$  is approximated with a second order power law function of the form  $at^{-b} + G_\infty$ , where  $a$ ,  $b$  and  $G_\infty$  are constant coefficients determined by curve fitting, transient shear stresses  $\tau$  can be written as follows:

$$\tau(t) = \dot{\gamma} \left( G_\infty t - \frac{a}{b-1} t^{1-b} \right) \quad (\text{A-19})$$

where the constant shear rate  $\dot{\gamma}$  is related to the shear strain  $\gamma$  and the frequency  $f$ :

$$\dot{\gamma}(t) = \gamma(t) \cdot \omega = \gamma(t) \cdot 2 \cdot \pi \cdot f \quad (\text{A-20})$$

In a parallel platens test setup in which small angles of twist are applied, the longitudinal shear strain  $\gamma_L$  can be calculated as follows:

$$\gamma_L(t) = \frac{H \cdot \theta_0(t)}{d} \quad (\text{A-21})$$

In order to maintain constant shear rates, experiments must be conducted for convenient variations of the angle of twist  $\theta_0$ .



## c Appendix to Chapter 4.1.4.2

### Determination of transverse viscosity from transverse tensile tests

The content of this section is based on [P3].

For transverse tensile tests, the Newtonian fluid model correlates transverse tensile stresses  $\sigma_t$  to the transverse viscosity  $\eta_t$  and the transverse tensile strain rate  $\dot{\epsilon}_t$  as follows:

$$\sigma_t = 2\eta_t\dot{\epsilon}_t \quad (\text{A-22})$$

Transverse strain rates  $\dot{\epsilon}_t$  in fluid systems subjected to large elongational deformations read [81]:

$$\dot{\epsilon}_t = \frac{V}{L} = \frac{V}{L_0 + D} \quad (\text{A-23})$$

where  $V$  is the current test speed,  $L$  is the current specimen length,  $L_0$  is the initial specimen free length and  $D$  is the displacement. The transverse viscosity  $\eta_t$  can be derived from transverse tensile tests by combining the equations (A-22) and (A-23):

$$\eta_t = \frac{\sigma_t(L_0 + D)}{2\dot{D}} \quad (\text{A-24})$$

Equation (A-24) is given as equation (4-8) in Chapter 4.1.4.2.

### Determination of PAM-FORM viscosity

As described in PAM-FORM solver notes [155], composite viscosity  $\eta_{PAM}$  is determined with respect to strain rates  $\dot{\epsilon}_{ij}$  and deviatoric stresses  $S_{ij}$ :

$$S_{ij} = 2\eta_{PAM}\dot{\epsilon}_{ij} \quad (\text{A-25})$$

The general expression of deviatoric stresses reads:

$$\sigma_{ij} = S_{ij} + \sigma_m I_{ij} \quad (\text{A-26})$$

where  $\sigma_{ij}$  is the Cauchy stress in ij-plane,  $S_{ij}$  is the deviatoric stress in ij-plane and  $\sigma_m$  is the hydrostatic stress and  $I_{ij}$  is the identity matrix.

By rewriting equation (A-26) for shell elements ( $\sigma_{33} = 0$ ):

$$\begin{aligned} \sigma_{11} &= 2S_{11} + S_{22} \\ \sigma_{22} &= S_{11} + 2S_{22} \\ \sigma_{12} &= S_{12} \end{aligned} \quad (\text{A-27})$$

By combining equations (A-25) and (A-27), a relation between PAM-FORM composite viscosity  $\eta_{PAM}$ , Cauchy stresses  $\sigma$  and strain rates  $\dot{\epsilon}$  can be derived:

$$\begin{aligned}\sigma_{11} &= 2\eta_{PAM}(2\dot{\epsilon}_{11} + \dot{\epsilon}_{22}) \\ \sigma_{22} &= 2\eta_{PAM}(\dot{\epsilon}_{11} + 2\dot{\epsilon}_{22}) \\ \sigma_{12} &= 2\eta_{PAM}\dot{\epsilon}_{12}\end{aligned}\quad (A-28)$$

Let consider a transverse tensile test similar to this presented in Fig. A-6.

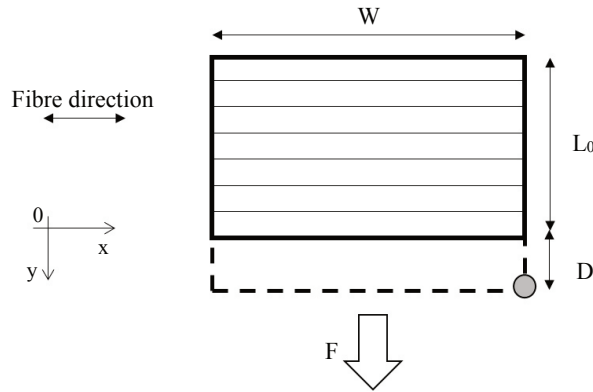


**Fig. A-6:** Schematic of a transverse tensile test

W: Width;  $L_0$ : Initial free length;  $h_0$ : Initial thickness; D: Displacement; F: Force.

By applying the principle of virtual power, the following expression can be derived:

$$F\dot{D} = V_{ol}\sigma_{ij}\dot{\epsilon}_{ij} \quad (A-29)$$

where  $F$  is the force,  $V_{ol}$  is the volume of the specimen,  $\sigma_{ij}$  is the Cauchy stress in  $ij$ -plane and  $\dot{\epsilon}_{ij}$  is the strain rate in  $ij$ -plane.

The assumption of incompressibility reads:

$$V_{ol} = (L_0 + D) \cdot W \cdot h_0 = constant \quad (A-30)$$

In transverse tensile tests, it can be assumed that all deformations occur perpendicular to fibre direction and thus, are dominated by matrix and fibre/matrix interface behaviour. According to equations (A-28) and (A-30), equation (A-29) reads:

$$F\dot{D} = 4V_{ol}\eta_{PAM}\dot{\epsilon}_t^2 \leftrightarrow \eta_{PAM} = \frac{\sigma_t(L_0 + D)}{4\dot{D}} \quad (A-31)$$

Using equations (A-24) and (A-31):

$$\eta_{PAM} = \frac{\eta_t}{2} \quad (A-32)$$

## d Appendix to Chapter 4.3.2

The cut-outs performed on the bottom sides of the base-platen and the specimen-platen aim to lighten the weight of the friction test setup. These are presented in Fig. A-7 left and Fig. A-7 right, respectively.

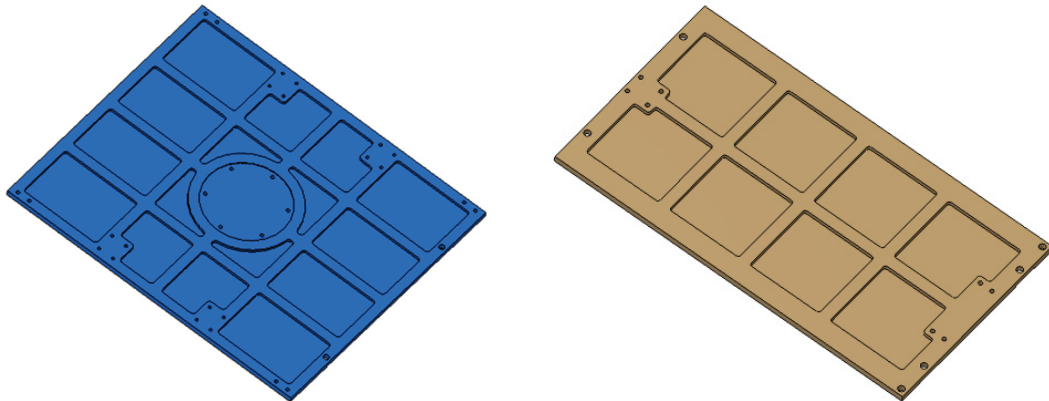


**Fig. A-7:** Cut-outs on the bottom side of the base-platen (left) and the specimen-platen (right) [S6]

As presented in Fig. A-8, positioning rods are used to ensure that the carrier is placed in a reproducible manner on the specimen-platen.

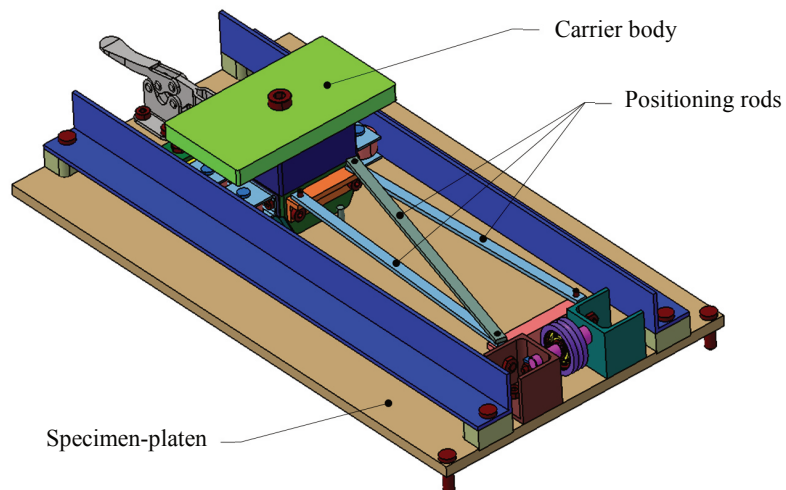


**Fig. A-8:** Carrier body positioned on top of the specimen-platen using positioning rods [S6]

## e Appendix to Chapter 4.3.3.2

This appendix details (i) the preparation of carrier specimens and (ii) the modifications performed on the carrier to prevent the specimens to rip off.

### Preparation of carrier specimens

A heat gun, such as this presented in Fig. A-9 left (HL 2010 E supplied by Steinel), is required to heat thermoplastic composite blanks above melting temperature. The tooling designed for specimen preparation (see Fig. 4-33) is protected with polyimide tape to ease specimen demoulding (see orange tape in Fig. A-9 right).



**Fig. A-9:** Heat gun used to heat thermoplastic specimens above melting temperature (left) and specimen preparation tooling protected with kapton tape (right) [S8]

Before being heated (see Fig. A-10 right), flat specimens ( $70 \times 77 \text{ mm}^2$ ) are properly positioned and clamped (see Fig. A-10 left).

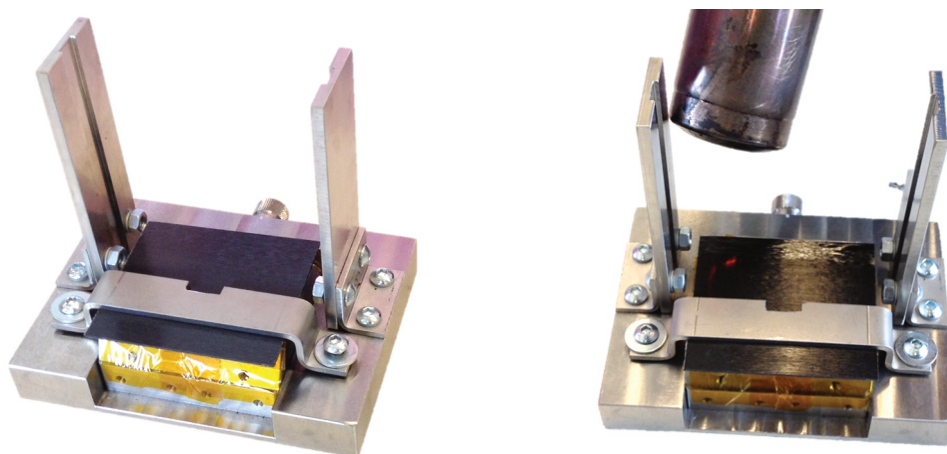


**Fig. A-10:** (Left) Thermoplastic specimen clamped at room temperature; (Right) Heat applied with a heat gun [S8]

The molten side of the specimen is formed into carrier geometry using a hood, i.e. mould having female carrier geometry (see Fig. A-11 left). Pressure is applied manually during ten seconds (see Fig. A-11 right).

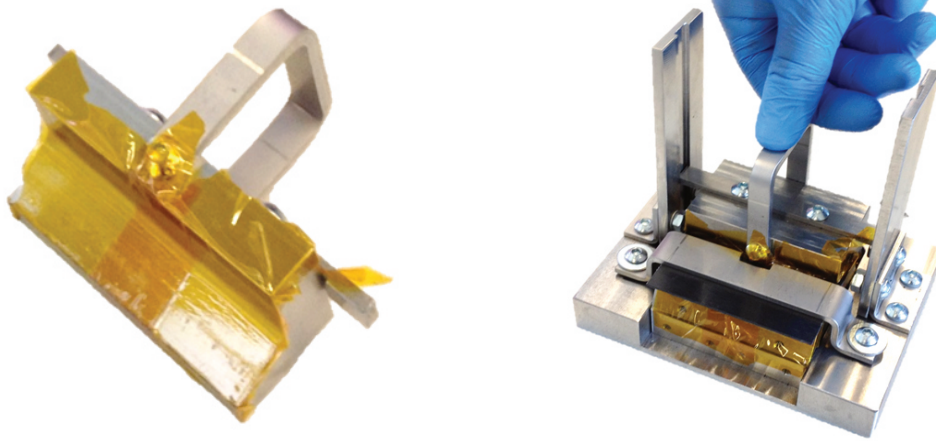


**Fig. A-11: (Left) Hood used to form a molten thermoplastic specimen; (Right) Forming of a molten thermoplastic specimen into carrier geometry [S8]**

Given that only one side can be formed at a time, the same procedure is repeated a second time to form the other side. A formed specimen is presented in Fig. A-12.

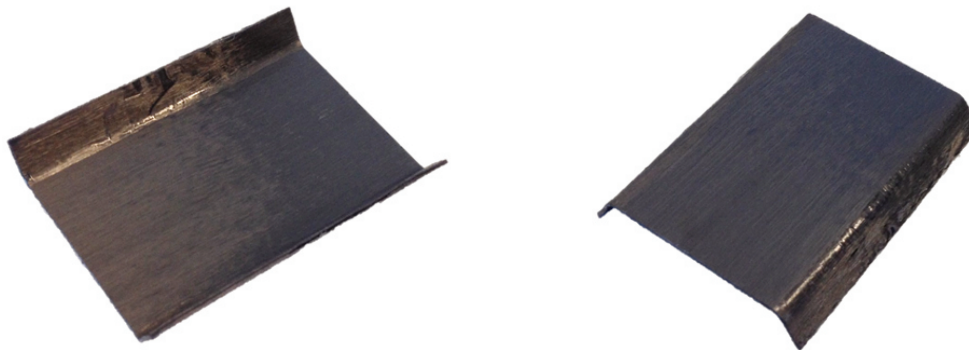


**Fig. A-12: Top (left) and bottom (right) views of a carrier specimen [S8]**

## Modifications of carrier design

To prevent the specimen to rip off, the design of the carrier is modified as follows:

- Supplementary screws are added on the specimen attachment plates to improve clamping capabilities (see Fig. A-13). These do not go through the specimen but increase the pressure applied on it,
- A metallic plate is added behind the carrier to prevent specimen slippage (see Fig. A-14).

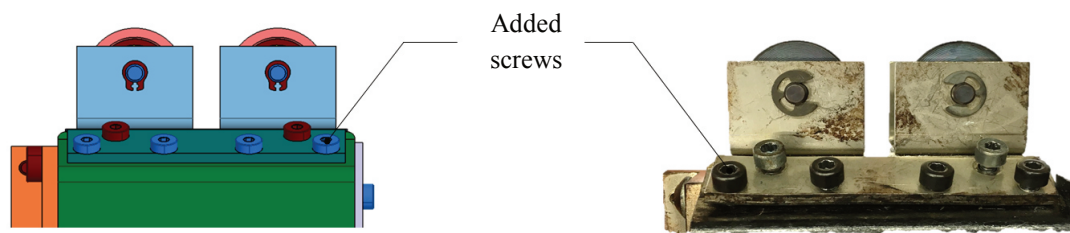


**Fig. A-13: Addition of screws on specimen attachment plates**  
Left: CAD model; Right: Carrier after modification.

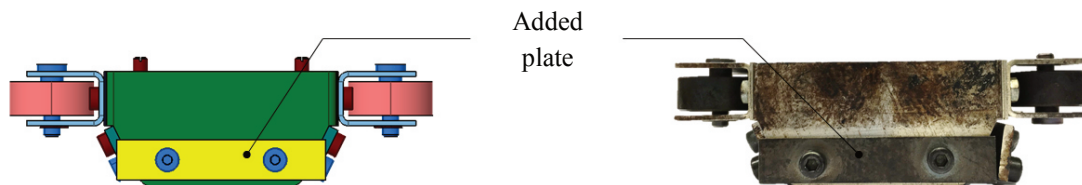


**Fig. A-14: Addition of a metallic plate behind the carrier**  
Left: CAD model; Right: Carrier after modification.

## f Appendix to Chapter 4.4.1

The preparation of prismatic specimens (see Fig. A-15) made out of thermoset composite tapes is relatively complex due to the soft and tacky aspects of the material at room temperature. To prevent the occurrence of important inter-laminar shear deformations, specimens are therefore cut in their frozen state.

However, because the material softens at the location of the cut, some inter-laminar shear deformations still arise (see Fig. A-16). These are nonetheless considered not to influence characterisation test results since they are localised at the tips of the specimens, which are clamped during testing.



**Fig. A-15:** Prismatic bar specimen made out of non-cured unidirectional thermoset tapes



**Fig. A-16:** Typical (left) and extreme (right) localised inter-ply shear deformations at the tips of the specimen

## g Appendix to Chapter 4.4.2

The outer layers of some specimens are examined using an optical measuring system (ProFactor sensor [177]) to control whether they have a homogeneous unidirectional fibre orientation aligned to the specimen side length (see Fig. A-17). Although measurements are not performed for all specimens, results are assumed to be representative.

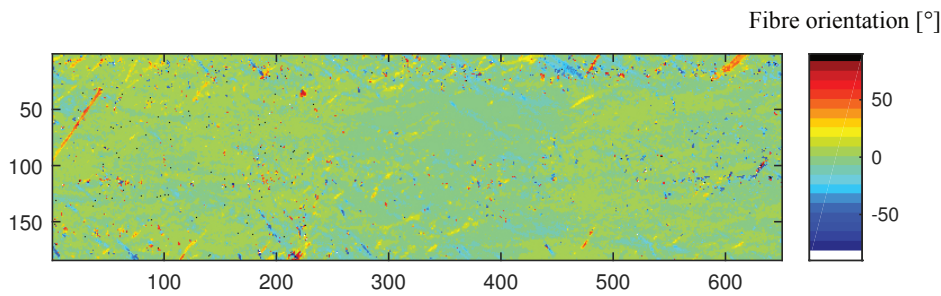


**Fig. A-17:** Typical external fibre orientation of a non-cured unidirectional thermoset specimen (scale [-90°, +90°])

An average fibre orientation of  $0.11^\circ$  ( $\pm 13.59^\circ$ ) with respect to the specimen side length is to be reported. Reorientations are mainly caused by the soft and tacky aspects of the material during specimen preparation (room temperature). Deviations can be especially noticed within the central region of the specimens, i.e. where the specimens are held (see Fig. A-18).

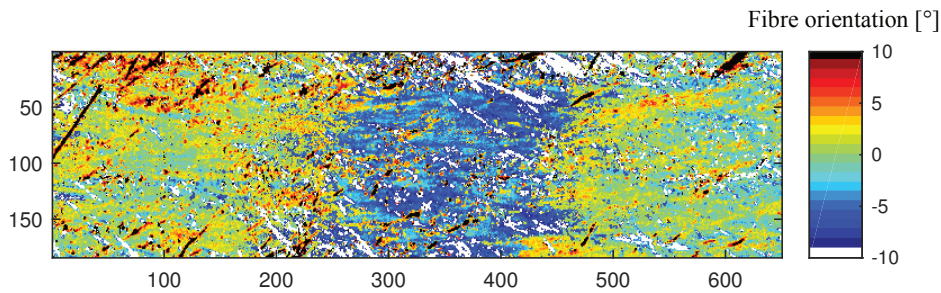


**Fig. A-18:** Typical external fibre orientation of a non-cured unidirectional thermoset specimen (scale [-10°, +10°])



## h Appendix to Chapter 4.4.3

The outer layers of some specimens are examined using an optical measuring system (ProFactor sensor [177]) to control whether they have a homogeneous unidirectional fibre orientation perpendicular to the specimen side length (see Fig. A-19). Although measurements are not performed for all specimens, results are assumed to be representative.

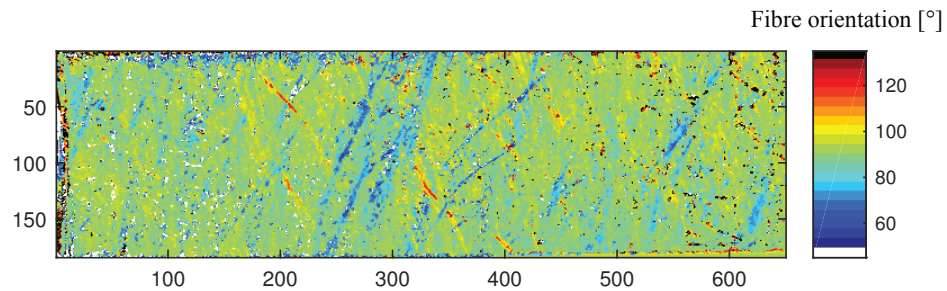


**Fig. A-19:** Typical external fibre orientation of a non-cured unidirectional thermoset specimen (scale [-45°, +135°])

An average fibre orientation of  $89.61^\circ (\pm 14.39^\circ)$  with respect to the specimen side length is to be reported. Reorientations are mainly caused by the soft and tacky aspects of the material during specimen preparation (room temperature).

## i Appendix to Chapter 5.1.4

This appendix (i) presents the analyses performed to select a convenient velocity scale factor and (ii) details how an initial intra-ply shear modulus of about 8 GPa is calculated.

### Velocity scale factor

To determine a suitable velocity scale factor, a preliminary study is conducted with the model developed for transverse tensile test simulations (see Chapter 5.1.2). To be considered as a kinematic boundary condition, the original loading rate (0.025 N/min) is approximated by a bilinear velocity curve (see example presented in Fig. 5-2).

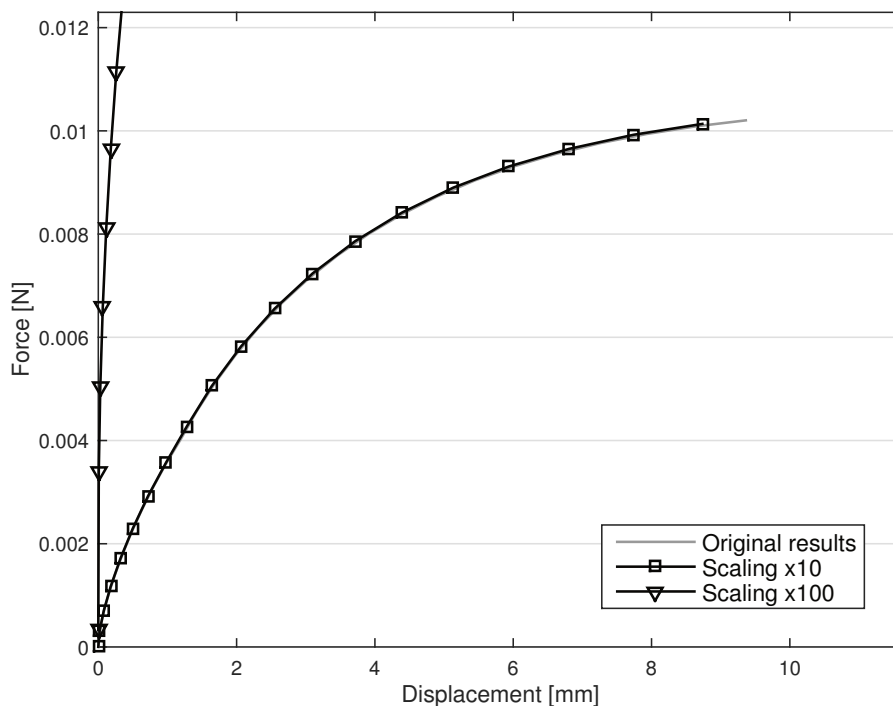


**Fig. A-20: Analyses performed to identify proper velocity scale factor**  
Investigations conducted for a transverse tensile test at 0.025 N/min.

Investigations performed with factors of 10 and 100 clearly highlight that only a velocity scale factor of 10 can be applied (see Fig. A-20). Compared to the original simulation, computations are about ten times faster.

### Initial intra-ply shear modulus calculation

The initial intra-ply shear modulus of about 8 GPa is calculated according to material characterisation test results, on the one hand, and the consideration of specific shear rate and shear strain values, on the other hand.

The first step consists in approximating the shear rate experienced by the material during a picture frame test conducted at a crosshead speed of 50 mm/min. This is achieved by deriving equation (A-33), which enables the determination of material shear angles  $\gamma$  during picture frame experiments [47]. The result is given in equation (A-34), where  $\dot{\gamma}$  is the shear strain rate,  $L_{frame}$  is the length of the frame (200 mm),  $\dot{d}$  is the crosshead speed (50 mm/min),  $t$  is the time and  $d$  is the crosshead displacement. The derivative is calculated assuming that  $L_{frame}$  and  $t$  are positive values [207].

$$\gamma(t) = \frac{\pi}{2} - 2 \cdot \arccos\left(\frac{1}{\sqrt{2}} - \frac{d(t)}{2L_{frame}}\right) \quad (A-33)$$

$$\dot{\gamma}(t) = \frac{\dot{d}(t)}{L_{frame} \sqrt{2L_{frame}^2 - d(t)(2\sqrt{2}L_{frame} + d(t))}} \quad (A-34)$$

Because shear rates are non-constant during picture frame tests performed at constant crosshead speeds, an average value over a displacement of 90 mm is calculated. An average shear rate of about 0.008 1/s is considered.

In a second step, the angle at which out-of-plane wrinkles occurs in a picture frame test, i.e. about  $10^\circ$  (see Chapter 4.1.1.2), is converted to a shear strain value for torsion bar tests. According to equation (A-35), the shear strain  $\gamma$  during a torsion bar test is related to the angle of twist  $\theta$ , the free length of the bar  $L$  (about 47 mm) and the thickness of the specimen  $T$  (about 11 mm) [62, 66].

$$\gamma(t) = \frac{\theta \cdot T}{L} \quad (A-35)$$

After calculation, the shear strain value is equal to about 0.04.

By using shear strain rate and shear strain data in combination with material characterisation results (equation (A-19) with the parameters identified from Fig. 4-9) and assuming linear behaviour, an intra-ply shear modulus of about 8 GPa is calculated.

## j Appendix to Chapter 5.1.5

Sensitivity analysis is conducted to investigate the stability, the convergence and the accuracy of the material model. For these purposes, the simulation time step is varied via  $E_l$ ,  $\rho$  and the mesh size (see equation (5-2)).

Sensitivity analysis results performed with transverse tensile tests are presented in Fig. A-21 and Fig. A-22 for variations of the longitudinal tensile modulus  $E_l$  and the mesh size, respectively.

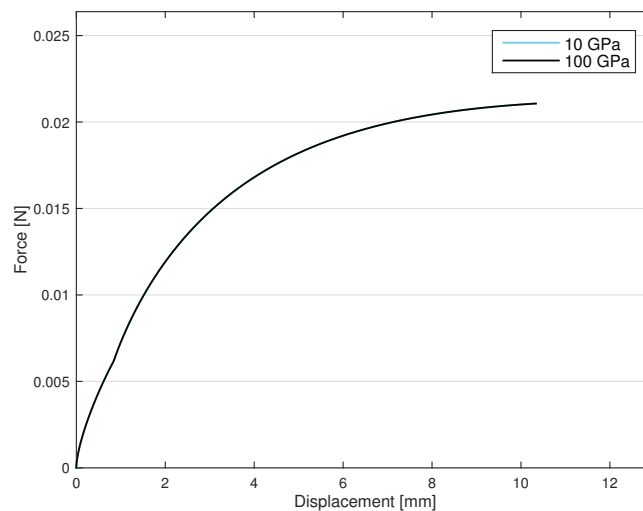


**Fig. A-21: Outcome of the sensitivity analysis (investigated parameter:  $E_l$ )**

Analysis conducted for transverse tensile tests performed at a loading rate of 0.125 N/min. Results for 0.1 GPa and 1 GPa are not presented because of important and slight numerical instabilities, respectively.

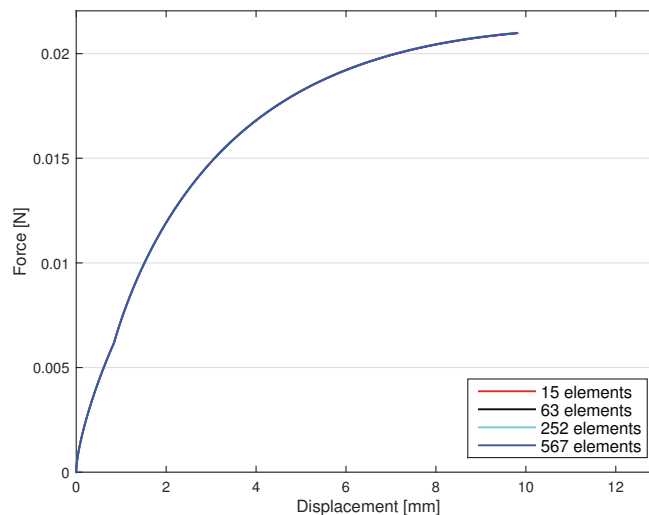


**Fig. A-22: Outcome of the sensitivity analysis (investigated parameter: mesh size)**

Analysis conducted for transverse tensile tests performed at a loading rate of 0.125 N/min. Identification analyses presented in Chapter 5.1.2 are performed with 63 elements.

Sensitivity analysis results performed with three-point bending tests are presented in Fig. A-23, Fig. A-24 and Fig. A-25 for variations of the longitudinal tensile modulus  $E_l$ , the density  $\rho$  and the mesh size, respectively.

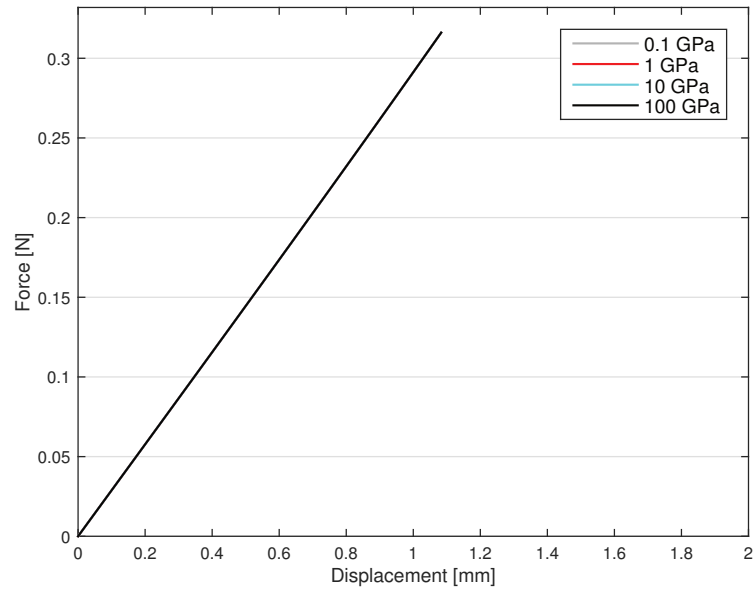


**Fig. A-23: Outcome of the sensitivity analysis (investigated parameter:  $E_l$ )**  
Analysis conducted for three-point bending tests performed at 10000  $\mu\text{m}/\text{min}$ .

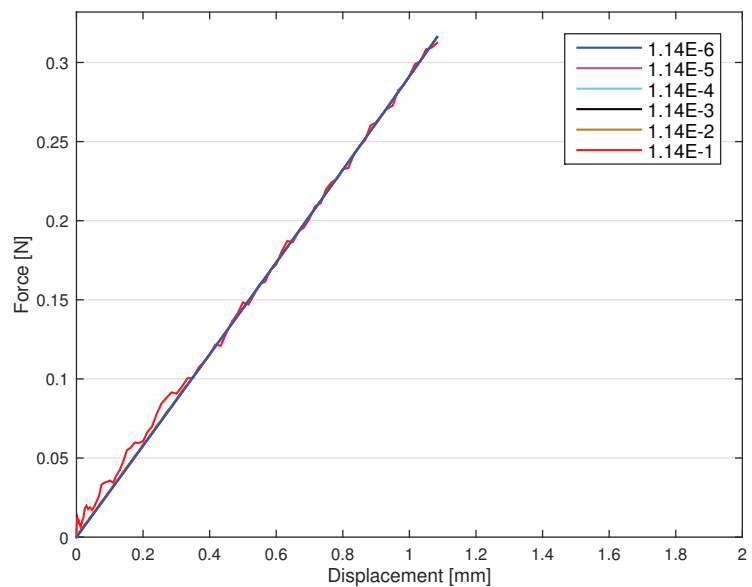


**Fig. A-24: Outcome of the sensitivity analysis (investigated parameter:  $\rho$ )**  
Analysis conducted for three-point bending tests performed at 10000  $\mu\text{m}/\text{min}$ .

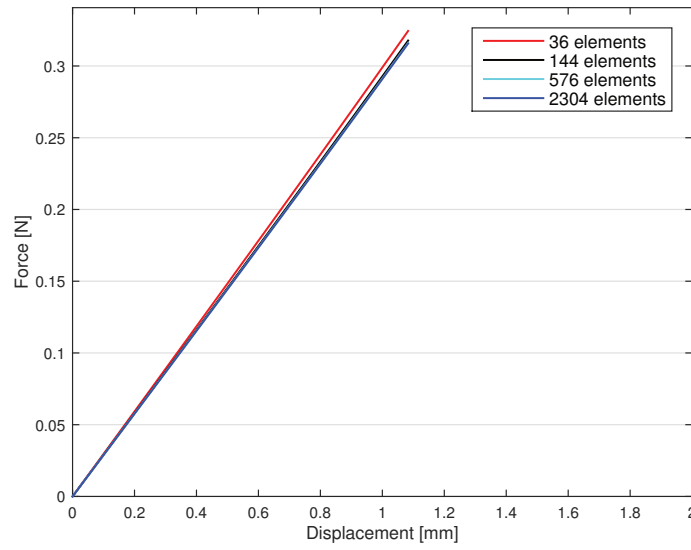


**Fig. A-25: Outcome of the sensitivity analysis (investigated parameter: mesh size)**  
Analysis conducted for three-point bending tests performed at 10000  $\mu\text{m}/\text{min}$ .  
Identification analyses presented in Chapter 5.1.3 are performed with 576 elements.

## k Appendix to Chapter 5.4

The Poisson's ratio  $\nu_{UD-CF/PA6}$  of the unidirectional composite tape (UD-CF/PA6) is approximated using the rule of mixtures:

$$\nu_{UD-CF/PA6} = V_f \cdot \nu_f + (1 - V_f) \cdot \nu_m \quad (\text{A-36})$$

where  $V_f$  is the fibre volume fraction,  $\nu_f$  is the fibre Poisson's ratio and  $\nu_m$  is the matrix Poisson's ratio.

**Tab. A-1: Matrix and fibre Poisson's ratios**

<b>Matrix Poisson's ratio [208]</b>	<b>Fibre Poisson's ratio [209]</b>
<b>[-]</b>	<b>[-]</b>
0.39	0.30

Based on equation (A-36) and material data presented in Tab. 1-1 and Tab. A-1, the composite Poisson's ratio reads:

$$\nu_{UD-CF/PA6} \approx 0.347 \quad (\text{A-37})$$

## I Appendix to Chapter 6.1.4

As presented in Chapter 5.3, Santner [203] reported a decrease of the frictional force when plies, composed of shell elements, are superimposed on top of each other (see Fig. A-26 left). To prevent such an issue to occur, thermoforming simulation models are developed with slightly disorganised film-composite-film layups (see Fig. A-26 right). Displacements of maximum 0.5 mm are applied between two adjacent plies.

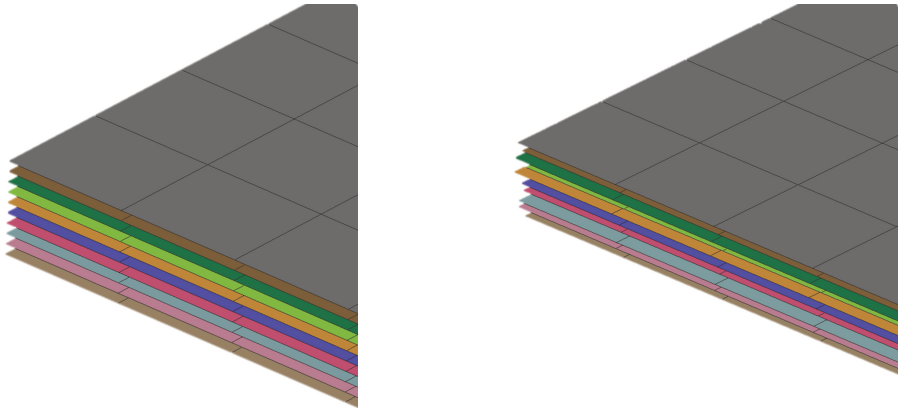


**Fig. A-26: Superimposed (left) and disorganised (right) layup**  
Example given for a generic stack of ten plies.



## m Appendix to Chapter 6.1.5.2

The marks left by the separation films on the surfaces of the preforms (see Fig. 6-7) are considered as fibre orientations by the Matlab routine [204] (see Fig. A-27 and Fig. A-28). Because they influence the calculation of average fibre orientations, measured values are filtered. In the scope of this work, all fibre orientations smaller than  $-20^\circ$  and larger than  $+20^\circ$  are considered as spurious and thus, discarded.

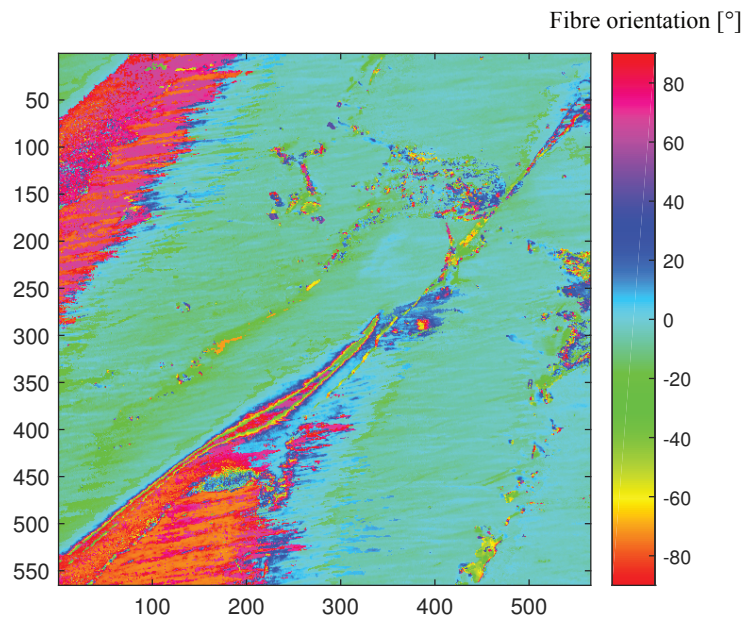


**Fig. A-27:** Typical fibre orientations detected from a measurement taken on a marked surface  
Example given for the  $[0]_8$  350 x 350 mm<sup>2</sup> stack (ROI 5).

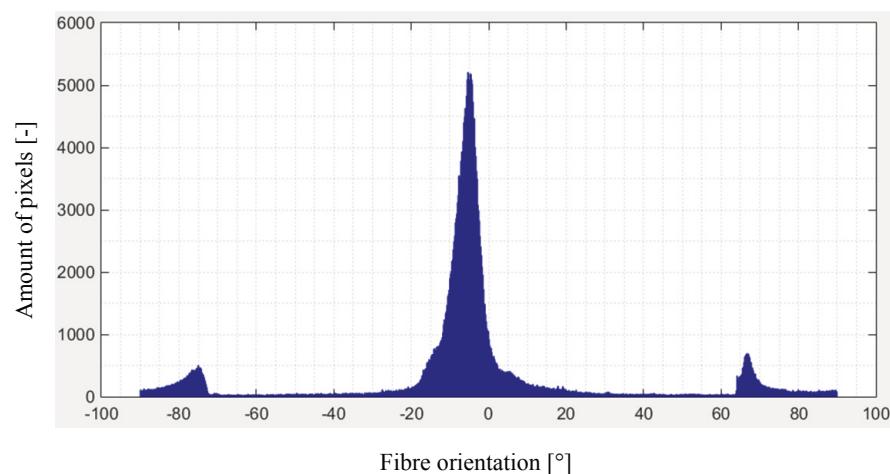


**Fig. A-28:** Histogram representing the distribution of fibre orientation of the measurement presented in Fig. A-27



## B Publications

### Scientific journal papers

- [P1] A. Margossian, S. Bel, J.M. Balvers, D. Leutz, R. Freitas and R. Hinterhölzl, “Finite element forming simulation of locally stitched non-crimp fabrics”, *Compos Part A-Appl S*, vol. 61, no. 0, pp. 152-162, 2014.
- [P2] A. Margossian, S. Bel and R. Hinterhölzl, “Bending characterisation of a molten unidirectional carbon fibre reinforced thermoplastic composite using a Dynamic Mechanical Analysis system”, *Compos Part A-Appl S*, vol. 77, no. 0, pp. 154-163, 2015.
- [P3] A. Margossian, S. Bel and R. Hinterhölzl, “On the characterisation of transverse tensile properties of molten unidirectional thermoplastic composite tapes for thermoforming simulations”, *Compos Part A-Appl S*, vol. 88, no. 0, pp. 48-58, 2016.

### Conferences

- [K1] R. Hinterhölzl, A. Margossian, J.M. Balvers, D. Leutz and R. Freitas, “Characterization and modelling of locally stitched Non-Crimp Fabrics for Forming Simulations” in *ESI DACH Forum*, Wiesbaden, Germany, 2013.
- [K2] A. Margossian, C. D’Angelo, J.M. Balvers, R. Hinterhölzl and R. Freitas, “Characterisation of Ultrasonic Spotwelds for Forming Simulations of multipolies layups” in *17<sup>th</sup> International ESAFORM Conference on Material Forming*, Espoo, Finland, 2014.
- [K3] A. Margossian, M. Ding, L. Avila Gray, S. Bel and R. Hinterhölzl, “Flexural Characterisation of Unidirectional Thermoplastic Tapes using a Dynamic Mechanical Analysis system” in *Proceedings of the 16<sup>th</sup> European Conference on Composite Materials (ECCM)*, Seville, Spain, 2014.
- [K4] C. D’Angelo, A. Margossian, J.M. Balvers, R. Freitas and R. Hinterhölzl, “Joining Techniques in multi-ply preforming operations – Characterization and modelling for virtual forming” in *Proceedings of the 63. Deutscher Luft- und Raumfahrtkongress (DLR-K)*, Augsburg, Germany, Sep. 2014.
- [K5] R. Hinterhölzl and A. Margossian, “Drapiersimulation von trockenen und duro- oder thermoplastischen imprägnierten Textilien” in *4. Fachkongress Composite Simulation*, Fellbach, Germany, 2015.
- [K6] A. Margossian, S. Bel and R. Hinterhölzl, “Characterisation of Tensile Properties Perpendicular to Fibre Direction of a Unidirectional Thermoplastic using a DMA system”, in *Proceedings of the 18<sup>th</sup> International ESAFORM Confer-*

- ence on Material Forming*, Graz, Austria, 2015, Key Engineering Materials, vol. 651-653, pp. 350-355.
- [K7] P. Hörmann, A. Margossian, L. Avila Gray, A. Carrels, K. Zemliana, and K. Drechsler, “Experimental investigation of the visco-elastic material behavior of a non-cured thermoset pre-impregnated fiber material” in *2<sup>nd</sup> International Symposium on Automated Composites Manufacturing*, Montreal, Canada, 2015.
- [K8] A. Margossian, P. Hörmann, K. Zemliana, L. Avila Gray, S. Bel and R. Hinterhölzl, “Shear characterisation of unidirectional thermoset pre-impregnated composites using a rheometer” in *Proceedings of the 19<sup>th</sup> Journées Nationales sur les Composites (JNC)*, Villeurbanne, France, 2015.
- [K9] R. Hinterhölzl and A. Margossian, “Material Characterization and Modelling of the Thermoforming Process” in *ESI DACH Forum*, Bamberg, Germany, 2015.
- [K10] A. Margossian, S. Bel and R. Hinterhölzl, “On the Modeling of Separation Foils in Thermoforming Simulations”, in *Proceedings of the 19<sup>th</sup> International ESAFORM Conference on Material Forming*, Nantes, France, 2016.
- [K11] A. Margossian, A. Reger, B. Singh Pardeshi, S. Bel and R. Hinterhölzl, “Interply Slip Characterisation in Thermoplastic Laminates for the Development of FE Thermoforming Simulations”, in *Proceedings of the 13<sup>th</sup> International Conference on Flow Processes in Composite Materials (FPCM)*, Kyoto, Japan, 2016.

## C Supervised student theses

During my employment at the *Chair of Carbon Composites* of the *Technical University of Munich (TUM-LCC)* I supervised the following student theses:

- [S1] K. Hildermann, confidential Master's thesis in cooperation with Voith Composites GmbH, Chair of Carbon Composites, TUM, 2014, disclosure in 2017.
- [S2] T. Steffen, confidential Master's thesis in cooperation with Voith Composites GmbH, Chair of Carbon Composites, TUM, 2014, disclosure in 2017.
- [S3] M.S. Ding, "Flexural Characterization in fibre direction of Unidirectional Thermoplastic Composites using a Dynamic Mechanical Analysis system", Master's thesis, Chair of Carbon Composites, TUM, 2014.
- [S4] M. Wegerer, "Kinematic and energy based draping simulations as essential preparation for simulation and manufacturing", Term project (Semesterarbeit), Chair of Carbon Composites, TUM, 2014.
- [S5] K. Dargahi, "Modeling and Testing the Material Behavior of CFRP pre-impregnated composites", Master's thesis, Chair of Carbon Composites, TUM, 2014.
- [S6] B. Singh Pardeshi, "Development of the new test setup for the frictional behavior characterization of pre-impregnated composites in a regulated environment", Bachelor's thesis, Chair of Carbon Composites, TUM, 2014.
- [S7] K. Zemliana, "Experimental Investigation of the Viscoelastic Shear Behaviour of Non-cured UD Thermoset Prepregs", Master's thesis, Chair of Carbon Composites, TUM, 2015.
- [S8] A. Reger, "Charakterisierung der Reibung eines thermoplastischen Composites", Term project (Semesterarbeit), Chair of Carbon Composites, TUM, 2015.
- [S9] J. Rösch, "Development of a Method for the Modeling of the Torsion Bar Test Setup Using a Finite Element Software", Term project (Semesterarbeit), Chair of Carbon Composites, TUM, 2015.
- [S10] F. Briza, "Charakterisierung der Schereigenschaften eines duroplastischen und thermoplastischen Materials für die Entwicklung einer Drapiersimulation", Term project (Semesterarbeit), Chair of Carbon Composites, TUM, 2015.
- [S11] O. Immele, "Characterisation of the mechanical properties of a thermoplastic composite material for the development of draping simulations", Term project (Semesterarbeit), Chair of Carbon Composites, TUM, 2016.

- [S12] D. Aziz, “Friction Characterization between Steel Tooling/Tedlar and Silicone Membrane/Wrightlon under Forming Process Conditions for FE Simulation Application”, Bachelor’s thesis, Chair of Carbon Composites, TUM, 2016.
- [S13] L. Tebbe, confidential Master’s thesis in cooperation with Voith Composites GmbH, Chair of Carbon Composites, TUM, 2016, disclosure in 2019.
- [S14] M. Schwab, “Calibration of a carbon-fiber reinforced thermoplastic composite material model for forming simulations with PAM-FORM 2G 2015”, Term project (Semesterarbeit), Chair of Carbon Composites, TUM, 2016.
- [S15] F. Briza, “Konstruktive Optimierung eines Reibungsprüfstands und Charakterisierung der Reibungseigenschaften eines thermoplastischen CFK-Materials für die Drapiersimulation”, Master’s thesis, Chair of Carbon Composites, TUM, 2016.
- [S16] M. Popp, confidential Master thesis in Cooperation with Fraunhofer ICT - Institutsteil Funktionsintegrierter Leichtbau (FIL), Chair of Carbon Composites, TUM, 2016, disclosure in 2019.
- [S17] A. Carrels, confidential Master thesis in Cooperation with BMW, Chair of Carbon Composites, TUM, 2016, disclosure in 2019.

Parts of above listed theses contributed to the underlying doctoral dissertation, as indicated within the text.